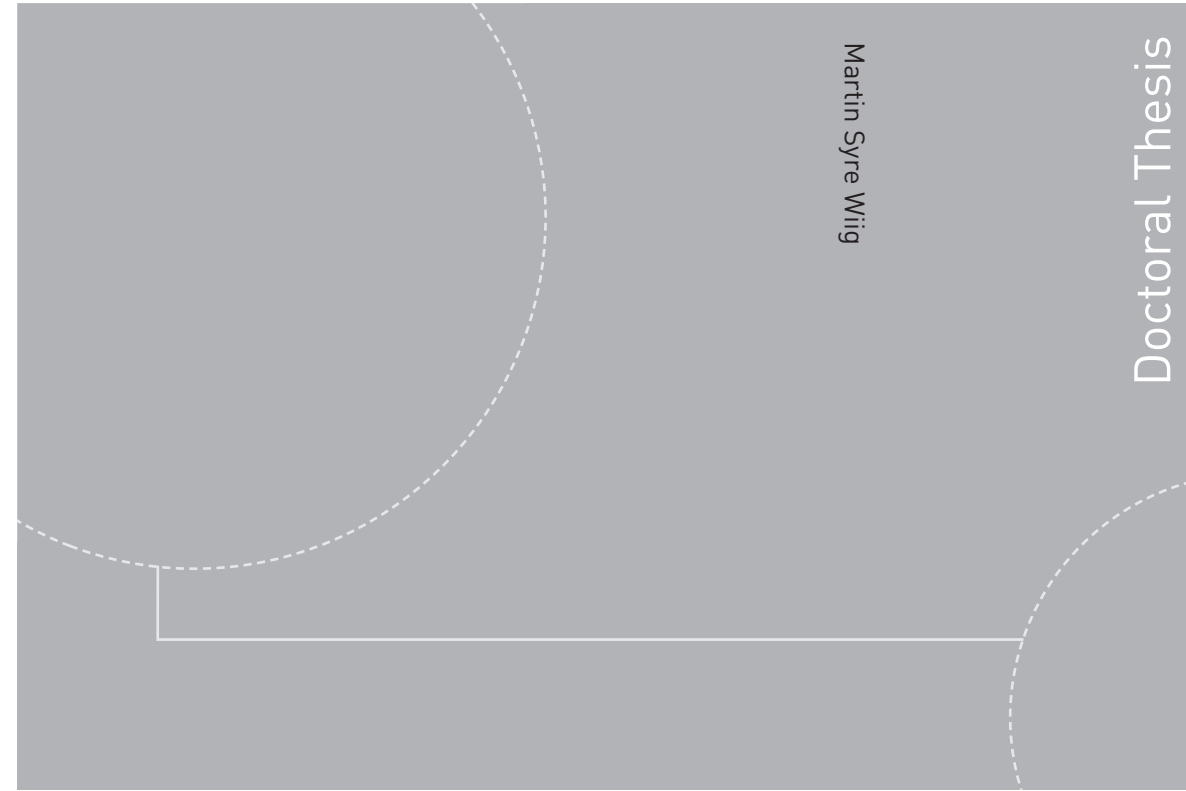


ISBN 978-82-326-3804-8 (printed version)
ISBN 978-82-326-3805-5 (electronic version)
ISSN 1503-8181



Doctoral theses at NTNU, 2019:103

Martin Syre Wiig

Collision Avoidance and Path Following for Underactuated Marine Vehicles

Doctoral theses at NTNU, 2019:103

NTNU
Norwegian University of
Science and Technology
Faculty of Information Technology
and Electrical Engineering
Department of Engineering Cybernetics

 **NTNU**
Norwegian University of
Science and Technology

 NTNU

 **NTNU**
Norwegian University of
Science and Technology

Martin Syre Wiig

Collision Avoidance and Path Following for Underactuated Marine Vehicles

Thesis for the degree of Philosophiae Doctor

Trondheim, April 2019

Norwegian University of Science and Technology
Faculty of Information Technology
and Electrical Engineering
Department of Engineering Cybernetics



Norwegian University of
Science and Technology

NTNU

Norwegian University of Science and Technology

Thesis for the degree of Philosophiae Doctor

Faculty of Information Technology
and Electrical Engineering
Department of Engineering Cybernetics

© Martin Syre Wiig

ISBN 978-82-326-3804-8 (printed version)

ISBN 978-82-326-3805-5 (electronic version)

ISSN 1503-8181

Doctoral theses at NTNU, 2019:103



Printed by Skipnes Kommunikasjon as

To Marie, my pillar in life, and to Jonas and Silje, our fireflies.

This page is intentionally left blank. Well, blankish.

Summary

In this thesis we propose and investigate a collision avoidance algorithm for under-actuated marine vehicles, both in two and three dimensions. We also investigate the stability properties of a path following algorithm for such vehicles, this too in two and three dimensions.

The first part of this thesis establishes some mathematical preliminaries, and provides a mathematical model of the vehicles in question. The underactuation of the vehicles become apparent in the vehicle model in that a part of the vehicle's velocity cannot be directly controlled, but is induced when the vehicle is maneuvering. Specifically, when a 2D vehicle turns, the momentum of the vehicle will transform some of its forward speed to a sideways (sway) speed. A similar phenomenon occurs when a 3D vehicle pitches, which will induce a heave speed along the normal axis of the vehicle. This effect is important to consider both during path following and during collision avoidance.

In the second part of the thesis we examine the integral line of sight (ILOS) guidance law for straight-line path following. The guidance law imitates the way an experienced helmsman steers a ship by aiming the vehicle a certain distance, called the lookahead distance, ahead of it on the path. Integral effect is added to compensate for an ocean current, which is modeled as a kinematic disturbance uniform in time and space.

The ILOS guidance law has been in successful use for several years, for example on the Hugin series of autonomous underwater vehicles (AUVs). In this thesis, we will examine the stability properties of the guidance law, and give conditions under which it can be shown to provide uniform semiglobal exponential stability (USGES) of the closed-loop error dynamics. Furthermore, we propose a new variant of the guidance law, where the lookahead distance is designed to increase with the vehicle speed, and we provide USGES conditions for the speed dependence. This design choice is motivated both by intuition and by practical considerations, and will make the vehicle avoid overshoot and oscillations caused by slow convergence or saturations in the underlying controllers. Finally, we will examine 3D path following, using the ILOS guidance law to steer both heading and pitch. We remove a common assumption that the vehicle is neutrally buoyant in water, and provide conditions of USGES in this scenario as well.

In the third part of the thesis, we focus on collision avoidance in two dimensions. We propose a collision avoidance algorithm, the constant avoidance angle (CAA) algorithm, which employs a novel mechanism for compensation of the obstacle's velocity. The intuition behind the algorithm is simple; the vehicle measures the

direction to the edges of the obstacle, and adds an avoidance angle to each of these edges in the direction away from the obstacle. Thus, the algorithm creates two safe directions, one on the port side of the obstacle, and one on the starboard side.

If the obstacle is moving, each of these edges are rotated to compensate for the obstacle's velocity. The resulting directions are safe at a given vehicle speed, which can thus be used as an input to the CAA algorithm. Unlike for algorithms which specify both the direction and magnitude of the velocity required to avoid an obstacle, the CAA algorithm thus provides flexibility in the design of the desired speed trajectory.

We will show how this flexibility can be utilized by applying the algorithm to a unicycle restricted to keep a constant speed, thus demonstrating how the algorithm is suitable for vehicles with a limited speed envelope. This includes both fixed-wing aircraft, which must avoid stalling, and many marine vehicles, which may have a high acceleration cost, and which can lose controllability at low speeds. In the unicycle case, we provide conditions under which safe avoidance of a moving obstacle is guaranteed. Specifically, we derive an upper bound on the required yaw rate during the maneuver, as well as a lower bound on the required distance from the obstacle at which, at the latest, the vehicle must start the avoidance maneuver in order to turn away safely.

We next apply the algorithm to an underactuated marine vehicle required to keep a constant forward speed. The underactuated sway components of the vehicle makes the vehicle's heading point in a different direction than the vehicle's course (i.e. the direction of the vehicle's velocity vector). Thus, even though the vehicle points in a safe direction, it may still move towards a collision. We solve this by the use of a course controller, where we employ a model of the underactuated dynamics in order to steer the vehicle course. We provide conditions under which safe avoidance is still guaranteed, and under which all the control signals in the system remain well defined. We furthermore combine the collision avoidance law both with a target reaching guidance law, and with a path following guidance law. The results are verified both in simulations and through full-scale experiments. In the experiments, we also demonstrate how multiple obstacles can be handled by the algorithm.

In the fourth and final part of the thesis, we extend the CAA algorithm to 3D. The vehicle now measures a three-dimensional cone to the outline of the obstacle, and each ray of this cone is rotated an avoidance angle away from it, creating an extended vision cone. Obstacle motion is compensated for by a transformation of this vision cone, using the same technique as in two dimensions. The resulting collection of rays constitute a compensated vision cone, where each ray is a provably safe direction. As in the 2D case, the vehicle speed is used as an input to the algorithm, and we first demonstrate this by applying the algorithm to a 3D vehicle with nonholonomic constraints in sway and heave, and with a constant forward speed. We utilize the flexibility offered by operating in 3D by choosing a safe direction which seeks to move behind the obstacle, while minimizing the required pitch and yaw rate. This enables us to build on the results from the analysis of the 2D algorithm in deriving upper bounds on the required pitch and yaw rate during the avoidance maneuver. Furthermore, we are able to limit the vehicle pitch during the maneuver, thus showing how the algorithm can make the vehicle comply

with operational constraints often present in practice. Finally, we derive conditions under which a safe avoidance maneuver can be guaranteed.

The 3D CAA algorithm is applied to an underactuated underwater vehicle with underactuation in sway and heave and with a constant desired forward speed. To steer the vehicle's velocity direction, we propose a Flow frame controller, where the Flow frame is defined as a frame aligned with the vehicle's velocity vector. Through the use of this frame, we derive conditions on the controller and on the CAA algorithm under which obstacle avoidance is ensured. The sway and heave speeds are furthermore guaranteed to be bounded during the maneuver, and bounds on the pitch of the vehicle's velocity vector are upheld. The results are verified through several simulations, as well as through full-scale experiments on the Hugin autonomous underwater vehicle, and it is demonstrated how the algorithm can be applied to a multi-obstacle scenario.

Contents

Summary	iii
Contents	vii
List of Figures	xi
List of Tables	xv
Preface	xix
1 Introduction	1
1.1 Path following	2
1.2 Collision avoidance	5
1.3 Contributions	11
1.4 Thesis outline	16
I Preliminaries	19
2 Mathematical Preliminaries	21
2.1 Notation	21
2.2 Reference frames	22
2.3 Utility functions	22
2.4 Stability definitions and theorems	23
3 Modeling of Underactuated Marine Vehicles	27
3.1 Kinematics	27
3.2 Dynamics	29
3.3 Ocean current and relative velocities	33
3.4 Assumptions summary	34
II Path Following	35
4 Integral Line of Sight Path Following for Surface Vehicles	37
4.1 System description	38
4.2 Control system	39
	vii

4.3	Closed-loop kinematic stability	40
4.4	Stability of the closed-loop kinematics and dynamics	43
4.5	Simulations	48
4.6	Conclusions	49
4.A	Functional expressions	50
5	ILOS Guidance with a Speed-dependent Lookahead Distance	53
5.1	System description	54
5.2	Control system	56
5.3	Error dynamics	57
5.4	Constant desired surge speed	59
5.5	Time-varying desired surge speed	61
5.6	Simulations	63
5.7	Experimental results	65
5.8	Conclusions	67
5.A	Functional expressions	67
6	Path Following for Underwater Vehicles Without Neutral Buoyancy	69
6.1	System description	69
6.2	Control system	72
6.3	Stability of the closed-loop system	73
6.4	Simulations	78
6.5	Conclusions	81
6.A	Functional expressions	81
6.B	Proof of Lemma 6.2	83
III	Collision Avoidance in 2D	87
7	The CAA Algorithm in 2D	89
7.1	Obstacle model	90
7.2	Algorithm definition	91
7.3	Algorithm analysis	96
7.4	Overview of Part III	99
8	The CAA Algorithm for Unicycles	101
8.1	System description	101
8.2	Control system	102
8.3	The CAA algorithm	103
8.4	Analysis	104
8.5	Simulations	108
8.6	Conclusions	112
9	Including the Underactuated Dynamics in the CAA Algorithm	113
9.1	System description	113
9.2	Control system	116

9.3	The CAA algorithm	116
9.4	Analysis	118
9.5	Simulations	125
9.6	Conclusions	127
9.A	Functional expressions	129
10	The CAA algorithm for underactuated surface vehicles	131
10.1	System description	132
10.2	The CAA algorithm	134
10.3	Nominal guidance laws	135
10.4	Course controller	136
10.5	Surge and yaw rate controllers	138
10.6	Analysis	139
10.7	Simulation results	146
10.8	Experimental results	150
10.9	Conclusions	154
10.A	Functional expressions	154
IV	Collision Avoidance in 3D	157
11	The CAA algorithm in 3D	159
11.1	Obstacle model	159
11.2	Algorithm definition	161
11.3	Algorithm analysis	166
11.4	Overview of Part IV	167
12	The CAA Algorithm for 3D Kinematic Vehicles	169
12.1	System description	170
12.2	The CAA algorithm in 3D	172
12.3	Control system	174
12.4	Analysis	175
12.5	Simulations	182
12.6	Conclusions	189
13	The CAA algorithm for underactuated underwater vehicles	191
13.1	System description	192
13.2	The CAA algorithm in 3D	196
13.3	Control system	199
13.4	Analysis	202
13.5	Simulations	213
13.6	Experiments	221
13.7	Conclusions	223
13.A	Functional expressions	227
14	Conclusions and Future Work	229

References

235

List of Figures

4.1	Geometry of the ILOS guidance law.	40
4.2	Position and heading during a path following simulation.	48
4.3	Cross track error during a path following simulation.	49
4.4	The natural logarithm of the error norm.	49
4.5	Position and heading when there is a heading measurement error.	50
4.6	Cross-track error when there is a heading measurement error.	50
5.1	The current compensation angle for a large and small vehicle velocity.	55
5.2	The lookahead distance increases linearly with speed.	56
5.3	The cross-track error for increasing lookahead distances.	64
5.4	The cross-track error for increasing speeds.	64
5.5	The cross-track error for increasing forward speeds.	64
5.6	The cross-track error during a time-varying forward speed.	65
5.7	The Odin USV.	65
5.8	The vehicle position during experiments with a speed-dependent lookahead distance.	66
5.9	The cross track error with different lookahead distances.	66
5.10	The cross track error for different forward speeds.	66
6.1	Position and pitch of the vehicle in the $x - z$ plane during the simulation.	79
6.2	Position and pitch of the vehicle in the $x - y$ plane during the simulation.	79
6.3	The relative heave velocity w_{rb} during the simulation.	79
6.4	The cross-track errors y_b^n and z_b^n of the vehicle.	80
6.5	The natural logarithm of $\ \mathbf{e}_{\text{tot}}\ $	80
6.6	Position and pitch of the vehicle in the $x - z$ plane when W_E is unknown to the controllers.	80
7.1	The vision cone \mathcal{V}_o from the vehicle to the obstacle.	91
7.2	The extended vision cone \mathcal{V}_e from the vehicle to the obstacle.	93
7.3	The desired velocity vector in collision avoidance	93
7.4	Switching rule	95
7.5	Decomposition of the angle ψ_{dca2}^n	97
7.6	The CAA algorithm as a vector field.	98

8.1	Geometry of the CAA algorithm.	104
8.2	Unicycle simulation with a head on obstacle	109
8.3	Unicycle simulation with a head on obstacle - details	109
8.4	Unicycle simulation with a circling obstacle	110
8.5	Unicycle simulation with a circling obstacle - details	110
8.6	Unicycle simulation with a concave obstacle	111
8.7	Unicycle simulation with a concave obstacle - distance	111
9.1	Geometry of the CAA algorithm.	117
9.2	Illustration of the minimum switching distance.	122
9.3	Avoiding a pursuing obstacle	126
9.4	Obstacle distance and vehicle sway in the second scenario.	126
9.5	The third scenario, where the obstacle has the shape of a ship.	127
9.6	Obstacle distance and vehicle sway in the third scenario.	128
10.1	Geometry of the CAA algorithm.	135
10.2	LOS guidance law	137
10.3	Minimum switching distance	142
10.4	Surface vehicle simulation in a head on scenario.	147
10.5	Surface vehicle simulation in a crossing scenario.	148
10.6	Surface vehicle simulation with path following and collision avoidance.	149
10.7	Obstacle distance during surface vehicle simulations.	149
10.8	Vehicle sway during surface vehicle simulations.	150
10.9	Surface vehicle simulation with a ship shaped obstacle.	151
10.10	Experimental run with surface vehicle and two obstacles.	152
10.11	Experimental run with surface vehicle and five obstacles.	153
11.1	The vision cone from the vehicle to the obstacle	161
11.2	The vision cone \mathcal{V}_o (black) and the extended vision cone \mathcal{V}_e	162
11.3	A cross-section of the compensated vision cone.	163
11.4	Creation of the motion compensated vision cone \mathcal{V}_c	164
11.5	The cost function used to select among the safe directions.	165
12.1	A cross-section of the compensated vision cone.	173
12.2	The extended vision cone \mathcal{V}_e and the compensated vision cone \mathcal{V}_c	173
12.3	Geometry of a collision avoidance maneuver in the vertical plane.	177
12.4	The triangle for finding γ_{ca} using the sine rule.	178
12.5	Illustration of the minimum required switching distance.	181
12.6	Static obstacle simulation	184
12.7	Obstacle distance	184
12.8	Required pitch and yaw rate	185
12.9	Crossing obstacle simulation	186
12.10	Obstacle distance	186
12.11	Required pitch and yaw rate	187
12.12	Pursuing obstacle simulation	187
12.13	Obstacle distance	188
12.14	Required pitch and yaw rate	188

13.1	A cross-section of the compensated vision cone.	197
13.2	The compensated vision cone \mathcal{V}_c	198
13.3	Geometry of a collision avoidance maneuver in the vertical plane.	205
13.4	Triangle for finding the motion compensation angle.	206
13.5	Illustration of the minimum required switching distance.	209
13.6	A scenario where the vehicle and the obstacle meet head on head.	214
13.7	The sway and heave speeds during a collision avoidance simulation.	214
13.8	Obstacle distance and Flow frame pitch during a collision avoidance simulation.	215
13.9	A scenario where the obstacle crosses horizontally in front of the vehicle.	216
13.10	The sway and heave speeds during a collision avoidance simulation.	216
13.11	Obstacle distance and Flow frame pitch during a collision avoidance simulation.	217
13.12	A scenario where the obstacle crosses vertically in front of the vehicle.	217
13.13	The sway and heave speeds during a collision avoidance simulation.	218
13.14	Obstacle distance and Flow frame pitch during a collision avoidance simulation.	218
13.15	Snapshots from a simulation where the vehicle meets a cluster of five obstacles.	219
13.16	The distances to each of the obstacles in the first multi-obstacle scenario.	220
13.17	Snapshots from a simulation where the vehicle meets three obstacles, two crossing in front of it and one moving towards it.	220
13.18	The distances to each of the obstacles in the second multi-obstacle scenario.	221
13.19	The Hugin HUS vehicle.	221
13.20	The surge speed u_b and the total vehicle speed U_b during run 4.	222
13.21	Snapshots from the maneuver during run 6.	224
13.22	The obstacle distance and Flow frame pitch during run 6.	224
13.23	The sideslip β_b and angle of attack α_b during run 6.	225
13.24	Snapshots from run 4, where the obstacle crosses horizontally in front of the vehicle.	225
13.25	The obstacle distance and Flow frame pitch during run 4.	226
13.26	The sideslip β_b and angle of attack α_b during run 4.	226

List of Tables

1	Acronyms	xvii
2.1	Reference frames	23
12.1	Simulation parameters	182
12.2	Simulation results	183
13.1	Simulation parameters	213
13.2	Experiment parameters	222
13.3	Experiments summary	223

Acronyms and Abbreviations

Table 1: Acronyms

Acronym	Explanation
2(3)D	2(3) dimensions/dimensional
AUV	Autonomous underwater vehicle
CAA	Constant avoidance angle
COLREGs	The International regulations for preventing collisions at sea
DOF	Degree(s) of freedom
ELOS	Enclosure-based line of sight
FFI	Norwegian Defence Research Establishment (Forsvarets forskningsinstitutt)
(U)GES	(Uniform) Global exponential stability
(U)LES	(Uniform) Local exponential stability
LOS	Line of sight
ILOS	Integral line of sight
MPC	Model predictive control
(U)GAS	(Uniform) Global asymptotic stability
(U)SGES	(Uniform) Semiglobal exponential stability
USV	Unmanned surface vehicle

Preface

This thesis is submitted in partial fulfillment of the requirements for the degree of philosophiae doctor (PhD) at the Norwegian University of Science and Technology (NTNU). The work has been carried out at the Department of Engineering Cybernetics and the Center for Autonomous Marine Operations and Systems (AMOS). My main supervisor has been Professor Kristin Ytterstad Pettersen and my co-supervisor has been Dr. Thomas Røbekk Krogstad at the Norwegian Defence Research Establishment (FFI).

The remainder of this Preface is organized as follows. In Section P.1 we extend our gratitude to.. nah, just kidding. This is the one place within this thesis where I can lay aside the formal, sometimes stilted (at least with my humble words) academic language, and write with a more free pen. I'm not saying that its going to be poetic, I'm an engineer at heart after all, but at least there will be no greek letters like ξ or γ (darn, blew that one right away).

Even though a PhD can be a rather selfish undertaking, at least it has been in my case, it is certainly not something one achieves by oneself. Throughout these last four and a half years there has been lots of people supporting me, pushing me on and cheering me up.

First of all, getting full score in all three categories, is of course Professor Kristin Ytterstad Pettersen. I am very grateful to her for giving me the opportunity to do my PhD at NTNU and AMOS, and not least for her continuous support, cheerful demeanor and earnest encouragement at all times. I have always walked a way from her supervisions with a strong motivational boost and a big smile on my face, both of which I have valued greatly. I'm sure every other PhD student of hers will agree.

I am also very grateful to my co-supervisor, Dr. Thomas R. Krogstad. He has not only been an everyday support at FFI, but is also a very good friend and colleague. In addition to his academic insights and nudges, I have especially valued his perspective as a former PhD student himself. By bringing the seemingly insurmountable challenges down to earth, and putting them into perspective with a nice splash of stolid engineering humor, he has been a staunch reminder that everything is going to be Okay. I am also very aware that his responsibilities at FFI did not become easier when I entered into the world of Lyapunov at NTNU, and I'm amazed that he was still able to find the time, will and energy to supervise me through the whole thing.

Among the more scary things Kristin made me do during my PhD was to go to Sydney and visit Professor Andrey Savkin at the University of New South Wales. The visit to Professor Savkin turned out not to be scary at all, but rather a pivotal

point in my work. Even though we only had two short meetings, his openness and insights lay the foundation for the collision avoidance algorithm I have since been working on and developing. He deserves, and has, my gratitude for welcoming me, and for being such an inspirational character.

At all times during the PhD work, I have cherished the support from all my colleagues at FFI, especially from the Hugin and Autonomy teams. André Pettersen deserves thanks for supporting me both morally and financially, and for never letting there be any doubt in his backing of my PhD work. Dr. Roy Edgar Hansen deserves thanks for nagging for several years about the importance of doing a PhD, before finally pushing me over the edge. Øivind, Solveig and Rikke have all struggled to try to get me to do FFI stuff, while not being too pushy. I'll promise to do better now! Erik has been a great office-mate at FFI, and he has made an effort to appear impressed at the equations I've been struggling with. He's an actual mathematician, so I don't really believe him, but I appreciate the gesture.

A special thanks goes to Ole Jacob Lorentzen and Dr. Marc Geilhufe for being Hugin operators during the experiments on the Hugin AUV, and for their can-do-attitude regarding these trials. And not least thanks to Dr. Petter Lågstad for letting me implement my software on the Hugin HUS AUV. I have a history of smashing his vehicle into stuff, so he is very brave each time he lets me back in.

I would also like to thank the great PhD community at AMOS and ITK. Each time I have been to Trondheim, they have been very welcoming to this weird, bearded guy suddenly in their midsts. I am especially grateful to Dr. Signe Moe for being my 'fadder' (godmother?) when I arrived, showing me around and helping me find my bearings. I also had the pleasure of working with her on the experiments on R/V Gunnerus, and she was a great help and inspiration when implementing our stuff into the software structure of an actual DP system. Thanks also to Anna, for helping me along, Erlend, for being a funny guy, Claudio, for showing me how it is possible not to be stressed at all, and Eleni for being painfully honest yet caringly warmhearted.

Thanks to Dr. Walter Caharija, my predecessor in many ways, for providing me with his insights into line of sight guidance, and for coming up with good ideas to help me along my track. He has been popping up at various conferences, and has always provided me with a pat on the back and lifting spirits.

During the experiments on the R/V Gunnerus, we had great help from Øystein Lurås, Inge Spangelo and Bjørn Ole Vinje at Kongsberg Maritime. They provided not only access to their control system API, but they also devoted a significant amount of time in giving us invaluable support before and during the experiments. I would also like to thank the crew of the Gunnerus for having us aboard, and for bravely letting us take control of their vehicle. Luckily, they were not aware of my smashing history with the Hugin.

The unsung heroes of many a saga is the HR people. During my PhD time I have had positions both at NTNU and FFI, with all that entails regarding wage calculations and vacation calculations and, not least, paternal leave calculations. The HR people at both places have been nothing but supportive, and have always been eager to help whenever I have stumbled around in the administrative jungle, making a mess of things.

I would like to offer sincere thanks to my family in Trondheim. Both my mother, my father and Maien have been more than eager to have me visiting during my many trips to Trondheim, and I have always been able to bring one of my kids, whom they have watched and spoiled while I have been working. My travels to Trondheim and my time away from home might easily have become a significant drawback of the PhD process, but by their warmth and flexibility to baby-sit, it has become a boon where Jonas and Silje have had the chance to get to know the Trondheim branch of the family really well. Thanks!

Finally, I would like to give my wife Marie my most heartfelt thanks. Finishing this work would not have been possible, nor desirable, without her continuous love and support. She's the one who has stayed home fixing things when I'm away on academic adventures, and she's the one bringing me up when I'm low (and sometimes down to earth when I'm too far up), and she has a wonderful ability to make me realize what's important in life. The greatest putters of things in perspective are, of course, Jonas and Silje. They are my jewels, and they have an impressive amount of patience for their dad's absentmindedness. I love you very much all three of you.

Chapter 1

Introduction

Begin at the beginning, the King said gravely, and go on till you come to the end: then stop.

— Lewis Carroll, *Alice in Wonderland*

Unmanned marine vehicles are often intended to operate with limited, delayed or no human supervision. They are employed in tasks such as transportation, seafloor mapping, oceanographic surveying or ocean surveillance [9, 69], and the environment they operate in can be dynamic or unknown, with only incomplete or partially erroneous a priori information available before the operation. An important function for such vehicles is the ability to react to the environment, for example to avoid collisions with obstacles, or to counteract disturbances such as an ocean current pushing the vehicle off a desired path. In this thesis, we will propose a collision avoidance algorithm, the constant avoidance angle (CAA) algorithm, which will safely make a vehicle achieve a goal such as target reaching or path following, both in 2D and 3D. In addition, we will examine the stability properties of a path following guidance law with disturbance rejection, the integral line of sight (ILOS) guidance law.

Both the proposed collision avoidance algorithms and ILOS guidance law are *reactive* algorithms [94], which is to say that they react directly to sensor input, without dependence on planning, and that the required sensor information is restricted (i.e. they do not require a comprehensive world model). Such algorithms are, in general, less computationally demanding than *deliberate* algorithms, which do rely on planning, usually through a computational search. Hence, reactive algorithms tend to be suitable as the primary steering algorithms for low-cost or small vehicles with limited processing power. They can also be used together with a deliberate algorithm in a hybrid architecture, where they can reduce the required planning complexity. For example, if the vehicle is equipped with a path following algorithm, the planner may only need to create plans with a limited (and perhaps smooth) curvature, rather than create a sequence of rudder angles. Finally, reactive algorithms can serve as backup algorithms for safety critical functions such as collision avoidance, should the deliberate algorithm fail.

In this thesis, we will specifically consider collision avoidance and path following for a class of vehicles known as *underactuated* marine vehicles. Many marine vehicles belong to this class, and they can be modeled as vehicles equipped with stern propellers generating forward (surge) thrust, steering rudders generating a

control moment in yaw and, in the case of underwater vehicles, sternplanes generating a control moment in pitch. There is no control force in the upwards (heave) or sideways (sway) directions, and hence there is an underactuation. Even though some vehicles are equipped with thrusters providing control forces in sway or heave, such thrusters lose effectiveness at maneuvering speeds [52], making these vehicles underactuated in this regime. Thus, when considering algorithms for marine vehicles operating at maneuvering speed, it is important to include the underactuated dynamics in the design and analysis of the control system, as discussed by Pettersen and Egeland [85]. While the sway and heave movement cannot be directly controlled for such vehicles, they are induced during turning and pitching, and can make the vehicle glide into an obstacle as it tries to turn away. It thus becomes an especially important factor to consider in the design and analysis of collision avoidance algorithms for such vehicles.

The algorithms we will propose and analyse in this thesis are at the guidance level. Algorithms at this level provide heading, pitch and surge reference trajectories to underlying controllers. Thus, guidance algorithms are of a modular nature, and can be easily implemented on a wide variety of vehicles. We will exploit this fact in our experiments.

Traditionally, guidance laws enable underactuated marine vehicles to achieve goals such as target tracking, path following and trajectory tracking [17, 27, 35]. When a vehicle is engaged in target tracking, the goal is to make the vehicle reach a (possibly moving) point in space. Path following is concerned with making the vehicle converge to and follow a path, without any constraints as to where on the path the vehicle should be at any given time. Trajectory tracking adds such a time constraint, and the goal of the vehicle is to follow a time-dependent trajectory in space. A review of algorithms for achieving such goals can be found in Ashrafiuon et al. [4]. In this thesis, we will treat collision avoidance as another guidance goal.

1.1 Path following

Precise path following is essential in operations such as inspection of submarine pipelines, seabed mapping, and subsea photography. Guidance laws for path following are hence highly relevant for the research and development of autonomous marine vehicles.

An early work in control of an underactuated marine vehicle is found in Pettersen and Egeland [85], which uses input-output linearization and backstepping in order to achieve set-point control of an underactuated marine vehicle. The results are extended to trajectory following of a curved trajectory in Pettersen and Nijmeijer [87], which motivated Indiveri et al. [48] and Indiveri et al. [49] to employ a design methodology previously used by Aicardi et al. [2] on unicycles to make an underactuated marine vehicle follow a straight-line path. The algorithm presented by Do et al. [25] also uses linearization and backstepping, and is able to achieve exponential convergence to a straight-line path.

The line of sight (LOS) family of guidance laws has proven well suited for underactuated vehicles. The algorithm mimics the way an experienced helmsman steers a ship by aiming towards a point that lies on the path ahead of the vessel.

It was first analyzed by Pettersen and Lefeber [86], and has been used in several papers [11, 15, 34, 36, 39, 67]. It is shown by Pettersen and Lefeber [86] that the algorithm provides uniform global κ -exponential stability (i.e. uniform global asymptotic stability (UGAS) and uniform local exponential stability (ULES) as defined by Sørдалen and Egeland [101]) of the path error and the state errors of a simple vehicle model in three degrees of freedom (3 DOF). More complete models of the vehicles are analyzed by Børhaug and Pettersen [11] and Fredriksen and Pettersen [39]. In Lekkas and Fossen [67], the LOS guidance scheme is applied to a fully actuated vehicle following curved paths parametrized as monotone cubic Hermite splines, and it is proven that the system is κ -exponentially stable. Finally, Fossen and Pettersen [36] proves uniform semiglobal exponential stability (USGES) of the LOS guidance when applied to an underactuated vehicle following straight-line paths.

USGES is as close to uniform global exponential stability (UGES) as it is possible to get with LOS guidance laws, as there is a trigonometric saturation in the kinematic representation when the vehicle surge speed is bounded [36]. Indeed, for any path following law with an upper bound on the vehicle surge speed, vehicle convergence to the path can never be faster than when moving straight towards the path, and hence global exponential results are not achievable.

In enclosure-based LOS (ELOS), described in Fossen [35], the vehicle is directed towards a point defined as one of the two intersection points between a circle centered on the vehicle and the desired path. This can be viewed as a lookahead-based approach with an implicitly time-varying lookahead distance, where the lookahead distance is dependent of the cross track error. A drawback with this method is that the circle radius must always be greater than or equal to the cross track error, in order to ensure that it intersects with the path. Several approaches have been proposed to overcome this requirement. Among them are using a circle radius that varies linearly with the cross track error, as in Moreira et al. [76], or exponentially as in Khaled and Chalhoub [54]. Another approach is to use a switching scheme to specify the circle radius. This is shown in Abdurahman et al. [1], where a constant circle radius is used for low cross track errors, and a linearly varying radius is used for large cross track errors.

To compensate for drift caused by environmental disturbances such as an ocean current, integral action is added to the LOS guidance law in Børhaug et al. [13]. The resulting integral line of sight (ILOS) guidance law is proven to be globally stable when the current is modeled on the kinematic level. By considering the vehicle velocity measured relative to the water, this result is extended to global κ -exponential stability in Caharija et al. [18], which also considers wind and wave disturbances on the kinetic level. The ILOS guidance law is furthermore extended to 3D in Caharija et al. [18], which employs a decoupled horizontal and vertical guidance law to provide global κ -exponential convergence to a straight-line 3D path in the presence of an ocean current with both vertical and horizontal components.

The integral term in the ILOS guidance law is modified in Fossen et al. [37] to achieve integral action using adaptive sideslip estimation, and USGES is achieved for a closed-loop kinematic model of an underactuated marine vehicle following straight-line paths. Although the vehicle dynamics are not included in the analysis, the path error is numerically shown to be bounded when the vehicle is following

paths consisting of straight line segments connected by circular turns (i.e. Dubins paths [26]).

By appropriate design of the desired surge speed, a path following guidance law can also be used for trajectory tracking or formation control. This is for example the approach of Lekkas and Fossen [68], where the ILOS guidance law is used to provide global κ -exponential path convergence, while a feedback linearizing surge speed trajectory is used to provide GES convergence to a desired, moving particle around the path. When the dynamics of the vehicle are included in the analysis, it is proven that the system obtains global κ -exponential stability when following straight-line paths.

Formation control can also be achieved by using the (I)LOS guidance law and an appropriately designed surge speed trajectory. In Børhaug et al. [14], a group of underactuated marine vehicles is kept in a formation following a straight-line path. Each vehicle uses the LOS guidance law to converge to a desired cross-track offset to the path, while the desired surge speed trajectory makes the vehicles keep a desired relative along-track distance. The formation is made to converge to a desired, constant speed. Vehicle dynamics are considered, and it is proved that the vehicles converge to the formation exponentially.

In Belleter and Pettersen [7] and Belleter and Pettersen [8], formation control of underactuated marine vehicles in the presence of a constant and irrotational ocean current is investigated. The algorithm presented uses the ILOS guidance law to drive the vehicles to within a desired cross-track offset to a straight-line path, where the offset is decided by the vehicle's position in the formation. The vehicles are set to maintain a constant forward speed, but each vehicle has an additional component to the desired forward speed in order to drive them to their desired along-track positions in the formation. Thus, the vehicles have a time-varying forward speed during the maneuver, until the speed settles at a steady state value as the system reaches its equilibrium.

An important design parameter for (I)LOS guidance laws is the lookahead distance Δ . In Lekkas and Fossen [66], the speed dependency of the optimal lookahead distance for a given vessel employing the LOS guidance law is investigated. It is shown that the optimal Δ increases with increasing surge speed of the vehicle. This matches with intuition, as a longer lookahead distance will give smoother turns at higher speed. In particular, it is to be expected that the overshoot of the system will be reduced, even in the presence of slow heading controllers. Furthermore, this also matches with how an experienced helmsman would steer a ship; the faster the ship goes, the further ahead the helmsman will look. These results are utilized in Flåten and Brekke [33], where an LOS guidance law with a speed-dependent lookahead distance is used in combination with a time-varying desired surge speed to achieve trajectory tracking of general curved paths. The analysis proves that the control system provides locally exponential convergence to a straight-line path, and ultimate boundedness for the path error when the path is curved.

The LOS path following law can be directly applied to a curved path, using a path parametrization such as the Serret-Frenet frame, in effect making the vehicle steer towards the path tangential. This is for example the approach used by Fossen and Pettersen [36], although the stability analysis in the paper assumes straight-line paths. Compensating for an ocean current is, however, more challenging when the

path is curved, as the cross-track effect of the current then becomes time-varying as the vehicle moves along the path. One solution to this problem is the use of current observers, as is done by Moe et al. [75], Maghenem et al. [71], and Belleter et al. [6].

1.2 Collision avoidance

The collision avoidance problem has been fairly well studied, particularly in 2D, with surveys of existing algorithms given in [47, 59, 103, 104]. The various algorithms are often sorted into two families [63]; reactive algorithms and motion planning algorithms.

Motion planning methods often rely on optimization, for example as in model predictive control (MPC) [23]. This can be computationally expensive, particularly for vehicles with complex dynamics such as underactuated marine vehicles. However, in Johansen et al. [53], the computational complexity is significantly reduced by constraining the number of controls available to a small discrete set. Specifically, the algorithm is allowed to give an offset to the nominal desired course and speed. For each pair of control inputs, the vehicle and obstacle trajectories are predicted a certain amount of time ahead. A cost is computed for each pair based on the risk of collision, adherence to the International regulations for preventing collisions at sea (COLREGs) and deviation from the nominal control input, and the pair with the lowest cost is chosen. After a short amount of time, the procedure is repeated to account for the new system state and new sensor inputs. This simulation-based MPC avoids the use of computationally expensive optimization techniques, and guarantees that a global optimal pair (among the discrete set of pairs available) is chosen by using the brute force technique of evaluating them all. Furthermore, it is possible to extend the cost function to include other criteria, such as costs for switching between different COLREGs scenarios used by Hagen et al. [42] in order to avoid oscillations.

In Filotheou et al. [31], a distributed nonlinear MPC algorithm for a multi-agent system is presented. The algorithm makes a set of general agents traverse an environment with obstacles, such that each agent reaches a target position. Throughout the maneuver, connectivity between the agents is maintained, and the agents avoid collision with both each other and the obstacles. The algorithm works for a very general class of agents with bounded inputs and disturbances, and it includes a limited sensing range. Moving obstacles are, however, not considered, nor is it clear what the computational costs are or if there always exists a feasible solution.

In Gawron and Michałek [40], a method for planning a smooth path to a target in an environment cluttered with obstacles is presented. The path is surrounded by an obstacle-free area, denoted a funnel. The vehicle is steered by a kinematic guidance law, which is used to set references of underlying controllers. The path is collision-free and feasible for the guidance law by construction, and the funnel accounts for any perturbation caused by the underlying dynamics. The approach thus shows robustness. The creation of the funnel can, however, be conservative, and moving obstacles are not accounted for.

For a double integrator with acceleration constraints, Hoffmann and Tomlin [46] generate safe trajectories using an efficient optimization algorithm. The vehicles create avoid sets similar to truncated collision cones, described in Chakravarthy and Ghose [21], and the collision avoidance maneuver is initiated if these sets touch. The computational requirement of the algorithm is shown to be low, and safety is guaranteed for two and three cooperating vehicles, and implied by simulations for a general multi-vehicle scenario. Nonholonomic constraints and vehicle dynamics are, however, not considered.

The dynamic window algorithm presented by Fox et al. [38] finds safe control inputs for vehicles with first-order nonholonomic constraints using a search among achievable trajectories, and is thus closely related to MPC control. It is extended to include the second-order nonholonomic constraints resulting from the underactuation of marine vehicles in Eriksen et al. [28], which is further extended in Eriksen et al. [29] to also include moving obstacles.

Motion planning algorithms can, particularly in 3D, become computationally intractable for vehicles with limited processing power, as the general motion planning problem is shown to be NP-hard in Canny and Reif [19]. Furthermore, even for vehicles capable of implementing motion planning, a safety critical function such as collision avoidance requires a level of redundancy. This can be achieved by having a computationally simpler, yet provably safe, algorithm as a backup. Thus, there is a need for reactive algorithms.

The early work in Leitmann and Skowronski [65] presents avoidance control, which is a general approach for the design and analysis collision avoidance algorithms. Avoidance control employs a Lyapunov-like avoidance function to provide sufficient conditions under which it is mathematically proved that the system state trajectory never enters an undesired set. The technique can be used constructively, in that the avoidance function can be used directly to design a feedback law that avoids collisions. However, as it often the case with Lyapunov-like techniques, determining the proper avoidance function is not trivial. Furthermore, the approach is only used to prove safety, while liveness¹ is unexplored.

The artificial potential field (APF) method described in Khatib [56], which guides the vehicle using repulsive and attractive fields, is intuitive and straightforward to implement even for complex environments. Furthermore, different fields can be combined in order to achieve simultaneous goals like formation control and obstacle avoidance [24, 83]. Stability issues is identified with the algorithm in Koren and Borenstein [58]. These can be countered by extending the algorithm to the polar domain as in the vector field histogram proposed by Borenstein and Koren [10].

Nonholonomic constraints are included in the APF in both Chang et al. [22] and Shimoda et al. [97]. In the former, a “gyroscopic force” is created by letting a unicycle turn away from a detected obstacle, without changing the vehicle speed. Thus, while an APF is employed to guide the vehicle towards a target, obstacle avoidance is solved by an auxiliary function to the field. In Shimoda et al. [97], a potential field is generated in a trajectory space of the vehicle curvature and forward

¹Liveness is the property of not getting stuck in a deadlock, that is the vehicle will not reach an equilibrium away from its goal.

speed. Thus, nonholonomic constraints and bounds on vehicle curvature can easily be included in the field. The local minima associated with artificial potential fields are approached using a randomization technique, which is shown to alleviate these problems in practice. These methods only consider static obstacles, though, and there are no safety guarantees.

The algorithm presented by Yang et al. [121] makes a fixed-wing aircraft avoid a single non-cooperating obstacle in three dimensions. The algorithm keeps a constant bearing and elevation to the target, and thus approaches the target in an equiangular spiral. The algorithm uses very limited sensor information, only the relative heading of the obstacle is required, and it is thus suitable for vehicles with limited sensing capabilities or computational power. The distances involved are, however, assumed to be large enough to treat both the vehicle and the obstacle as point masses, and there is no analysis of the resulting vehicle movement.

A variant of the artificial potential field is the navigation function, which was first proposed in Rimon and Koditschek [89]. A navigation function is a potential field which by construction does not have any local minima. This approach is employed in in Rahmani et al. [88], where it is employed to make aircraft avoid collisions with multiple obstacles, as well as achieve path following of a straight-line path. While the navigation function is employed to ensure liveness of the algorithm, it is not analyzed, nor is vehicle dynamics considered.

In Roussos et al. [93], a reactive algorithm employing a dipolar navigation function is used to make an aircraft-like vehicle avoid obstacles. The navigation function is generated so that there is a single minimum at the target, and maxima at the obstacles. The algorithm provably makes the vehicle reach the target position while avoiding obstacles. However, there is an underlying assumption that the vehicle is able to follow the integral curves. Furthermore, actuator constraints are not included, nor is there any analysis on the behavior of the vehicle forward speed. Specifically, it is not guaranteed that the forward speed is always positive.

The navigation function must often be tuned to the size of the working space, and to the number of obstacles. It is not necessarily clear how to do such a tuning automatically. This is the motivation behind the navigation vector field, proposed by Panagou [80], where a class of vector functions is used to create a field flowing around obstacles and towards a target. It is proven that a unicycle is almost globally guaranteed to safely reach a target position without collision in a scenario with multiple, static, circular obstacles. The approach is extended to multiple polygonal obstacles by Hegde and Panagou [45], which create a navigation vector field flowing around the polygons.

The navigation vector field approach is further extended to a multi-agent scenario in Panagou [81]. Here, agents of two different classes participate; cooperative and uncooperative agents. The cooperative agents follow a navigation vector field like the one presented in Panagou [80] to their respective goal configurations. Conflicts among cooperative agents are solved by adjusting the forward speed of the vehicle. It is proven that all cooperative agents will reach their goals while avoiding collisions and deadlocks. The case of two cooperative agents is investigated in particular detail, while scenarios with more than two agents are covered more briefly. In particular, there is no explicit analysis of a scenario where three or more agents are within each other's region of influence at once. For vehicles with a lim-

ited speed envelope, such as fixed-wing aircraft, the approach of freely adjusting the forward speed can be problematic. In particular, the vehicle can be required to stop completely or even move backwards, which is unfeasible for many vehicles. Still, the methodology is very promising, and future research may show that the approach is applicable also to vehicles with restrictions on the forward speed.

An avoidance-like control for unicycles is presented in Mastellone et al. [72], where the vehicle can avoid static obstacles and cooperative agents, and a group of vehicles can achieve formations and trajectory tracking. Trajectory tracking is achieved by pointing the vehicles towards a moving virtual particle, and an avoidance function is used to push the vehicle away from obstacles. The algorithm is provably safe both for single vehicles and vehicles moving in formation along the trajectory, but the analysis does not include dynamics or actuator constraints.

Another method related to artificial potential fields and avoidance control is the use of barrier functions. A barrier function is a concept used originally in constrained optimization, as described in Nocedal and Wright [77, Chapter 17], and is a function whose value goes to infinity at a point or curve. A barrier function is usually smooth, although the initial results using nonsmooth barrier functions in Glotfelter et al. [41] are promising. In optimization, barrier functions are used to keep the solutions away from forbidden domains during the search, and can hence be applied to optimization-based control [3, 110]. It can also be used for reactive control, as in Panagou et al. [82], where barrier functions are used on the individual of a group to keep them within communication range from the leader, while avoiding collisions with each other and static obstacles. The vehicles are proved to almost surely reach their targets while maintaining safety and communication. Neither vehicle dynamics, non-cooperating obstacles nor too crowded environments are considered, however.

Representing the obstacle in the velocity space is the main idea behind the velocity obstacle approach proposed by Fiorini and Shiller [32]. By choosing a vehicle velocity outside of the set of velocity obstacles, algorithms implementing velocity obstacles inherently include moving obstacles. An additional cost function can be added to safe velocities in order to choose an optimal safe velocity in some sense, for example to minimize the risk of the resulting maneuver as in Kim and Oh [57]. It is furthermore shown by Owen and Montano [78] how optimization techniques can be used to generate motion plans in the velocity space.

In the reciprocal velocity obstacle approach proposed by Van Den Berg et al. [106], the vehicles choose a velocity which is the average of the current velocity and a chosen velocity outside of the velocity obstacle. It is shown that the algorithm can thus be successfully applied to a multi-agent scenario, but it is still prone to reciprocal dances. The hybrid velocity obstacle defined by Snape et al. [100] seeks to avoid this by defining that the a vehicle should preferably keep other vehicles on its port side. The velocity obstacle associated with another agent is enlarged on the wrong side, pushing the vehicles in the right direction. This method can also be used to include traffic rules such as COLREGs, as is done in Kuwata et al. [60]. Another reciprocal approach with velocity obstacles is presented by van den Berg et al. [107], where the set of allowable velocities is evenly distributed between two agents. The result has very little computational overhead, and both simulations and experiments show successful avoidance and target reaching in very dense scenarios.

The acceleration velocity obstacle presented by van den Berg et al. [108] includes acceleration constraints by limiting the allowable velocities in the next step to reachable velocities. The approach can be further extended to include unicycle-type nonholonomic constraints, but becomes restrictive if the forward acceleration or turning rate of the vehicle is limited. The complete vehicle dynamics are included in the generalized velocity obstacle proposed by Wilkie et al. [120], which is extended to reciprocal velocity obstacles in Bareiss and van den Berg [5]. The generalized approaches represent the obstacles in the control input space which is not trivial to compute, especially for vehicles with complex dynamics and shapes.

The velocity obstacle approach is elegantly extended to 3D in Jenie et al. [50] and Jenie et al. [51]. Here, the 3D velocity space is divided into a set of discrete planes, and the 2D velocity obstacle approach is applied to each plane. This is an intuitive extension, but the problems pertaining to vehicle constraints and dynamics in the velocity obstacle approach remain unaddressed.

In Lalish and Morgansen [61], the collision cone concept [21] is employed in a distributed reactive algorithm for multiple vehicles. The algorithm provably makes a set of cooperating vehicles remain collision free if they start in a conflict free state, and a deconfliction algorithm for reaching such a state is given. The algorithm incorporates actuator constraints, and is suitable also for vehicles with a limited speed envelope. However, while the results are strong, the dynamics of the vehicles are not included, and the conditions for safe deconfliction can become overly conservative in the case of passive obstacles.

The collision cone approach is extended to 3D in [20, 30, 62, 99]. The 3D collision cone is analytically defined in Carbone et al. [20], which defines a safe maneuver using either speed, pitch or yaw movement. In Fasano et al. [30], this work was extended to include combinations of these maneuvers, reducing the control cost of the overall maneuver. Possible non-cooperating obstacles are considered in Smith et al. [99], which employs 3D collision cones in an air traffic control problem, however no analytical guarantees are provided.

The work in Lalish and Morgansen [62] extends the earlier work of Lalish and Morgansen [61], and shows how a multi-agent system can be made to provably reach and remain in a conflict-free state. Both limited speed envelopes and acceleration constraints are included, making the results very solid. Vehicle dynamics are, however, not explicitly accounted for, which may be a problem for underactuated vehicles.

The nonholonomic constraints of a unicycle vehicle is removed in the algorithm presented by Rodríguez-Seda et al. [91] by using input-output linearization. Inspired by Leitmann and Skowronski [65], a Lyapunov-like analysis is used to rigorously prove that the algorithm achieves collision avoidance for vehicles with bounded actuators. The input-output linearization will, however, introduce overly restrictive bounds on the available controls when the maximum linear acceleration and maximum angular acceleration of the vehicles differ by a large extent. This is for example the case of marine vehicles such as ships. The results of Rodríguez-Seda et al. [91] are extended in Rodríguez-Seda et al. [92] to include the avoidance of non-cooperating obstacles, albeit for double integrators rather than unicycles.

A similar approach to Rodríguez-Seda et al. [91] is proposed in Rodríguez-Seda [90], which examines a multi-agent scenario of cooperating, circular agents modeled

as unicycles with bounded turning rates and constant forward speed. Rather than using feedback linearization, an auxiliary system is here created by considering the center of the turning circle of each vehicle. Such a system can be viewed as a double integrator, on which an avoidance control method can be applied. Steering the center of the vehicle’s turning circle is also the method of Pallottino et al. [79], which ensures that a set of cooperating, circular unicycles avoid each other and reach their targets by “rolling” on each other’s turning circles.

The algorithm proposed by Moe and Pettersen [74] uses circular path following to avoid moving obstacles, and the paper gives sufficient conditions for successful avoidance. By using set-based theory to switch between path following mode and collision avoidance mode, the algorithm is combined with the LOS guidance law for following of straight-line path segments. It is not, however, clear how to extend the algorithm to non-circular obstacles, nor is a minimum distance for when the vehicle should start the collision avoidance maneuver provided.

A local, range-only-based collision avoidance algorithm for nonholonomic vehicles is proposed in Matveev et al. [73], which considers moving obstacles of arbitrary and time-varying shapes. The sensing requirements on a vehicle using the algorithm is very limited, but the algorithm places heavy restrictions on the obstacle velocities.

The algorithm presented in Savkin and Wang [96] resembles the vector field histogram of Borenstein and Koren [10], and uses sensor measurements directly to obtain obstacle-free directions ahead of the vehicle. It is proved that the algorithm makes a nonholonomic vehicle safely traverse a complex environment with multiple moving obstacles. The algorithm does not, however, make use of the obstacle velocity, something which can give overly conservative restrictions to obstacle movement in cases where obstacle velocity measurements are available.

Inspired by the way a squirrel will keep a constant avoidance angle to a tree when circling it, as described in Lee [64], Teimoori and Savkin [105] propose an algorithm which makes a unicycle with limited turning radius avoid static obstacles of bounded curvature. The algorithm makes the vehicle keep a constant avoidance angle to the obstacle, and it is then ensured that the vehicle will keep a minimum distance to it. The algorithm is extended to include moving obstacles in Savkin and Wang [95], where a time-varying compensation term is added to the avoidance angle in order to compensate for the obstacle velocity. This approach has the advantage that, unlike for velocity obstacles, knowledge of the obstacle shape is not required for implementation, only the vision cone to the obstacle. However, while the algorithm provides safe heading references, it also imposes a strict requirement on the vehicle speed trajectory during the avoidance maneuver. The flexibility to design the speed trajectory of the vehicle independently is thus removed, which complicates the implementation on underactuated vehicles and is a significant drawback for vehicles with a limited speed envelope. Furthermore, the vehicle dynamics is not considered, and the speed requirement also leads to a singularity in the required yaw rate.

The constant avoidance angle algorithm is extended to 3D in Wang et al. [109]. Here, a plane is created containing the vehicle, the obstacle and the vehicle’s velocity vector. The vehicle will operate in this plane, employing the algorithm from Savkin and Wang [95] in order to avoid the obstacle. While this is an intuitive extension, it does not fully exploit the 3D structure of the system, and the issues

of the 2D algorithm have not been addressed.

In Parts III and IV of this thesis, we will propose a constant avoidance algorithm which enables the vehicle to maintain any desired forward speed, and we will show how it can be used on vehicles required to keep a constant forward speed. Thus, the singularity in Savkin and Wang [95] is removed, and the algorithm becomes suitable for vehicles with speed restraints. We will extend the algorithm to 3D, and provide an analysis which includes the complete dynamic model of an underactuated marine vehicle.

1.3 Contributions

1.3.1 Path following

Part II of this thesis considers path following of underactuated marine vehicles in 2D and 3D. In Chapter 4 we consider the integral line of sight (ILOS) path following guidance law proposed by Børhaug et al. [13], applied to an underactuated marine vehicle with kinematics and dynamics modeled in 3 DOF. The vehicle is tasked with following a straight-line path, and there is a kinematic disturbance from an ocean current which is uniform in time and space. The algorithm is proved to provide global κ -exponential convergence in Caharija et al. [18], and the main contribution of this chapter is an extension of this result, motivated by the results of Fossen and Pettersen [36], to prove that an underactuated marine vessel controlled by the ILOS guidance law achieves the stronger stability results of USGES and UGAS.

USGES was previously thought to provide stronger convergence and robustness properties than κ -exponential stability. Specifically, since the USGES property implies that a sufficiently large region of attraction in which there is exponential convergence can always be chosen, Khalil [55, Lemma 9.2] could suggest that it should be possible to obtain robustness (uniform boundedness of the solutions) regardless of the size of the perturbation. This is a stronger robustness property than for κ -exponential stability, which according to Khalil [55, Lemma 9.3] requires the perturbation to be small to ensure a uniformly bounded solution. The robustness properties of a system achieving USGES was, however, examined more closely in Pettersen [84], where it is proved that in the general case, the size of a perturbation must still be small in order to ensure that the solution of the system remains bounded. This is in particular shown to be the case for systems using LOS guidance laws.

In Chapter 5 we investigate the effect of the vehicle speed on the path convergence, with particular focus on vehicles where the convergence of the underlying controllers are slow, which indeed they are for many real system. In this chapter, we design the lookahead distance of the ILOS guidance law to increase linearly with the desired surge speed. The vehicle will then make slower, smoother turns at high speed, reducing overshoot. This is inspired both by the results of Lekkas and Fossen [66], which showed that the optimal lookahead distance increased with vehicle speed, and by practical considerations when implementing the algorithm on FFI's Odin USV. Such a speed-dependent lookahead distance makes it possible for the vehicle to converge to the desired path without overshoot for a broad range

of speeds, without having to tune the guidance separately for low-speed tasks, such as AUV following or seabed surveying, and high-speed tasks such as transit.

For the special case when the desired surge speed is constant, we provide conditions under which the path following convergence remains USGES. While we in Chapter 4 will employ the Comparison lemma [55, Lemma 3.4] to prove USGES of the ILOS guidance law, we will in Chapter 5 demonstrate the use of the more convenient Lyapunov-sufficient conditions proposed by Pettersen [84]. Furthermore, we show that the solutions of the system remain ultimately bounded when the desired surge speed is time-varying. Unlike previous works, we do not look at a specific function for forward speed. Rather, we let it be a general function, with no required bound on the desired acceleration. Thus, the result can be used for any desired surge speed trajectory, including but not limited to those used for trajectory tracking in Flåten and Brekke [33] or formation control in Belleter and Pettersen [7].

In Chapter 6 we look at path following in 3D, using the 3D ILOS guidance law proposed by Caharija et al. [18] applied to an underactuated underwater vehicle modeled in 5 DOF. Specifically, this chapter investigates the effect of positive or negative buoyancy on an underactuated underwater vehicle controlled by an ILOS guidance law. The 5 DOF kinematic and dynamic model used in Caharija et al. [18], which includes kinematic disturbances from constant and irrotational ocean currents, is extended to include effects caused by the lack of neutral buoyancy. The main contribution of Chapter 6 is thus to extend the results of Chapters 4 and 5 to prove that the closed-loop cross track error dynamics are UGAS and USGES, even when the vehicle is not neutrally buoyant.

1.3.2 Collision avoidance in 2D

The main contribution of Part III of the thesis is the design and analysis of the constant avoidance angle (CAA) algorithm for collision avoidance of underactuated marine vehicles operating in the horizontal plane. Chapter 7 gives a detailed description of the algorithm, which is a reactive algorithm building on the results of Savkin and Wang [95]. The main idea behind the algorithm is to make the vehicle maintain a constant avoidance angle between its velocity vector and the edge of the obstacle. If the obstacle is moving, a compensation term is added to the avoidance angle to ensure that the vehicle behavior with respect to the obstacle remains the same. This compensation approach is closely related to the velocity obstacle algorithm proposed by Fiorini and Shiller [32]. The main difference is that the CAA algorithm does not require knowledge of the obstacle shape for implementation, and that we provide an analytical expression for the velocity compensation for any given vehicle speed.

The use of vehicle speed as an input rather than an output furthermore separates the CAA algorithm from the algorithm proposed in Savkin and Wang [95]. The CAA algorithm proposed in this thesis is designed to provide safe heading references for the current vehicle speed, and it is thus possible to steer the speed independently. This feature provides flexibility and makes the approach suitable for a wide range of vehicles, including vehicles with a limited speed envelope, high ac-

celeration cost or underactuated speed components. All of these issues are relevant for marine vehicles.

Another contribution of Chapter 7 is the introduction of an unsafe vision cone. This is the set of all velocity directions which, at the current vehicle speed, can make the vehicle come closer than the required safety distance to the obstacle. Thus, the output of the algorithm is the outermost edges of this cone. The unsafe cone is used to determine when the vehicle should start a collision avoidance maneuver, and when the maneuver can safely be considered complete. Thus, we are able to design smooth and intuitive transitions between collision avoidance mode and nominal operations.

A preliminary analysis of the algorithm is performed in Section 7.3, where we prove that if a vehicle follows the steering references from the CAA algorithm, it is ensured that it will always stay at least a minimum safety distance away from the obstacle. The safety distance is a function of the constant avoidance angle and the radius of the obstacle. Thus, if the radius (or maximum curvature of a non-circular obstacle) is known, the avoidance angle can be tuned to achieve a desired minimum safety distance. Since the avoidance maneuver is based on circumventing the obstacle, we require the vehicle to move faster than it. In this case, the safety result will hold regardless of the obstacle behavior, and we do not require the obstacle to be cooperating.

The algorithm is applied to a unicycle in Chapter 8, where we demonstrate that the algorithm can be used on vehicles with a limited speed envelope by restricting the vehicle to keep a constant forward speed. The unicycle furthermore has a limited turning rate. The unicycle model and constraints are used to derive conditions under which it is mathematically guaranteed that a moving, non-cooperating obstacle will be avoided. We will find both the distance to the obstacle at which the vehicle, at the latest, must start to turn away, and an upper bound on the yaw rate required on the unicycle during the maneuver. The results are validated through simulations, which include a scenario with an obstacle of a more complex, concave shape. The latter demonstrates, at least qualitatively, that the algorithm can be used also on non-circular obstacles.

In Chapter 9, we include the underactuated sway dynamics of marine vehicles steered with a rudder and propeller, but assume that the directly actuated surge and heading remain perfectly controlled. The underactuated sway dynamics complicates the analysis of the collision avoidance maneuver. First, the direction of the vehicle's velocity is no longer equivalent to the orientation of the vehicle. In nautical terms, the direction of the vehicle's velocity is called the vehicle course, while the vehicle's horizontal orientation is called the vehicle heading. Since the vehicle course is of main interest during a collision avoidance maneuver, we will design a new course controller. We furthermore provide conditions under which this controller is feasible, conditions which hold for most marine vehicles.

Secondly, even though the vehicle is still set to maintain a constant forward speed, there is now an underactuated component to the vehicle's total speed as a sway speed is induced when the vehicle turns. The time-varying speed is readily handled by the CAA algorithm, which is modified in this chapter to use the vehicle's total speed rather than the forward speed when calculating the obstacle velocity compensation angle. The analysis of the required turning rate in Chapter 8 is thus

extended to include the time-varying speed, and conditions are derived under which we are ensured that the required course rate is well defined and the induced sway is bounded. These results are then included in the safety analysis, and used to derive a new distance at which the obstacle must at the latest turn away in order to ensure safety, as well as conditions on the course controller and avoidance angle in order to ensure both safety and well-definedness of the maneuver, while also ensuring that the induced sway speed is upper bounded. Again, these results are validated through simulations which confirms that an underactuated vehicle is able to avoid collisions.

Chapter 10 finalizes Part III, extending the vehicle model to a complete maneuvering model as defined in Fossen [35], including both the underactuated sway dynamics and the directly actuated yaw and surge dynamics. We ensure that the vehicle is able to always follow the required surge and yaw rates by designing a bump function which is employed during the discontinuous switch between nominal operation and collision avoidance mode. Thus, we are able to use the results of Chapter 9 on a vehicle with a complete dynamic model.

In Chapters 8 and 9 the nominal goal of the vehicle is to reach a target position, for which we use the pure pursuit guidance law described in Breivik and Fossen [17]. In Chapter 10, the performance of the CAA algorithm in combination with the LOS path following guidance law is analyzed. By proving that the vehicle is able to safely reach its control objectives in both a target reaching and a path following scenario, we demonstrate the modular nature of the algorithm. The results are validated through both numerical simulations and through full-scale experiments on the R/V Gunnerus.

The analysis of the algorithm considers a single moving obstacle of circular shape. However, the algorithm can be used to avoid an obstacle of any shape without any modification, which we demonstrate in the simulation section. Furthermore, while the analysis of dense multi-obstacle scenarios is beyond the scope of this thesis, we will provide a method for extending the algorithm to such scenarios. This is demonstrated in the experimental section, where we validate the results through the experiments on R/V Gunnerus.

1.3.3 Collision avoidance in 3D

In Part IV, the CAA algorithm is extended to 3D, enabling an underactuated underwater vehicle to avoid a moving obstacle using limited sensor measurements. Where the 2D algorithm provides two safe velocity directions, one to either side of the obstacle, the 3D algorithm creates a continuum of such directions around the obstacle in an extended 3D vision cone. For each ray, a compensation term is added in order to compensated for the obstacle velocity using the same technique as in 2D. Thus, a 3D unsafe cone valid for the current vehicle speed is created. This procedure is described in Chapter 11, where a preliminary analysis proves that a vehicle following any direction along this cone is able to keep at least a minimum safety distance to a moving obstacle.

The continuum of safe directions provided by the algorithm offers flexibility. This flexibility is utilized in Chapter 11 by making the algorithm choose a direction going behind the obstacle, while also minimizing the required turning and pitching

rate. Furthermore, the algorithm is able to make the vehicle adhere to limitations in the allowed pitch, which is often a safety limitation of 3D vehicles.

The minimization of the required pitch and turning rate enables us to extend the 2D results in Chapter 8 to 3D in Chapter 12. Specifically, we are able to derive bounds on the maximum required turning and pitching rate during an avoidance maneuver in order to enable a kinematically modeled vehicle with nonholonomic constraints in sway and heave to avoid a moving obstacle. As in the 2D case, we do not require that the obstacle is cooperating, and successful avoidance is shown even when the obstacle is in pursuit of the vehicle. The results are proved analytically, and the analysis shows how the avoidance angle can be tuned in order to ensure that the maneuvering requirements of the collision avoidance maneuver do not exceed the capabilities of the vehicle.

In Chapter 13 we extend the vehicle model to include the full 5 DOF dynamics of an underactuated marine vehicle. This includes underactuation in sway and heave, which cannot be directly controlled, but are induced when turning and pitching. These underactuated degrees of freedom are included in the control system by the design of a Flow frame controller, where the Flow frame is a reference frame where the x -axis points along the direction of the vehicle's velocity vector. Thus, the Flow frame controller is a 3D generalization of the 2D course controller.

Similarly to Chapter 10, the dynamics of the directly actuated pitch and yaw rates are included by smoothing the desired rates during the discrete switch from nominal operation when starting the collision avoidance maneuver, thus ensuring that the actuated control signals of the system remain well defined also during the switch.

Conditions under which an underactuated underwater vehicle is analytically guaranteed to avoid a moving obstacle are provided in the main theorem of Chapter 13. It is also shown how these conditions ensure that the induced sway and heave speeds are upper bounded. These results are validated through several simulations, as well as through full-scale experiments on the Hugin AUV. The simulations furthermore provide a qualitative demonstration of use of the algorithm in a multi-obstacle scenario.

1.3.4 Publication list

This section presents a list of publications produced during, and relevant to, the work in this thesis. The list contains both accepted and submitted publications.

Journal papers

M. S. Wiig, K. Y. Pettersen, and T. R. Krogstad. Collision Avoidance for Underactuated Marine Vehicles Using the Constant Avoidance Angle Algorithm. *IEEE Transactions on Control Systems Technology*, 2019. *Accepted, in press.*

M. S. Wiig, K. Y. Pettersen, and T. R. Krogstad. A 3D Reactive Collision Avoidance Algorithm for Underactuated Underwater Vehicles. *Journal of Field Robotics*, 2019. *Submitted.*

Conference papers

M. S. Wiig, K. Y. Pettersen, and T. R. Krogstad. Uniform semiglobal exponential stability of integral line-of-sight guidance laws. In *Proc. 10th IFAC Conference on Manoeuvring and Control of Marine Craft*, Copenhagen, Denmark, 2015.

M. S. Wiig, W. Caharija, T. R. Krogstad, and K. Y. Pettersen. Integral Line-of-Sight Guidance of Underwater Vehicles Without Neutral Buoyancy. In *Proc. 10th IFAC Conference on Control Applications in Marine Systems*, Trondheim, Norway, 2016.

M. S. Wiig, K. Y. Pettersen, and T. R. Krogstad. A reactive collision avoidance algorithm for vehicles with underactuated dynamics. In *Proc. 56th IEEE Conference on Decision and Control*, Melbourne, Australia, 2017.

M. S. Wiig, K. Y. Pettersen, and A. V. Savkin. A reactive collision avoidance algorithm for nonholonomic vehicles. In *Proc. 1st IEEE Conference on Control Technology and Applications*, Kohala Coast, HI, USA, 2017.

M. S. Wiig, K. Y. Pettersen, and T. R. Krogstad. A 3D Reactive Collision Avoidance Algorithm for Nonholonomic Vehicles. In *Proc. 2nd IEEE Conference on Control Technology and Applications*, Copenhagen, Denmark, 2018.

M. S. Wiig, K. Y. Pettersen, and T. R. Krogstad. A 3D Reactive Collision Avoidance Algorithm for Underactuated Vehicles. In *Proc. 57th IEEE Conference on Decision and Control*, Miami Beach, FL, USA, 2018.

M. S. Wiig, K. Y. Pettersen, E.-L. M. Ruud, and T. R. Krogstad. An Integral Line-of-Sight Guidance Law with a Speed-dependent Lookahead Distance. In *Proc. IEEE European Control Conference*, Limassol, Cyprus, 2018.

Publications not part of this thesis

B. O. H. Eriksen, M. Breivik, K. Y. Pettersen, and M. S. Wiig. A Modified Dynamic Window Algorithm for Horizontal Collision Avoidance for AUVs. In *Proc. IEEE Conference on Control Applications*, Buenos Aires, Brazil, 2016.

1.4 Thesis outline

This thesis consists of 14 chapters:

Chapter 2 provides some mathematical preliminaries, and introduces some of the notation used in this thesis.

Chapter 3 presents a mathematical maneuvering model of an underactuated marine vehicle in 3 DOF and 5 DOF. The dynamics are expressed both in terms of velocities relative to the water, which are used in Part II, and in velocities relative

to NED, which are used in Parts [III](#) and [IV](#).

Chapter 4 analyses the stability properties of the ILOS guidance law applied to an underactuated surface vehicle. It is proved that the guidance law achieves the USGES stability property, and this is verified in simulations.

Chapter 5 modifies the ILOS guidance law to have a speed-dependent lookahead distance. The path convergence is shown to be USGES when the desired surge speed is constant, and the path error is shown to be ultimately bounded when the speed is time-varying. The results are verified both through simulations, and through full-scale experiments on the Odin USV.

Chapter 6 analyses the stability properties of the 3D ILOS guidance law applied to an underactuated underwater vehicle. The analysis shows that the path convergence is USGES, even if the vehicle is not neutrally buoyant. The results are verified in simulations.

Chapter 7 describes the CAA collision avoidance angle algorithm in 2D, and provides a preliminary analysis where it is shown that as long as a vehicle is able to follow the references from the algorithm, it is guaranteed to remain at least a minimum safety distance away from the obstacle.

Chapter 8 applies the CAA algorithm to a unicycle-type vehicle which is restricted to keep a constant forward speed. The vehicle is tasked with reaching a target position, and encounters an obstacle on the way. An upper bound on the required turning rate of the vehicle is given, and a minimum switching distance from the obstacle at which the vehicle can start the avoidance maneuver and still be safe is derived. These results are verified in simulations.

Chapter 9 includes the underactuated dynamics of a marine vehicle steered with a rudder and propeller into the vehicle model. The CAA algorithm is then set to steer the vehicle course rather than the vehicle heading, which enables it to compensate for the vehicle underactuation in sway. Conditions are derived under which the vehicle is still guaranteed to avoid a moving obstacle while ensuring that the induced sway speed is upper bounded. These results are verified in simulations.

Chapter 10 applies the CAA algorithm to an underactuated marine surface vehicle, which is modeled using a complete maneuvering model. It is shown how a bump function can be used to avoid discontinuities in the reference signal for the directly actuated yaw rate of the vehicle, ensuring that it can always be controlled with exponential convergence. Conditions are given under which the vehicle is guaranteed to avoid a moving obstacle and continue with the nominal operation, both in combination with a target reaching guidance law and with the LOS path following guidance law. The results are verified both through simulations, and through full-scale experiments on the R/V Gunnerus.

Chapter 11 describes the CAA algorithm in 3D, including a 3D extended vi-

sion cone and a compensation term added to each ray of the cone to compensate for the obstacle velocity, creating a compensated vision cone. A preliminary analysis shows that if the vehicle's velocity direction always lies along the surface of the compensated vision cone, then the vehicle is guaranteed to stay at least a minimum safety distance away from the obstacle. Furthermore, it is shown how a safe direction can be chosen which makes the vehicle move behind the obstacle, minimizes the required pitch and yaw rate, and ensures that the desired pitch is limited.

Chapter 12 applies the 3D CAA algorithm to a kinematic model of a vehicle with nonholonomic constraints in sway and heave. The vehicle is restricted to keep a constant forward speed, has a limited pitch and yaw rate, and is tasked with reaching a target position. Furthermore, the vehicle is required to have a safety limitation on the allowed pitch range. Upper bounds are derived on the required yaw and pitch rate during the collision avoidance maneuver, and conditions are derived under which the vehicle is guaranteed to avoid a moving obstacle and reach the target, while also adhering to the pitch limitations.

Chapter 13 applies the 3D CAA algorithm to an underactuated underwater vehicle modeled using a complete maneuvering model. The underactuated sway and heave dynamics are compensated for by the design of a Flow frame controller, which steers the direction of the vehicle's velocity vector in 3D, and conditions are given on the vehicle's maneuvering capabilities under which this controller is always feasible. The 3D CAA algorithm provides references to the Flow frame controller, and conditions are provided under which collision avoidance is guaranteed while the induced sway and heave motion are upper bounded. These results are verified both in simulations and in full-scale experiments on the Hugin AUV.

Chapter 14 gives some concluding remarks, and some thoughts on future paths of research.

Part I

Preliminaries

Chapter 2

Mathematical Preliminaries

My spelling is wobbly. It's good spelling, but it Wobbles, and the words get in the wrong places.

— A.A. Milne, *Winnie-the-Pooh*

In this chapter, we will provide some mathematical preliminaries to the work presented in this thesis. We will, specifically, present the mathematical notation of the thesis in Section 2.1, as well as a list of the most important reference frames in Section 2.2 and some utility functions in Section 2.3. Finally, we will present stability definitions and theorems from the literature in Section 2.4.

2.1 Notation

We will here give an overview of the notation used in this thesis. The notation employed is largely based on the notation in Fossen [35] and Khalil [55].

The space \mathbb{R}^n is the Euclidean space of dimension n , while \mathbb{R}^+ is the set of all non-negative real numbers. The p -norm of a vector $\mathbf{u} \in \mathbb{R}^n$ is denoted $\|\mathbf{u}\|_p$, for $p \in [1; \infty]$. When a norm is written without subscript, such as $\|\mathbf{u}\|$, the Euclidean norm is implied. The ball $B_r \in \mathbb{R}^n$ is a ball of radius $r > 0$, centered at origo, $B_r \triangleq \{\mathbf{x} \in \mathbb{R}^n \mid \|\mathbf{x}\| \leq r\}$.

A vector \mathbf{u} represented in a reference frame n is denoted \mathbf{u}^n . The position of a reference frame b with respect to reference frame n is denoted $\mathbf{p}_b^n = [x_b^n, y_b^n, z_b^n]^T$. The velocity vector of frame b with respect to n , represented in n is denoted $\mathbf{v}_{b/n}^n$, where the superscript n signifies that the velocity is represented in n , while the subscript b/n signifies that the vector holds the velocity of b with respect to n . The rotation matrix used to rotate a vector from reference frame b to frame n is denoted \mathbf{R}_b^n , so that $\mathbf{v}^n = \mathbf{R}_b^n \mathbf{v}^b$. The angular velocity vector of frame b with respect to n , represented in b , is denoted $\boldsymbol{\omega}_{b/n}^b$.

The Euler angles roll (ϕ), pitch (θ) and yaw (ψ) are used to decompose a rotation

into three principal rotations using the zyx -convention. The principal rotations are

$$\begin{aligned} \mathbf{R}_x(\phi) &\triangleq \begin{bmatrix} 1 & 0 & 0 \\ 0 & c(\phi) & -s(\phi) \\ 0 & s(\phi) & c(\phi) \end{bmatrix}, \mathbf{R}_y(\theta) \triangleq \begin{bmatrix} c(\theta) & 0 & s(\theta) \\ 0 & 1 & 0 \\ -s(\theta) & 0 & c(\theta) \end{bmatrix}, \\ \mathbf{R}_z(\psi) &\triangleq \begin{bmatrix} c(\psi) & -s(\psi) & 0 \\ s(\psi) & c(\psi) & 0 \\ 0 & 0 & 1 \end{bmatrix}. \end{aligned} \tag{2.1}$$

For brevity, the trigonometric functions $\sin(\cdot)$, $\cos(\cdot)$ and $\tan(\cdot)$ have been denoted $s(\cdot)$, $c(\cdot)$ and $t(\cdot)$, respectively. This notation is used throughout the thesis. Combining these principal rotations gives the rotation matrix

$$\mathbf{R}_{zyx}(\phi, \theta, \psi) \triangleq \mathbf{R}_z(\psi)\mathbf{R}_y(\theta)\mathbf{R}_x(\phi). \tag{2.2}$$

For convenience we also define the matrix

$$\mathbf{R}_{zy}(\theta, \psi) \triangleq \mathbf{R}_z(\psi)\mathbf{R}_y(\theta), \tag{2.3}$$

which we use in cases where the roll angle is not of interest or assumed to be zero.

To denote the roll, pitch and yaw of a reference frame b with respect to n we use the notation ϕ_b^n , θ_b^n and ψ_b^n . Hence, the rotation from from b to n can be written

$$\mathbf{R}_b^n = \mathbf{R}_{zyx}(\phi_b^n, \theta_b^n, \psi_b^n). \tag{2.4}$$

2.2 Reference frames

Throughout this thesis there are various reference frames used to model the vehicle and the obstacle, and to describe the collision avoidance and path following algorithms. In Table 2.1, we list the most important reference frames, along with a short summary of each.

2.3 Utility functions

To steer the vehicle in the direction of a vector $\mathbf{u} = [u_x, u_y, u_z]^T$, it is useful to know the heading and pitch angle corresponding to the vector. To this end, we define the functions:

$$\Psi(\mathbf{u}) = \text{atan2}(u_y, u_x), \tag{2.5}$$

$$\Theta(\mathbf{u}) = -\sin^{-1}\left(\frac{u_z}{\|\mathbf{u}\|}\right). \tag{2.6}$$

We also define the angular distance $\xi(\mathbf{u}_1, \mathbf{u}_2)$ between the vectors \mathbf{u}_1 and \mathbf{u}_2 as

$$\xi(\mathbf{u}_1, \mathbf{u}_2) \triangleq \sqrt{(\Psi(\mathbf{u}_2) - \Psi(\mathbf{u}_1))^2 + (\Theta(\mathbf{u}_2) - \Theta(\mathbf{u}_1))^2}. \tag{2.7}$$

Table 2.1: Reference frames

Frame	Description
n	The inertial North-East-Down (NED) reference frame.
b	The Body reference frame, which is attached to and aligned with the vehicle.
f	The Flow reference frame, which is attached to the vehicle and aligned with the vehicle's velocity vector.
n_b	A Body-fixed reference frame oriented along the NED frame. This frame is used to represent positions relative to the vehicle.
o	The Obstacle reference frame, which is attached to the center of the obstacle.
b_{bo}	A Body-fixed reference frame oriented such that its x -axis points towards the obstacle.

2.4 Stability definitions and theorems

We will throughout this thesis apply the stability definitions presented in this section. The stability definitions apply for a nonautonomous system

$$\dot{\mathbf{x}} = f(t, \mathbf{x}), \quad (2.8)$$

where $f : [0, \infty) \times D \rightarrow \mathbb{R}^n$ is piecewise continuous in t and locally Lipschitz in \mathbf{x} on $[0, \infty) \times D$, where $D \subset \mathbb{R}^n$ is a domain which contains the origin $\mathbf{x} = \mathbf{0}$. We denote the initial condition as $\mathbf{x}_0 \triangleq \mathbf{x}(t_0)$.

The class of functions in the next two definitions are used as comparison functions when defining the different stability properties:

Definition 2.1. Khalil [55, Definition 4.2]. A continuous function $\alpha : [0, a) \rightarrow [0, \infty)$ is said to belong to class \mathcal{K} if it is strictly increasing and $\alpha(0) = 0$. It is said to belong to class \mathcal{K}_∞ if $a = \infty$ and $\alpha(r) \rightarrow \infty$ as $r \rightarrow \infty$.

Definition 2.2. Khalil [55, Definition 4.3]. A continuous function $\beta : [0, a) \times [0, \infty) \rightarrow [0, \infty)$ is said to belong to class \mathcal{KL} if, for each fixed s , the mapping $\beta(r, s)$ belongs to class \mathcal{K} with respect to r and, for each fixed r , the mapping $\beta(r, s)$ is decreasing with respect to s and $\beta(r, s) \rightarrow 0$ as $s \rightarrow \infty$.

From Khalil [55] and Loria and Panteley [70] we then define:

Definition 2.3. Khalil [55, Lemma 4.5]. The equilibrium point $\mathbf{x} = \mathbf{0}$ of (2.8) is

- *uniformly stable (US)* if and only if there exists a class \mathcal{K} function α and a positive constant c , independent of t_0 , such that

$$\|\mathbf{x}(t)\| \leq \alpha(\|\mathbf{x}_0\|), \quad \forall t \geq t_0, \quad \forall \|\mathbf{x}_0\| < c. \quad (2.9)$$

- *uniformly asymptotically stable (UAS)* if and only if there exist a class \mathcal{KL} function β and a positive constant c , independent of t_0 , such that

$$\|\mathbf{x}(t)\| \leq \beta(\|\mathbf{x}_0\|, t - t_0), \quad \forall t \geq t_0, \quad \forall \|\mathbf{x}_0\| < c. \quad (2.10)$$

- *uniformly globally asymptotically stable (UGAS)* if and only if inequality (2.10) is satisfied for any initial state $\mathbf{x}(t_0)$, i.e. $c \rightarrow \infty$.

Definition 2.4. Loria and Panteley [70, Definition 2.7]. The origin of system (2.8) is said to be uniformly (locally) exponentially stable (ULES) if there exist constants γ_1, γ_2 and $r > 0$ such that for all $(t_0, \mathbf{x}_0) \in \{\mathbb{R}^+ \times B_r\}$,

$$\|\mathbf{x}(t; t_0, \mathbf{x}_0)\| \leq \gamma_1 \|\mathbf{x}_0\| e^{-\gamma_2(t-t_0)} \quad \forall t \geq t_0. \quad (2.11)$$

If for each $r > 0$ there exist γ_1, γ_2 such that condition (2.11) holds for all $(t_0, \mathbf{x}_0) \in \{\mathbb{R}^+ \times \mathbb{R}^n\}$, then the system is said to be *uniformly semiglobally exponentially stable (USGES)*.

Finally, the origin of system (2.8) is said to be *uniformly globally exponentially stable (UGES)* if there exist γ_1, γ_2 such that (2.11) holds for all $(t_0, \mathbf{x}_0) \in \{\mathbb{R}^+ \times \mathbb{R}^n\}$.

2.4.1 USGES stability

In Pettersen [84], a slightly different definition of USGES is presented. We will present this definition here for completeness, along with Lyapunov-sufficient conditions for proving USGES of the parametrized nonlinear time-varying system

$$\dot{\mathbf{x}} = f(t, \mathbf{x}, \boldsymbol{\rho}), \quad (2.12)$$

where $t \in \mathbb{R}^+, \mathbf{x} \in \mathbb{R}^n$ and $\boldsymbol{\rho} \in P \subset \mathbb{R}^m$ is a constant parameter.

Definition 2.5. Pettersen [84, Definition 1]. Let $P \in \mathbb{R}^m$ be a set of parameters. The system (2.12) is USGES on P if, for any $\Delta > 0$, there exists a parameter $\boldsymbol{\rho}^*(\Delta) \in P$ and positive constants k_Δ, λ_Δ , all independent of t_0 , such that $\forall \mathbf{x}_0 \in B_\Delta$

$$\|\mathbf{x}(t; t_0, \mathbf{x}_0, \boldsymbol{\rho}^*)\| \leq k_\Delta \|\mathbf{x}_0\| e^{-\lambda_\Delta(t-t_0)}. \quad (2.13)$$

Definition 2.5 is a special case of the USGES definition in Definition 2.4. Specifically, Definition 2.5 explicitly shows the parameter dependency that may be part of the USGES property. Hence, any system that satisfies Definition 2.5 also satisfies Definition 2.4.

The next theorem provides Lyapunov-sufficient conditions under which the equilibrium point $\mathbf{x} = \mathbf{0}$ of system (2.12) is USGES.

Theorem 2.1. Pettersen [84, Theorem 5]. Consider the system given in (2.12). If, for any $\Delta > 0$, there exist a parameter $\boldsymbol{\rho}^*(\Delta) \in P$, a continuously differentiable Lyapunov function $V_\Delta : \mathbb{R}^+ \times B_\Delta \rightarrow \mathbb{R}^+$, and positive constants $k_{1\Delta}, k_{2\Delta}, k_{3\Delta}$ and a such that, $\forall \mathbf{x} \in B_\Delta$,

$$k_{1\Delta} \|\mathbf{x}\|^a \leq V_\Delta(t, \mathbf{x}) \leq k_{2\Delta} \|\mathbf{x}\|^a, \quad (2.14)$$

$$\frac{\partial V_\Delta}{\partial t} + \frac{\partial V_\Delta}{\partial \mathbf{x}} f(t, \mathbf{x}, \boldsymbol{\rho}^*) \leq -k_{3\Delta} \|\mathbf{x}\|^a, \quad (2.15)$$

$\forall t \geq t_0 \geq 0$, then the origin of the system (2.12) is USGES on P .

If the system (2.12) is perturbed by a function $g(t, \mathbf{x}, \boldsymbol{\rho})$, which is locally Lipschitz in \mathbf{x} and piecewise continuous in t for all $\boldsymbol{\rho} \in P$, we obtain the system

$$\dot{\mathbf{x}} = f(t, \mathbf{x}, \boldsymbol{\rho}) + g(t, \mathbf{x}, \boldsymbol{\rho}). \quad (2.16)$$

We will employ the next lemma to investigate the boundedness of such a system in Chapter 5.

Lemma 2.2. *Pettersen [84, Lemma 12]. Assume that the conditions of Theorem 2.1 are satisfied, and that there exist a positive constant $k_{4\Delta}$ and a constant $0 < c < 1$ such that, $\forall \mathbf{x} \in B_\Delta$,*

$$\left\| \frac{\partial V_\Delta}{\partial \mathbf{x}} \right\| \leq k_{4\Delta} \|\mathbf{x}\|^{a-1}, \quad (2.17)$$

$$\|g(t, \mathbf{x}, \boldsymbol{\rho})\| \leq \delta < \frac{k_{3\Delta}}{k_{4\Delta}} \left(\frac{k_{1\Delta}}{k_{2\Delta}} \right)^{\frac{1}{a}} \Delta c, \quad (2.18)$$

$\forall t \geq t_0 \geq 0$. Then, $\forall \mathbf{x} \in B_\Delta$, there is a $T > 0$ such that the solution $x(t; t_0, \mathbf{x}_0, \boldsymbol{\rho}^*)$ of the perturbed system (2.16) satisfies

$$\|x(t; t_0, \mathbf{x}_0, \boldsymbol{\rho}^*)\| \leq \left(\frac{k_{2\Delta}}{k_{1\Delta}} \right)^{\frac{1}{a}} \|\mathbf{x}_0\| e^{-\frac{(1-c)k_{3\Delta}}{ak_{2\Delta}}(t-t_0)} \quad (2.19)$$

$\forall t_0 \leq t \leq t_0 + T$, and

$$\|x(t; t_0, \mathbf{x}_0, \boldsymbol{\rho}^*)\| \leq \frac{k_{4\Delta}}{k_{3\Delta}} \left(\frac{k_{2\Delta}}{k_{1\Delta}} \right)^{\frac{1}{a}} \frac{\delta}{c} \quad \forall t \geq t_0 + T. \quad (2.20)$$

2.4.2 Cascaded systems

In Part II of this thesis we will employ cascaded systems theory to investigate the stability properties of the control system. In this section, we will state results pertaining to cascaded systems. We consider a nonlinear, time-varying system in cascaded form:

$$\dot{\mathbf{x}}_1 = f_1(t, \mathbf{x}_1) + g(t, \mathbf{x}) \mathbf{x}_2, \quad (2.21a)$$

$$\dot{\mathbf{x}}_2 = f_2(t, \mathbf{x}_2), \quad (2.21b)$$

where $\mathbf{x}_1 \in \mathbb{R}^n$, $\mathbf{x}_2 \in \mathbb{R}^m$, $\mathbf{x} = [\mathbf{x}_1^T, \mathbf{x}_2^T]^T$, and $f_1(t, \mathbf{x}_1)$ and $f_2(t, \mathbf{x}_2)$ are continuously differentiable in their arguments. We can view this as a nominal system,

$$\dot{\mathbf{x}}_1 = f_1(t, \mathbf{x}_1), \quad (2.22)$$

being perturbed by the perturbing system (2.21b) through the perturbation term $g(t, \mathbf{x}) \mathbf{x}_2$. We make the following assumption on the nominal system:

Assumption 2.1. The nominal system (2.22) is UGAS.

Theorem 2.3. *Loria and Panteley [70, Theorem 2.1]. Let Assumption 2.1 hold and suppose that the trajectories of (2.21b) are uniformly globally bounded. If moreover, Assumptions 2.2-2.4 below are satisfied, then the solutions $\mathbf{x}(t; t_0, \mathbf{x}_0)$ of the system (2.21) are uniformly globally bounded. If, furthermore, the origin of system (2.21b) is UGAS, then so is the origin of the cascade (2.21).*

Assumption 2.2. There exist constants $c_1, c_2, \eta > 0$ and a Lyapunov function $V(t, \mathbf{x}_1)$ for (2.22) such that $V : \mathbb{R}^+ \times \mathbb{R}^n \rightarrow \mathbb{R}^+$ is positive definite, radially unbounded, $V(t, \mathbf{x}_1) \leq 0$ and

$$\left\| \frac{\partial V}{\partial \mathbf{x}_1} \right\| \|\mathbf{x}_1\| \leq c_1 V(t, \mathbf{x}_1) \quad \forall \|\mathbf{x}_1\| \geq \eta, \quad (2.23)$$

$$\left\| \frac{\partial V}{\partial \mathbf{x}_1} \right\| \leq c_2 \quad \forall \|\mathbf{x}_1\| \leq \eta. \quad (2.24)$$

Assumption 2.3. There exist two continuous functions $\theta_1, \theta_2 : \mathbb{R}^+ \rightarrow \mathbb{R}^+$, such that $g(t, \mathbf{x})$ satisfies

$$\|g(t, \mathbf{x})\| \leq \theta_1(\|\mathbf{x}_2\|) + \theta_2(\|\mathbf{x}_2\|)\|\mathbf{x}_1\|. \quad (2.25)$$

Assumption 2.4. There exists a class \mathcal{K} function $\alpha(\cdot)$ such that, for all $t_0 \geq 0$, the trajectories of the system (2.21b) satisfy

$$\int_{t_0}^{\infty} \|\mathbf{x}_2(t; t_0, \mathbf{x}_2(t_0))\| dt \leq \alpha(\|\mathbf{x}_2(t_0)\|). \quad (2.26)$$

The next proposition extends the results of Theorem 2.3 to USGES.

Proposition 2.1. *Loria and Panteley [70, Proposition 2.3]. If, in addition to the assumptions in Theorem 2.3, the systems (2.21b) and (2.22) are USGES, then the cascaded system (2.21) is USGES and UGAS. Moreover, if the subsystems are UGES the cascade is UGES.*

Chapter 3

Modeling of Underactuated Marine Vehicles

When you are a Bear of Very Little Brain, and you Think of Things, you find sometimes that a Thing which seemed very Thingish inside you is quite different when it gets out into the open and has other people looking at it.

— A.A. Milne, *Winnie-the-Pooh*

This chapter contains an introduction to the modeling of marine vehicles operating at maneuvering speed. The modeling is based on Fossen [35], where more details and a more in-depth derivation of the equations of motion can be found.

The same notation will be used for positions, velocities and generalized velocities in 6 DOF, 5 DOF and 3 DOF, as the dimensionality of the vectors and matrices will be consistent within each of the remaining chapters of the thesis, and will be clear from the context.

3.1 Kinematics

To describe the vehicle kinematics, we will employ the inertial North-East-Down (NED) reference frame n , and the Body frame b . The Body frame is attached to the vehicle, and has its axes forward (surge), to starboard (sway) and towards the keel (heave). The position of the vehicle in n is denoted $\mathbf{p}_b^n \triangleq [x_b^n, y_b^n, z_b^n]^T$, while the orientation is modeled using the Euler angles roll (ϕ_b^n), pitch (θ_b^n) and yaw (ψ_b^n). The position and orientation of the vehicle is collected in the generalized coordinates vector

$$\boldsymbol{\eta}_b^n \triangleq \begin{bmatrix} \mathbf{p}_b^n \\ \phi_b^n \\ \theta_b^n \\ \psi_b^n \end{bmatrix}. \quad (3.1)$$

The velocities of the vehicle are usually measured in b , and the vehicle dynamics in Section 3.2 are modeled in b . The velocities in b are denoted

$$\boldsymbol{\nu}_{b/n}^b \triangleq \begin{bmatrix} \mathbf{v}_{b/n}^b \\ \boldsymbol{\omega}_{b/n}^b \end{bmatrix}, \quad (3.2)$$

where $\mathbf{v}_{b/n}^b$ and $\boldsymbol{\omega}_{b/n}^b$ are the linear and angular velocity vectors of b , respectively:

$$\mathbf{v}_{b/n}^b \triangleq \begin{bmatrix} u_b \\ v_b \\ w_b \end{bmatrix}, \quad \boldsymbol{\omega}_{b/n}^b \triangleq \begin{bmatrix} p_b \\ q_b \\ r_b \end{bmatrix}. \quad (3.3)$$

The linear velocities are the surge speed u_b , sway speed v_b and heave speed w_b , while the angular velocities are the roll rate p_b , pitch rate q_b and yaw rate r_b .

The linear velocity vector in n , $\mathbf{v}_{b/n}^n$, is obtained using the rotation matrix $\mathbf{R}_b^n \triangleq \mathbf{R}_{zyx}(\phi_b^n, \theta_b^n, \psi_b^n)$, where \mathbf{R}_{zyx} is defined in Chapter 2. Thus,

$$\mathbf{v}_{b/n}^n = \dot{\mathbf{p}}_b^n = \mathbf{R}_b^n \mathbf{v}_{b/n}^b. \quad (3.4)$$

To obtain the Euler angle rates, we use that

$$\boldsymbol{\omega}_{b/n}^b = \begin{bmatrix} \dot{\phi}_b^n \\ 0 \\ 0 \end{bmatrix} + \mathbf{R}_x(\phi_b^n)^T \begin{bmatrix} 0 \\ \dot{\theta}_b^n \\ 0 \end{bmatrix} + \mathbf{R}_x(\phi_b^n)^T \mathbf{R}_y(\theta_b^n)^T \begin{bmatrix} 0 \\ 0 \\ \dot{\psi}_b^n \end{bmatrix}. \quad (3.5)$$

Hence,

$$\boldsymbol{\omega}_{b/n}^b = \begin{bmatrix} 1 & 0 & -s(\theta_b^n) \\ 0 & c(\phi_b^n) & c(\theta_b^n)s(\phi_b^n) \\ 0 & -s(\phi_b^n) & c(\theta_b^n)c(\phi_b^n) \end{bmatrix} \begin{bmatrix} \dot{\phi}_b^n \\ \dot{\theta}_b^n \\ \dot{\psi}_b^n \end{bmatrix} := (\mathbf{T}_b^n)^{-1} \begin{bmatrix} \dot{\phi}_b^n \\ \dot{\theta}_b^n \\ \dot{\psi}_b^n \end{bmatrix} \quad (3.6)$$

and

$$\begin{bmatrix} \dot{\phi}_b^n \\ \dot{\theta}_b^n \\ \dot{\psi}_b^n \end{bmatrix} = \mathbf{T}_b^n \boldsymbol{\omega}_{b/n}^b = \begin{bmatrix} 1 & s(\phi_b^n)t(\theta_b^n) & c(\phi_b^n)t(\theta_b^n) \\ 0 & c(\phi_b^n) & -s(\phi_b^n) \\ 0 & s(\phi_b^n)/c(\theta_b^n) & c(\phi_b^n)/c(\theta_b^n) \end{bmatrix} \boldsymbol{\omega}_{b/n}^b. \quad (3.7)$$

Note the well known Euler singularity when $\theta_b^n = \pm\pi/2$, at which point $\dot{\psi}_b^n$ becomes undefined.

The complete vehicle kinematics in 6 degrees of freedom (DOF) are:

$$\dot{\boldsymbol{\eta}}_b^n = \mathbf{J}_b^n \boldsymbol{\nu}_{b/n}^b = \begin{bmatrix} \mathbf{R}_b^n & \mathbf{0}_{3 \times 3} \\ \mathbf{0}_{3 \times 3} & \mathbf{T}_b^n \end{bmatrix} \boldsymbol{\nu}_{b/n}^b. \quad (3.8)$$

3.1.1 3 DOF Kinematics

In this thesis, surface vehicles will be modeled in 3 DOF: surge, sway and yaw. The vehicle will be assumed to be passively stabilized in roll, which is hence neglected. This assumption is usually valid for maneuvering vehicles, both to prevent capsizing of the vessel and to avoid the energy consumption of active roll stabilization. Movement in pitch and heave are assumed to be wave-induced disturbances, which we also neglect in the model, as these are high-frequent disturbances which we do not want the control system to respond to¹. Thus, the kinematics in 3 DOF are:

$$\begin{bmatrix} \dot{x}_b^n \\ \dot{y}_b^n \\ \dot{\psi}_b^n \end{bmatrix} = \begin{bmatrix} c(\psi_b^n) & -s(\psi_b^n) & 0 \\ s(\psi_b^n) & c(\psi_b^n) & 0 \\ 0 & 0 & 1 \end{bmatrix} \begin{bmatrix} u_b \\ v_b \\ r_b \end{bmatrix}. \quad (3.9)$$

¹In practical implementations of marine control systems, such disturbances are often filtered out using low-pass or wave filters [35, 102].

3.1.2 5 DOF Kinematics

For underwater vehicles, pitch and heave needs to be included in the model. Roll is, however, still assumed to be passively stabilized. Hence, we model underwater vehicles in 5 DOF. The rotation matrix from b to n is

$$\mathbf{R}_b^n = \mathbf{R}_{zy}(\theta_b^n, \psi_b^n) = \begin{bmatrix} c(\psi_b^n)c(\theta_b^n) & -s(\psi_b^n) & c(\psi_b^n)s(\theta_b^n) \\ s(\psi_b^n)c(\theta_b^n) & c(\psi_b^n) & s(\psi_b^n)s(\theta_b^n) \\ -s(\theta_b^n) & 0 & c(\theta_b^n) \end{bmatrix}, \quad (3.10)$$

while the angular transformation matrix in 5 DOF is

$$\mathbf{T}_b^n = \begin{bmatrix} 1 & 0 \\ 0 & 1/c(\theta_b^n) \end{bmatrix}. \quad (3.11)$$

The complete vehicle kinematics in 5 DOF are

$$\begin{bmatrix} \dot{x}_b^n \\ \dot{y}_b^n \\ \dot{z}_b^n \\ \dot{\theta}_b^n \\ \dot{\psi}_b^n \end{bmatrix} = \begin{bmatrix} c(\psi_b^n)c(\theta_b^n) & -s(\psi_b^n) & c(\psi_b^n)s(\theta_b^n) & 0 & 0 \\ s(\psi_b^n)c(\theta_b^n) & c(\psi_b^n) & s(\psi_b^n)s(\theta_b^n) & 0 & 0 \\ -s(\theta_b^n) & 0 & c(\theta_b^n) & 0 & 0 \\ 0 & 0 & 0 & 1 & 0 \\ 0 & 0 & 0 & 0 & 1/c(\theta_b^n) \end{bmatrix} \begin{bmatrix} u_b \\ v_b \\ w_b \\ q_b \\ r_b \end{bmatrix}. \quad (3.12)$$

3.2 Dynamics

The vehicles considered in this thesis are modeled using a maneuvering model as described in Fossen [35]. This is a model which assumes that the vehicle keeps at least a certain minimum surge speed, which depends on the vehicle but is typically more than 1 m/s. When maneuvering at such speeds, it is possible to approximate frequency-dependent added mass and damping components as constants, which simplifies the model.

The structure of the maneuvering model is

$$\mathbf{M}\dot{\boldsymbol{\nu}}_{b/n}^b + \mathbf{C}(\boldsymbol{\nu}_{b/n}^b)\boldsymbol{\nu}_{b/n}^b + \mathbf{D}\boldsymbol{\nu}_{b/n}^b + \mathbf{g}(\boldsymbol{\eta}_b^n) = \mathbf{B}\mathbf{f}, \quad (3.13)$$

where $\mathbf{M} = \mathbf{M}^T > 0$ is the mass and inertia matrix including hydrodynamic added mass, while \mathbf{C} contains Coriolis and centripetal terms, and \mathbf{D} is the hydrodynamic damping matrix. Throughout this thesis we will model the damping as linear, i.e. \mathbf{D} will contain only constant parameters. As noted in Caharija et al. [18], the passive nature of any nonlinear damping forces should enhance the directional stability of the vehicle.

Gravitational forces and moments are gathered in the gravity restoration vector \mathbf{g} . Control input from the vehicle actuators are contained in \mathbf{f} , and converted to control forces and moments through the actuator configuration matrix \mathbf{B} . In the next two sections, we will describe this model in more detail for 3 and 5 DOF.

3.2.1 3 DOF Dynamics

In 3 DOF, we can neglect the effects of gravity, as we only consider movement in surge, sway and yaw. By assuming that the vehicle is port-starboard symmetric,

and that the origin of b lies along the centerline of the vehicle, we obtain the following structure for \mathbf{M} and \mathbf{D} :

$$\mathbf{M} = \begin{bmatrix} m_{11} & 0 & 0 \\ 0 & m_{22} & m_{23} \\ 0 & m_{23} & m_{33} \end{bmatrix}, \quad \mathbf{D} = \begin{bmatrix} d_{11} & 0 & 0 \\ 0 & d_{22} & d_{23} \\ 0 & d_{32} & d_{33} \end{bmatrix} \quad (3.14)$$

The Coriolis and centripetal matrix \mathbf{C} is obtained from \mathbf{M} as described in Fossen [35]:

$$\mathbf{C} = \begin{bmatrix} 0 & 0 & -m_{22}v_b - m_{23}r_b \\ 0 & 0 & m_{11}u_b \\ m_{22}v_b + m_{23}r_b & -m_{11}u_b & 0 \end{bmatrix}, \quad (3.15)$$

The control input vector is $\mathbf{f} = [T_u, T_r]^T$, where T_u is the surge thrust and T_r the rudder angle. The surge thrust is assumed to affect only the surge dynamics, while the rudder angle can affect both the sway and yaw dynamics. The structure of \mathbf{B} thus becomes

$$\mathbf{B} = \begin{bmatrix} b_{11} & 0 \\ 0 & b_{22} \\ 0 & b_{33} \end{bmatrix}. \quad (3.16)$$

The effect of the rudder on the underactuated sway dynamics through b_{22} complicates the design and analysis of control systems on the vehicle. However, by assuming that the origin of b lies in the pivot point of the vehicle, i.e. the point around which the vehicle turns, this effect is removed since then

$$\mathbf{M}^{-1}\mathbf{B}\mathbf{f} = [\tau_u, 0, \tau_r]^T. \quad (3.17)$$

Here, τ_u is the control force in vehicle surge, while τ_r is the control moment in vehicle yaw.

If the origin of b is not originally located in the pivot point of the ship, it is always possible to perform a coordinate transform translate it there. This procedure is described in Fossen [35].

The dynamics can be expressed in component form by solving for $\dot{\nu}_{b/n}^b$:

$$\dot{u}_b = F_u(u_b, v_b, r_b) + \tau_u, \quad (3.18a)$$

$$\dot{v}_b = X_v(u_b)r_b + Y_v(u_b)v_b, \quad (3.18b)$$

$$\dot{r}_b = F_r(u_b, v_b, r_b) + \tau_r, \quad (3.18c)$$

where

$$F_u(u_b, v_b, r_b) \triangleq \frac{1}{m_{11}}(m_{22}v_b + m_{23}r_b)r_b - \frac{d_{11}}{m_{11}}u_b, \quad (3.19)$$

$$F_r(u_b, v_b, r_b) \triangleq \frac{m_{23}d_{22} + m_{22}(d_{32} + (m_{22} - m_{11})u_b)}{m_{22}m_{33} - m_{23}^2}v_b + \frac{m_{23}(d_{23} - m_{11}u_b) - m_{22}(d_{33} + m_{23}u_b)}{m_{22}m_{33} - m_{23}^2}r_b, \quad (3.20)$$

$$X_v(u_b) \triangleq \frac{m_{23}^2 - m_{11}m_{33}}{m_{22}m_{33} - m_{23}^2}u_b + \frac{d_{33}m_{23} - d_{23}m_{33}}{m_{22}m_{33} - m_{23}^2}, \quad (3.21)$$

and

$$Y_v(u_b) \triangleq \frac{(m_{22} - m_{11})m_{23}}{m_{22}m_{33} - m_{23}^2}u_b - \frac{d_{22}m_{33} - d_{32}m_{23}}{m_{22}m_{33} - m_{23}^2}, \quad (3.22)$$

The surge (3.18a) and yaw (3.18c) dynamics are directly actuated through τ_u and τ_r . Hence, the nonlinearities of F_u and F_r can be canceled using feedback linearizing controllers. The sway dynamics (3.18b), however, are underactuated. When turning at maneuvering speed, the inertia of the vehicle will make the vehicle's velocity vector lag behind. Hence, a sway speed is induced, which is captured by the $X(u_b)r_b$ term. As the vehicle moves sideways through the water, it will encounter damping, which is captured by the $Y(u_b)v_b$ term. Hence, it is reasonable to assume that $Y(u_b)$ and $X(u_b)$ are negative. These assumptions will be formalized as needed throughout the thesis.

3.2.2 5 DOF dynamics

When modeling the vehicle in 5 DOF, we include the pitch and heave dynamics, as well as the effect from gravity. As in the 3 DOF case, we assume that the vehicle is port-starboard symmetric, and that the origin of b is positioned along the center-line of the vehicle. By making the additional assumptions that the vehicle is symmetric also in the $x-z$ plane, and that it has a large length to width ratio, the structure of \mathbf{M} and \mathbf{D} are obtained as

$$\mathbf{M} \triangleq \begin{bmatrix} m_{11} & 0 & 0 & 0 & 0 \\ 0 & m_{22} & 0 & 0 & m_{25} \\ 0 & 0 & m_{33} & m_{34} & 0 \\ 0 & 0 & m_{34} & m_{44} & 0 \\ 0 & m_{25} & 0 & 0 & m_{55} \end{bmatrix}, \mathbf{D} \triangleq \begin{bmatrix} d_{11} & 0 & 0 & 0 & 0 \\ 0 & d_{22} & 0 & 0 & d_{25} \\ 0 & 0 & d_{33} & d_{34} & 0 \\ 0 & 0 & d_{43} & d_{44} & 0 \\ 0 & d_{25} & 0 & 0 & d_{55} \end{bmatrix}. \quad (3.23)$$

The Coriolis and centripetal matrix \mathbf{C} is again obtained from \mathbf{M} as described in Fossen [35]:

$$\mathbf{C} \triangleq \begin{bmatrix} 0 & 0 & 0 & m_{33}w_b + m_{34}q_b & -m_{22}v_b - m_{25}r_b \\ 0 & 0 & 0 & 0 & m_{11}u_b \\ 0 & 0 & 0 & -m_{11}u_b & 0 \\ -m_{33}w_b - m_{34}q_b & 0 & m_{11}u_b & 0 & 0 \\ m_{22}v_b + m_{25}r_b & -m_{11}u_b & 0 & 0 & 0 \end{bmatrix}. \quad (3.24)$$

The vehicle is assumed to be neutrally buoyant, and we also assume that the center of gravity CG is on the center-line of the vehicle, and that the center of buoyancy is on the same z -axis in b as CG. The gravity restoration vector \mathbf{g} can then be constructed as $\mathbf{g}(\boldsymbol{\eta}_b^n) \triangleq [0, 0, 0, BG_z W \sin(\theta_b^n), 0]^T$, where BG_z is the vertical distance between CG and CB, and W is the vehicle weight.²

The control input vector $\mathbf{f} \triangleq [T_u, T_q, T_r]^T$ contains surge thrust (T_u), pitch rudder angle (T_q) and yaw rudder angle (T_r). These are converted to control forces

²In Chapter 6 we examine the effect on path following in the case where the vehicle is not neutrally buoyant. Informally, the vehicle then has to use more surge thrust in order to counteract the resultant buoyancy effects when following the path.

and moments using the actuator configuration matrix \mathbf{B} . We assume that the surge thrust does not affect the other degrees of freedom, and we only consider couplings in sway-yaw and heave-pitch. The structure of \mathbf{B} is then obtained as:

$$\mathbf{B} \triangleq \begin{bmatrix} b_{11} & 0 & 0 \\ 0 & 0 & b_{23} \\ 0 & b_{32} & 0 \\ 0 & b_{42} & 0 \\ 0 & 0 & b_{53} \end{bmatrix}. \quad (3.25)$$

By choosing the origin of b to lie in the pivot point of the vehicle, we ensure that $\mathbf{M}^{-1}\mathbf{B}\mathbf{f} = [\tau_u, 0, 0, \tau_q, \tau_r]^T$, where τ_u , τ_q and τ_r are control signals in surge, pitch and yaw, respectively. Specifically, τ_u is the control force in surge, and τ_q and τ_r are the control moments in pitch and yaw. When expressed in component form, the 5 DOF dynamics are

$$\dot{u}_b = F_u(u_b, v_b, w_b, r_b, q_b) + \tau_u, \quad (3.26a)$$

$$\dot{v}_b = X_v(u_b)r_b + Y_v(u_b)v_b, \quad (3.26b)$$

$$\dot{w}_b = X_w(u_b)q_b + Y_w(u_b)w_b + Z_w \sin(\theta_b^n), \quad (3.26c)$$

$$\dot{q}_b = F_q(\theta_b^n, u_b, w_b, q_b) + \tau_q. \quad (3.26d)$$

$$\dot{r}_b = F_r(u_b, v_b, r_b) + \tau_r. \quad (3.26e)$$

The functions F_u , X_v , Y_v , X_w , Y_w , Z_w , F_q and F_r contain hydrodynamic parameters from \mathbf{M} and \mathbf{D} , and are defined as:

$$F_u \triangleq \frac{1}{m_{11}} [(m_{22}v_b + m_{25}r_b)r_b - (m_{33}w_b + m_{34}q_b)q_b - d_{11}u_b] \quad (3.27)$$

$$X_v \triangleq \frac{m_{25}^2 - m_{11}m_{55}}{m_{22}m_{55} - m_{25}^2}u_b + \frac{d_{55}m_{25} - d_{25}m_{55}}{m_{22}m_{55} - m_{25}^2}, \quad (3.28)$$

$$Y_v \triangleq \frac{(m_{22} - m_{11})m_{25}}{m_{22}m_{55} - m_{25}^2}u_b - \frac{d_{22}m_{55} - d_{52}m_{25}}{m_{22}m_{55} - m_{25}^2}, \quad (3.29)$$

$$X_w \triangleq \frac{-m_{34}^2 - m_{11}m_{44}}{m_{33}m_{44} - m_{34}^2}u_b + \frac{d_{44}m_{34} - d_{34}m_{44}}{m_{33}m_{44} - m_{34}^2}, \quad (3.30)$$

$$Y_w \triangleq \frac{(m_{11} - m_{33})m_{34}}{m_{33}m_{44} - m_{34}^2}u_b - \frac{d_{33}m_{44} - d_{43}m_{34}}{m_{33}m_{44} - m_{34}^2}, \quad (3.31)$$

$$Z_w \triangleq \frac{BG_z W m_{34}}{m_{33}m_{44} - m_{34}^2}, \quad (3.32)$$

$$F_q \triangleq -\frac{BG_z W m_{33}}{m_{33}m_{44} - m_{34}^2} \sin(\theta_b^n) + \frac{m_{34}d_{33} - m_{33}(d_{43} - (m_{33} - m_{11})u_b)}{m_{33}m_{44} - m_{34}^2}w_b \\ + \frac{m_{34}(d_{34} - m_{11}u_b) - m_{33}(d_{44} - m_{34}u_b)}{m_{33}m_{44} - m_{34}^2}q_b, \quad (3.33)$$

$$\begin{aligned}
 F_r \triangleq & \frac{m_{25}d_{22} - m_{22}(d_{52} + (m_{22} - m_{11})u_b)}{m_{22}m_{55} - m_{25}^2} v_b \\
 & + \frac{m_{25}(d_{25} + m_{11}u_b) - m_{22}(d_{55} + m_{25}u_b)}{m_{22}m_{55} - m_{25}^2} r_b.
 \end{aligned} \tag{3.34}$$

The surge (3.26a), pitch (3.26d) and yaw (3.26e) dynamics are directly actuated through τ_u , τ_q and τ_r , while the sway (3.26b) and heave (3.26c) dynamics are underactuated. Movement in heave is induced when pitching, in the same manner as movement in sway as described in the previous section. However, in heave there is an additional component, $Z_w \sin(\theta_b^n)$, which is due to a moment induced around the center of buoyancy when the vehicle pitch is nonzero.

3.3 Ocean current and relative velocities

Part II of this thesis examines path following in the presence of ocean currents. In this section we will show how a constant and irrotational current affects the vehicle model.

The current is modeled at the kinematic level, with the current velocity contained in the vector $\boldsymbol{\nu}_{c/n}^n$:

$$\boldsymbol{\nu}_{c/n}^n \triangleq \begin{bmatrix} V_x \\ V_y \\ 0 \end{bmatrix} \quad (3\text{DOF}), \quad \boldsymbol{\nu}_{c/n}^n \triangleq \begin{bmatrix} V_x \\ V_y \\ V_z \\ 0 \\ 0 \end{bmatrix} \quad (5\text{DOF}). \tag{3.35}$$

The kinematics of the vehicle can now be represented in terms of the vehicle's velocity relative to water,

$$\boldsymbol{\nu}_{rb/n}^b \triangleq \boldsymbol{\nu}_{b/n}^b - \boldsymbol{\nu}_{c/n}^b, \tag{3.36}$$

where $\boldsymbol{\nu}_{c/n}^b$ is the velocity vector of the ocean current in the body frame. Hence,

$$\boldsymbol{\nu}_{rb/n}^b = \begin{bmatrix} u_{rb} \\ v_{rb} \\ r_b \end{bmatrix} \quad (3\text{DOF}), \quad \boldsymbol{\nu}_{rb/n}^b = \begin{bmatrix} u_{rb} \\ v_{rb} \\ w_{rb} \\ q_b \\ r_b \end{bmatrix} \quad (5\text{DOF}). \tag{3.37}$$

The kinematics of the vehicle when in the presence of an ocean current are expressed as

$$\dot{\boldsymbol{\eta}}_b^n = \mathbf{J}_b^n \boldsymbol{\nu}_{rb/n}^b + \boldsymbol{\nu}_{c/n}^n. \tag{3.38}$$

It is shown in Fossen [35] that when the ocean current is constant and irrotational, the vehicle dynamics can be expressed in terms of the relative velocities:

$$\mathbf{M} \dot{\boldsymbol{\nu}}_{rb/n}^b + \mathbf{C}(\boldsymbol{\nu}_{rb/n}^b) \boldsymbol{\nu}_{rb/n}^b + \mathbf{D} \boldsymbol{\nu}_{rb/n}^b + \mathbf{g}(\boldsymbol{\eta}_b^n) = \mathbf{B} \mathbf{f}. \tag{3.39}$$

The system matrices in (3.39) are the same as the ones presented in Section 3.2.1 in 3 DOF, and Section 3.2.2 in 5 DOF.

3.4 Assumptions summary

This section contains a summary of the assumptions made during the modeling, listed for convenience. These assumptions generally hold for slender AUVs [35] and are valid for many commercial AUVs.

Assumption 3.1. The vehicle model is expressed the Body frame b , which is located on the center line of the vehicle. The distance from the center of gravity (CG) to the origin of b is $(x_g, 0, 0)$, and hence CG is also on the center line.

Assumption 3.2. The center of buoyancy (CB) and CG is on the same vertical axis in b .

Assumption 3.3. Any nonlinear damping parameters can be neglected, so that only linear damping is considered.

Assumption 3.4. The vehicle is symmetric in the $x - z$ plane and in the $x - y$ plane. Furthermore, the length-to-width ratio of the vehicle is large.

Assumption 3.5. The vehicle is passively stable in roll, and roll motion can hence be neglected.

Assumption 3.6. The vehicle is neutrally buoyant.

Assumption 3.7. The control input in surge does not affect the other degrees of freedom. Furthermore, only couplings in sway-yaw and heave-pitch need to be considered.

Assumption 3.8. The ocean current is constant and irrotational.

Part II

Path Following

Chapter 4

Integral Line of Sight Path Following for Surface Vehicles

The road goes ever on and on.

— J.R.R. Tolkien, *The Hobbit*

In this chapter, we will examine the straight-line path following problem for underactuated surface vehicles, or for underwater vehicles operating in the horizontal plane. To this end, we will apply the integral line of sight (ILOS) guidance law proposed by Børhaug et al. [13]. This guidance law makes the vehicle converge to and follow a straight-line path even when disturbed by a constant and irrotational current. The guidance law has been extensively analyzed, and was shown to achieve κ -exponential stability in Caharija et al. [18]. This was achieved by formulating the kinematics and dynamics of the vehicle using relative velocities, as described in Section 3.3.

In Fossen and Pettersen [36], the comparison lemma in Khalil [55, Lemma 3.4] was applied in order to provide conditions under which the line of sight (LOS) guidance law, without integral effect, provided uniform semiglobal exponential stability (USGES) of the origin of the error dynamics. This is the strongest stability result achievable by path following guidance laws, due to a saturation bounding the system gain when the vehicle is far away from the path and the surge speed is bounded. Informally, a vehicle with bounded forward speed will not be able to converge faster to a path than when moving straight towards it, giving an approximately linear convergence rate when the distance to the path is large.

We will in this chapter apply the comparison lemma to a surface vehicle guided by the ILOS guidance law in order to find control parameters providing USGES in the presence of an unknown ocean current uniform in time and space. Thus, the results presented here build on the results of Caharija et al. [18], using the technique of Fossen et al. [37].

The remainder of this chapter is organized as follows. Section 4.1 gives a description of the vehicle model in 3-DOF, and states the control objective. Section 4.2 describes the ILOS guidance law and the surge and speed controllers that are analyzed in this chapter. A stability analysis of the closed-loop kinematic system is presented in Section 4.3, while the stability of the complete closed-loop kinematic and dynamic system is analyzed in Section 4.4. The analyzes show both systems to be USGES, which is the main result of this chapter. Simulations that demonstrate

the exponential stability of the system are shown in Section 4.5, before the chapter is concluded in Section 4.6.

The work presented in this chapter is based on Wiig et al. [111].

4.1 System description

4.1.1 System model

The vehicle is modeled in 3 DOF using the relative velocity model presented in Section 3.3. The vehicle is operating in the presence of an ocean current, which we assume to be constant, irrotational and bounded:

Assumption 4.1. The ocean current $\boldsymbol{v}_{c/n}^n \triangleq [V_x, V_y, 0]^T$ is assumed to be constant, irrotational and bounded. Hence, there exists a constant $V_{\max} \geq 0$ such that $V_{\max} \geq \sqrt{V_x^2 + V_y^2}$.

Thus, the vehicle kinematics and dynamics in component form are

$$\dot{x}_b^n = u_{rb} \cos(\psi_b^n) - v_{rb} \sin(\psi) + V_x, \quad (4.1a)$$

$$\dot{y}_b^n = u_{rb} \sin(\psi_b^n) + v_{rb} \cos(\psi) + V_y, \quad (4.1b)$$

$$\dot{\psi}_b^n = r_b, \quad (4.1c)$$

$$\dot{u}_{rb} = F_u(u_{rb}, v_{rb}, r_b) + \tau_u, \quad (4.1d)$$

$$\dot{v}_{rb} = X_v(u_{rb})r_b + Y_v(u_{rb})v_{rb}, \quad (4.1e)$$

$$\dot{r}_b = F_r(u_{rb}, v_{rb}, r_b) + \tau_r. \quad (4.1f)$$

The functions F_u , F_r , X_v and Y_v are defined in Section 3.2.1, and restated in Appendix 4.A for convenience.

To ensure that the system is nominally stable in sway, we make the following assumption:

Assumption 4.2. The function Y_v satisfies

$$Y_v(u_{rb}) < 0, \quad \forall u_{rb} > 0. \quad (4.2)$$

This is justified by noticing that $Y_v(u_{rb}) \geq 0$ implies that the system is undamped or nominally unstable in sway, which is not the case for commercial vessels by design.

4.1.2 Control objective

The objective of the control system is to make the vehicle modeled by (4.1) converge to and follow a straight-line path. This objective should be met in the presence of an unknown, constant and irrotational current while keeping a constant relative surge speed $u_{rd} > 0$. To simplify the analysis, without any loss of generality, the desired path \mathcal{P} lies along the x -axis of the n frame:

$$\mathcal{P} \triangleq \{(x, y) \in \mathbb{R}^2 : y = 0\}. \quad (4.3)$$

The objectives of the control system are formalized as

$$\lim_{t \rightarrow \infty} y_b^n(t) = 0, \quad (4.4a)$$

$$\lim_{t \rightarrow \infty} \psi_b^n(t) = \psi_{ss}, \quad \psi_{ss} \in \left(-\frac{\pi}{2}, \frac{\pi}{2}\right), \quad (4.4b)$$

$$\lim_{t \rightarrow \infty} u_{rb}(t) = u_{rd}, \quad (4.4c)$$

where ψ_{ss} is a constant yaw angle required to keep the underactuated vessel at the path in the presence of current. Note that, even though the vessel will sideslip along the path, the drift angle with respect to the water flow will converge to zero due to port-starboard symmetry. The following assumption ensures that the vessel is able to follow the path for any direction of the ocean current:

Assumption 4.3. The propulsion system is capable of achieving a relative surge speed u_{rd} such that $u_{rd} > V_{\max}$.

4.2 Control system

This section presents a control system for solving the path following problem presented in Section 4.1.2.

4.2.1 The ILOS guidance law

The desired heading ψ_d^n is given by the ILOS guidance law introduced in Børhaug et al. [13]:

$$\psi_d^n \triangleq -\tan^{-1}\left(\frac{y_b^n + \sigma y_{\text{int}}^n}{\Delta}\right), \quad (4.5a)$$

$$\dot{y}_{\text{int}}^n \triangleq \frac{\Delta y_b^n}{(y_b^n + \sigma y_{\text{int}}^n)^2 + \Delta^2}. \quad (4.5b)$$

The lookahead distance Δ and the integral gain σ are constant, positive design parameters.

An illustration of the ILOS guidance law is shown in Figure 4.1. The intuition behind the law is to mimic the way an experienced helmsman steers a vehicle by aiming the vehicle towards a point lying a lookahead distance Δ meters ahead of it on the path. Thus, if the vehicle is far away from the path, it will move on an almost perpendicular trajectory towards it. As the vehicle gets closer to the path, it will steer on a more parallel course, ensuring a that the turn onto the path is not too sharp.

An integral effect is added to counter the ocean current. Without this effect, any ocean current acting in the transversal direction of the desired path would push the vessel away from the path and thus create a steady state error. With the integral effect, the vehicle aims towards a virtual path parallel to the desired path. A nonzero desired heading is thus created even when the cross-track error is zero, and the vehicle is able to sideslip along the desired path \mathcal{P} . By design, the integral term growth rate (4.5b) will decrease for large cross-track errors y_b^n , reducing the risk of wind-up effects.

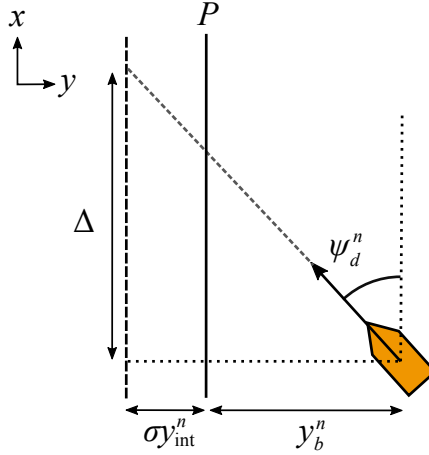


Figure 4.1: Geometry of the ILOS guidance law.

4.2.2 Surge and yaw controllers

Surge and yaw are controlled using the following feedback linearizing controllers like the ones described in Børhaug et al. [14]:

$$\tau_u = -F_u(u_{rb}, v_{rb}, r_b) + \dot{u}_{rd} - k_u(u_{rb} - u_{rd}), \quad (4.6a)$$

$$\tau_r = -F_r(u_{rb}, v_{rb}, r_b) + \ddot{\psi}_d^n - k_\psi(\psi_b^n - \psi_d^n) - k_r(r_b - \dot{\psi}_d^n), \quad (4.6b)$$

where k_u , k_ψ and k_r are constant, positive gains.

4.3 Closed-loop kinematic stability

This section analyzes the stability properties of the closed-loop kinematic system by assuming zero sway speed, $v_{rb} = 0$, perfectly controlled surge, $u_{rb} = u_{rd}$, and perfectly controlled heading $\psi_b^n = \psi_d^n$. Substituting (4.5a) into (4.1b) then gives the following expression for the y_b^n kinematics:

$$\dot{y}_{\text{int}}^n = \frac{\Delta y_b^n}{(y_b^n + \sigma y_{\text{int}}^n)^2 + \Delta^2}, \quad (4.7a)$$

$$\dot{y}_b^n = -u_{rd} \frac{y_b^n + \sigma y_{\text{int}}^n}{\sqrt{(y_b^n + \sigma y_{\text{int}}^n)^2 + \Delta^2}} + V_y. \quad (4.7b)$$

The equilibrium point of (4.7) is at the point

$$y_{\text{int}}^n = y_{\text{int}}^{\text{eq}} \triangleq \frac{\Delta}{\sigma} \frac{V_y}{\sqrt{u_{rd}^2 - V_y^2}}, \quad (4.8a)$$

$$y_b^n = 0. \quad (4.8b)$$

Note that the saturation introduced by the sinusoidal function of the y_b^n dynamics in (4.1b) makes the system gain in (4.7) decrease with the magnitude of the cross-track error. Hence, GES cannot be achieved.

Theorem 4.1. *If Assumptions 4.1 and 4.3 hold and the gain σ satisfies*

$$0 < \sigma < u_{rd} - V_{\max} \quad (4.9)$$

then the ILOS guidance law (4.5) applied to the cross-track error dynamics (4.7) renders the equilibrium point (4.8) USGES.

Proof. The proof follows along the lines of Caharija et al. [18], while also making use of the comparison lemma in Khalil [55, Lemma 3.4] along the lines of the analysis in Fossen and Pettersen [36].

A change of variables is introduced to obtain a system with the equilibrium point at the origin:

$$e_1 \triangleq y_{\text{int}}^n - y_{\text{int}}^{\text{eq}}, \quad (4.10a)$$

$$e_2 \triangleq y + \sigma e_1. \quad (4.10b)$$

The dynamics of the new system are:

$$\dot{e}_1 = -\frac{\Delta\sigma e_1}{l(e_2)} + \frac{\Delta e_2}{l(e_2)}, \quad (4.11a)$$

$$\dot{e}_2 = -\frac{\Delta\sigma^2 e_1}{l(e_2)} + V_y f(e_2) - \left[u_{rd} \sqrt{l(e_2)} - \sigma \Delta \right] \frac{e_2}{l(e_2)}, \quad (4.11b)$$

where $l(e_2)$ is defined as

$$l(e_2) \triangleq (e_2 + \sigma y_{\text{int}}^{\text{eq}})^2 + \Delta^2, \quad (4.12)$$

and $f(e_2)$ is defined as

$$f(e_2) \triangleq 1 - \frac{\sqrt{(\sigma y_{\text{int}}^{\text{eq}})^2 + \Delta^2}}{\sqrt{l(e_2)}}. \quad (4.13)$$

The following bound holds for $f(e_2)$ and will be used in the analysis:

$$|f(e_2)| \leq \frac{|e_2|}{\sqrt{l(e_2)}} \quad (4.14)$$

Consider the Lyapunov function candidate

$$V = \frac{\sigma^2}{2} e_1^2 + \frac{1}{2} e_2^2 = \frac{1}{2} e^T \mathbf{P} e, \quad (4.15)$$

where $\mathbf{e} \triangleq [e_1, e_2]^T$ and $\mathbf{P} \triangleq \text{diag}\{\sigma^2, 1\} > 0$. The time-derivative of V is

$$\begin{aligned} \dot{V} = & - \left[u_{rd} \sqrt{l(e_2)} - \sigma \Delta \right] \frac{e_2^2}{l(e_2)} \\ & - \frac{\Delta\sigma^3 e_1^2}{l(e_2)} + V_y f(e_2), \end{aligned} \quad (4.16)$$

which can be shown to satisfy

$$\dot{V} \leq -\frac{1}{l(e_2)} e^T \mathbf{Q} e, \quad (4.17)$$

where \mathbf{Q} is defined as

$$\mathbf{Q} \triangleq \text{diag}\{\sigma^3, \Delta(u_{rd} - V_{\max} - \sigma)\}. \quad (4.18)$$

Under the assumption that σ satisfies (13), $\mathbf{Q} > 0$ and hence $\dot{V} \leq 0$. By [55, Theorem 4.8], this implies that the equilibrium $e = \mathbf{0}$ is uniformly stable.

The term $\sigma y_{\text{int}}^{\text{eq}}$ in (4.12) can be bounded using (4.8) and Assumption 4.1 to

$$\sigma y_{\text{int}}^{\text{eq}} = \frac{\Delta V y}{\sqrt{u_{rd}^2 - V_y^2}} \leq \frac{\Delta V_{\max}}{\sqrt{u_{rd}^2 - V_{\max}^2}} := \kappa. \quad (4.19)$$

Hence

$$\dot{V} \leq -\frac{1}{(e_2 + \kappa)^2 + \Delta^2} e^T \mathbf{Q} e. \quad (4.20)$$

Furthermore, for each $r > 0$ and $|e_2| \leq r$ we have

$$\frac{1}{(e_2 + \kappa)^2 + \Delta^2} \geq \frac{1}{(r + \kappa)^2 + \Delta^2} := c(r). \quad (4.21)$$

Consequently,

$$\dot{V} \leq -c(r) e^T \mathbf{Q} e \leq -2c(r) \frac{q_{\min}}{p_{\max}} V, \quad \forall \|e(t)\| \leq r, \quad (4.22)$$

where $p_{\max} = \max\{\sigma^2, 1\}$ and $q_{\min} = \min\{\sigma^3, \Delta(u_{rd} - V_{\max} - \sigma)\}$.

The inequality in (4.22) is valid for all trajectories generated by the initial conditions $e(t_0)$ since the system is uniformly stable. The comparison lemma [55, Lemma 3.4] can then be invoked by noticing that the linear system

$$\dot{z} = -2 \frac{q_{\min}}{p_{\max}} c(r) z \quad (4.23)$$

has the solution

$$z(t) = e^{-2 \frac{q_{\min}}{p_{\max}} c(r) (t-t_0)} z(t_0). \quad (4.24)$$

This implies that for $v(t) = V(t, e(t))$,

$$v(t) \leq e^{-2 \frac{q_{\min}}{p_{\max}} c(r) (t-t_0)} v(t_0). \quad (4.25)$$

It follows that

$$\|e(t)\| \leq \sqrt{\frac{p_{\max}}{p_{\min}}} e^{-\frac{q_{\min}}{p_{\max}} c(r) (t-t_0)} \|e(t_0)\|, \quad (4.26)$$

where $p_{\min} \triangleq \min\{\sigma^2, 1\}$. This holds for all $t \geq t_0$, $\|e(t)\| \leq r$ and any $r > 0$, and it shows the equilibrium point $e = \mathbf{0}$ to be USGES as defined in Definition 2.4. \square

4.4 Stability of the closed-loop kinematics and dynamics

In this section we analyze the stability properties of the complete vessel kinematics and dynamics with the ILOS guidance law (4.5) in a cascaded configuration with the surge and yaw controllers (4.6). Specifically, we provide conditions under which the resulting equilibrium point of the closed-loop system is proved to be USGES. In the following, the notation $X_{vd} = X_v(u_{rd})$ and $Y_{vd} = Y_v(u_{rd})$ is used for brevity.

4.4.1 Cascaded system description

The error signals in surge, sway and yaw are collected in $\zeta \triangleq [\tilde{u}_{rb}, \tilde{\psi}_b^n, \tilde{r}_b]^T$, where $\tilde{u}_{rb} \triangleq u_{rb} - u_{rd}$, $\tilde{\psi}_b^n \triangleq \psi_b^n - \psi_d^n$ and $\tilde{r}_b \triangleq r_b - \dot{\psi}_d^n$. The dynamics of ζ are obtained by combining the system equations (4.1c), (4.1d) and (4.1f) with the control laws in surge (4.6a) and yaw (4.6b):

$$\dot{\zeta} = \begin{bmatrix} -k_u & 0 & 0 \\ 0 & 0 & 1 \\ 0 & -k_\psi & -k_r \end{bmatrix} \zeta \triangleq \Sigma \zeta. \quad (4.27)$$

The $y_b^n - v_{rb}$ subsystem is then obtained from (4.1b), (4.1e) and (4.5b):

$$\dot{y}_{\text{int}}^n = \frac{\Delta y_b^n}{(y_b^n + \sigma y_{\text{int}}^n)^2 + \Delta^2}, \quad (4.28a)$$

$$\dot{y}_b^n = (\tilde{u}_{rb} + u_{rd}) \sin(\tilde{\psi}_b^n + \psi_d^n) + v_{rb} \cos(\tilde{\psi}_b^n + \psi_d^n) + V_y, \quad (4.28b)$$

$$\dot{v}_{rb} = X_v(\tilde{u}_{rb} + u_{rd})(r_b + \dot{\psi}_d^n) + Y_v(\tilde{u}_{rb} + u_{rd})v_{rb}. \quad (4.28c)$$

The equilibrium point of (4.28) on the manifold $\zeta = \mathbf{0}$ is

$$y_{\text{int}}^n = y_{\text{int}}^{\text{eq}} \triangleq \frac{\Delta}{\sigma} \frac{V_y}{\sqrt{u_{rd}^2 - V_y^2}}, \quad (4.29a)$$

$$y_b^n = 0, \quad (4.29b)$$

$$v_{rb} = 0. \quad (4.29c)$$

A change of variables is introduced to obtain a system with the equilibrium point at the origin:

$$e_1 \triangleq y_{\text{int}}^n - y_{\text{int}}^{\text{eq}}, \quad (4.30a)$$

$$e_2 \triangleq y_b^n + \sigma e_1, \quad (4.30b)$$

$$e_3 \triangleq v_{rb}. \quad (4.30c)$$

After factorizing with respect to ζ , the interconnected dynamics of (4.27) and (4.28) can be expressed in cascade form as

$$\dot{\hat{e}} = \mathbf{A}(e_2)\hat{e} + \mathbf{B}(e_2) + \mathbf{H}(e_2, e_3, \psi_d^n, \zeta)\zeta, \quad (4.31a)$$

$$\dot{\zeta} = \Sigma \zeta, \quad (4.31b)$$

where $\hat{e} \triangleq [e_1, e_2, e_3]^T$,

$$\mathbf{A} \triangleq \begin{bmatrix} -\frac{\sigma\Delta}{l(e_2)} & \frac{\Delta}{l(e_2)} & 0 \\ -\frac{\sigma^2\Delta}{l(e_2)} & -\frac{u_{rd}}{\sqrt{l(e_2)}} + \frac{\sigma\Delta}{l(e_2)} & \frac{\Delta}{\sqrt{l(e_2)}} \\ \frac{\sigma^2\Delta^2 X_{vd}}{l(e_2)^2} & \left(\frac{u_{rd}\Delta X_{vd}}{l(e_2)^{3/2}} - \frac{\sigma\Delta^2 X_{vd}}{l(e_2)^2} \right) & \left(Y^{u_{rd}} - \frac{\Delta^2 X_{vd}}{l(e_2)^{3/2}} \right) \end{bmatrix}, \quad (4.32)$$

and

$$\mathbf{B}(e_2) \triangleq \begin{bmatrix} 0 \\ V_y \\ -\frac{\Delta X_{vd} V_y}{l(e_2)} \end{bmatrix} f(e_2). \quad (4.33)$$

The interconnection matrix \mathbf{H} contains all the terms vanishing at $\zeta = 0$ and is given by

$$\mathbf{H}(e_2, e_3, \psi_d^n, \zeta) \triangleq \begin{bmatrix} 0 & 0 \\ 1 & 0 \\ -\frac{\Delta X_v(\tilde{u}_{rb} + u_{rd})}{l(e_2)} & 1 \end{bmatrix} \begin{bmatrix} \mathbf{h}_{e_2}^T \\ \mathbf{h}_{e_3}^T \end{bmatrix}, \quad (4.34)$$

where \mathbf{h}_{e_2} and \mathbf{h}_{e_3} are given in Appendix 4.A. The function $f(e_2)$ is as defined in (4.13).

4.4.2 Stability of the nominal system

The nominal system of the cascade in (4.31) is

$$\dot{\hat{e}} = \mathbf{A}(e_2)\hat{e} + \mathbf{B}(e_2). \quad (4.35)$$

Lemma 4.2. *If Assumptions 4.1 to 4.3 hold and the lookahead distance Δ and the integral gain σ satisfy*

$$\Delta > \frac{|X_{vd}|}{|Y_{vd}|} \left[\frac{5u_{rd} + V_{\max} + \sigma}{4u_{rd} - V_{\max} - \sigma} + 1 \right], \quad (4.36)$$

$$0 < \sigma < u_{rd} - V_{\max}, \quad (4.37)$$

then the equilibrium point of (4.35) is USGES.

Proof. The proof follows along the lines of Caharija et al. [18], while making use of the comparison lemma [55, Lemma 3.4] along the lines of the analysis in Fossen and Pettersen [36].

Consider the Lyapunov function candidate:

$$W \triangleq \frac{1}{2}\sigma^2 e_1^2 + \frac{1}{2}e_2^2 + \frac{1}{2}\mu e_3^2, \quad \mu > 0. \quad (4.38)$$

The time-derivative of W is

$$\begin{aligned}
 \dot{W} &= -\frac{\sigma^3 \Delta}{l(e_2)} e_1^2 + \left[\sigma \Delta - u_{rd} \sqrt{l(e_2)} \right] \frac{e_2^2}{l(e_2)} \\
 &+ \frac{\Delta}{\sqrt{l(e_2)}} e_2 e_3 + V_y f(e_2) e_2 - \mu \frac{\Delta X_{vd} V_y}{l(e_2)} f(e_2) e_3 \\
 &- \mu \left[\frac{\Delta^2 X_{vd}}{(l(e_2))^{3/2}} - Y_{vd} \right] e_3^2 \\
 &+ \mu \left[\frac{u_{rd} \Delta X_{vd}}{l(e_2)} - \frac{\sigma \Delta^2 X_{vd}}{(l(e_2))^{3/2}} \right] \frac{e_2 e_3}{\sqrt{l(e_2)}} + \frac{\mu \sigma^2 \Delta^2 X_{vd}}{(l(e_2))^2} e_1 e_3
 \end{aligned} \tag{4.39}$$

Using Assumptions 4.1 and 4.2, and the bound on $f(e_2)$ in (4.14), the following bound can be found for \dot{W} :

$$\begin{aligned}
 \dot{W} &\leq -\frac{\sigma^3 \Delta}{l(e_2)} e_1^2 - \frac{\Delta(u_{rd} - V_{\max} - \sigma)}{l(e_2)} e_2^2 + \frac{\Delta e_2 e_3}{\sqrt{l(e_2)}} \\
 &+ \frac{\mu \sigma^2 |X_{vd}|}{\Delta} \frac{e_1 e_3}{\sqrt{l(e_2)}} + \mu \frac{|X_{vd}|(u_{rd} + V_{\max} + \sigma)}{\Delta \sqrt{l(e_2)}} e_2 e_3 \\
 &- \mu \left(|Y_{vd}| - \frac{|X_{vd}|}{\Delta} \right) e_3^2
 \end{aligned} \tag{4.40}$$

This bound can be rearranged as

$$\dot{W} \leq -L_1(\hat{e}_{13}) - L_2(\hat{e}_{23}), \tag{4.41}$$

where $\hat{e}_{13} \triangleq [e_1, e_3]^T$ and $\hat{e}_{23} \triangleq [e_2, e_3]^T$. L_1 is defined as

$$L_1 = \frac{1}{l(e_2)} \hat{e}_{13}^T \mathbf{Q}_1 \hat{e}_{13}, \tag{4.42}$$

where \mathbf{Q}_1 is

$$\mathbf{Q}_1 \triangleq \begin{bmatrix} \frac{\sigma^3 \Delta}{2\Delta} & -\frac{\mu \sigma^2 \sqrt{l(e_2)} |X_{vd}|}{2\Delta} \\ -\frac{\mu \sigma^2 \sqrt{l(e_2)} |X_{vd}|}{2\Delta} & \mu \eta l(e_2) \left(|Y_{vd}| - \frac{|X_{vd}|}{\Delta} \right) \end{bmatrix} \tag{4.43}$$

and $0 < \eta < 1$. L_2 is defined as

$$L_2 \triangleq \frac{\Delta}{l(e_2)} \hat{e}_{23}^T \mathbf{Q}_2 \hat{e}_{23}, \tag{4.44}$$

where \mathbf{Q}_2 is

$$\mathbf{Q}_2 \triangleq \begin{bmatrix} \beta & -\alpha \sqrt{l(e_2)} \\ -\alpha \sqrt{l(e_2)} & l(e_2) \frac{\alpha(2\alpha-1)}{\beta} \end{bmatrix}. \tag{4.45}$$

Here, $\beta \triangleq u_{rd} - V_{\max} - \sigma$ and α is given by

$$\alpha \triangleq (1 - \eta) \frac{(u_{rd} - V_{\max} - \sigma)(\Delta |Y_{vd}| - |X_{vd}|)}{|X_{vd}|(u_{rd} + V_{\max} + \sigma)}. \tag{4.46}$$

The parameter μ is chosen as

$$\mu \triangleq \frac{\Delta^2(2\alpha - 1)}{|X_{vd}|(u_{rd} + V_{\max} + \sigma)}. \quad (4.47)$$

If \mathbf{Q}_1 and \mathbf{Q}_2 are positive definite, then \dot{W} is negative definite and the system (4.35) is uniformly stable. \mathbf{Q}_1 is positive definite if

$$\Delta > \frac{|X_{vd}|}{|Y_{vd}|}, \quad (4.48)$$

$$\mu < \frac{4\eta\Delta^2(\Delta|Y_{vd}| - |X_{vd}|)}{\sigma|X_{vd}|^2}. \quad (4.49)$$

(4.48) is met as long as (4.36) holds. It can be shown that $\eta \geq 1/5$ is a sufficient condition for μ to satisfy (4.49). Thus, without loss of generality, η is set to $1/5$, and positive definiteness of \mathbf{Q}_1 is ensured.

\mathbf{Q}_2 is positive definite if $\beta > 0$ and $\alpha > 1$. Assumption 4.3 and condition (4.37) ensure that $\beta > 0$, while conditions (4.36) and (4.37) ensure that $\alpha > 1$. With positive definite \mathbf{Q}_1 and \mathbf{Q}_2 it follows that $\dot{W} < 0$. Since $W > 0$, we can use Khalil [55, Theorem 4.8] to show that the equilibrium $\hat{e} = \mathbf{0}$ is uniformly stable.

The Lyapunov function candidate W from (4.38) is split into

$$W = W_1(\hat{e}_{13}) + W_2(\hat{e}_{23}), \quad (4.50)$$

where

$$W_1 \triangleq \frac{1}{2}\hat{e}_{13}^T P_1 \hat{e}_{13}, \quad (4.51)$$

$$W_2 \triangleq \frac{1}{2}\hat{e}_{23}^T P_2 \hat{e}_{23}, \quad (4.52)$$

$P_1 = \text{diag}\{\sigma, \frac{1}{2}\mu\} > 0$ and $P_2 = \text{diag}\{1, \frac{1}{2}\mu\} > 0$. Hence, using (4.42) and (4.44),

$$\dot{W}_1 \leq \frac{-2}{l(e_2)} \frac{q_{1,\min}}{p_{1,\max}} W_1, \quad (4.53)$$

$$\dot{W}_2 \leq \frac{-2\Delta}{l(e_2)} \frac{q_{2,\min}}{p_{2,\max}} W_2. \quad (4.54)$$

where $q_{i,\min} \triangleq \lambda_{\min}(\mathbf{Q}_i)$, $p_{i,\max} \triangleq \lambda_{\max}(\mathbf{P}_i)$, $i \in \{1, 2\}$. Applying the bound (4.21) on $l(e_2)$ in (4.53) and (4.54) leads to

$$\dot{W}_1 \leq -2c(r) \frac{q_{1,\min}}{p_{1,\max}} W_1, \quad \forall \|\hat{e}(t)\| \leq r, \quad (4.55)$$

$$\dot{W}_2 \leq -2\Delta c(r) \frac{q_{2,\min}}{p_{2,\max}} W_2, \quad \forall \|\hat{e}(t)\| \leq r. \quad (4.56)$$

Similarly to the derivation of (4.26), it is then possible to invoke the comparison lemma, which implies that for $w_1(t) = W_1(t, \hat{e}(t))$ and $w_2(t) = W_2(t, \hat{e}(t))$,

$$w_1 \leq e^{-2(\frac{q_{1,\min}}{p_{1,\max}})c(r)(t-t_0)} w_1(t_0), \quad (4.57)$$

$$w_2 \leq e^{-2\left(\frac{q_{2,\min}}{p_{2,\max}}\right)\Delta c(r)(t-t_0)} w_2(t_0). \quad (4.58)$$

Consequently, for $w(t) = W(t, \hat{e}(t))$,

$$w \leq e^{-2\rho c(r)(t-t_0)} w(t_0) \quad (4.59)$$

where

$$\rho = \min \left\{ \frac{q_{1,\min}}{p_{1,\max}}, \frac{\Delta q_{2,\min}}{p_{2,\max}} \right\}. \quad (4.60)$$

Therefore, with $p_{\max} \triangleq \max(\sigma^2, 1, \mu)$ and $p_{\min} \triangleq \min(\sigma^2, 1, \mu)$,

$$\|\hat{e}(t)\| \leq \sqrt{\frac{p_{\max}}{p_{\min}}} e^{-\rho c(r)(t-t_0)} \|\hat{e}(t_0)\|. \quad (4.61)$$

Hence, the equilibrium point $\hat{e} = \mathbf{0}$ is USGES as defined in Definition 2.4. \square

4.4.3 Stability property of the closed-loop system

Theorem 4.3. *If Assumptions 4.1 to 4.3 hold and the lookahead distance Δ and the integral gain σ satisfy*

$$\Delta > \frac{|X_{vd}|}{|Y_{vd}|} \left[\frac{5}{4} \frac{u_{rd} + V_{\max} + \sigma}{u_{rd} - V_{\max} - \sigma} + 1 \right], \quad (4.62)$$

$$0 < \sigma < u_{rd} - V_{\max}, \quad (4.63)$$

then the controllers (4.6a) and (4.6b), where the desired heading ψ_d^n is given by (4.5), guarantee achievement of the control objectives (4.4). Control objective (4.4b) is fulfilled with

$$\psi_{ss} = -\tan^{-1}(V_y / \sqrt{u_{rd}^2 - V_y^2}). \quad (4.64)$$

Furthermore, the equilibrium point of the error dynamics (4.31) is USGES and UGAS.

Proof. The system (4.31) is a cascaded system, consisting of a linear system (4.31b) which perturbs the dynamics (4.31a) through the interconnection matrix \mathbf{H} . The interconnection matrix \mathbf{H} can be shown to satisfy $\|\mathbf{H}\| \leq \theta_1(\|\zeta\|)(|y| + |y_{\text{int}}| + |v_{rb}|) + \theta_2(\|\zeta\|)$, where $\theta_1(\cdot)$ and $\theta_2(\cdot)$ are some continuous non-negative functions.

The perturbing system (4.31b), described in detail in (4.27), is a linear, time-invariant system. Furthermore, since the gains $k_{u_{rd}}$, k_ψ , k_r and the term d_{11}/m_{11} are all strictly positive, the system matrix Σ is Hurwitz and the origin $\zeta = \mathbf{0}$ is UGES. Note, however, that any set of controllers providing USGES (or UGES) of the surge and yaw error dynamics will give the same result. This is due to the modular properties of the cascaded systems control theory that is used in the analysis.

The nominal system is USGES by Lemma 4.2. Hence all the conditions of Proposition 2.1 are satisfied, guaranteeing USGES and UGAS of the origin of (4.31).

Finally, ψ_{ss} can be shown to satisfy (4.64) by inserting the equilibrium values (4.29) into the ILOS control law (4.5a). \square

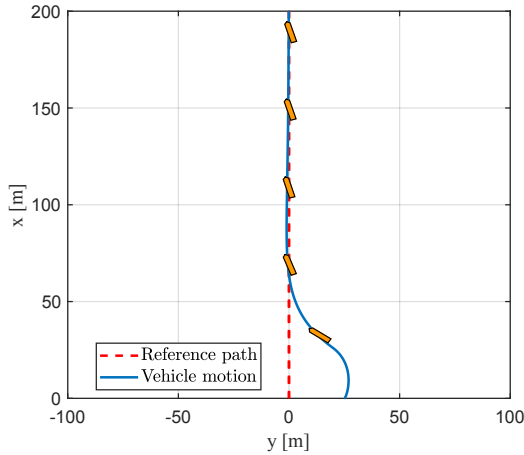


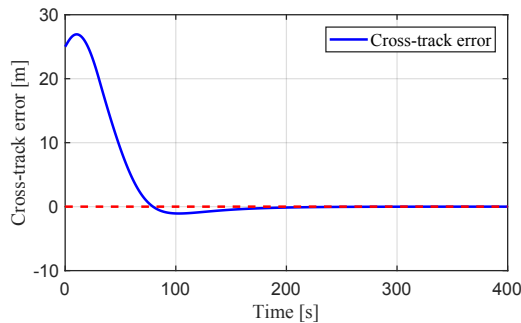
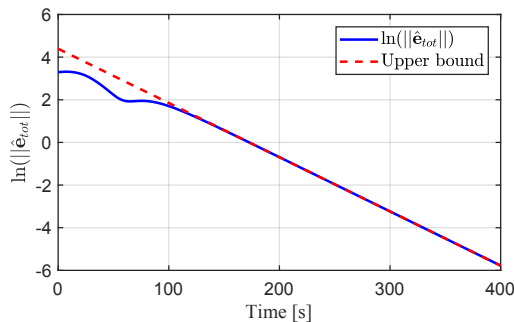
Figure 4.2: Position and heading of the vehicle during the simulation. The time interval 0 - 180s is considered in the figure.

4.5 Simulations

This section presents results from numerical simulations of the ILOS guidance law applied to an underactuated AUV. The AUV is modeled in 3 DOF and tasked to follow a horizontal path along the x -axis. The desired relative surge speed is $u_{rd} = 1$ m/s. The current is set to $\boldsymbol{\nu}_{c/n}^n = [0.1 \text{ m/s}, 0.3 \text{ m/s}, 0 \text{ rad/s}]$. The ocean current intensity is $\|\boldsymbol{\nu}_{c/n}^n\| = 0.3261$ m/s, which fulfills Assumptions 4.1 and 4.3. It can be verified that Assumption 4.2 is satisfied with $Y_{vd} = -0.91 \text{ s}^{-1}$, and that (4.36) and (4.62) are satisfied with $|X_{vd}| = 0.20$. The ILOS lookahead distance and integral gain are $\Delta = 10$ m and $\sigma = 0.2$ m, which satisfy (4.62)-(4.63). The surge and yaw controllers (4.6a)-(4.6b) are implemented with $k_u = 0.5$, $k_\psi = 1$ and $k_r = 2$. The initial position of the vehicle is 25 m east of the path and the initial direction is parallel to the path, $\boldsymbol{p}_b^n(t_0) = [0 \text{ m}, 25 \text{ m}, 0 \text{ rad}]$ and the initial velocity is zero.

In Figure 4.2 the position and heading of the vehicle in are shown. The vehicle maintains a constant sideslip angle after converging to the path to counteract the current. Relative sway velocity v_{rb} , and hence the drift angle with respect to the water flow, stabilizes at zero. Figure 4.3 shows how the cross-track error converges to zero. The cross-track error increases in the beginning, while the vehicle is accelerating and turning to counter the current, and there is an overshoot due to the integral effect. Figure 4.4 shows the natural logarithm of the Euclidean norm of the error variables in (4.31), where $\hat{\boldsymbol{e}}_{\text{tot}} \triangleq [\hat{\boldsymbol{e}}^T \boldsymbol{\zeta}^T]^T$. Notice that $\ln(\|\hat{\boldsymbol{e}}_{\text{tot}}\|)$ is upper bounded by a straight, descending line, corresponding to a bounding exponential function of the form $\gamma_1 e^{-\gamma_2(t-t_0)} \|\hat{\boldsymbol{e}}_{\text{tot}}(t_0)\|$, for positive constants γ_1 and γ_2 . Hence, for these initial conditions, exponential convergence of the system is verified.

The vehicle heading can be difficult to measure in practice. Magnetic compasses, for example, are prone to errors due to disturbances in the surrounding magnetic

Figure 4.3: The cross-track error y_b^n of the vehicle.Figure 4.4: The natural logarithm of $\|\hat{e}_{tot}\|$.

field. Gyrocompasses, which estimate true north based on the rotation of the earth, need a long settling time, especially when used in the high north. It is therefore of interest to investigate the performance of the guidance law in the presence of measurement errors in heading. While analysis of the robustness properties of the system is beyond the scope of this thesis, Figures 4.5 and 4.6 show the vehicle trajectory and cross track error when the system is simulated with a significant heading measurement error of 25 degrees. The vehicle still converges to the path, due to the integral effect in the guidance law, however the overshoot is larger and the convergence time slower.

4.6 Conclusions

In this chapter, we have investigated the stability properties of an underactuated marine vessel controlled by an ILOS guidance law. The system has been proved to be USGES, which is a stronger stability property than κ -exponential stability which has been proven in the literature before. The underactuated marine vehicle has been modeled in 3 DOF using relative velocities, and the results are applicable both for surface vessels and for underwater vehicles moving in a horizontal plane.

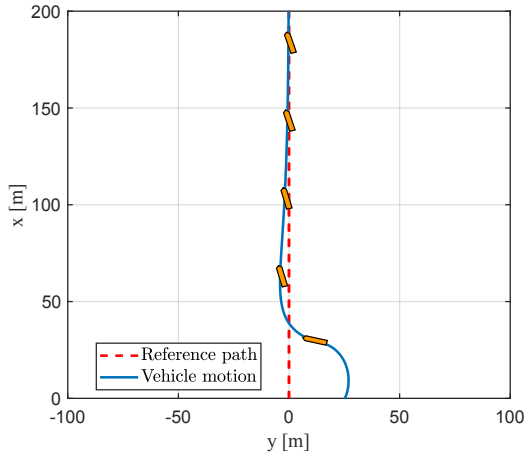


Figure 4.5: Position and heading of the vehicle during the simulation with a heading measurement error of 25 degrees.

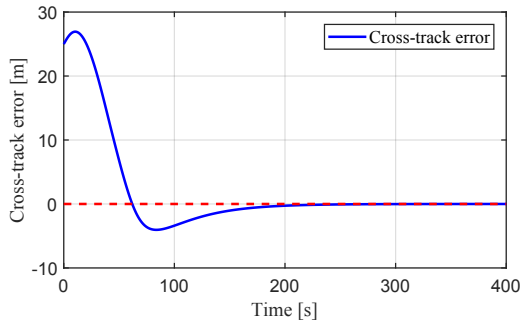


Figure 4.6: The cross-track error y_b^n during the simulation with a heading measurement error of 25 degrees.

As an example of the latter, an AUV has been simulated in an ocean environment containing constant and irrotational currents, demonstrating exponential stability. The simulation also included runs with a significant error in the heading measurement, which showed that the vehicle was still able to converge to and follow the path.

4.A Functional expressions

The functions F_u , F_r , X_v and Y_v are defined in Section 3.2.1, and are included here for convenience:

$$F_u(u_b, v_b, r_b) \triangleq \frac{1}{m_{11}}(m_{22}v_b + m_{23}r_b)r_b - \frac{d_{11}}{m_{11}}u_b, \quad (4.65)$$

$$\begin{aligned}
 F_r(u_b, v_b, r_b) &\triangleq \frac{m_{23}d_{22} + m_{22}(d_{32} + (m_{22} - m_{11})u_b)}{m_{22}m_{33} - m_{23}^2}v_b \\
 &+ \frac{m_{23}(d_{23} - m_{11}u_b) - m_{22}(d_{33} + m_{23}u_b)}{m_{22}m_{33} - m_{23}^2}r_b,
 \end{aligned} \tag{4.66}$$

$$X_v(u_b) \triangleq \frac{m_{23}^2 - m_{11}m_{33}}{m_{22}m_{33} - m_{23}^2}u_b + \frac{d_{33}m_{23} - d_{23}m_{33}}{m_{22}m_{33} - m_{23}^2}, \tag{4.67}$$

$$Y_v(u_b) \triangleq \frac{(m_{22} - m_{11})m_{23}}{m_{22}m_{33} - m_{23}^2}u_b - \frac{d_{22}m_{33} - d_{32}m_{23}}{m_{22}m_{33} - m_{23}^2}, \tag{4.68}$$

The function \mathbf{h}_{e_2} is defined as $\mathbf{h}_{e_2} \triangleq [h_{e_21}, h_{e_22}, h_{e_23}]^T$, where

$$h_{e_21} = \sin(\tilde{\psi}_b^n + \psi_d^n), \tag{4.69a}$$

$$h_{e_23} = 0, \tag{4.69b}$$

$$\begin{aligned}
 h_{e_22} &= u_{rd} \left[\frac{\sin(\tilde{\psi}_b^n)}{\tilde{\psi}_b^n} \cos(\psi_d^n) + \frac{\cos(\tilde{\psi}_b^n) - 1}{\tilde{\psi}_b^n} \sin(\psi_d^n) \right] \\
 &+ e_3 \left[\frac{\cos(\tilde{\psi}_b^n) - 1}{\tilde{\psi}_b^n} \cos(\psi_d^n) - \frac{\sin(\tilde{\psi}_b^n)}{\tilde{\psi}_b^n} \sin(\psi_d^n) \right].
 \end{aligned} \tag{4.69c}$$

The function \mathbf{h}_{e_3} is defined as $\mathbf{h}_{e_3} \triangleq [h_{e_31}, h_{e_32}, h_{e_33}]^T$, where

$$h_{e_31} = \frac{X_v(\tilde{u}_{rb} + u_{rd}) - X_{vd}}{\tilde{u}_{rb}} \gamma(e_2, e_3) + e_3 \frac{Y_v(\tilde{u}_{rb} + u_{rd}) - Y_{vd}}{\tilde{u}_{rb}}, \tag{4.70a}$$

$$h_{e_32} = 0, \tag{4.70b}$$

$$h_{e_33} = X_v(\tilde{u}_{rb} + u_{rd}). \tag{4.70c}$$

The limits of h_{e_22} for $\tilde{\psi}_b^n \rightarrow 0$ and h_{e_31} as $\tilde{u}_{rb} \rightarrow 0$ exist and are finite. The expression $\gamma(e_2, e_3)$ used in h_{e_31} is defined as

$$\gamma(e_2, e_3) \triangleq \frac{\Delta u_{rd}(e_2 + \sigma y_{\text{int}}^{\text{eq}}) - \Delta^2 e_3}{l(e_2)^{3/2}} - \frac{\sigma \Delta^2}{l(e_2)^2} y_b^n - \frac{\Delta V_y}{l(e_2)} \tag{4.71}$$

Chapter 5

ILOS Guidance with a Speed-dependent Lookahead Distance

What is the airspeed velocity of an unladen swallow?

— Monthly Python, *Monty Python and the Holy Grail*

In this chapter we consider a single vessel, with kinematics and dynamics modeled in 3 DOF. The vessel should follow a straight-line path in the presence of an ocean current that is uniform in time and space, and to this end we employ an ILOS guidance scheme. However, unlike in the previous chapter, we allow the lookahead distance to increase linearly with the desired surge speed u_{rd} , thus making the vehicle make slower, smoother turns at high speed, reducing overshoot. It is thus possible to make the vehicle converge to the desired path without overshoot for a broad range of values of u_{rd} , without having to tune the guidance law each time u_{rd} changes. When u_{rd} is constant, we give conditions under which the system achieves USGES.

If the vehicle speed changes along the path, the heading required to compensate for the current will not be constant, and there will not be an equilibrium point of the system unless the desired surge speed settles at a constant value. This is the case during the transient phase of the formation control algorithm presented in Belleter and Pettersen [7] and Belleter and Pettersen [8], where the vehicle heading is steered by the ILOS guidance law, and exponential convergence of the system was proved.

We will in this chapter show that the solutions of the system remain ultimately bounded when u_{rd} is time-varying. Unlike previous works, we do not look at a specific function for u_{rd} . Rather, we let u_{rd} be a general function, with no required bound on the size of the time derivative of u_{rd} . Thus, the result can be used for any desired surge trajectory, including but not limited to those used for trajectory tracking in Flåten and Brekke [33] or formation control in Belleter and Pettersen [7].

The remainder of this chapter is organized as follows. Section 5.1 gives a mathematical description of the system involved, while the control system is presented in Section 5.2 and the resulting error dynamics are derived in Section 5.3. In Section 5.4 we show that the system achieves USGES when u_{rd} is constant, while we

in Section 5.5 show that the solutions of the system are ultimately bounded when u_{rd} is time-varying. The guidance law is applied to a simulated underwater vehicle operation in the horizontal plane in Section 5.6, and experiments on an unmanned surface vehicle are described in Section 5.7. Finally, some concluding remarks are given in Section 5.8.

The work presented in this chapter is based on Wiig et al. [117].

5.1 System description

5.1.1 System model

As in the previous chapter, we will model the vehicle in 3 DOF using the relative velocities. Recall that the model is:

$$\dot{x}_b^n = u_{rb} \cos(\psi_b^n) - v_{rb} \sin(\psi) + V_x, \quad (5.1a)$$

$$\dot{y}_b^n = u_{rb} \sin(\psi_b^n) + v_{rb} \cos(\psi) + V_y, \quad (5.1b)$$

$$\dot{\psi}_b^n = r_b, \quad (5.1c)$$

$$\dot{u}_{rb} = F_u(u_{rb}, v_{rb}, r_b) + \tau_u, \quad (5.1d)$$

$$\dot{v}_{rb} = X_v(u_{rb})r_b + Y_v(u_{rb})v_{rb}, \quad (5.1e)$$

$$\dot{r}_b = F_r(u_{rb}, v_{rb}, r_b) + \tau_r. \quad (5.1f)$$

The functions F_u , F_r , X_v and Y_v are defined in Section 3.2.1, and restated in Appendix 5.A for convenience. The ocean current is again assumed to be bounded and uniform in space and time:

Assumption 5.1. The ocean current $\mathbf{v}_{c/n}^n \triangleq [V_x, V_y, 0]^T$ is assumed to be bounded and uniform in space and time. Hence, there exists a constant $V_{\max} \geq 0$ such that $V_{\max} \geq \sqrt{V_x^2 + V_y^2}$.

5.1.2 Desired surge speed

The desired surge speed, u_{rd} , can be time-varying, and satisfies the following assumptions:

Assumption 5.2. The desired surge speed is bounded by $u_{rd} \in [u_{\min}, u_{\max}]$, where u_{\min} and u_{\max} are positive constants and $u_{\min} > V_{\max}$.

Assumption 5.3. The time derivative of u_{rd} , \dot{u}_{rd} , is piecewise continuous in t and bounded.

In order to analyze the effect of the time-varying part of u_{rd} , we divide u_{rd} into a constant and a time-varying component:

$$u_{rd}(t) = u_c + u_t(t), \quad (5.2)$$

such that $\dot{u}_c = 0$ and $\dot{u}_t = \dot{u}_{rd}$.

The following assumption is made on $Y_v(u_{rb})$:

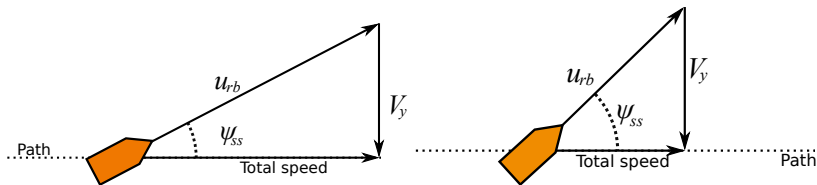


Figure 5.1: The current compensation angle ψ_{ss} for a large (left) and small (right) vehicle velocity.

Assumption 5.4. The function $Y_v(u_{rb})$ satisfies

$$Y_v(u_{rb}) \leq -Y_{v \min} < 0, \quad \forall u_{rb} \in [u_{\min}, u_{\max}]. \quad (5.3)$$

Remark 5.1. The negativity of $Y_v(u_{rb})$ is justified by noticing that $Y_v(u_{rb}) > 0$ would imply that the system is undamped or nominally unstable in sway, which is generally not the case by the mechanical design of the vehicle.

Furthermore, the function $X_v(u_{rb})$ is a linear function in u_{rb} as seen in (5.49), hence it is bounded by

$$|X_v(u_{rb})| \leq X_{v \max}, \quad \forall u_{rb} \in [u_{\min}, u_{\max}]. \quad (5.4)$$

5.1.3 Control objectives

The control objectives are to make a vehicle modeled by (5.1) converge to a straight-line path in the presence of the unknown ocean current $\boldsymbol{\nu}_{c/n}^n$, while maintaining the desired relative surge speed $u_{rd}(t)$.

The formalized control objectives, with the desired path \mathcal{P} aligned with the x -axis of n , are

$$\lim_{t \rightarrow \infty} y_b^n(t) = 0, \quad (5.5a)$$

$$\lim_{t \rightarrow \infty} \psi_b^n(t) = \psi_{ss}, \quad \psi_{ss} \in \left(-\frac{\pi}{2}, \frac{\pi}{2}\right), \quad (5.5b)$$

$$\lim_{t \rightarrow \infty} u_{rb}(t) = u_{rd}(t), \quad (5.5c)$$

where ψ_{ss} is a constant yaw angle required to keep the underactuated vessel at the path in the presence of current. This angle will depend on the cross-track component of the ocean current, as well as on the magnitude of the vehicle velocity. For large vehicle velocities with respect to the path transversal ocean current, the current compensation angle will be small, and vice versa. This is illustrated in Figure 5.1.

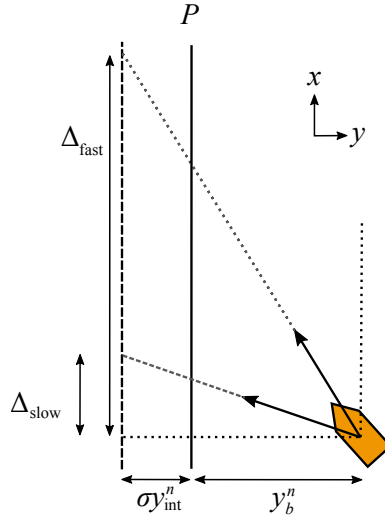


Figure 5.2: The lookahead distance increases linearly with speed.

5.2 Control system

In this section we present an ILOS guidance scheme, along with the surge and yaw control laws, for solving the path following control problem presented in the previous section.

5.2.1 The ILOS guidance law

The desired heading ψ_d^n is given by an ILOS guidance law:

$$\psi_d^n \triangleq -\tan^{-1}\left(\frac{y_b^n + \sigma y_{\text{int}}^n}{k_{\Delta} u_{rd}}\right), \quad (5.6a)$$

$$\dot{y}_{\text{int}}^n \triangleq \frac{k_{\Delta} u_{rd} y_b^n}{(y_b^n + \sigma y_{\text{int}}^n)^2 + (k_{\Delta} u_{rd})^2}. \quad (5.6b)$$

The lookahead gain $k_{\Delta} > 0$ and the integral gain $\sigma > 0$ are constant design parameters.

Unlike the guidance law presented in Børhaug et al. [13] and used in the previous chapter, this guidance law is designed to depend on the desired relative surge speed, u_{rd} , such that the lookahead distance is given as $\Delta(u_{rd}) \triangleq k_{\Delta} u_{rd}$.¹ By looking farther ahead for large u_{rd} , the required maneuvering capabilities of the vehicle at high speed are reduced. Thus, the guidance law keeps the behavior of approaching the path perpendicularly when far away, while also making the vehicle approach the path more gently as it gets closer, and to reduce the demands on the yaw controller and actuators. The guidance law is illustrated in Figure 5.2.

¹We use the desired relative surge speed u_{rd} , rather than the measured relative surge speed u_{rb} , to decrease the coupling between the vehicle surge dynamics and the guidance law.

5.2.2 Surge and yaw controllers

The surge and yaw controllers are as in Section 4.2.2, restated here for convenience:

$$\tau_u = -F_u(u_{rb}, v_{rb}, r_b) + \dot{u}_{rd} - k_u(u_{rb} - u_{rd}), \quad (5.7a)$$

$$\tau_r = -F_r(u_{rb}, v_{rb}, r_b) + \ddot{\psi}_d^n - k_\psi(\psi_b^n - \psi_d^n) - k_r(r_b - \dot{\psi}_d^n), \quad (5.7b)$$

where k_u , k_ψ and k_r are constant, positive gains.

5.3 Error dynamics

In this section we describe the error dynamics around the equilibrium point obtained when the desired surge speed is constant. For brevity, we will use the notation $X_{vd} = X_v(u_{rd})$ and $Y_{vd} = Y_v(u_{rd})$ in the remainder of the chapter.

5.3.1 Actuated dynamics

The error signals of the actuated variables surge, yaw and yaw rate are collected in $\zeta \triangleq [\tilde{u}_{rb}, \tilde{\psi}_b^n, \tilde{r}_b]^T$, where $\tilde{u}_{rb} \triangleq u_{rb} - u_{rd}$, $\tilde{\psi}_b^n = \psi_b^n - \psi_d^n$ and $\tilde{r}_b \triangleq r_b - \dot{\psi}_d^n$. When the control laws in surge (5.7a) and yaw (5.7b) are applied to the system (5.1c), (5.1d) and (5.1f), the error dynamics of ζ becomes:

$$\dot{\zeta} = \begin{bmatrix} -k_u & 0 & 0 \\ 0 & 0 & 1 \\ 0 & -k_\psi & -k_r \end{bmatrix} \zeta \triangleq \Sigma \zeta. \quad (5.8)$$

Since the gains k_u , k_ψ and k_r are all strictly positive, Σ is Hurwitz and the origin, $\zeta = \mathbf{0}$, is UGES.

5.3.2 Underactuated dynamics

The underactuated $y_b^n - v_{rb}$ dynamics are obtained from (5.1b), (5.1e) and (5.6b):

$$\dot{y}_{\text{int}}^n = \frac{\Delta y_b^n}{(y_b^n + \sigma y_{\text{int}}^n)^2 + \Delta^2}, \quad (5.9a)$$

$$\dot{y}_b^n = (\tilde{u}_{rb} + u_{rd}) \sin(\tilde{\psi}_b^n + \psi_d^n) + v_{rb} \cos(\tilde{\psi}_b^n + \psi_d^n) + V_y, \quad (5.9b)$$

$$\dot{v}_{rb} = X_v(\tilde{u}_{rb} + u_{rd})(r_b + \dot{\psi}_d^n) + Y_v(\tilde{u}_{rb} + u_{rd})v_{rb}. \quad (5.9c)$$

The heading required to compensate for the current varies with u_{rd} , as discussed in Section 5.1.3. The heading compensation angle ψ_{ss} is found by the integration (5.9a) of the cross track error. Hence, if there is a change in u_{rd} , the vehicle will diverge slightly from the path in order to find a new compensation angle. It follows that if the desired surge speed varies over time, i.e. when $\dot{u}_{rd} \neq 0$, there is no equilibrium point of (5.9). However, in the case when u_{rd} is constant, we obtain from (5.2) that $u_{rd} = u_c$. There is then an equilibrium point of (5.9) on the manifold

$\zeta = \mathbf{0}$, which is

$$y_{\text{int}}^n = y_{\text{int}}^{\text{eq}} \triangleq \frac{\Delta}{\sigma} \frac{V_y}{\sqrt{u_{rd}^2 - V_y^2}}, \quad (5.10a)$$

$$y_b^n = 0, \quad (5.10b)$$

$$v_{rb} = 0. \quad (5.10c)$$

The error dynamics around this point is obtained by performing a change of variables:

$$e_1 \triangleq y_{\text{int}}^n - y_{\text{int}}^{\text{eq}}, \quad (5.11a)$$

$$e_2 \triangleq y_b^n + \sigma e_1, \quad (5.11b)$$

$$e_3 \triangleq v_{rb}. \quad (5.11c)$$

Factorizing with respect to ζ , allows us to express the interconnected dynamics of (5.8) and (5.9) in cascaded form:

$$\dot{\mathbf{e}} = \mathbf{A}(e_2)\mathbf{e} + \mathbf{B}(e_2) + \mathbf{G}(e_2) + \mathbf{H}(e_2, e_3, \psi_d^n, \zeta)\zeta, \quad (5.12a)$$

$$\dot{\zeta} = \Sigma\zeta, \quad (5.12b)$$

where $\mathbf{e} \triangleq [e_1, e_2, e_3]^T$, \mathbf{A} is

$$\mathbf{A} \triangleq \begin{bmatrix} -\frac{\sigma k_\Delta}{l(e_2)} & \frac{k_\Delta}{l(e_2)} & 0 \\ -\frac{\sigma^2 k_\Delta}{l(e_2)} & -\frac{u_{rd}}{\sqrt{l(e_2)}} + \frac{\sigma k_\Delta}{l(e_2)} & \frac{k_\Delta}{\sqrt{l(e_2)}} \\ \frac{\sigma^2 k_\Delta^2 X_{vd}}{l(e_2)^2} & \left(\frac{u_{rd} k_\Delta X_{vd}}{l(e_2)^{3/2}} - \frac{\sigma k_\Delta^2 X_{vd}}{l(e_2)^2} \right) & \left(Y^{u_{rd}} - \frac{k_\Delta^2 X_{vd}}{l(e_2)^{3/2}} \right) \end{bmatrix}, \quad (5.13)$$

while

$$\mathbf{B} \triangleq \begin{bmatrix} 0 \\ V_y f(e_2) \\ -\frac{k_\Delta u_{rd} X_{vd} V_y}{l(e_2)} f(e_2) \end{bmatrix}. \quad (5.14)$$

The function $l(e_2)$ is defined as

$$l(e_2) \triangleq (e_2 + \sigma y_{\text{int}}^{\text{eq}})^2 + \Delta^2, \quad (5.15)$$

and $f(e_2)$ is defined as

$$f(e_2) \triangleq 1 - \frac{\sqrt{(\sigma y_{\text{int}}^{\text{eq}})^2 + (k_\Delta u_{rd})^2}}{\sqrt{l(e_2)}}. \quad (5.16)$$

Note that $f(e_2)$ is bounded by:

$$|f(e_2)| \leq \frac{|e_2|}{\sqrt{l(e_2)}}. \quad (5.17)$$

The terms that vanish when $\zeta = 0$ are collected in \mathbf{H} :

$$\mathbf{H} \triangleq \begin{bmatrix} 0 & 0 \\ 1 & 0 \\ -\frac{k_\Delta u_{rd} X(\dot{u}_r + u_{rd})}{l(e_2)} & 1 \end{bmatrix} \begin{bmatrix} \mathbf{h}_{e_2}^T \\ \mathbf{h}_{e_3}^T \end{bmatrix}, \quad (5.18)$$

where \mathbf{h}_{e_2} and \mathbf{h}_{e_3} are given in Appendix 5.A. The vector \mathbf{G} contains the terms that vanish when $\dot{u}_{rd} = \dot{u}_t = 0$ and $u_t = 0$:

$$\mathbf{G} \triangleq \begin{bmatrix} 0 \\ -\frac{\sigma y_{\text{int}}^{\text{eq}}}{\sqrt{l(e_2)}} u_t \\ \frac{X_{vd} k_\Delta}{l(e_2)} \left[\left(\frac{(u_t + 2u_c) \sigma y_{\text{int}}^{\text{eq}}}{\sqrt{l(e_2)}} - V_y \right) u_t + (\sigma y_{\text{int}}^{\text{eq}} + e_2) \dot{u}_{rd} \right] \end{bmatrix}. \quad (5.19)$$

5.4 Constant desired surge speed

This section analyzes the stability properties of the system when u_{rd} is constant, which means that $u_{rd} = u_c$, $u_t = 0$ and $\dot{u}_{rd} = 0$. We use the analysis to find analytical bounds on the ILOS parameters k_Δ and σ , ensuring USGES of the equilibrium point of the closed-loop error dynamics. The analysis in this section is mostly equivalent to the analysis in Section 4.4. However, in order to prove USGES of the origin of the error dynamics, we will show that the Lyapunov sufficient conditions provided in Pettersen [84] are satisfied. Thus, we show how the recent results in Pettersen [84] can be utilized as an alternative to direct application of the comparison lemma.

5.4.1 Stability of the nominal system

When $\dot{u}_{rd} = u_t = 0$ we have that $\mathbf{G} = 0$ as seen from (5.19). The nominal system of the cascade in (5.12) is then given by

$$\dot{\mathbf{e}} = \mathbf{A}(e_2)\mathbf{e} + \mathbf{B}(e_2). \quad (5.20)$$

Lemma 5.1. *If Assumptions 5.1 to 5.2 hold, $\dot{u}_{rd} = 0$, and the lookahead distance gain k_Δ and the integral gain σ satisfy*

$$k_\Delta > \frac{|X_{v\max}|}{|Y_{v\min}| u_{\min}} \left[\frac{5}{4} \frac{u_{\max} + V_{\max} + \sigma}{u_{\min} - V_{\max} - \sigma} + 1 \right], \quad (5.21)$$

$$0 < \sigma < u_{\min} - V_{\max}, \quad (5.22)$$

then the equilibrium point of (5.20) is USGES.

Proof. The proof is equivalent to the proof of Lemma 4.2 until equation (5.34), at which point we will make use of the results in Pettersen [84] to prove USGES.

Consider the Lyapunov function candidate (LFC):

$$V \triangleq \frac{1}{2} \sigma^2 e_1^2 + \frac{1}{2} e_2^2 + \frac{1}{2} \mu e_3^2, \quad \mu > 0. \quad (5.23)$$

Using Assumption 5.1 to 5.4, and equations (5.4) and (5.17), the following bound can be found for \dot{V} :

$$\dot{V} \leq -\frac{1}{l(e_2)} (L_1(e_{13}) + L_2(e_{23})), \quad (5.24)$$

Where $e_{13} \triangleq [|e_1|, |e_3|]^T$ and $e_{23} \triangleq [|e_2|, |e_3|]^T$. L_1 is

$$L_1 \triangleq e_{13}^T \mathbf{Q}_1 e_{13}^T, \quad (5.25)$$

where \mathbf{Q}_1 is

$$\mathbf{Q}_1 \triangleq \begin{bmatrix} k_\Delta \sigma^3 u_{\min} & -\frac{1}{2} \frac{\mu \sigma^2 \sqrt{l(e_2)} |X_{v\max}|}{k_\Delta u_{\min}} \\ -\frac{1}{2} \frac{\mu \sigma^2 \sqrt{l(e_2)} |X_{v\max}|}{k_\Delta u_{\min}} & \mu \eta l(e_2) \left(|Y_{v\min}| - \frac{|X_{v\max}|}{k_\Delta u_{\min}} \right) \end{bmatrix}, \quad (5.26)$$

and $0 < \eta < 1$. L_2 is defined as

$$L_2 \triangleq k_\Delta u_{\min} e_{23}^T \mathbf{Q}_2 e_{23}, \quad (5.27)$$

where \mathbf{Q}_2 is

$$\mathbf{Q}_2 \triangleq \begin{bmatrix} \beta & -\alpha \sqrt{l(e_2)} \\ -\alpha \sqrt{l(e_2)} & l(e_2) \frac{\alpha(2\alpha-1)}{\beta} \end{bmatrix}. \quad (5.28)$$

Here, $\beta \triangleq u_{\min} - V_{\max} - \sigma$ and α is given by

$$\alpha \triangleq (1 - \eta) \frac{(u_{\min} - V_{\max} - \sigma)(k_\Delta u_{\min} |Y_{v\min}| - |X_{v\max}|)}{|X_{v\max}|(u_{\max} + V_{\max} + \sigma)}. \quad (5.29)$$

The parameter μ is chosen as

$$\mu \triangleq \frac{(k_\Delta u_{\min})^2 (2\alpha - 1)}{|X_{v\max}|(u_{\max} + V_{\max} + \sigma)}. \quad (5.30)$$

If \mathbf{Q}_1 and \mathbf{Q}_2 are positive definite, then \dot{V} is negative definite. Positive definiteness of \mathbf{Q}_1 is ensured when

$$k_\Delta > \frac{|X_{v\max}|}{|Y_{v\min}| u_{\min}}, \quad (5.31)$$

$$\mu < \frac{4\eta k_\Delta^2 u_{\min} (k_\Delta u_{\min} |Y_{v\min}| - |X_{v\max}|)}{\sigma |X_{v\max}|^2}. \quad (5.32)$$

Condition (5.31) is met as long as (5.21) holds. It can be shown that $\eta \geq 1/5$ is a sufficient condition for μ to satisfy (5.32). Thus, without loss of generality, η is set to $1/5$, and positive definiteness of \mathbf{Q}_1 is ensured.

Positive definiteness of \mathbf{Q}_2 is ensured if $\beta > 0$ and $\alpha > 1$. Assumption 5.2 and (5.22) ensure that $\beta > 0$, while conditions (5.21) and (5.22) ensure that $\alpha > 1$.

Let \mathbf{Q} be the symmetric 3×3 matrix defined from $L_1(e_{13})$ and $L_2(e_{23})$ so that

$$e^T \mathbf{Q} e = L_1(e_{13}) + L_2(e_{23}). \quad (5.33)$$

Since both \mathbf{Q}_1 and \mathbf{Q}_2 are positive definite, so is \mathbf{Q} . Hence, the following bound holds:

$$\dot{V} \leq -\frac{1}{l(e_2)} q_{\min} \|e\|^2, \quad (5.34)$$

where $q_{\min} \triangleq \lambda_{\min}(\mathbf{Q})$, the minimum eigenvalue of \mathbf{Q} . In any ball

$$\mathcal{B}_r \triangleq \{|e_2| < r\}, r > 0 \quad (5.35)$$

the function $l(e_2)$ is upper bounded as

$$l(e_2) \leq (r + \sigma y_{\text{int}}^{\text{eq}})^2 + (k_{\Delta} u_{rd})^2 := c(r). \quad (5.36)$$

Hence, for any $r > 0$

$$\dot{V} \leq -\frac{q_{\min}}{c(r)} \|e\|^2 \quad (5.37)$$

Thus, the conditions of Theorem 2.1 is fulfilled with $k_1 = \frac{1}{2} \min\{\sigma^2, 1, \mu\}$, $k_2 = \frac{1}{2} \max\{\sigma^2, 1, \mu\}$ and $k_3 = \frac{q_{\min}}{c(r)}$. Hence, the equilibrium point $e = \mathbf{0}$ is USGES as defined in Definition 2.4. \square

5.4.2 Stability property of the closed-loop system

Theorem 5.2. *If Assumptions 5.1 to 5.2 hold, $\dot{u}_{rd} = 0$, and the lookahead distance gain k_{Δ} and the integral gain σ satisfy*

$$k_{\Delta} > \frac{|X_{v\max}|}{|Y_{v\min}| u_{\min}} \left[\frac{5 u_{\max} + V_{\max} + \sigma}{4 u_{\min} - V_{\max} - \sigma} + 1 \right], \quad (5.38)$$

$$0 < \sigma < u_{\min} - V_{\max}, \quad (5.39)$$

then the controllers (5.7a) and (5.7b), where ψ_d is given by (5.6), guarantee achievement of the control objectives (5.5). Furthermore, the equilibrium point of the error dynamics (5.12) is USGES and UGAS.

Proof. The proof is equivalent to the proof of Theorem 4.3. The system (5.12) is a cascaded system, where (5.12b) perturbs the dynamics (5.12a) through the interconnection matrix \mathbf{H} . The interconnection matrix \mathbf{H} can be shown to satisfy $\|\mathbf{H}\| \leq \theta_1(\|\zeta\|)(|y_b^n| + |y_{\text{int}}^n| + |v_{rb}|) + \theta_2(\|\zeta\|)$, where $\theta_1(\cdot)$ and $\theta_2(\cdot)$ are some continuous non-negative functions. The perturbing system is UGES as shown in Section 5.3.1, and the nominal system is USGES by Lemma 5.1. Hence all the conditions of Proposition 2.1 are satisfied, guaranteeing USGES and UGAS of the origin of (5.12). \square

5.5 Time-varying desired surge speed

In this section we allow u_{rd} to vary with time: $\dot{u}_{rd} \neq 0$ and $u_t \neq 0$. As noted in Section 5.3.2, there is no equilibrium point of the system in this case. However, inspired by the approach in Belleter and Pettersen [7], we will treat the time-varying u_t component of u_{rd} as a disturbance. It can then be proved that the solutions of

the system remain bounded around the equilibrium point obtained in (5.10). To this end we will apply Lemma 2.2.

We will use the following constants:

$$k_1 \triangleq \frac{1}{2} \min\{\sigma^2, 1, \mu\}, \quad (5.40a)$$

$$k_2 \triangleq \frac{1}{2} \max\{\sigma^2, 1, \mu\}, \quad (5.40b)$$

$$k_3 \triangleq \frac{q_{\min}}{c(r)}, \quad (5.40c)$$

$$k_4 \triangleq 2k_2, \quad (5.40d)$$

where k_1 to k_3 are obtained from the proof of Lemma 5.1.

5.5.1 Boundedness of the nominal system

Since $\dot{u}_{rd} \neq 0$, the nominal system of the cascade (5.12) becomes:

$$\dot{\mathbf{e}} = \mathbf{A}(e_2)\mathbf{e} + \mathbf{B}(e_2) + \mathbf{G}(e_2). \quad (5.41)$$

Lemma 5.3. *Assume that the conditions of Theorem 5.2 are satisfied, with the exception that $\dot{u}_{rd} \neq 0$. Then there exists a positive constant δ , a constant $c \in (0, 1)$ and a time $T \geq 0$, such that the solutions of (5.41) satisfy*

$$\|\mathbf{e}(t)\| \leq \sqrt{\frac{k_2}{k_1}} \|\mathbf{e}(t_0)\| e^{-\frac{(1-c)k_3}{2*k_2}(t-t_0)} \quad (5.42)$$

$\forall t_0 \leq t \leq t_0 + T$, and

$$\|\mathbf{e}(t)\| \leq \frac{k_4}{k_3} \sqrt{\frac{k_2}{k_1}} \frac{\delta}{c} \quad \forall t \geq t_0 + T. \quad (5.43)$$

Proof. The partial derivative of (5.23) with respect to \mathbf{e} is bounded by

$$\left\| \frac{\partial V}{\partial \mathbf{e}} \right\| \leq \max\{\sigma^2, 1, \mu\} \|\mathbf{e}\|. \quad (5.44)$$

Hence, condition (2.17) of Lemma 2.2 is satisfied with $k_4 = \max\{\sigma^2, 1, \mu\} = 2k_2$ and $a = 2$. It remains to show that $\|\mathbf{G}\|$ is bounded for large $\|\mathbf{e}\|$. We do this by noticing that the denominators in \mathbf{G} are strictly positive functions of higher order of e_2 than the numerators. Hence, it is always possible to choose an $r_b > 0$ large enough so that in a ball $\mathcal{B}_{r_b} \triangleq \{|e_2| < r_b\}$, we have that

$$\|\mathbf{G}\| \leq \delta < \frac{k_3}{k_4} \sqrt{\frac{k_1}{k_2}} r_b c, \quad (5.45)$$

for some $\delta > 0$ and $c \in (0, 1)$. Hence, the conditions of Lemma 2.2 are satisfied, and the solutions of (5.41) are uniformly globally bounded by (5.42) and (5.43). \square

Notice that the solutions of (5.43) are bounded regardless of the maximum magnitude of \dot{u}_{rd} .

5.5.2 Boundedness of the complete system

Finally, we will show that the complete cascade (5.12) is uniformly bounded as well.

Theorem 5.4. *Assume that the conditions of Theorem 5.2 are satisfied, with the exception that $\dot{u}_{rd} \neq 0$. Then the solutions of the cascaded system (5.12) are uniformly bounded.*

Proof. We define the constant $\bar{\delta}$ as the bound on $\|e(t)\|$ in (5.43):

$$\bar{\delta} \triangleq \frac{k_4}{k_3} \sqrt{\frac{k_2}{k_1}} \frac{\delta}{c}. \quad (5.46)$$

It follows from (5.42) that the ball $\mathcal{B}_{\bar{\delta}}$ is UGAS. Furthermore, the interconnection matrix \mathbf{H} can be shown to satisfy $\|\mathbf{H}\| \leq \theta_3(\|\boldsymbol{\zeta}\|)(|y_b^n| + |y_{\text{int}}^n| + |v_{rb}|) + \theta_4(\|\boldsymbol{\zeta}\|)$, where $\theta_3(\cdot)$ and $\theta_4(\cdot)$ are some continuous non-negative functions. The perturbing system (5.12b) is UGES as shown in Section 5.3.1. Hence all the conditions of Proposition 2.1 are satisfied, which implies that the set $\mathcal{B}_{\bar{\delta}} \cup \{\mathbf{0}\}$ is UGAS. This also implies that the solutions of the complete cascade (5.12) are uniformly globally bounded, which concludes the proof. \square

5.6 Simulations

In this section we present the results from numerical simulations of a system where the ILOS guidance law with speed-dependent lookahead distance (5.6) is applied to an underactuated AUV operating in the horizontal plane. The path is aligned with the x -axis, and the AUV is modeled in 3 DOF as in (5.1).

The desired relative surge speeds are in the range $u_{rd} \in [1.5, 2.5]$ m/s. The current is set to $\boldsymbol{\nu}_{c/n}^n = [0 \text{ m/s}, 0.4 \text{ m/s}, 0 \text{ rad/s}]$, which fulfills Assumptions 5.1 and 5.2. It can be verified that Assumption 5.4 is satisfied with $Y_{\min} = 1.01 \text{ s}^{-1}$, and that $X_{v\max} = 1.84 \text{ s}^{-1}$. The integral gain is $\sigma = 0.3 \text{ m/s}$, which satisfies (5.39). From these parameters, a lower limit on k_{Δ} is found from (5.38) as $k_{\Delta} = 7.34 \text{ s}$. The surge controller gain is set to $k_u = 0.5$, while the heading controller gains are $k_{\psi} = 0.025$ and $k_r = 0.1$. The heading controller gains ensure that resulting yaw dynamics of the vehicle are quite slow, thus simulating the effect of low-speed actuators.

In the first simulation scenario, we look at the effect of increasing k_{Δ} . The desired relative surge speed is kept constant at $u_{rd} = 2.5 \text{ m/s}$, while k_{Δ} goes from 8 s to 14 s in steps of 2 s. The initial position of the vehicle is 50 m away from the path, pointing straight towards the path with the initial relative surge speed set to $u_r = u_{rd}$. The cross track error for the different values of k_{Δ} are shown in Figure 5.3. It can be seen that for lower values of k_{Δ} there is an overshoot, which disappears for $k_{\Delta} = 12 \text{ s}$. The system remains exponentially stable for all values of k_{Δ} , which verifies Theorem 5.2.

In the next simulation we use a fixed $k_{\Delta} = 12 \text{ s}$, but vary the desired relative surge speed from 1.5 m/s to 2.5 m/s in steps of 0.5 m/s. For each run, the vehicle

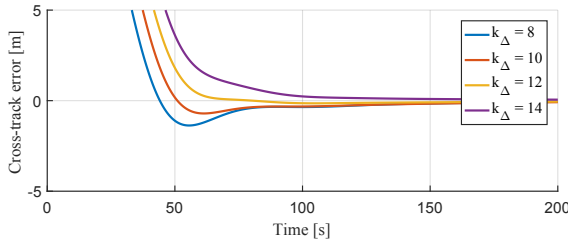


Figure 5.3: The cross-track error y_b^n for increasing values of k_Δ with $u_{rd} = 2.5$ m/s.

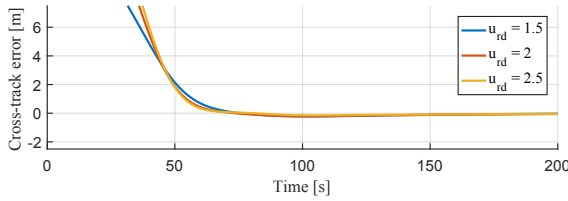


Figure 5.4: The cross-track error y_b^n for increasing values of u_{rd} with $k_\Delta = 12$ s.

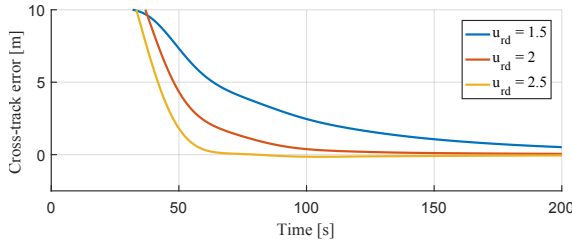


Figure 5.5: The cross-track error y_b^n for increasing values of u_{rd} with constant lookahead distance $\Delta = 30$ m.

initial position is set to $20u_{rd}$ m away from the path, with the initial relative surge speed set to $u_{rb}(t_0) = u_{rd}$. Thus, the vehicle will use approximately the same amount of time to reach the path, making the results easier to compare. The cross track error of the three runs are displayed in Figure 5.4, and it can be seen that in each case the vehicle converges to the path without any overshoot.

Figure 5.5 shows the result from a scenario where the lookahead distance was kept constant at $k_\Delta u_{rd} = 30$ m. It can be seen that the convergence times when $u_{rd} = 2.0$ m and $u_{rd} = 1.5$ m are significantly slower compared to the convergence times in Figure 5.4.

In the last scenario, we simulate a case with time-varying u_{rd} . Here $u_{rd} = u_c + u_t$, where $u_c = 2.0$ m/s and u_t is a sine wave with amplitude 0.5 m and period 60 s. From Figure 5.6, it is clear that the cross-track error converges to a bounded set around $y_b^n = 0$. Thus, the simulation verifies Lemma 5.3 for this particular case.

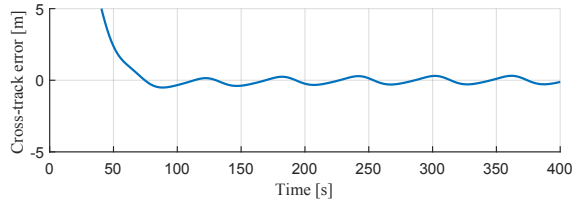


Figure 5.6: The cross-track error y_b^n for a time-varying u_{rd} .



Figure 5.7: The Odin USV.

5.7 Experimental results

In this section we present the results from experiments at sea. The experiments were carried out on the Odin unmanned surface vehicle (USV), which is depicted in Figure 5.7. The vehicle developed by FFI and Kongsberg Maritime, is 11 m long and 3.5 m wide, and is propelled by a dual waterjet system. At maneuvering speeds, the vehicle is underactuated. The ILOS guidance law was implemented with k_Δ varying from 6 s to 12 s, and integral gain $\sigma = 0.02$ m/s. The vehicle heading is controlled by a PD controller, which has been tuned to provide asymptotic stability of the heading.

The USV was tasked to follow a square pattern at different forward velocities. The waypoint switching distance was set to $9u_{rd}$ m. Thus, the initial conditions for each line was similar to the initial conditions used in the simulations in Section 5.6, with the vehicle approaching the line at a perpendicular angle with initial offset increasing with desired surge speed.

Figure 5.9 displays the cross-track error for two lines with $u_{rd} = 6$ m/s and $k_\Delta = 6$ s and 12 s. In both cases, the cross-track error converges towards zero, however the overshoot is slightly larger for $k_\Delta = 6$ s.

Figure 5.10 shows the cross-track error during four lines with u_{rd} increasing from 4 m/s to 10 m/s with a lookahead gain of $k_\Delta = 6$ s. In each case, the cross-track error reaches 0 m after approximately 11 s. We see that the overshoot increases slightly with increasing speed. A larger value of k_Δ would likely decrease this effect, as would a larger waypoint switching distance.

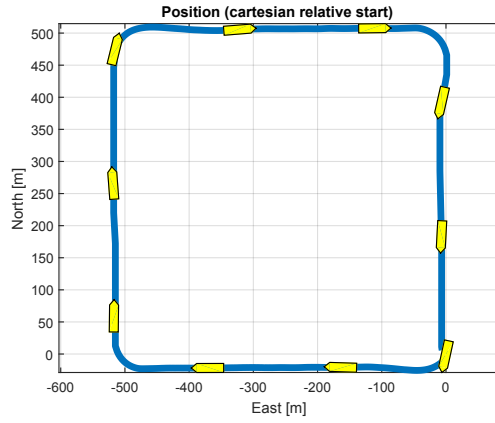


Figure 5.8: The vehicle position relative to the starting position during a run with $u_{rd} = 6$ m/s. The size of the vehicle has been increased in the figure.

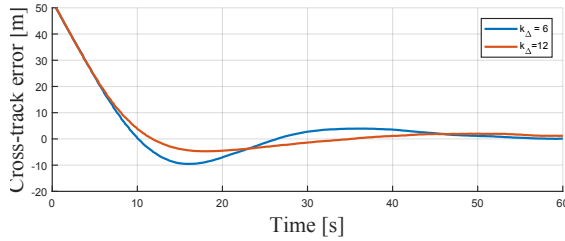


Figure 5.9: The cross-track error for $k_{\Delta} = 6$ s and 12 s with $u_{rd} = 2.5$ m/s.

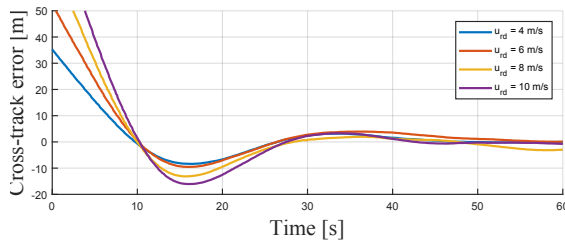


Figure 5.10: The cross-track error for increasing values of u_{rd} with $k_{\Delta} = 6$ s

5.8 Conclusions

In this chapter we have investigated an ILOS guidance law where the lookahead distance increases linearly with the desired surge speed u_{rd} . The work is motivated by the need to keep the maneuvering demands on a vehicle within acceptable limits, even when the surge speed is large. This is of particular importance if the dynamics of the vehicle yaw controller and actuators are slow with respect to the surge speed, in which case a small lookahead distance can lead to overshoots and oscillatory behavior.

Both the case when u_{rd} is constant along the path and the case where u_{rd} is time-varying have been explored. For a constant u_{rd} , we have derived a lower bound on the lookahead gain and an upper bound on the ILOS integral gain in order to guarantee USGES of the system. In the case of a time-varying u_{rd} , we have proved that the solutions of the system remain bounded for bounded u_{rd} . This holds for general u_{rd} trajectories, with the only assumption that the trajectories are lower bounded above the level of the maximum ocean current, so that the vehicle is able to move forward even when it is heading directly against the ocean currents.

The stability and boundedness results have been verified in simulations of an underwater vehicle with slow yaw dynamics, moving in the horizontal plane. In particular, the simulations show how increasing the lookahead distance linearly with u_{rd} results in convergence to the desired path without overshoot for several values of u_{rd} . This is achieved without having to tune the guidance law each time u_{rd} changes. A simulation with a time-varying u_{rd} has also been presented, demonstrating that the cross-track error remains bounded in this case.

The ILOS guidance law with speed-dependent lookahead distance has also been implemented on the Odin USV, which has been used for experimental verification of the stability properties. We have shown that by increasing the lookahead distance linearly with u_{rd} the increase in overshoot at higher speeds are limited, and that the vehicle converges to the path for high and low values of u_{rd} .

5.A Functional expressions

The functions F_u , F_r , X_v and Y_v are defined in Section 3.2.1, and are included here for convenience:

$$F_u(u_b, v_b, r_b) \triangleq \frac{1}{m_{11}}(m_{22}v_b + m_{23}r_b)r_b - \frac{d_{11}}{m_{11}}u_b, \quad (5.47)$$

$$F_r(u_b, v_b, r_b) \triangleq \frac{m_{23}d_{22} + m_{22}(d_{32} + (m_{22} - m_{11})u_b)}{m_{22}m_{33} - m_{23}^2}v_b + \frac{m_{23}(d_{23} - m_{11}u_b) - m_{22}(d_{33} + m_{23}u_b)}{m_{22}m_{33} - m_{23}^2}r_b, \quad (5.48)$$

$$X_v(u_b) \triangleq \frac{m_{23}^2 - m_{11}m_{33}}{m_{22}m_{33} - m_{23}^2}u_b + \frac{d_{33}m_{23} - d_{23}m_{33}}{m_{22}m_{33} - m_{23}^2}, \quad (5.49)$$

$$Y_v(u_b) \triangleq \frac{(m_{22} - m_{11})m_{23}}{m_{22}m_{33} - m_{23}^2}u_b - \frac{d_{22}m_{33} - d_{32}m_{23}}{m_{22}m_{33} - m_{23}^2}, \quad (5.50)$$

The function \mathbf{h}_{e_2} is defined as $\mathbf{h}_{e_2} \triangleq [h_{e_21}, h_{e_22}, h_{e_23}]^T$, where

$$h_{e_21} = \sin(\tilde{\psi}_b^n + \psi_d^n), \quad (5.51a)$$

$$h_{e_23} = 0, \quad (5.51b)$$

$$h_{e_22} = u_{rd} \left[\frac{\sin(\tilde{\psi}_b^n)}{\tilde{\psi}_b^n} \cos(\psi_d^n) + \frac{\cos(\tilde{\psi}_b^n) - 1}{\tilde{\psi}_b^n} \sin(\psi_d^n) \right] + e_3 \left[\frac{\cos(\tilde{\psi}_b^n) - 1}{\tilde{\psi}_b^n} \cos(\psi_d^n) - \frac{\sin(\tilde{\psi}_b^n)}{\tilde{\psi}_b^n} \sin(\psi_d^n) \right]. \quad (5.51c)$$

The function \mathbf{h}_{e_3} is defined as $\mathbf{h}_{e_3} \triangleq [h_{e_31}, h_{e_32}, h_{e_33}]^T$, where

$$h_{e_31} = \frac{X_v(\tilde{u}_{rb} + u_{rd}) - X_{vd}}{\tilde{u}_{rb}} \gamma(e_2, e_3) + e_3 \frac{Y_v(\tilde{u}_{rb} + u_{rd}) - Y_{vd}}{\tilde{u}_{rb}}, \quad (5.52a)$$

$$h_{e_32} = 0, \quad (5.52b)$$

$$h_{e_33} = X_v(\tilde{u}_{rb} + u_{rd}). \quad (5.52c)$$

The limits of h_{e_22} for $\tilde{\psi}_b^n \rightarrow 0$ and h_{e_31} as $\tilde{u}_{rb} \rightarrow 0$ exist and are finite. The expression $\gamma(e_2, e_3)$ used in h_{e_31} is defined as

$$\gamma(e_2, e_3) \triangleq \frac{\Delta u_{rd}(e_2 + \sigma y_{\text{int}}^{\text{eq}}) - \Delta^2 e_3}{l(e_2)^{3/2}} - \frac{\sigma \Delta^2}{l(e_2)^2} y_b^n - \frac{\Delta V_y}{l(e_2)} \quad (5.53)$$

Chapter 6

Path Following for Underwater Vehicles Without Neutral Buoyancy

I'm not fat, I'm big boned!

— Eric Cartman, *South Park*

In this chapter, we examine a 3D ILOS path following guidance law for underwater vehicles with a constant desired relative surge speed. Specifically, we will show that the USGES results of Chapters 4 and 5 can be extended to 3D. Moreover, we will examine the case when the vehicle is not neutrally buoyant. This is often the case in practice, as the water density changes with salinity, temperature and depth. Thus, even if the vehicle is initially perfectly ballasted, the buoyancy can change during an operation.

We will show that conditions under which the control system achieve USGES are a little bit stricter when the vehicle is not neutrally buoyant, when compared to the results of Caharija et al. [18], which showed κ -exponential stability for neutrally buoyant underwater vehicles.

This chapter is organized as follows: Section 6.1 gives a description of the vehicle model in 5 DOF, and states the control objective. Section 6.2 describes the ILOS guidance law and the surge, pitch and yaw controllers. The stability of the closed-loop system is analyzed in Section 6.3. Simulations demonstrating exponential stability are shown in Section 6.4, and some concluding remarks are given in Section 6.5.

The work presented in this chapter is based on Wiig et al. [112].

6.1 System description

The vehicle is modeled in 5 DOF using the relative velocities model presented in Section 3.3. However, we will not assume that the vehicle is neutrally buoyant. Rather, we will assume that there is a constant, known difference between the vehicle weight W and buoyancy B . Hence, we will in this chapter replace Assumption 3.6 with the following, relaxed assumption:

Assumption 6.1. The difference between the vehicle weight W and buoyancy B , defined as $W_E = W - B$, is assumed known and constant.

The vehicle will operate in the presence of an ocean current, which we assume to be bounded and uniform in time and space:

Assumption 6.2. The ocean current $\boldsymbol{\nu}_{c/n}^n \triangleq [V_x, V_y, V_z, 0, 0]^T$ is assumed to be constant, irrotational and bounded. Hence, there exists a constant $V_{\max} \geq 0$ such that $V_{\max} \geq \sqrt{V_x^2 + V_y^2 + V_z^2}$.

Recall then, from Chapter 3, that the structure of the vehicle model is on the form

$$\dot{\boldsymbol{\eta}}_b^n = \mathbf{J}_b^n \boldsymbol{\nu}_{rb/n}^b + \boldsymbol{\nu}_{c/n}^n, \quad (6.1a)$$

$$\mathbf{M} \boldsymbol{\nu}_{rb/n}^b + \mathbf{C}(\boldsymbol{\nu}_{rb/n}^b) \boldsymbol{\nu}_{rb/n}^b + \mathbf{D} \boldsymbol{\nu}_{rb/n}^b + \mathbf{g}(\boldsymbol{\eta}_b^n) = \mathbf{B} \mathbf{f}, \quad (6.1b)$$

where

$$\boldsymbol{\eta}_b^n \triangleq \begin{bmatrix} x_b^n \\ y_b^n \\ x_b^n \\ \theta_b^n \\ \psi_b^n \end{bmatrix} \quad (6.2)$$

and

$$\boldsymbol{\nu}_{rb/n}^b = \begin{bmatrix} u_{rb} \\ v_{rb} \\ w_{rb} \\ q_b \\ r_b \end{bmatrix}. \quad (6.3)$$

The system matrices are described in Section 3.3, with the exception of the gravity restoration vector $\mathbf{g}(\boldsymbol{\eta}_b^n)$, which by Assumption 6.1 is modeled as

$$\mathbf{g}(\boldsymbol{\eta}_b^n) \triangleq \begin{bmatrix} W_E \sin(\theta_b^n) \\ 0 \\ -W_E \cos(\theta_b^n) \\ (BG_z W + W_E z_b) \sin(\theta_b^n) \\ 0 \end{bmatrix}. \quad (6.4)$$

Compared to the gravity restoration vector in Section 3.3, the vector $\mathbf{g}(\boldsymbol{\eta})$ includes additional forces in surge and heave resulting from W_E , as well as an addition to the moment in pitch.

The 5 DOF model in (6.1) represented in component form is:

$$\dot{x}_b^n = u_{rb} c(\psi_b^n) c(\theta_b^n) - v_{rb} s(\psi_b^n) + w_{rb} c(\psi_b^n) s(\theta_b^n) + V_x, \quad (6.5a)$$

$$\dot{y}_b^n = u_{rb} s(\psi_b^n) c(\theta_b^n) + v_{rb} c(\psi_b^n) + w_{rb} s(\psi_b^n) s(\theta_b^n) + V_y, \quad (6.5b)$$

$$\dot{z}_b^n = -u_{rb} s(\theta_b^n) + w_{rb} c(\theta_b^n) + V_z, \quad (6.5c)$$

$$\dot{\theta}_b^n = q, \quad (6.5d)$$

$$\dot{\psi}_b^n = r/c(\theta_b^n), \quad (6.5e)$$

$$\dot{u}_{rb} = \bar{F}_u(u_{rb}, v_{rb}, w_{rb}, r_b, q_b) + \tau_u, \quad (6.5f)$$

$$\dot{v}_{rb} = X_v(u_{rb})r_b + Y_v(u_{rb})v_{rb}, \quad (6.5g)$$

$$\dot{w}_{rb} = X_w(u_{rb})q_b + Y_w(u_{rb})w_{rb} + Z_{ws}s(\theta_b^n) + Z_{wc}c(\theta_b^n), \quad (6.5h)$$

$$\dot{q}_b = \bar{F}_q(\theta_b^n, u_{rb}, w_{rb}, q_b) + \tau_q. \quad (6.5i)$$

$$\dot{r}_b = F_r(u_{rb}, v_{rb}, r_b) + \tau_r. \quad (6.5j)$$

The terms X_v , Y_v , X_w , Y_w , and F_r are defined Section 3.2.2 and restated in Appendix 6.A for convenience. The lack of neutral buoyancy affects \dot{u}_{rb} , \dot{w}_{rb} and \dot{q}_b through \bar{F}_u , Z_{ws} , Z_{wc} and \bar{F}_q , which are defined in Appendix 6.A. To ensure that the system is nominally stable in both sway and heave, we make the following assumption on Y_v and Y_w :

Assumption 6.3. For all $u_{rb} > 0$, the functions $Y_v(u_{rb})$ and $Y_w(u_{rb})$ satisfy

$$Y_v(u_{rb}) < 0, \quad (6.6)$$

$$Y_w(u_{rb}) < 0. \quad (6.7)$$

This assumption holds for most AUVs.

6.1.1 Control objective

The objective of the control system is to make the vehicle modeled by (6.1) converge to and follow a straight-line path.

Assumption 6.4. The desired path \mathcal{P} is horizontal.

Remark 6.1. A non-horizontal path will result in an additional bounded constant disturbance due to gravity, which the control system presented in this chapter compensates for.

The path should be followed in the presence of an unknown, constant and irrotational current while keeping a constant relative surge speed $u_{rd} > 0$. Without any loss of generality, the path is assumed to be aligned with the x -axis of the inertial frame n , so that $\mathcal{P} \triangleq \{(x, y, z) \in \mathbb{R}^3 : y = 0, z = 0\}$. The objectives of the control system are formalized as

$$\lim_{t \rightarrow \infty} y_b^n(t) = 0, \quad (6.8a)$$

$$\lim_{t \rightarrow \infty} \psi_b^n(t) = \psi_{ss}, \quad \psi_{ss} \in \left(-\frac{\pi}{2}, \frac{\pi}{2}\right), \quad (6.8b)$$

$$\lim_{t \rightarrow \infty} z_b^n(t) = 0, \quad (6.8c)$$

$$\lim_{t \rightarrow \infty} \theta_b^n(t) = \theta_{ss}, \quad \theta_{ss} \in \left(-\frac{\pi}{2}, \frac{\pi}{2}\right), \quad (6.8d)$$

$$\lim_{t \rightarrow \infty} u_{rb}(t) = u_{rd}, \quad (6.8e)$$

where ψ_{ss} and θ_{ss} is a constant yaw and heading angle required to keep the underactuated vessel at the path, compensating for a constant and irrotational ocean current, as well as for W_E .

The following assumption ensures that the vessel is able to follow the path for any direction of the ocean current:

Assumption 6.5. The desired relative surge speed u_{rd} is such that

$$u_{rd} > \max \left\{ V_{\max} + \frac{5}{2} \frac{|Z_{ws}| + 0.5|Z_{wc}|}{|Y_w(u_{rd})|}, 2V_{\max} + 2 \frac{|Z_{ws}| + 0.5|Z_{wc}|}{|Y_w(u_{rd})|} \right\}. \quad (6.9)$$

Note that Assumption 6.5 is stricter than the assumption on u_{rd} in Caharija et al. [18]. This is due to the presence of W_E in Z_{ws} and Z_{wc} . This bound will follow from the analysis in Section 6.3.

6.2 Control system

This section presents a control system for the path following problem presented in Section 6.1.1.

6.2.1 The ILOS guidance law

The desired pitch θ_d^n and heading ψ_d^n are given by the ILOS guidance law introduced in Caharija et al. [18]:

$$\theta_d^n \triangleq \tan^{-1} \left(\frac{z_b^n + \sigma_z z_{\text{int}}^n}{\Delta_z} \right), \quad \Delta_z > 0, \quad \sigma_z > 0, \quad (6.10a)$$

$$\dot{z}_{\text{int}}^n \triangleq \frac{\Delta_z z_b^n}{(z_b^n + \sigma_z z_{\text{int}}^n)^2 + \Delta_z^2}, \quad (6.10b)$$

$$\psi_d^n \triangleq -\tan^{-1} \left(\frac{y_b^n + \sigma_y y_{\text{int}}^n}{\Delta_y} \right), \quad \Delta_y > 0, \quad \sigma_y > 0, \quad (6.10c)$$

$$\dot{y}_{\text{int}}^n \triangleq \frac{\Delta_y y_b^n}{(y_b^n + \sigma_y y_{\text{int}}^n)^2 + \Delta_y^2}. \quad (6.10d)$$

The lookahead distances Δ_z and Δ_y , and the integral gains σ_z and σ_y are constant design parameters. The auxiliary integral states z_{int}^n and y_{int}^n creates a nonzero desired heading and pitch even when the vehicle is on the path, making the vehicle counteract disturbances. The integral term growth rates (6.10b) and (6.10d) are designed to decrease for large cross-track errors z_b^n and y_b^n , reducing the risk of wind-up effects.

6.2.2 Surge, pitch and yaw controllers

Surge, pitch and yaw are controlled using feedback linearizing controllers like the ones used in Caharija et al. [18], but with added integral effect in surge:

$$\tau_u = -\bar{F}_u(u_{rb}, v_{rb}, w_{rb}, \theta_b^n, r_b, q_b) - k_u(u_{rb} - u_{rd}) - k_{ui} \int_{t_0}^t (u_{rb} - u_{rd}), \quad (6.11a)$$

$$\tau_q = -\bar{F}_q(\theta_b^n, u_{rb}, w_{rb}, w_b) + \ddot{\theta}_d^n - k_\theta(\theta - \theta_d^n) - k_q(q_b - \dot{\theta}_d^n), \quad (6.11b)$$

$$\begin{aligned} \tau_r = & -F_r(u_{rb}, v_{rb}, r_b) - q_b \sin(\theta_b^n) \dot{\psi}_b^n \\ & + \cos(\theta_b^n) \left[\ddot{\psi}_d^n - k_\psi(\psi_b^n - \psi_d^n) - k_r(\dot{\psi}_b^n - \dot{\psi}_d^n) \right]. \end{aligned} \quad (6.11c)$$

The control gains k_u , k_{ui} , k_θ , k_q , k_ψ and k_r are constant and positive, and t_0 denotes the starting time. The integral term in the control law for τ_u has been added for robustness to modeling errors in the terms canceled out by \bar{F}_u , e.g. the buoyancy error term W_E . Since the references for pitch and yaw are set by an outer control loop which includes integral term (namely (6.10a) and (6.10c)), no integral terms are added to τ_q and τ_r .

6.3 Stability of the closed-loop system

This section analyzes the stability properties of the complete vessel kinematics and dynamics when the vehicle is controlled by the control system presented in the previous section. The terms $X_{wd} = X_w(u_{rd})$, $Y_{wd} = Y_w(u_{rd})$, $X_{vd} = X_v(u_{rd})$ and $Y_{vd} = Y_v(u_{rd})$ are used for brevity. Furthermore, the constants Γ_{\max} and Γ_{\inf} and the functions $\Gamma(\xi)$ and $\rho(\sigma_z)$ are defined as:

$$\Gamma(\xi) \triangleq u_{rd} \frac{1}{\sqrt{\xi^2 + 1}} - \frac{Z_{ws}\xi + Z_{wc}}{Y_{wd}} \frac{\xi}{\xi^2 + 1}, \quad (6.12)$$

$$\Gamma_{\inf} \triangleq \frac{1}{\sqrt{5}} u_{rd} - \frac{4|Z_{ws}| + 0.5|Z_{wc}|}{5|Y_{wd}|}, \quad \Gamma_{\max} \triangleq u_{rd}, \quad (6.13)$$

$$\rho(\sigma_z) \triangleq \frac{u_{rd} - V_{\max} - \sigma_z}{u_{rd} - V_{\max} - \sigma_z - \frac{5|Z_{ws}| + 0.5|Z_{wc}|}{2|Y_{wd}|}}. \quad (6.14)$$

The constant ξ is defined in Section 6.3.1, where it is shown that $\Gamma_{\inf} < \Gamma(\xi) \leq \Gamma_{\max}$.

Theorem 6.1. *If Assumptions 6.1 to 6.5 hold and the lookahead distances Δ_y and Δ_z satisfy*

$$\Delta_y > \frac{|X_{vd}|}{|Y_{vd}|} \left[\frac{5\Gamma_{\max} + V_{\max} + \sigma_y}{4\Gamma_{\inf} - V_{\max} - \sigma_y} + 1 \right], \quad (6.15)$$

$$\Delta_z > \frac{|X_{wd}|}{|Y_{wd}|} \rho(\sigma_z) \left[\frac{5u_{rd} + V_{\max} + \sigma_z}{4u_{rd} - V_{\max} - \sigma_z} + 1 \right], \quad (6.16)$$

and the integral gains σ_y and σ_z satisfy

$$0 < \sigma_y < \Gamma_{\inf} - V_{\max}, \quad (6.17)$$

$$0 < \sigma_z < u_{rd} - V_{\max} - \frac{5|Z_{ws}| + 0.5|Z_{wc}|}{2|Y_{wd}|}, \quad (6.18)$$

then the controllers (6.11a) - (6.11c) and guidance laws (6.10) guarantee achievement of the control objectives (6.8). The control objectives (6.8b) and (6.8d) are fulfilled with $\psi_{ss} = -\tan^{-1}(V_y/\sqrt{\Gamma(\xi)^2 - V_y^2})$ and $\theta_{ss} = \tan^{-1}(\xi)$, respectively. Furthermore, the equilibrium point of the error dynamics is USGES and UGAS.

Remark 6.2. The Z_{wc} term in the bound on u_{rd} , Δ_y , Δ_z , σ_y and σ_z is the result of the vehicle not being neutrally buoyant, as can be seen in the definition of Z_{wc} (6.50).

6.3.1 Proof of Theorem 6.1

The error signals of the actuated dynamics are collected in

$$\zeta \triangleq \begin{bmatrix} u_{\text{int}}^n \\ \tilde{u}_{rb} \\ \tilde{\theta}_b^n \\ \tilde{q}_b \\ \psi_b^n \\ \dot{\psi}_b^n \end{bmatrix} \triangleq \begin{bmatrix} \int_{t_0}^t (\tilde{u}_{rb}) \\ u_{rb} - u_{rd} \\ \theta_b^n - \theta_d^n \\ q_b - \dot{\theta}_d^n \\ \psi_b^n - \psi_d^n \\ \psi_b^n - \psi_d^n \end{bmatrix}. \quad (6.19)$$

The closed-loop dynamics of ζ are obtained by combining the system equations (6.5d), (6.5e), (6.5f), (6.5i) and (6.5j) with the control laws in surge (6.11a), pitch (6.11b) and yaw (6.11c):

$$\dot{\zeta} = \begin{bmatrix} 0 & 1 & 0 & 0 & 0 & 0 \\ -k_{ui} & -k_u & 0 & 0 & 0 & 0 \\ 0 & 0 & 0 & 1 & 0 & 0 \\ 0 & 0 & -k_\theta & -k_q & 0 & 0 \\ 0 & 0 & 0 & 0 & 0 & 1 \\ 0 & 0 & 0 & 0 & -k_\psi & -k_r \end{bmatrix} \zeta \triangleq \Sigma \zeta. \quad (6.20)$$

The $z_b^n - w_{rb}$ subsystem is obtained from (6.5c), (6.5h) and (6.10b):

$$\dot{z}_{\text{int}}^n = \frac{\Delta_z z_b^n}{(z_b^n + \sigma_z z_{\text{int}}^n)^2 + \Delta_z^2}, \quad (6.21a)$$

$$\dot{z}_b^n = -u_{rb} \sin(\tilde{\theta}_b^n + \theta_d^n) + w_{rb} \cos(\tilde{\theta}_b^n + \theta_d^n) + V_z, \quad (6.21b)$$

$$\begin{aligned} \dot{w}_{rb} &= X_w(\tilde{u}_{rb} + u_{rd})(\tilde{q}_b + \dot{\theta}_d^n) + Y_w(\tilde{u}_{rb} + u_{rd})w_{rb} \\ &\quad + Z_{ws} \sin(\tilde{\theta}_b^n + \theta_d^n) + Z_{wc} \cos(\tilde{\theta}_b^n + \theta_d^n). \end{aligned} \quad (6.21c)$$

Note that the buoyancy terms Z_{ws} and Z_{wc} show up in the underactuated heave dynamics (6.21c).

The calculation of the equilibrium point of (6.21) on the manifold $\zeta = \mathbf{0}$ gives the equations

$$\xi \sqrt{\xi^2 + 1} = \frac{V_z}{u_{rd}} (\xi^2 + 1) - \frac{Z_{ws}\xi + Z_{wc}}{u_{rd}Y_{wd}}, \quad (6.22a)$$

$$w_{rb}^{\text{eq}} = u_{rd}\xi - V_z \sqrt{\xi^2 + 1}, \quad (6.22b)$$

where $\xi \triangleq \sigma_z z_{\text{int}}^{\text{eq}} / \Delta_z$, and $z_{\text{int}}^{\text{eq}}$ and w_{rb}^{eq} is the value of z_{int}^n and w_{rb} at equilibrium.

Using the technique of Caharija et al. [18, Lemma IV.1] it can be shown that there exists at least one real solution for (6.22). Since the equilibrium point is later proven to be UGAS and USGES, the solution is unique. Furthermore, Assumption 6.5 can be used to give the following bound:

$$\left| \frac{V_z}{u_{rd}} (\xi^2 + 1) - \frac{Z_{ws}\xi + Z_{wc}}{u_{rd}Y_{wd}} \right| < \frac{1}{2} (\xi^2 + 3 + |\xi|) \quad (6.23)$$

Inserting (6.22a) into (6.23) and solving for $\xi_{\text{sup}} > |\xi| > 0$ gives $\xi_{\text{sup}} \approx 2$. Hence, $\Gamma_{\text{inf}} < \Gamma(\xi) \leq \Gamma_{\text{max}}$ holds, where $\Gamma(\xi)$ is defined in (6.12), and Γ_{inf} and Γ_{max} in (6.13).

A change of variables is introduced to obtain a system with the equilibrium point at the origin:

$$e_{z1} \triangleq z_{\text{int}}^n - z_{\text{int}}^{\text{eq}}, \quad e_{z2} \triangleq z_b^n + \sigma_z e_{z1}, \quad e_{z3} \triangleq w_{rb} - w_{rb}^{\text{eq}}. \quad (6.24)$$

After factorizing with respect to ζ , the interconnected dynamics of (6.20) and (6.21) can be expressed in cascade form as

$$\dot{e}_z = \mathbf{A}_z(e_z)e_z + \mathbf{B}_z(e_z) + \mathbf{H}_z(z_b^n, z_{\text{int}}^n, \theta_d^n, w_{rb}, \zeta)\zeta, \quad (6.25a)$$

$$\dot{\zeta} = \Sigma\zeta, \quad (6.25b)$$

where $e_z \triangleq [e_{z1}, e_{z2}, e_{z3}]^T$,

$$\mathbf{A}_z \triangleq \begin{bmatrix} -\frac{\sigma_z \Delta_z}{l_z(e_{z2})} & \frac{\Delta_z}{l_z(e_{z2})} & 0 \\ -\frac{\sigma_z^2 \Delta_z}{l_z(e_{z2})} & -\frac{u_{rd}}{\sqrt{l_z(e_{z2})}} + \frac{\sigma_z \Delta_z}{l_z(e_{z2})} & \frac{\Delta_z}{\sqrt{l_z(e_{z2})}} \\ -\frac{\sigma_z^2 \Delta_z^2 X_{wd}}{l_z(e_{z2})^2} & \left(\frac{-u_{rd} \Delta_z X_{wd}}{l_z(e_{z2})^{3/2}} + \frac{\sigma_z \Delta_z^2 X_{wd}}{l_z(e_{z2})^2} + \frac{Z_{ws}}{\sqrt{l_z(e_{z2})}} \right) & \left(Y_{wd} + \frac{\Delta_z^2 X_{wd}}{l_z(e_{z2})^{3/2}} \right) \end{bmatrix}, \quad (6.26)$$

while

$$\mathbf{B}_z \triangleq \begin{bmatrix} 0 \\ V_z f(e_{z2}) \\ \frac{\Delta_z X_{wd} V_z f(e_{z2})}{l_z(e_{z2})} - \frac{Z_{ws} \xi + Z_{wc}}{\sqrt{\xi^2 + 1}} f(e_{z2}) \end{bmatrix} \quad (6.27)$$

The interconnection matrix \mathbf{H}_z contains all the terms vanishing at $\zeta = 0$ and is given by

$$\mathbf{H}_z \triangleq \begin{bmatrix} 0 & 0 \\ 1 & 0 \\ \frac{\Delta_z (X_w(\bar{u} + u_{rd}) - X_{wd})}{l_z(e_{z2})} & 1 \end{bmatrix} \begin{bmatrix} \mathbf{h}_z^T \\ \mathbf{h}_w^T \end{bmatrix}, \quad (6.28)$$

where \mathbf{h}_z and \mathbf{h}_w are given in Appendix 6.A. The term $l_z(e_{z2})$ is defined as

$$l_z(e_{z2}) \triangleq (e_{z2} + \sigma_z z_{\text{int}}^{\text{eq}})^2 + \Delta_z^2, \quad (6.29)$$

and $f(e_{z2})$ is defined as

$$f(e_{z2}) \triangleq 1 - \frac{\sqrt{(\sigma_z z_{\text{int}}^{\text{eq}})^2 + \Delta_z^2}}{\sqrt{l_z(e_{z2})}}. \quad (6.30)$$

Note that $f(e_{z2})$ is bounded by

$$|f(e_{z2})| \leq \frac{|e_{z2}|}{\sqrt{l_z(e_{z2})}}. \quad (6.31)$$

The nominal system of the cascade in (6.25) is

$$\dot{e}_z = \mathbf{A}_z(e_z)e_z + \mathbf{B}_z(e_z). \quad (6.32)$$

Lemma 6.2. *Under the conditions of Theorem 6.1, the equilibrium point of the system (6.32) is UGAS and USGES.*

Proof. The proof of Lemma 6.2 is given in Appendix 6.B □

Lemma 6.3. *Under the conditions of Theorem 6.1, the equilibrium point of the complete system (6.25) is UGAS and USGES.*

Proof. The system (6.25) is a cascaded system, consisting of a linear system (6.25b) which perturbs the dynamics (6.25a) through the interconnection matrix \mathbf{H}_z . The matrix \mathbf{H}_z can be shown to satisfy $\|\mathbf{H}_z\| \leq \delta_1(\|\zeta\|)(|z_b^n| + |z_{\text{int}}^n| + |w_{rb}|) + \delta_2(\|\zeta\|)$, where $\delta_1(\cdot)$ and $\delta_2(\cdot)$ are some continuous non-negative functions.

The perturbing system (6.25b) is a linear, time-invariant system. Furthermore, since the gains k_u, k_{ui}, k_ψ, k_r are all strictly positive, the system matrix Σ is Hurwitz and the origin $\zeta = \mathbf{0}$ is UGES. Note, however, that due to the modular properties of cascaded systems theory, any set of controllers providing USGES (or UGES) in surge, pitch and yaw will give the same result.

The nominal system is USGES by Lemma 6.2. Hence all the conditions of Proposition 2.1 are satisfied, guaranteeing USGES and UGAS of the equilibrium point $(e_z, \zeta) = (\mathbf{0}, \mathbf{0})$ of (6.25). □

By Lemma 6.3, the control objectives (6.8c)-(6.8e) are achieved with exponential convergence properties and steady state pitch angle $\theta_{ss} = \tan^{-1}\left(\frac{\sigma_z z_{\text{int}}^{\text{eq}}}{\Delta_z}\right)$. Let $\chi = [e_z^T, \zeta^T]$ be a vector containing the exponentially converging error variables from (6.25). The complete vehicle kinematics and dynamics form another cascaded system, where (6.25) perturbs the $y_b^n - v_{rb}$ subsystem, which is obtained from (6.5b), (6.5g) and (6.10d):

$$\dot{y}_{\text{int}}^n = \frac{\Delta_y y_b^n}{(y_b^n + \sigma_y y_{\text{int}}^n)^2 + \Delta_y^2}, \quad (6.33a)$$

$$\begin{aligned} \dot{y}_b^n &= u_{rb} \sin(\tilde{\psi}_b^n + \psi_d^n) \cos(\tilde{\theta}_b^n + \theta_d^n) + v_{rb} \cos(\tilde{\psi}_b^n + \psi_d^n) \\ &\quad + w_{rb} \sin(\tilde{\psi}_b^n + \psi_d^n) \sin(\tilde{\theta}_b^n + \theta_d^n) + V_y, \end{aligned} \quad (6.33b)$$

$$\dot{v}_{rb} = X_v(\tilde{u}_{rb} + u_{rd})(\dot{\tilde{\psi}}_b^n + \dot{\psi}_d^n) \cos(\tilde{\theta}_b^n + \theta_d^n) + Y_v(\tilde{u}_{rb} + u_{rd})v_{rb}. \quad (6.33c)$$

The equilibrium point of (6.33) on the manifold $\chi = \mathbf{0}$ is given by

$$y_{\text{int}}^n = y_{\text{int}}^{\text{eq}} \triangleq \frac{\Delta_y}{\sigma_y} \frac{V_y}{\sqrt{\Gamma(\xi)^2 - V_y^2}}, \quad (6.34a)$$

$$y_b^n = 0, \quad (6.34b)$$

$$v_{rb} = 0. \quad (6.34c)$$

where $\Gamma(\xi)$ is defined in (6.12). A change of variables is introduced to obtain a system with the equilibrium point at the origin:

$$e_{y1} \triangleq y_{\text{int}}^n - y_{\text{int}}^{\text{eq}}, \quad e_{y2} \triangleq y_b^n + \sigma_y e_{y1}, \quad e_{y3} \triangleq v_{rb}. \quad (6.35)$$

After factorizing with respect to χ and substituting (6.10c) and (6.10a) for ψ_d^n and θ_d^n , the system in cascaded form becomes

$$\dot{e}_y = \mathbf{A}_y e_y + \mathbf{B}_y + \mathbf{H}_y (y_b^n, y_{\text{int}}^n, \theta_d^n, \psi_d^n, v_{rb}, \chi) \chi, \quad (6.36a)$$

$$\dot{\chi} = \begin{bmatrix} \mathbf{A}_z & \mathbf{H}_z \\ \mathbf{0} & \zeta \end{bmatrix} \chi + \begin{bmatrix} \mathbf{B}_z \\ \mathbf{0} \end{bmatrix} \quad (6.36b)$$

where $e_y \triangleq [e_{y1}, e_{y2}, e_{y3}]^T$,

$$\mathbf{A}_y \triangleq \begin{bmatrix} -\frac{\sigma_y \Delta_y}{l_y(e_{y2})} & \frac{\Delta_y}{l_y(e_{y2})} & 0 \\ -\frac{\sigma_y^2 \Delta_y}{l_y(e_{y2})} & -\frac{\Gamma(\xi)}{\sqrt{l_y(e_{y2})}} + \frac{\sigma_y \Delta_y}{l_y(e_{y2})} & \frac{\Delta_y}{\sqrt{l_y(e_{y2})}} \\ \frac{1}{\sqrt{\xi^2+1}} \frac{\sigma_y^2 \Delta_y^2 X_{vd}}{l_y(e_{y2})^2} & \frac{1}{\sqrt{\xi^2+1}} \left(\frac{\Gamma(\xi) \Delta_y X_{vd}}{l_y(e_{y2})^{3/2}} - \frac{\sigma_y \Delta_y^2 X_{vd}}{l_y(e_{y2})^2} \right) & \left(Y_{vd} - \frac{\Delta_y^2 X_{vd}}{l_y(e_{y2})^{3/2} \sqrt{\xi^2+1}} \right) \end{bmatrix} \quad (6.37)$$

while

$$\mathbf{B}_y(e_{y2}) \triangleq \begin{bmatrix} 0 \\ V_y g(e_{y2}) \\ -\frac{1}{\sqrt{\xi^2+1}} \frac{\Delta_y X_{vd} V_y}{l_y(e_{y2})} g(e_{y2}) \end{bmatrix}. \quad (6.38)$$

The interconnection matrix \mathbf{H}_y contains all the terms vanishing at $\chi = 0$ and is given by

$$\mathbf{H}_y \triangleq \begin{bmatrix} 0 & 0 \\ 1 & 0 \\ -\frac{\Delta_y (X_v (\tilde{u}_{rb} + u_{rd}) - X_{vd}) \cos(\tilde{\theta}_b^n + \theta_d^n)}{l_y(e_{y2})} & 1 \end{bmatrix} \begin{bmatrix} \mathbf{h}_y^T \\ \mathbf{h}_v^T \end{bmatrix}, \quad (6.39)$$

where \mathbf{h}_y and \mathbf{h}_v are given in Appendix 6.A. The term $l_y(e_{y2})$ is defined as

$$l_y(e_{y2}) \triangleq (e_{y2} + \sigma_y y_{\text{int}}^{\text{eq}})^2 + \Delta_y^2, \quad (6.40)$$

and $g(e_{y2})$ is defined as

$$g(e_{y2}) \triangleq 1 - \frac{\sqrt{(\sigma_y y_{\text{int}}^{\text{eq}})^2 + \Delta_y^2}}{\sqrt{l_y(e_{y2})}}, \quad (6.41)$$

which is bounded by

$$|g(e_{y2})| \leq \frac{|e_{y2}|}{\sqrt{l_y(e_{y2})}}. \quad (6.42)$$

Lemma 6.4. *Under the conditions of Theorem 6.1, the origin of the system (6.36) is UGAS and USGES.*

Proof. Consider the nominal system

$$\dot{e}_y = \mathbf{A}_y(e_{y2}) + \mathbf{B}_y(e_{y2}). \quad (6.43)$$

This system is similar to the system (6.32), with the exception of the unknown constants ξ and $\Gamma(\xi)$. However, since $\Gamma(\xi)$ is bounded in (6.13), it is possible to

apply Lemma 6.2 to conclude UGAS and USGES of the origin of (6.43). The origin of the perturbing system (6.36b) is shown in Lemma 6.3 to be UGAS and USGES as well. Finally, the interconnection matrix \mathbf{H}_y can be shown to satisfy $\|\mathbf{H}_y\| \leq \delta_3(\|\boldsymbol{\chi}\|)(|y_b^n| + |y_{\text{int}}^n| + |v_{rb}|) + \delta_4(\|\boldsymbol{\chi}\|)$, where $\delta_3(\cdot)$ and $\delta_4(\cdot)$ are some continuous non-negative functions. Hence all the conditions of Proposition 2.1 are satisfied, guaranteeing USGES and UGAS of the equilibrium point $(\mathbf{e}_y, \boldsymbol{\chi}) = (\mathbf{0}, \mathbf{0})$ of (6.36). \square

By Lemma 6.4, the control objectives (6.8a) and (6.8b) are achieved with exponential convergence properties and $\psi_{ss} = \tan^{-1}(V_y/\sqrt{\Gamma(\xi)^2 - V_y^2})$. Hence, all the control objectives are met and the proof of Theorem 6.1 is concluded.

6.4 Simulations

This section presents results from numerical simulations of the ILOS guidance law applied to an underactuated AUV modeled in 5 DOF. The AUV is tasked to follow a horizontal path along the x -axis. The desired relative surge speed is $u_{rd} = 2 \text{ m/s}$. The current is $\boldsymbol{\nu}_{c/n}^n = [0.1 \text{ m/s}, 0.3 \text{ m/s}, 0.3 \text{ m/s}, 0, 0]$. The terms $|X_{vd}| = |X_{wd}| = 1.59 \text{ s}^{-1}$ and $|Y_{vd}| = |Y_{wd}| = 1.10 \text{ s}^{-1}$. The weight of the AUV is 1380 kg, which is 30 kg too heavy to be neutrally buoyant. This gives $Z_{ws} = 0.08$ and $Z_{wc} = 0.14$. The ILOS lookahead distances and integral gains are $\Delta_y = \Delta_z = 10 \text{ m}$ and $\sigma_y = \sigma_z = 0.2 \text{ m/s}$. The surge, yaw and pitch controllers (6.11a)-(6.11c) are implemented with $k_u = 0.5$, $k_{ui} = 0.01$, $k_\psi = k_\theta = 1$ and $k_r = k_q = 3$. It can be confirmed that the conditions of Theorem 6.1 are met. The initial position of the vehicle is 25 m east of and 25 m below the path, the initial direction is parallel to the path and the initial velocity is zero.

Figures 6.1 and 6.2 show the track of the AUV in the $x - z$ and $x - y$ plane, respectively. The vehicle maintains a constant sideslip and pitch angle after converging to the path, counteracting the current and vehicle weight. The relative sway velocity v_{rb} stabilizes at zero, while the relative heave velocity w_{rb} , shown in Figure 6.3, stabilizes at 0.14 m/s due to the error in buoyancy. Figure 6.4 shows how the cross-track errors y_b^n and z_b^n converge to zero. Figure 6.5 shows the natural logarithm of the Euclidean norm of the error variables in (6.36), where $\mathbf{e}_{tot} \triangleq [e_y^T, \boldsymbol{\chi}^T]^T$. Like in Chapter 4, this term is upper bounded by a straight, descending line, corresponding to a bounding exponential function. Hence, for these initial conditions and parameters, exponential convergence of the system is verified.

In many scenarios, the difference between vehicle weight and buoyancy, W_E , will not be readily available. To investigate robustness with respect to W_E , the vehicle has been simulated with the negative buoyancy unknown to the controllers. Figure 6.6 shows the resulting $x - z$ track of the vehicle, which is still able to follow the path, albeit with slightly slower convergence.

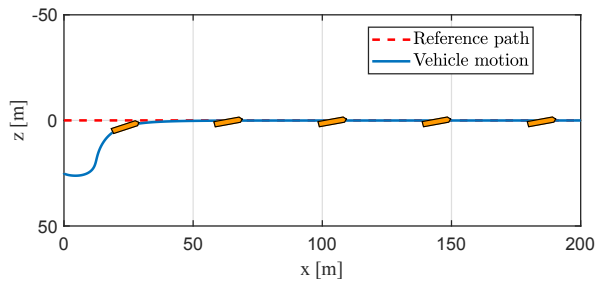


Figure 6.1: Position and pitch of the vehicle in the $x-z$ plane during the simulation.

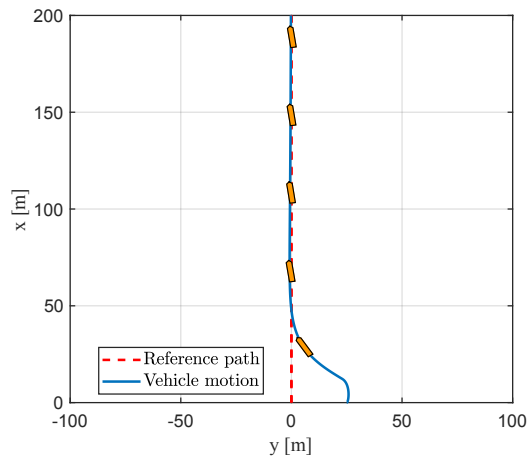


Figure 6.2: Position and pitch of the vehicle in the $x-y$ plane during the simulation.

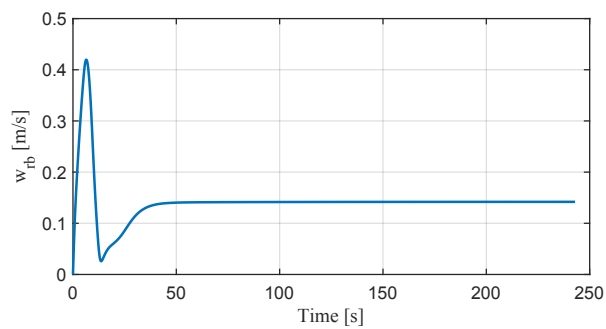


Figure 6.3: The relative heave velocity w_{rb} during the simulation.

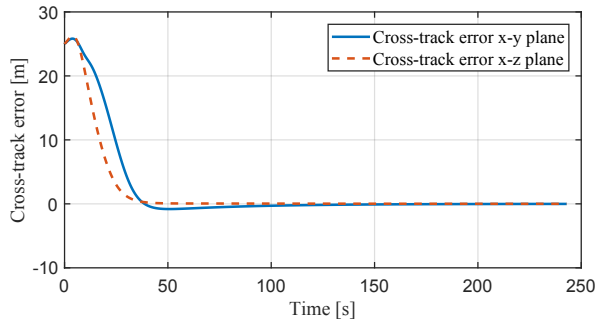


Figure 6.4: The cross-track errors y_b^n and z_b^n of the vehicle.

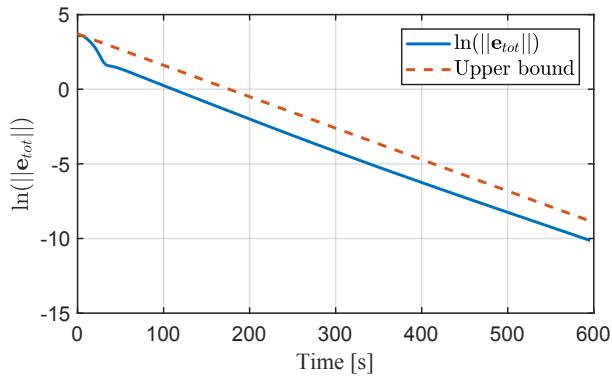


Figure 6.5: The natural logarithm of $\|e_{tot}\|$.

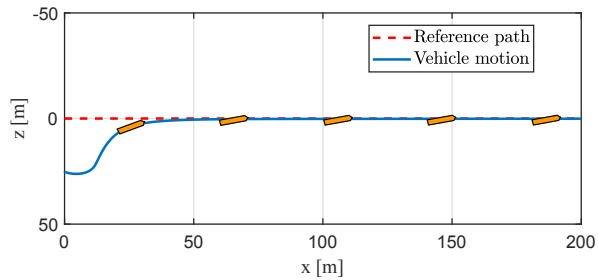


Figure 6.6: Position and pitch of the vehicle in the $x-z$ plane when W_E is unknown to the controllers.

6.5 Conclusions

In this chapter the stability properties of an underactuated underwater vehicle controlled by an ILOS guidance law have been investigated. Cascaded system analysis has been used to prove that the 5 DOF closed-loop error dynamics are USGES, and this property was shown to hold also when the vehicle is not neutrally buoyant, which is often the case in practice. Specifically, we have provided conditions on the lookahead distance, integral gain and on the constant desired surge speed in order to guarantee USGES. These conditions are stricter due to the presence of the positive or negative buoyancy term. In particular, the lookahead distance must be larger, the integral gain lower and the desired relative surge speed faster than if the vehicle were perfectly ballasted, which matches with intuition.

A negatively buoyant AUV modeled in 5 DOF has been simulated in an ocean environment containing constant and irrotational current, demonstrating exponential stability of the closed-loop error system. It is also demonstrated that the vehicle is able to follow the path, even when the negative buoyancy is unknown, which shows robustness of the system.

6.A Functional expressions

The terms X_v , Y_v , X_w , Y_w , and F_r are defined Section 3.2.2 and restated here for convenience.

$$X_v \triangleq \frac{m_{25}^2 - m_{11}m_{55}}{m_{22}m_{55} - m_{25}^2}u_b + \frac{d_{55}m_{25} - d_{25}m_{55}}{m_{22}m_{55} - m_{25}^2}, \quad (6.44)$$

$$Y_v \triangleq \frac{(m_{22} - m_{11})m_{25}}{m_{22}m_{55} - m_{25}^2}u_b - \frac{d_{22}m_{55} - d_{52}m_{25}}{m_{22}m_{55} - m_{25}^2}, \quad (6.45)$$

$$X_w \triangleq \frac{-m_{34}^2 - m_{11}m_{44}}{m_{33}m_{44} - m_{34}^2}u_b + \frac{d_{44}m_{34} - d_{34}m_{44}}{m_{33}m_{44} - m_{34}^2}, \quad (6.46)$$

$$Y_w \triangleq \frac{(m_{11} - m_{33})m_{34}}{m_{33}m_{44} - m_{34}^2}u_b - \frac{d_{33}m_{44} - d_{43}m_{34}}{m_{33}m_{44} - m_{34}^2}, \quad (6.47)$$

$$F_r \triangleq \frac{m_{25}d_{22} - m_{22}(d_{52} + (m_{22} - m_{11})u_b)}{m_{22}m_{55} - m_{25}^2}v_b + \frac{m_{25}(d_{25} + m_{11}u_b) - m_{22}(d_{55} + m_{25}u_b)}{m_{22}m_{55} - m_{25}^2}r_b. \quad (6.48)$$

The lack of neutral buoyancy is present in the terms Z_{ws} , Z_{wc} , \bar{F}_u and \bar{F}_q , which are defined as

$$Z_{ws} \triangleq \frac{(BG_zW + z_bW_E)m_{34}}{m_{33}m_{44} - m_{34}^2}, \quad (6.49)$$

$$Z_{wc} \triangleq \frac{W_E m_{44}}{m_{33}m_{44} - m_{34}^2}, \quad (6.50)$$

$$\bar{F}_u \triangleq \frac{1}{m_{11}} [(m_{22}v_b + m_{25}r_b)r_b - (m_{33}w_b + m_{34}q_b)q_b - d_{11}u_b - W_E \sin(\theta_b^n)] \quad (6.51)$$

$$\begin{aligned} \bar{F}_q \triangleq & -\frac{(BG_z W + z_b W_E) m_{33}}{m_{33}m_{44} - m_{34}^2} \sin(\theta_b^n) + \frac{W_E m_{34}}{m_{33}m_{44} - m_{34}^2} \cos(\theta_b^n) \\ & + \frac{m_{34}d_{33} - m_{33}(d_{43} - (m_{33} - m_{11})u_b)}{m_{33}m_{44} - m_{34}^2} w_b \\ & + \frac{m_{34}(d_{34} - m_{11}u_b) - m_{33}(d_{44} - m_{34}u_b)}{m_{33}m_{44} - m_{34}^2} q_b. \end{aligned} \quad (6.52)$$

The vectors $\mathbf{h}_z \triangleq [\{h_{zi}\}]^T$ and $\mathbf{h}_w \triangleq [\{h_{wi}\}]^T, i = 1..6$, are defined as

$$h_{z2} = -\sin(\tilde{\theta}_b^n + \theta_d^n) \quad (6.53)$$

$$\begin{aligned} h_{z3} = & -u_{rd} \left[\frac{\sin(\tilde{\theta}_b^n)}{\tilde{\theta}_b^n} \cos(\theta_d^n) + \frac{\cos(\tilde{\theta}_b^n) - 1}{\tilde{\theta}_b^n} \sin(\theta_d^n) \right] \\ & + w_{rb} \left[\frac{\cos(\tilde{\theta}_b^n) - 1}{\tilde{\theta}_b^n} \cos(\theta_d^n) - \frac{\sin(\tilde{\theta}_b^n)}{\tilde{\theta}_b^n} \sin(\theta_d^n) \right], \end{aligned} \quad (6.54)$$

$$h_{z1} = h_{z4} = h_{z5} = h_{z6} = 0, \quad (6.55)$$

$$\begin{aligned} h_{w2} = & \frac{X_w(\tilde{u}_{rb} + u_{rd}) - X_{wd}}{\tilde{u}_{rb}} \gamma_w(z_{\text{int}}^n, z_b^n, w_{rb}) \\ & + \frac{Y_w(\tilde{u}_{rb} + u_{rd}) - Y_{wd}}{\tilde{u}_{rb}} w_{rb} \end{aligned} \quad (6.56)$$

$$h_{w3} = Z_{ws} \left[\frac{\sin(\tilde{\theta}_b^n)}{\tilde{\theta}_b^n} \cos(\theta_d^n) + \frac{\cos(\tilde{\theta}_b^n) - 1}{\tilde{\theta}_b^n} \sin(\theta_d^n) \right] \quad (6.57)$$

$$h_{w4} = X_w(\tilde{u}_{rb} + u_{rd}), \quad (6.58)$$

$$h_{w1} = h_{w5} = h_{w6} = 0. \quad (6.59)$$

The vector $\mathbf{h}_y \triangleq [\{h_{yi}\}]^T, i = 1..9$ is defined as

$$\begin{aligned} h_{y2} = & \frac{u_{rd}}{e_{z2}} \left[\frac{\Delta_z}{\sqrt{l_z(e_{z2})}} - \frac{1}{\sqrt{\xi^2 + 1}} \right] \\ & - \frac{Z_{ws}\xi}{e_{z2}Y_{wd}\sqrt{\xi^2 + 1}} \left[\frac{e_{z2} + \sigma_z z_{\text{int}}^{\text{eq}}}{\sqrt{l_z(e_{z2})}} - \frac{\xi}{\sqrt{\xi^2 + 1}} \right], \end{aligned} \quad (6.60)$$

$$h_{y3} = \sin(\theta_b^n) \sin(\psi_b^n), \quad (6.61)$$

$$h_{y4} = \cos(\theta_b^n) \sin(\psi_b^n), \quad (6.62)$$

$$\begin{aligned} h_{y6} = & u_{rd} \sin(\psi_d^n) \left[\frac{\cos(\tilde{\theta}_b^n) - 1}{\tilde{\theta}_b^n} \cos(\theta_d^n) - \frac{\sin(\tilde{\theta}_b^n)}{\tilde{\theta}_b^n} \sin(\theta_d^n) \right] \\ & - \frac{Z_{ws}\xi \sin(\psi_d^n)}{Y_{wd}\sqrt{\xi^2 + 1}} \left[\frac{\sin(\tilde{\theta}_b^n)}{\tilde{\theta}_b^n} \cos(\theta_d^n) + \frac{\cos(\tilde{\theta}_b^n) - 1}{\tilde{\theta}_b^n} \sin(\theta_d^n) \right] \end{aligned} \quad (6.63)$$

$$h_{y8} = \left[u_{rd} \cos(\tilde{\theta}_b^n + \theta_d^n) - \frac{Z_{ws}\xi}{Y_{wd}\sqrt{\xi^2 + 1}} \sin(\tilde{\theta}_b^n + \theta_d^n) \right] \cdot \left[\frac{\sin(\tilde{\psi}_b^n)}{\tilde{\psi}_b^n} \cos(\psi_d^n) + \frac{\cos(\tilde{\psi}_b^n) - 1}{\tilde{\psi}_b^n} \sin(\psi_d^n) \right] \quad (6.64)$$

$$+ v_{rb} \left[\frac{\cos(\tilde{\psi}_b^n) - 1}{\tilde{\psi}_b^n} \cos(\psi_d^n) - \frac{\sin(\tilde{\psi}_b^n)}{\tilde{\psi}_b^n} \sin(\psi_d^n) \right] \\ h_{y1} = h_{y4} = h_{y7} = h_{y9} = 0. \quad (6.65)$$

The terms in $\mathbf{h}_v \triangleq [\{h_{vi}\}]^T, i = 1..9$ are defined as

$$h_{v2} = \frac{X_{vd}}{e_{z2}} \left[\frac{\Delta_z}{\sqrt{l_z(e_{z2})}} - \frac{1}{\xi^2 + 1} \right] \gamma_v(y_{\text{int}}^n, y_b^n, v_{rb}), \quad (6.66)$$

$$h_{v5} = \frac{X_v(\tilde{u}_{rb} + u_{rd}) - X_{vd}}{\tilde{u}_{rb}} \cos(\tilde{\theta}_b^n + \theta_d^n) \gamma_v(y_{\text{int}}^n, y_b^n, v_{rb}) \\ + v_{rb} \frac{Y_v(\tilde{u}_{rb} + u_{rd}) - Y_{vd}}{\tilde{u}_{rb}} \quad (6.67)$$

$$h_{v6} = \left[\frac{\cos(\tilde{\theta}_b^n) - 1}{\tilde{\theta}_b^n} \cos(\theta_d^n) - \frac{\sin(\tilde{\theta}_b^n)}{\tilde{\theta}_b^n} \sin(\theta_d^n) \right] \\ \cdot X_{vd} \gamma_v(y_{\text{int}}^n, y_b^n, v_{rb}), \quad (6.68)$$

$$h_{v9} = X_v(\tilde{u}_{rb} + u_{rd}) \cos(\tilde{\theta}_b^n + \theta_d^n), \quad (6.69)$$

$$h_{v1} = h_{v3} = h_{v4} = h_{v7} = h_{v8} = 0. \quad (6.70)$$

6.B Proof of Lemma 6.2

The proof follows along the lines of Caharija et al. [18], while making use of Theorem 2.1 to show that the conditions of Lemma 6.2 are sufficient for USGES.

Consider the Lyapunov function candidate:

$$V \triangleq \frac{1}{2} \sigma_z^2 e_{z1}^2 + \frac{1}{2} e_{z2}^2 + \frac{1}{2} \mu e_{z3}^2, \quad \mu > 0. \quad (6.71)$$

Using (6.31) and Assumptions 6.2 and 6.3, the following bound can be found for \dot{V} :

$$\dot{V} \leq -W_1(\mathbf{e}_{z13}) - W_2(\mathbf{e}_{z23}), \quad (6.72)$$

where $\mathbf{e}_{z13} \triangleq [|\mathbf{e}_{z1}|, |\mathbf{e}_{z3}|]^T$ and $\mathbf{e}_{z23} \triangleq [|\mathbf{e}_{z2}|, |\mathbf{e}_{z3}|]^T$.

The function W_1 is defined as

$$W_1 = \frac{1}{l_z(e_{z2})} \mathbf{e}_{z13}^T \mathbf{Q}_1 \mathbf{e}_{z13}, \quad (6.73)$$

where \mathbf{Q}_1 is

$$\mathbf{Q}_1 \triangleq \begin{bmatrix} \sigma_z^3 \Delta_z & -\frac{\mu \sigma_z^2 \sqrt{l_z(e_{z2})} |X_{wd}|}{2 \Delta_z} \\ -\frac{\mu \sigma_z^2 \sqrt{l_z(e_{z2})} |X_{wd}|}{2 \Delta_z} & \mu \eta l_z(e_{z2}) \left(|Y_{wd}| - \frac{|X_{wd}|}{\Delta_z} \right) \end{bmatrix} \quad (6.74)$$

and $0 < \eta < 1$. W_2 is defined as

$$W_2 \triangleq \frac{\Delta_z}{l_z(e_{z2})} e_{z23}^T \mathbf{Q}_2 e_{z23}, \quad (6.75)$$

where \mathbf{Q}_2 is

$$\mathbf{Q}_2 \triangleq \begin{bmatrix} \beta & -\alpha \sqrt{l_z(e_{z2})} \\ -\alpha \sqrt{l_z(e_{z2})} & l_z(e_{z2}) \frac{\alpha(2\alpha-1)}{\beta} \end{bmatrix}. \quad (6.76)$$

Here, $\beta \triangleq u_{rd} - V_{\max} - \sigma_z$ and α is given by

$$\alpha \triangleq (1 - \eta) \frac{(u_{rd} - V_{\max} - \sigma_z)(\Delta_z |Y_{wd}| - |X_{wd}|)}{|X_{wd}|(u_{rd} + V_{\max} + \sigma_z + \Delta_z \frac{2|Z_{ws}| + |Z_{wc}|}{|X_{wd}|})}. \quad (6.77)$$

The parameter μ is chosen as

$$\mu \triangleq \frac{2\alpha - 1}{\frac{|X_{wd}|}{\Delta_z^2}(u_{rd} + V_{\max} + \sigma_z) + \frac{2|Z_{ws}| + |Z_{wc}|}{\Delta_z}}. \quad (6.78)$$

If \mathbf{Q}_1 and \mathbf{Q}_2 are positive definite, then \dot{V} is negative definite. \mathbf{Q}_1 is positive definite if

$$\Delta_z > \frac{|X_{wd}|}{|Y_{wd}|}, \quad (6.79)$$

$$\mu < \frac{4\eta \Delta_z^2 (\Delta_z |Y_{wd}| - |X_{wd}|)}{\sigma_z |X_{wd}|^2}. \quad (6.80)$$

(6.79) is met as long as (6.16) holds. It can be shown that $\eta \geq 1/5$ is a sufficient condition for μ to satisfy (6.80). Thus, without loss of generality, η is set to $1/5$, and positive definiteness of \mathbf{Q}_1 is ensured.

\mathbf{Q}_2 is positive definite if $\beta > 0$ and $\alpha > 1$. Assumption 6.5 and (6.18) ensure that $\beta > 0$, while conditions (6.16) and (6.18) ensure that $\alpha > 1$. Note that the presence of the buoyancy term Z_{wc} in \mathbf{Q}_2 influences the requirements on u_{rd} in Assumption 6.5, Δ_z in (6.16), and σ_z in (6.18).

Let \mathbf{Q} be the symmetric 3×3 matrix defined from $W_1(e_{z13})$ and $W_2(e_{z23})$ so that

$$e_z^T \mathbf{Q} e_z = W_1(e_{z13}) + W_2(e_{z23}). \quad (6.81)$$

Since both \mathbf{Q}_1 and \mathbf{Q}_2 are positive definite, so is \mathbf{Q} . Hence, the following bound holds:

$$\dot{V} \leq -\frac{1}{l(e_2)} q_{\min} \|e_z\|^2, \quad (6.82)$$

where $q_{\min} \triangleq \lambda_{\min}(\mathbf{Q})$, the minimum eigenvalue of \mathbf{Q} .

The function $1/l_z(e_{z2})$ can be bounded by bounding $\sigma_z z_{\text{int}}^{\text{eq}}$ using (6.22a):

$$\sigma_z z_{\text{int}}^{\text{eq}} = \frac{\xi}{\Delta_z} < \frac{\xi_{\text{sup}}}{\Delta_z} := \kappa, \quad (6.83)$$

where ξ_{sup} is the upper bound of ξ from Section 6.3.1. In any ball

$$\mathcal{B}_r \triangleq \{|e_{z2}| < r\}, r > 0 \quad (6.84)$$

the function $l_z(e_{z2})$ is upper bounded as

$$l_z(e_{z2}) \leq (r + \kappa)^2 + \Delta_z^2 := c(r). \quad (6.85)$$

Hence, for any $r > 0$

$$\dot{V} \leq -\frac{q_{\min}}{c(r)} \|e_z\|^2 \quad (6.86)$$

Thus, the conditions of Theorem 2.1 is fulfilled with $k_1 = \frac{1}{2} \min\{\sigma_z^2, 1, \mu\}$, $k_2 = \frac{1}{2} \max\{\sigma_z^2, 1, \mu\}$ and $k_3 = \frac{q_{\min}}{c(r)}$. Hence, the equilibrium point $e_z = \mathbf{0}$ is USGES as defined in Definition 2.5.

Part III

Collision Avoidance in 2D

Chapter 7

The CAA Algorithm in 2D

If this goes badly and I make a crater, I want it named after me!

— Iain M. Banks, *Against a Dark Background*

Part III of this thesis focuses on the constant avoidance angle (CAA) algorithm in 2 dimensions. In this chapter, we will present the CAA algorithm itself, along with a preliminary analysis. In Chapters 8-10 we will provide an analysis of the algorithm when applied to systems of increasing complexity.

The algorithm will make the vehicle avoid an obstacle by steering the vehicle so that its velocity vector keeps a constant avoidance angle to the obstacle. In the case of a moving obstacle, a compensation term will be added to the avoidance angle in order to ensure that the vehicle behavior with respect to the obstacle remains the same. The compensation angle is calculated using the current vehicle speed as input, which provides flexibility both when designing the desired speed trajectory, and when implementing the algorithm on vehicles with a limited speed envelope.

The vehicle will be in one of two modes during the operation. In *nominal guidance mode*, the vehicle will follow a guidance law in order to reach a nominal goal, such as target reaching or path following. In *collision avoidance mode*, the vehicle will follow the heading references from the CAA algorithm. In order to switch between these two modes, we will introduce an unsafe vision cone. If the obstacle is too close and the desired velocity direction from the nominal guidance law is within this cone, the vehicle will enter collision avoidance mode. If the desired direction from guidance comes outside this cone, nominal guidance is resumed. The switching criterion is described in detail in this chapter, while example guidance laws will be specified in Chapters 8-10.

Finally, we will in this chapter provide a preliminary analysis of the CAA algorithm. We will prove that a vehicle following the references of the algorithm is ensured to safely avoid a moving obstacle, even though the obstacle may not be cooperating.

In Part II, we considered the effect of ocean current on the vehicle during path following. When looking at collision avoidance, however, we limit the scope to omit such disturbances, focusing on the behavior of the vehicle under ideal conditions.¹ Similarly, while we are concerned with keeping the measurement requirements of

¹Note, that the kinematic disturbance used to model the current in Part II is inherently handled when using course control as described in Chapters 9 and 10.

the algorithm as low as possible, the area of obstacle detection and tracking is not included.

In Section 7.1 of this chapter we describe the mathematical model of the obstacle, as well as the obstacle measurements required by the algorithm. Section 7.2 defines the algorithm, including the rule for choosing when to enter and leave collision avoidance mode and whether to take a port or starboard maneuver. In Section 7.3, we perform a preliminary analysis of the algorithm, proving that a vehicle that has turned soon enough and is able to follow the references from the collision avoidance law will perform a safe collision avoidance maneuver. Finally, in Section 7.4, we conclude this chapter with an overview of the remainder of Part III

The work presented in this chapter is based on Wiig et al. [114], Wiig et al. [113] and Wiig et al. [119].

7.1 Obstacle model

In this section we will describe the obstacle model, as well as the obstacle measurements required to implement the collision avoidance algorithm described in Section 7.2.

The obstacle is modeled as a moving circular domain \mathcal{D}_o with radius R_o , and we define the obstacle frame o to be attached to the center of the domain. Since it can be difficult to estimate the dynamic parameters of the obstacle, it is modeled as a unicycle-type vehicle:

$$\dot{x}_o^n = u_o \cos(\psi_o^n), \quad (7.1a)$$

$$\dot{y}_o^n = u_o \sin(\psi_o^n), \quad (7.1b)$$

$$\dot{\psi}_o^n = r_o, \quad (7.1c)$$

$$\dot{u}_o = a_o, \quad (7.1d)$$

where x_o^n and y_o^n are the Cartesian coordinates of the obstacle, u_o and a_o are the forward speed and acceleration, and ψ_o^n and r_o are the obstacle heading and yaw rate, respectively. The obstacle's position is denoted $\mathbf{p}_o^n \triangleq [x_o^n, y_o^n]^T$, while the obstacle's velocity is denoted $\mathbf{v}_{o/n}^n \triangleq \dot{\mathbf{p}}_o^n$.

The proposed collision avoidance algorithm can also be applied to non-circular obstacles. An analysis of such scenarios is beyond the scope of this thesis, but successful avoidance of noncircular obstacles are demonstrated in simulations in Chapters 8-10.

To ensure that the vehicle is able to circumvent the obstacle, we need to assume that the obstacle speed is less than the vehicle surge speed:

Assumption 7.1. The obstacle forward speed u_o satisfies $u_o \in [0, u_{o\max}]$, where $u_{o\max} < u_b$.

We also assume that the obstacle has a bounded acceleration and yaw rate:

Assumption 7.2. The obstacle forward acceleration a_o and yaw rate r_o are bounded by

$$a_o \in [-a_{o\max}, a_{o\max}], \quad (7.2)$$

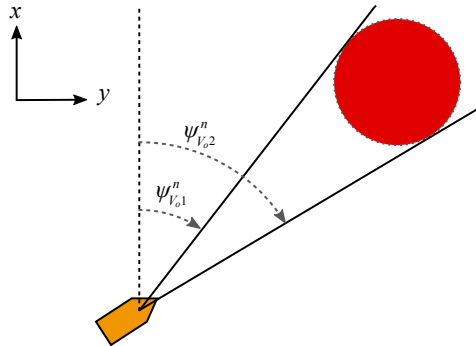


Figure 7.1: The vision cone \mathcal{V}_o from the vehicle to the obstacle.

$$r_o \in [-r_{o\max}, r_{o\max}], \quad (7.3)$$

where $a_{o\max} \geq 0$ and $r_{o\max} \geq 0$ are constant parameters.

If Assumptions 7.1 and 7.2 do not hold, it is in general impossible to guarantee obstacle avoidance without assuming that the obstacle is cooperating. However, by choosing to move behind a moving obstacle, it will in practice still be possible to execute a successful avoidance maneuver. Analysis of such scenarios is beyond the scope of this thesis.

7.1.1 Required obstacle measurements

In order to decide when to start an avoidance maneuver, the vehicle must be able to sense the distance $d_{ob} \triangleq \|\mathbf{p}_b^n - \mathbf{p}_o^n\|$ to the obstacle. To obtain a safe course, the vehicle must furthermore be able to sense the vision cone \mathcal{V}_o to the obstacle, as illustrated in Figure 7.1. Specifically, the angles $\psi_{V_o,1}^n$ and $\psi_{V_o,2}^n$ to the edges of the \mathcal{V}_o are required. Finally, the vehicle must know the obstacle velocity $\mathbf{v}_{o/n}^n$ in order to compensate for it.

The obstacle distance d_{ob} and the vision cone can be readily obtained from sensors such as a lidar, radar or sonar. If the sensor has Doppler capabilities, the obstacle velocity is available as well. Otherwise, the obstacle velocity can be obtained by using a tracking algorithm.

7.2 Algorithm definition

In this section we will describe the proposed CAA algorithm for collision avoidance. We define that the control system will be either in nominal guidance mode, where it follows a nominal guidance law, like the integral line of sight guidance law described

in Part II, or in collision avoidance mode². The control system will enter collision avoidance mode if the vehicle comes at risk of colliding with an obstacle, according to a criterion we will define in Section 7.2.2. The CAA algorithm will then make the vehicle circumvent the obstacle by steering the vehicle outside of the vision cone \mathcal{V}_o defined in Section 7.1.1. Specifically, by maintaining a constant avoidance angle α_o to the vision cone, it is ensured that the vehicle will not come within a specified minimum distance of the obstacle. If the obstacle is moving, a compensation term is added to the avoidance angle.

The desired heading during collision avoidance, including the compensation for the obstacle velocity, is described in detail in Section 7.2.1 below. The rules for entering and leaving collision avoidance mode are given in Section 7.2.2, while finally an example rule for deciding if the vehicle should move to the port or starboard side of the obstacle is given in Section 7.2.3.

7.2.1 Safe heading references

To create heading references that will safely avoid the obstacle, the CAA algorithm extends the vision cone \mathcal{V}_o by $\pm\alpha_o$ to either side. Thus, an extended vision cone \mathcal{V}_e is created, as shown in Figure 7.2. The heading angles of the extended vision cone edges are denoted $\psi_{V_e1}^n$ and $\psi_{V_e2}^n$. Two velocity vectors, $\mathbf{v}_{V_e1}^n$ and $\mathbf{v}_{V_e2}^n$, are defined along the edges of the \mathcal{V}_e :

$$\mathbf{v}_{V_ej}^n \triangleq u_{\alpha_o} [\cos(\psi_{V_ej}^n), \sin(\psi_{V_ej}^n)], \quad j = \{1, 2\}, \quad (7.4)$$

where the length of the vectors, $u_{\alpha_o} > 0$, will be defined later.

If the obstacle is moving, each edge of the extended vision cone will be rotated around the origin of b in order to compensate for the obstacle velocity. Thus, in a reference frame aligned with n but moving with the obstacle, the course references of the CAA algorithm will follow $\mathbf{v}_{V_ej}^n$. The rotated edges define a new, compensated vision cone \mathcal{V}_c , which is illustrated in Figure 7.3. Two velocity vectors are defined along the edges of \mathcal{V}_c as

$$\mathbf{v}_{dcaj}^n \triangleq \mathbf{v}_{V_ej}^n + \mathbf{v}_{o/n}^n, \quad j = \{1, 2\}. \quad (7.5)$$

The velocity vectors \mathbf{v}_{dcaj}^n will keep the constant avoidance angle α_o to the obstacle, and will hence be used as candidates for the desired vehicle velocity in collision avoidance mode. Therefore, their lengths are set to the current vehicle speed $U_b = \sqrt{u_b^2 + v_b^2}$, where u_b is the vehicle surge speed and v_b is the vehicle's sway speed as described in Section 3.1.

$$\|\mathbf{v}_{dcaj}^n\| \triangleq U_b. \quad (7.6)$$

²When the vehicle is in collision avoidance mode, the integral effect of the ILOS guidance law should be disabled during the avoidance maneuver. As we do not investigate collision avoidance in the presence of current in this thesis, we will only examine the performance of the algorithm in combination with line-of-sight guidance without integral effect, as well as a simple target reaching algorithm described in the subsequent chapters.

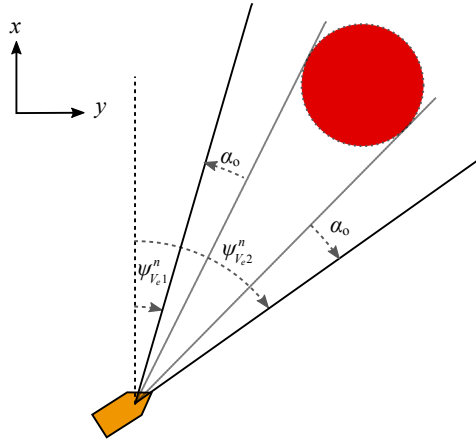


Figure 7.2: The extended vision cone \mathcal{V}_e from the vehicle to the obstacle.

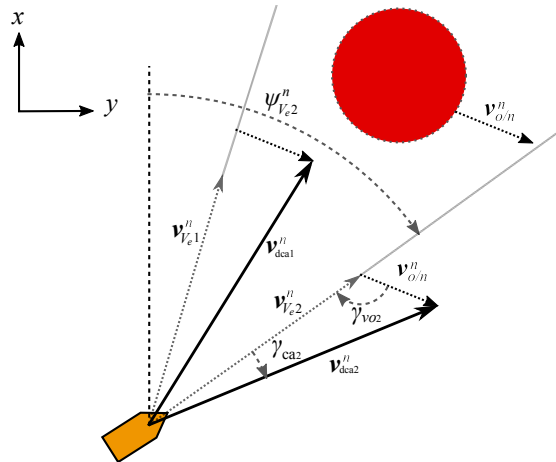


Figure 7.3: The desired velocity vector candidates \mathbf{v}_{dca1}^n and \mathbf{v}_{dca2}^n , which define the sides of the compensated vision cone \mathcal{V}_c .

The compensation angle γ_{caj} is found using the sine rule on the triangle defined by $\mathbf{v}_{V_{ej}}^n$, $\mathbf{v}_{o/n}^n$ and \mathbf{v}_{dcaj}^n :

$$\gamma_{caj} = \sin^{-1} \left(\frac{\|\mathbf{v}_{o/n}^n\| \sin(\gamma_{voj})}{U_b} \right), \quad j = \{1, 2\}. \quad (7.7)$$

where $\|\mathbf{v}_{o/n}^n\| = u_o$ as seen in (7.1). The angle γ_{voj} is found geometrically as

$$\gamma_{voj} = \pi - (\psi_o^n - \psi_{V_{ej}}^n), \quad j = \{1, 2\}. \quad (7.8)$$

The two candidate heading angles in collision avoidance mode are then defined as

$$\psi_{dcaj}^n \triangleq \psi_{V_{ej}}^n + \gamma_{caj}, \quad j = \{1, 2\}. \quad (7.9)$$

Section 7.2.3 provides a rule for choosing between these two candidates.

The definition of the obstacle velocity compensation angle uses the current vehicle speed. Thus, the definition of the collision avoidance heading angles (7.9) provides safe vehicle headings at any vehicle speed, as long as (7.7) is well defined, which is ensured by Assumption 7.1. In this way, the vehicle speed is used as an input rather than an output of the algorithm, which provides flexibility in designing the vehicle speed trajectory. We will exploit this flexibility both to include a strict requirement of a constant vehicle forward speed in Chapters 8-10, and by including the underactuated sway component of the vehicle speed in Chapters 9 and 10.

7.2.2 Switching rule

The compensated vision cone \mathcal{V}_c is used to define a set of unsafe directions. Thus, we define that the control system enters collision avoidance mode at a time t_1 if the vehicle is too close to the obstacle while the desired heading given by the guidance law, denoted ψ_{dg}^n , is within \mathcal{V}_c :

$$\psi_{dg}^n(t_1) \in \mathcal{V}_c(t_1), \quad (7.10a)$$

$$d_{ob}(t_1) \leq d_{switch}, \quad (7.10b)$$

where $d_{switch} > d_{safe}$ is a constant design parameter.

Nominal guidance towards the target will resume at a time t_2 when $\psi_{dg}^n(t_2)$ moves outside $\mathcal{V}_c(t_2)$,

$$\psi_{dg}^n(t_2) \notin \mathcal{V}_c(t_2). \quad (7.11)$$

To avoid making the vehicle heading cross \mathcal{V}_c when approaching ψ_{dg}^n , we require that ψ_{dg}^n is on the same side of \mathcal{V}_c as the vehicle course when exiting collision avoidance:

$$\begin{aligned} j = 1 : \psi_{dg}^n(t_2) - \psi_{dca1}^n(t_2) &\leq 0, \\ j = 2 : \psi_{dg}^n(t_2) - \psi_{dca2}^n(t_2) &\geq 0. \end{aligned} \quad (7.12)$$

The angular difference is mapped to the interval

$$(\psi_{dg}^n(t_2) - \psi_{dcaj}^n(t_2)) \in (-\pi, \pi], \quad j = \{1, 2\}, \quad (7.13)$$

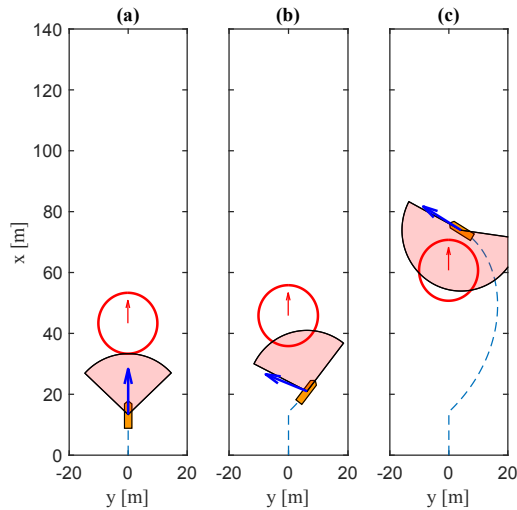


Figure 7.4: Illustration of the switching rule. The vehicle (orange) encounters an obstacle (red circle). The compensated vision cone \mathcal{V}_c is drawn in a transparent red, the obstacle velocity is shown as a red arrow and the desired heading provided by the guidance law is shown as a blue arrow.

which ensures that the vehicle makes the shortest turn towards the desired course.

The switching rule is illustrated in an overtaking scenario in Figure 7.4. In Figure 7.4(a), the vehicle comes too close to an obstacle on collision course and enters collision avoidance. In Figure 7.4(b), the desired course from guidance is outside the vision cone, but the vehicle has to cross \mathcal{V}_c to reach it. Hence, the control system remains in collision avoidance mode. In Figure 7.4(c), the desired heading from guidance is safe, and the control system enters nominal guidance mode.

7.2.3 Turning direction

The proposed CAA algorithm (7.9) provides two candidate headings for safe maneuvering, resulting in either a clockwise or counterclockwise collision avoidance maneuver. Both of the candidates are safe, which provides flexibility to consider different scenario preferences or traffic rules. In this thesis, we will use a conservative approach, where we make the vehicle move behind the obstacle. Specifically, at a time t_1 at which the control system enters collision avoidance, the turning parameter j is chosen according to:

$$j = \arg \max_{j=1,2} |\psi_o^n(t_1) - \psi_{dcaj}^n(t_1)|, \quad d_{ob}(t_1) = d_{\text{switch}}. \quad (7.14)$$

The difference between the obstacle heading and ψ_{dcaj}^n are mapped to the interval $(-\pi, \pi]$. If the obstacle is closer than d_{switch} when the vehicle enters collision

avoidance mode, the vehicle will make the shortest turn towards a safe direction,

$$j = \arg \min_{j=1,2} |\psi_b^n(t_1) - \psi_{dcaj}^n(t_1)|, \quad d_{ob}(t_1) < d_{switch}. \quad (7.15)$$

Once a turning direction has been chosen, it is kept throughout the collision avoidance maneuver in order to avoid chattering due to measurement noise.

Remark 7.1. An alternative approach is to choose the turning direction to comply with the International regulations for preventing collisions at sea (COLREGs), as in Kuwata et al. [60] and Moe and Pettersen [74]. The vehicle would then turn to starboard when the obstacle comes from starboard, when the obstacle comes head on, or if the vehicle overtakes the obstacle from behind. If the obstacle approaches from the port side, the vehicle would not yield, i.e. the control system would not enter collision avoidance mode.

7.2.4 Multiple obstacles

The proposed CAA algorithm can be extended to multiple obstacles. While a thorough analysis of a multiobstacle scenario is beyond the scope of this thesis, we will in this section present a rule for using the CAA algorithm to safely navigate clusters of obstacles.

We create a compensated vision cone for each obstacle closer to the vehicle than d_{switch} . If any of these cones overlap, they are merged into a single cone. When the control system enters collision avoidance mode, there might thus be more than one obstacle in the current unsafe cone. The closest obstacle is then used to choose the turning direction according to (7.14).

If a new obstacle joins the cone currently used for avoidance during the maneuver, the cone is extended to include the new obstacle. The vehicle will keep the turning direction, and will follow the corresponding edge of the new vision cone.

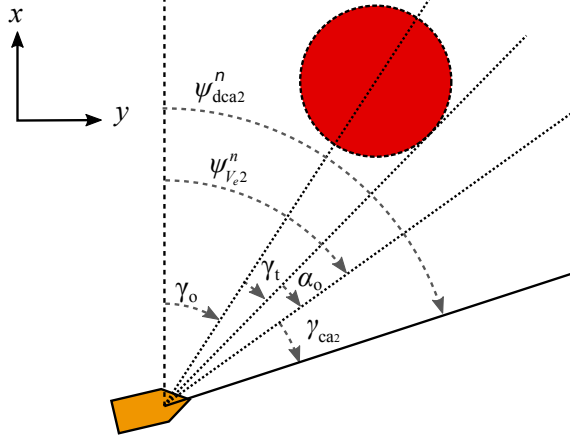
Examples of multiobstacle scenarios are presented in the experimental results in Chapter 10.

7.3 Algorithm analysis

We will here present a preliminary analysis of the CAA algorithm, proving that a vehicle following the heading references defined in (7.9) will always maintain at least a minimum distance to the obstacle. We will prove this for a static obstacle in Lemma 7.1, before including obstacle motion in Lemma 7.2.

Lemma 7.1. *Consider a static obstacle, and let the avoidance angle be in the interval $\alpha_o \in (0, \frac{\pi}{2})$. Furthermore, let a vehicle maintain the velocity $\mathbf{v}_{V_{e_j}}^n$ (7.4) for $j = 1$ or $j = 2$, for $t \geq t_1$ and with a positive speed $u_{\alpha_o} = U_b > 0$. Then, if $d_{ob}(t_1) \geq 0$, the vehicle will converge to a circle \mathcal{C} with center at the obstacle center and radius $R_c = \frac{R_o}{\cos(\alpha_o)}$. Furthermore, if the vehicle starts outside \mathcal{C} , then*

$$d_{ob}(t) \geq d_{min} \triangleq \frac{R_o}{\cos(\alpha_o)} - R_o, \quad \forall t \in [t_1, t_2], \quad (7.16)$$


 Figure 7.5: Decomposition of the angle ψ_{dca2}^n .

where $t_2 > t_1$ is the time when the vehicle exits collision avoidance in accordance with the switching rule in (7.11) and (7.12).

Proof. When maintaining the velocity $\mathbf{v}_{V_ej}^n$, the vehicle will keep a constant avoidance angle α_o to one of the tangents from the vehicle to the obstacle, as shown in Figure 7.2. The time derivative of d_{ob} can then be found geometrically as

$$\dot{d}_{ob} = -u_{\alpha_o} \cos(\gamma_t + \alpha_o), \quad (7.17)$$

where γ_t is the angle from the line connecting the vehicle and the center of the obstacle to the tangent line as seen in Figure 7.5:

$$\gamma_t \triangleq \sin^{-1} \left(\frac{R_o}{R_o + d_{ob}} \right), \quad d_{ob} \geq 0. \quad (7.18)$$

When $d_{ob} > d_{\min}$, we obtain $\gamma_t + \alpha_o < \frac{\pi}{2}$, which gives $\dot{d}_{ob} < 0$. Similarly, when $d_{ob} < d_{\min}$, $\dot{d}_{ob} > 0$. Finally, when $d_{ob} = d_{\min}$, $\dot{d}_{ob} = 0$. Hence, the vehicle will converge to \mathcal{C} , and if $d_{ob}(t_1) > d_{\min}$ then $d_{ob}(t) \geq d_{\min} \forall t \geq t_0$. \square

The proof of Lemma 7.1 is illustrated in Figure 7.6, which shows the output of the CAA law as a vector field. The arrows of the field show the direction of $\mathbf{v}_{V_e1}^n$, i.e. when the turning direction $j = 1$. The field can be seen to converge to the black circle \mathcal{C} around the red obstacle. The dotted black line shows an integral curve of the field, which converges to \mathcal{C} in an equiangular spiral.

It follows from Lemma 7.1 that if the avoidance angle α_o is chosen to satisfy

$$\alpha_o \in \left[\cos^{-1} \left(\frac{R_o}{R_o + d_{\text{safe}}} \right), \pi/2 \right), \quad d_{\text{safe}} > 0, \quad (7.19)$$

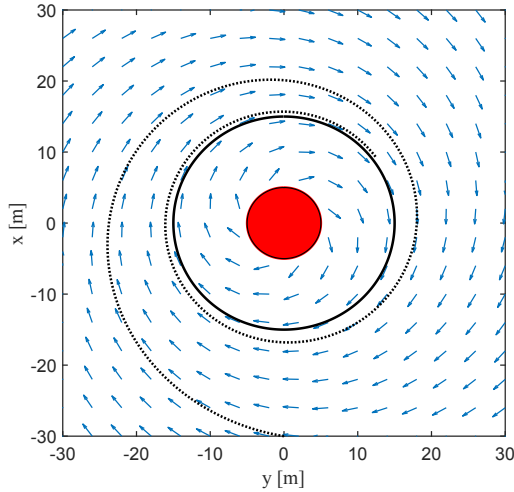


Figure 7.6: A vector field showing the output from the CAA algorithm when the turning direction $j = 1$ as a vector field. The red circle is the obstacle, the black circle represents d_{\min} and the dotted black line shows an example integral curve of the field.

then, under the conditions that the obstacle is static, the vehicle starts outside \mathcal{C} and keeps the velocity $\mathbf{v}_{V_ej}^n$ (7.4),

$$d_{ob}(t) \geq d_{\text{safe}} \quad \forall t \geq t_0. \quad (7.20)$$

Thus, if knowledge of the obstacle curvature is available, it is possible to design the avoidance angle in order to assure that the vehicle will keep at least a minimum safety distance d_{safe} from the obstacle during the maneuver. The next lemma shows that this also applies for a moving obstacle.

Lemma 7.2. *Consider an obstacle moving with a time-varying velocity satisfying Assumption 7.1. Let the avoidance angle satisfy (7.19), and let a vehicle maintain the velocity \mathbf{v}_{dcaj}^n (7.5), where $\|\mathbf{v}_{dcaj}^n\| = U_b$ and the heading of \mathbf{v}_{dcaj}^n is defined in (7.9) for $j = 1$ or $j = 2$ and $t \geq t_1$. Then, if $d_{ob}(t_1) \geq d_{\text{safe}}$,*

$$d_{ob}(t) \geq d_{\text{safe}} \quad \forall t \in [t_1, t_2], \quad (7.21)$$

where $t_2 > t_1$ is the time when the vehicle exits collision avoidance in accordance with the switching rule in (7.11) and (7.12).

Proof. Consider a coordinate frame n_o which is attached to the obstacle and aligned with the n frame. Thus, the frame n_o has the velocity $\mathbf{v}_{n_o/n}^n = \mathbf{v}_{o/n}^n$. In this frame, the obstacle is static and the vehicle velocity is

$$\mathbf{v}_{b/n_o}^{n_o} = \mathbf{v}_{b/n}^n - \mathbf{v}_{o/n}^n = \mathbf{v}_{V_ej}^n, \quad (7.22)$$

where $\|\mathbf{v}_{Vej}^n\| = u_{\alpha_o}$ (7.4). From Figure 7.3, it can be seen that u_{α_o} achieves minimum when $\gamma_{voj} = 0$, for which

$$u_{\alpha_o, \min} = U_b - u_o. \quad (7.23)$$

Since $u_o < U_b$ by Assumption 7.1, $u_{\alpha_o, \min} > 0$. Lemma 7.1 and the bound (7.19) can then be applied, and it follows that the vehicle will remain at least a minimum safety distance away from the obstacle:

$$d_{ob}(t) \geq d_{\text{safe}} \quad \forall t \in [t_1, t_2]. \quad (7.24)$$

□

7.4 Overview of Part III

In this chapter, we have presented the constant avoidance angle algorithm in 2D, and performed a preliminary analysis of the algorithm. Specifically, Lemma 7.1 guarantees that if the vehicle is able to start the collision avoidance maneuver soon enough to be able to turn away from the obstacle before reducing the obstacle distance to below d_{safe} , and if the vehicle is able to follow the desired heading (7.9) from the collision avoidance law, then it will maintain a greater distance than d_{safe} throughout the maneuver. Since the vehicle moves faster than the obstacle, it will eventually have circumvented it. Hence, for a well-defined nominal guidance law, it is ensured that the vehicle will eventually exit collision avoidance mode and proceed with its nominal operation. The transfer from collision avoidance to nominal guidance will be formally analyzed in the remaining chapters of Part III.

To determine the minimum switching distance we can require of the vehicle, we need to look at how fast the vehicle is able to turn, and how close to the obstacle the vehicle will get while turning. Similarly, knowledge of the maneuvering capabilities of the vehicle is required in order to ensure that the vehicle is able to follow the references from the collision avoidance law, and that these references remain well defined throughout the maneuver. In the next chapter, we will investigate the performance of the algorithm when applied to a unicycle, where only kinematics are considered. We will then, in Chapter 9, include the underactuated dynamics of a marine vehicle steered by a rudder and propeller, before we in Chapter 10 include the full 3 DOF maneuvering model of an underactuated marine vehicle.

Chapter 8

The CAA Algorithm for Unicycles

Now, that's what I call a close encounter.

— Will Smith, *Independence Day*

The CAA algorithm presented in the previous chapter will in this chapter be applied to a unicycle, which we will model at the kinematic level. The unicycle has a limited turning rate and is required to keep a constant forward speed. The unicycle model and constraints are used to derive conditions under which it is mathematically guaranteed that a moving, non-cooperating obstacle will be avoided. We will find both the distance to the obstacle at which the vehicle, at the latest, must start to turn away, and an upper bound on the yaw rate required of the unicycle during the maneuver. The results are validated through simulations, including a scenario with an obstacle of a more complex, concave shape.

The remainder of this chapter is organized as follows. Section 8.1 describes the vehicle model and the control objective of the system. Section 8.2 states the heading controller and the target reaching guidance law employed when the vehicle is not in collision avoidance mode. Section 8.3 reiterates the CAA collision avoidance algorithm, before the conditions under which collision avoidance can be mathematically proved is derived in Section 8.4. The analysis is supported by simulations in Section 8.5. Finally, concluding remarks are given in Section 8.6.

The work presented in this chapter is based on Wiig et al. [114].

8.1 System description

The vehicle is modeled as a kinematic unicycle-type vehicle. Hence, we use the model described in Section 3.1.1, with the sway speed set to zero:

$$\dot{x}_b^n = u_b \cos(\psi), \quad (8.1a)$$

$$\dot{y}_b^n = u_b \sin(\psi), \quad (8.1b)$$

$$\dot{\psi}_b^n = r_b, \quad (8.1c)$$

Assumption 8.1. The vehicle forward speed $u_b > 0$ is constant.

Assumption 8.2. The heading rate r_b is directly controlled, and bounded by

$$r_b \in [-r_{\max}, r_{\max}], \quad (8.2)$$

where $r_{\max} > 0$ is a constant parameter.

8.1.1 Obstacle model

Recall from Section 7.1 that the obstacle is modeled as a unicycle-type, circular vehicle of radius R_o :

$$\dot{x}_o^n = u_o \cos(\psi_o^n), \quad (8.3a)$$

$$\dot{y}_o^n = u_o \sin(\psi_o^n), \quad (8.3b)$$

$$\dot{\psi}_o^n = r_o, \quad (8.3c)$$

$$\dot{u}_o = a_o, \quad (8.3d)$$

where the obstacle yaw rate and acceleration are limited:

Assumption 8.3. The obstacle forward acceleration a_o and course rate r_o are bounded by

$$a_o \in [-a_{o\max}, a_{o\max}], \quad (8.4)$$

$$r_o \in [-r_{o\max}, r_{o\max}], \quad (8.5)$$

where $a_{o\max} \geq 0$ and $r_{o\max} \geq 0$ are constant parameters.

As in Chapter 7, we assume that the obstacle speed is upper bounded by the vehicle speed:

Assumption 8.4. The obstacle forward speed u_o satisfies $u_o \in [0, u_{o\max}]$, where $u_{o\max} < u_b$.

8.1.2 Control objective

Let $\mathbf{p}_t^n \triangleq [x_t^n, y_t^n]^T$ be a target position in the NED frame n . The objective of the control system and collision avoidance algorithm is to make the vehicle come within an acceptance distance $d_a \geq u_b/r_{\max}$ of the target position \mathbf{p}_t^n at some unspecified time $t_f \in [0, \infty)$, i.e.

$$\|\mathbf{p}_t^{n_b}(t_f)\| \leq d_a, \quad (8.6)$$

where $\mathbf{p}_t^{n_b} = \mathbf{p}_t^n - \mathbf{p}_b^n$ is the target position in a frame n_b , which is fixed to b aligned with NED. This goal should be achieved while keeping at least a minimum safety distance d_{safe} to the obstacle, i.e. the distance d_{ob} between the vehicle and the obstacle should satisfy:

$$d_{ob}(t) \geq d_{\text{safe}} > 0 \quad \forall t \in [t_0, t_f]. \quad (8.7)$$

8.2 Control system

The control system has two modes; guidance mode and collision avoidance mode. In guidance mode, the guidance law given in Section 8.2.2 will make the vehicle move straight towards the target. If the obstacle comes within range and the desired heading from the guidance law is unsafe, the control system will enter collision avoidance mode, and start to follow the references from the collision avoidance law. The definition of the heading references in collision avoidance mode, as well as the switching rule, is given in Section 7.2.

8.2.1 Heading controller

To make the vehicle reach the target heading as fast as possible, it is made to turn towards the desired heading ψ_d^n at the maximum turning rate:

$$r_b(\psi_d^n) \triangleq \begin{cases} 0 & \tilde{\psi}_b^n = 0 \\ r_{\max} & \tilde{\psi}_b^n \in (-\pi, 0) \\ -r_{\max} & \tilde{\psi}_b^n \in (0, \pi]. \end{cases} \quad (8.8)$$

The heading error variable $\tilde{\psi}_b^n \triangleq \psi_b^n - \psi_d^n$ is chosen to belong to the interval $\tilde{\psi}_b^n \in (-\pi, \pi]$, to ensure that the vehicle always makes the shortest turn towards ψ_d^n .

8.2.2 Guidance law

When the control system is in guidance mode, the heading is guided by a pure pursuit guidance law [16, 44]. This is a target reaching guidance law which we will employ to make the vehicle reach the target position \mathbf{p}_t^n . To reach the target as soon as possible, we set the desired course to point towards the target position:

$$\psi_{dg}^n \triangleq \Psi(\mathbf{p}_t^n) = \text{atan2}(y_t^n - y_b^n, x_t^n - x_b^n), \quad (8.9)$$

where $\psi_{dg}^n \in [0, 2\pi)$ is the desired heading and the function Ψ is defined in (2.5).

8.3 The CAA algorithm

The CAA algorithm defined in Section 7.2 is summarized here for convenience. The geometry of the algorithm is shown in Figure 8.1. Recall that the two heading reference candidates during collision avoidance are

$$\psi_{dcaj}^n \triangleq \psi_{V_{ej}}^n + \gamma_{caj}, \quad j = \{1, 2\}, \quad (8.10)$$

where $\psi_{V_{ej}}^n$ is the heading of edge j of the extended vision cone and γ_{caj} is the compensation angle for the obstacle velocity:

$$\gamma_{caj} = \sin^{-1} \left(\frac{u_o \sin(\gamma_{voj})}{U_b} \right), \quad j = \{1, 2\}, \quad (8.11)$$

where the angle γ_{voj} is

$$\gamma_{voj} = \pi - (\psi_o^n - \psi_{V_{ej}}^n), \quad j = \{1, 2\}. \quad (8.12)$$

The vehicle will enter collision avoidance mode if the desired heading from the nominal guidance law is within \mathcal{V}_c when the vehicle is too close to the obstacle:

$$\psi_{dg}^n(t_1) \in \mathcal{V}_c(t_1), \quad (8.13a)$$

$$d_{ob}(t_1) \leq d_{\text{switch}}, \quad d_{\text{switch}} > d_{\text{safe}}. \quad (8.13b)$$

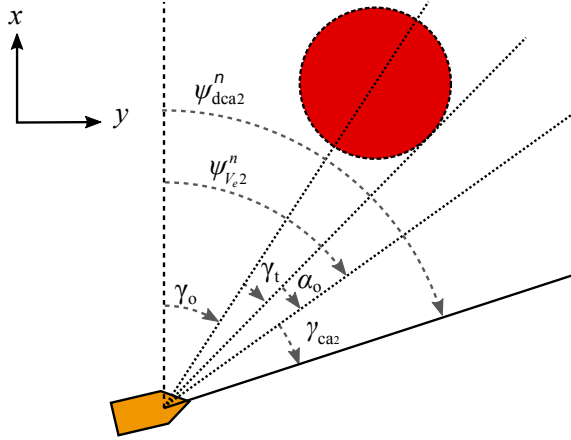


Figure 8.1: Geometry of the CAA algorithm.

Nominal guidance towards the target will resume at a time t_2 when $\psi_{dg}^n(t_2)$ moves outside $\mathcal{V}_c(t_2)$, in such a way that the vehicle course will not cross \mathcal{V}_c ,

$$\begin{aligned} j = 1 &: \psi_{dg}^n(t_2) - \psi_{dca1}^n(t_2) \leq 0, \\ j = 2 &: \psi_{dg}^n(t_2) - \psi_{dca2}^n(t_2) \geq 0. \end{aligned} \quad (8.14)$$

The turning parameter j is chosen to make the vehicle seek to move behind the obstacle:

$$j = \arg \max_{j=1,2} |\psi_o^n(t_1) - \psi_{dcaj}^n(t_1)|, \quad d_{ob}(t_1) = d_{\text{switch}}. \quad (8.15)$$

However, if the obstacle is closer than d_{switch} when the vehicle enters collision avoidance mode, the vehicle will make the shortest turn towards a safe direction:

$$j = \arg \min_{j=1,2} |\psi_b^n(t_1) - \psi_{dcaj}^n(t_1)|, \quad d_{ob}(t_1) < d_{\text{switch}}. \quad (8.16)$$

8.4 Analysis

This section presents a mathematical analysis of the closed-loop control system. This includes the case when the control system is in nominal guidance mode, where the desired heading ψ_d^n in (8.8) is given by the pure pursuit guidance law in (8.9), and the case when the control system is in collision avoidance mode, when ψ_d^n is given by the collision avoidance law (8.10). The switching between these two modes, which we defined in Section 7.2.2, is also included.

Specifically, Lemma 8.1 gives a bound on the angular velocity of ψ_{dcaj}^n given by (8.10) when avoiding a moving obstacle. This lemma is used along with Lemma 7.2 in the proof of Theorem 8.2, which states that the control objectives (8.6) and (8.7) are met for a vehicle (8.1) controlled by the controller (8.8), guidance law (8.9) and

collision avoidance law (8.10), in the presence of an obstacle with time-varying velocity.

To ensure that the vehicle is able to follow ψ_{dcaj}^n , it is required that $r_{\max} \geq |\dot{\psi}_{dcaj}^n|$ during the collision avoidance maneuver. The following lemma gives a bound on $|\dot{\psi}_{dcaj}^n|$ that holds both for static and dynamic obstacles:

Lemma 8.1. *Consider a vehicle described by (8.1), and an obstacle modeled by (7.1). If Assumptions 8.4, 8.3 and 8.1 hold, and ψ_{dcaj}^n is given by (8.10), $\dot{\psi}_{dcaj}^n$ is bounded by*

$$|\dot{\psi}_{dcaj}^n| < \dot{\psi}_{dcaj}^n \triangleq \frac{a_{\max}}{\sqrt{u_b^2 - u_{\max}^2}} + \frac{u_{\max}}{u_b} r_{\max} + \frac{(u_b + u_{\max})^2}{u_b \sqrt{(R_o + d_{\text{safe}})^2 - R_o^2}}. \quad (8.17)$$

Proof. Without loss of generality, $j = 2$ in the following analysis. Furthermore, the dependency on time will be omitted in the notation. Equation (8.10) gives

$$\dot{\psi}_{dca2}^n = \dot{\psi}_{V_e2}^n + \dot{\gamma}_{ca2} \quad (8.18)$$

Figure 8.1 shows that $\psi_{V_e2}^n = \gamma_o + \gamma_t + \alpha_o$, and hence

$$\dot{\psi}_{V_e2}^n = \dot{\gamma}_o + \dot{\gamma}_t. \quad (8.19)$$

The angular velocity of γ_o can be found geometrically as

$$\dot{\gamma}_o = \frac{1}{R_o + d_{ob}} (u_o \sin(\psi_o^n - \gamma_o) - u_b \sin(\psi_b^n - \gamma_o)). \quad (8.20)$$

The tangent angle γ_t is

$$\gamma_t = \sin^{-1}\left(\frac{R_o}{R_o + d_{ob}}\right), \quad (8.21)$$

which gives

$$\dot{\gamma}_t = -\dot{d}_{ob} \frac{R_o}{(R_o + d_{ob}) \sqrt{(R_o + d_{ob})^2 - R_o^2}}. \quad (8.22)$$

The time derivative \dot{d}_{ob} of d_{ob} is found geometrically as

$$\dot{d}_{ob} = u_o \cos(\psi_o^n - \gamma_o) - u_b \cos(\psi_b^n - \gamma_o). \quad (8.23)$$

Combining (8.20) - (8.23), applying Assumption 8.4 to bound the obstacle speed and Assumption 8.1 to bound the vehicle speed, and then maximizing with respect to ψ_b^n and ψ_o^n give the following bound:

$$|\dot{\psi}_{V_e2}^n| = |\dot{\gamma}_o + \dot{\gamma}_t| \leq \frac{u_b + u_{\max}}{\sqrt{(R_o + d_{\text{safe}})^2 - R_o^2}}. \quad (8.24)$$

The time derivative of $\dot{\gamma}_{ca}$ is found by using (8.11),

$$\dot{\gamma}_{ca2} = \frac{\dot{u}_o \sin(\gamma_{vo2}) + u_o \cos(\gamma_{vo2}) \dot{\gamma}_{vo2}}{\sqrt{u_b^2 - u_o^2 \sin^2(\gamma_{vo2})}}, \quad (8.25)$$

where $\dot{\gamma}_{vo2}$ is found from $\gamma_{vo2} = \pi - (\psi_o^n - \psi_{V_e2}^n)$ (8.12) as

$$\dot{\gamma}_{vo2} = -r_o + \dot{\psi}_{V_e2}^n. \quad (8.26)$$

We now use Assumptions 8.1, 8.4 and 8.3 to bound the vehicle speed and the obstacle speed, acceleration and heading rate in the expression for $\dot{\gamma}_{ca2}$, which gives

$$|\dot{\gamma}_{ca2}| < \frac{a_{o\max}}{\sqrt{u_b^2 - u_{o\max}^2}} + \frac{u_{o\max}}{u_b} r_{o\max} + \frac{u_{o\max}}{u_b} |\dot{\psi}_{V_e2}^n|. \quad (8.27)$$

Inserting (8.24) and (8.27) into (8.18) gives

$$\begin{aligned} |\dot{\psi}_{dca2}^n| &< \frac{a_{o\max}}{\sqrt{u_b^2 - u_{o\max}^2}} + \frac{u_{o\max}}{u_b} r_{o\max} + \frac{(u_b + u_{o\max})^2}{u_b \sqrt{(R_o + d_{\text{safe}})^2 - R_o^2}} \\ &=: \dot{\psi}_{dca\text{sup}}^n, \end{aligned} \quad (8.28)$$

which concludes the proof. \square

Remark 8.1. The bound (8.17) on $|\dot{\psi}_{dcaj}^n(t)|$ agrees with intuition. In particular, note that the bound increases as the maximum forward velocity $u_{o\max}$, acceleration $a_{o\max}$ and turning rate $r_{o\max}$ of the obstacle increase. Furthermore, with larger maximum vehicle velocity, the contributions from the obstacle acceleration and turning rate on the required vehicle turning rate becomes less significant.

Before we state the main theorem, we need to make the following assumption to ensure that the target is outside the circle of convergence around the obstacle:

Assumption 8.5. The distance d_{ot} from an obstacle to the target position \mathbf{p}_t^n satisfies

$$d_{ot}(t) > \frac{R_o}{\cos(\alpha_o)} - R_o \quad \forall t \geq t_0. \quad (8.29)$$

Remark 8.2. Vehicle safety is guaranteed even if this assumption is not met, however it is then not ensured that the target will be reached.

In addition, the vehicle should be able to start safely:

Assumption 8.6. The initial distance between the vehicle and the obstacle satisfies

$$d_{ob}(t_0) > d_{\text{switch}}. \quad (8.30)$$

Finally, we assume that the obstacles are sparsely spaced, so that the vehicle can consider one obstacle at a time:

Assumption 8.7. The distance between any two obstacles are always at least $2d_{\text{switch}}$.

The main theorem of this chapter is now ready to be stated.

Theorem 8.2. *If Assumptions 8.1-8.7 hold, the avoidance angle satisfies*

$$\alpha_o \in \left[\cos^{-1} \left(\frac{R_o}{R_o + d_{\text{safe}}} \right), \frac{\pi}{2} \right), \quad (8.31)$$

the maximum vehicle turning rate satisfies

$$r_{\text{max}} \geq \dot{\psi}_{d_{\text{casup}}}^n, \quad (8.32)$$

and the switching distance satisfies

$$d_{\text{switch}} \geq \frac{2u_b + \pi u_{o\text{max}}}{r_{\text{max}}} + d_{\text{safe}}, \quad (8.33)$$

then a vehicle described by (8.1), controlled by the controller (8.8), guidance law (8.9) and collision avoidance law (8.10), will maneuver among obstacles described by (7.1) while ensuring that

$$d_{ob}(t) \geq d_{\text{safe}} > 0, \quad \forall t \geq t_0. \quad (8.34)$$

Furthermore, if there is just one obstacle, then there is a time $t_f > t_0$ at which the vehicle will arrive at the target position \mathbf{p}_t^n .

Proof. The proof follows along the lines of the proof used in Savkin and Wang [95], which argues that as long as the vehicle is able to follow the desired heading reference from the collision avoidance algorithm, it will successfully avoid the obstacle. To achieve this we use the bound on $\dot{\psi}_{d_{caj}}^n$ from Lemma 8.1, thus extending the analysis to the algorithm presented in Chapter 7, while avoiding a singularity that occurred in the proof used in Savkin and Wang [95]. Furthermore, the proof uses the new switching criterion presented in Section 8.3, as well as the bound on the switching distance d_{switch} from (8.33).

The switching distance d_{switch} given in (8.33) ensures that the vehicle is able to turn 180° before the obstacle can be within distance d_{safe} of the vehicle's turning circle. There is then a time t_1 when $d_{ob}(t_1) \geq d_{\text{safe}}$ and $\psi_b^n(t_1) = \psi_{d_{ca}}^n(t_1)$. Applying Lemma 8.1 gives $|\dot{\psi}_{d_{caj}}^n(t)| < \dot{\psi}_{d_{casup}}^n$. Hence $r_{\text{max}} \geq |\dot{\psi}_{d_{caj}}^n(t)| \forall t > t_0$, and the vehicle is able to follow (8.10),

$$\psi_b^n(t) = \psi_{d_{ca}}^n(t), \forall t \in [t_1, t_2], \quad (8.35)$$

where t_2 is the time when the vehicle will exit collision avoidance mode.

The conditions of Lemma 7.2 are now satisfied, and it is guaranteed that

$$d_{ob}(t) \geq d_{\text{safe}} \quad \forall t \in [t_1, t_2], \quad (8.36)$$

which satisfies control objective (8.7).

Since the vehicle circles around the obstacle, Assumption 8.5 ensures that there will be a time t_2 when the line of sight to the target \mathbf{p}_t^n will be outside of the compensated and unsafe vision cone \mathcal{V}_c . The vehicle will then exit collision avoidance mode and proceed towards the target. It follows from Lemma 7.1 that any

direction outside of the cone \mathcal{V}_c ensures that $d_{ob} > d_{\text{safe}}$, and hence the direction towards \mathbf{p}_t^n is safe.

The obstacle may turn so that the line of sight to \mathbf{p}_t^n comes within \mathcal{V}_c before $d_{ob} > d_{\text{switch}}$, making the vehicle enter collision avoidance mode again. However, since \mathbf{v}_{dca1}^n and \mathbf{v}_{dca2}^n are first order differentiable with angular velocity less than $\dot{\psi}_{dca\text{sup}}^n$, and ψ_{dca}^n is then chosen to be the closest of \mathbf{v}_{dca1}^n and \mathbf{v}_{dca2}^n by (8.16), the vehicle is immediately able to follow ψ_{dca}^n to avoid the obstacle again.

Finally, since $u_b > u_{\text{omax}}$, the vehicle will eventually be able to escape the obstacle and reach the target. This satisfies control objective (8.6) and concludes the proof. \square

8.5 Simulations

This section presents numerical simulations of three scenarios using the CAA algorithm. The first two scenarios contain a circular obstacle of radius $R_o = 3$ m. The third scenario demonstrates the use of the CA algorithm on a convex obstacle. The vehicle speed in all scenarios is set to $u_b = 1$ m/s and the maximum vehicle turning rate is set to $r_{\text{max}} = 1$ rad/s. The safety distance is set to $d_{\text{safe}} = 1$ m, and the constant avoidance angle was set using (8.31) to $a_{\text{omin}} = 0.72$ rad.

The speed of the circular obstacle is set to $u_o = u_{\text{omax}} = 0.7$ m/s, while the maximum obstacle acceleration and turning rate are set to $a_{\text{omax}} = 0$ and $r_{\text{omax}} = 0.15$ rad/s. The switching distance was set using these parameters to $d_{\text{switch}} = 5.2$ m, which satisfies (8.33). By Lemma 8.1, $\dot{\psi}_{dca\text{sup}}^n = 0.98$ s⁻¹ for the circular obstacle, and thus $r_{\text{max}} > \dot{\psi}_{dca\text{sup}}^n$, satisfying (8.32).

In the first scenario, shown in Figure 8.2, the vehicle and the obstacle are initially on a head-on collision course where the obstacle moves along a straight trajectory towards the vehicle. At time $t_1 = 6.96$ s the distance to the obstacle satisfies $d_{ob}(t_1) = d_{\text{switch}}$, and the vehicle enters collision avoidance mode. Since the vehicle and the obstacle meets head on, the choice of direction parameter j becomes random. In this particular case $j = 2$ and the vehicle turns to the right.

Figure 8.3 shows that $|\dot{\psi}_{dca2}^n| < \dot{\psi}_{dca\text{sup}}^n$ during the simulation. Hence, since $\dot{\psi}_{dca\text{sup}}^n < r_{\text{max}}$, the vehicle is able to perfectly follow ψ_{dca2}^n after a transition period, which agrees with $r_{\text{max}} \geq \dot{\psi}_{dca\text{sup}}^n$. The obstacle distance remains greater than d_{safe} , as seen in the top half of Figure 8.3. The simulation thus supports the theoretical results given by Theorem 8.2. At time 13.68 s, the line of sight to the target is outside of the cone $\mathcal{V}_c(t)$, and the vehicle enters guidance mode. The vehicle then proceeds towards the target in accordance with the pure pursuit guidance law (8.9).

In the second scenario, shown in Figure 8.4, the obstacle approaches the vehicle along a circular trajectory from the left. The turning rate of the obstacle is set to $r_o = r_{\text{omax}} = 0.15$ rad/s. The vehicle enters CA mode at time 5.49 s, and moves behind the obstacle in accordance with (8.15).

Figure 8.5 shows that, like in the first scenario, $|\dot{\psi}_{dca1}^n| < \dot{\psi}_{dca\text{sup}}^n$ and $d_{ob}(t) \geq d_{\text{safe}}$ during the simulation. Thus, the second simulation also supports the results given in Theorem 8.2.

The third scenario, shown in Figure 8.6, contains a concave obstacle moving straight towards the vehicle with speed $u_o = u_{\text{omax}} = 0.5$ m/s. The obstacle consists

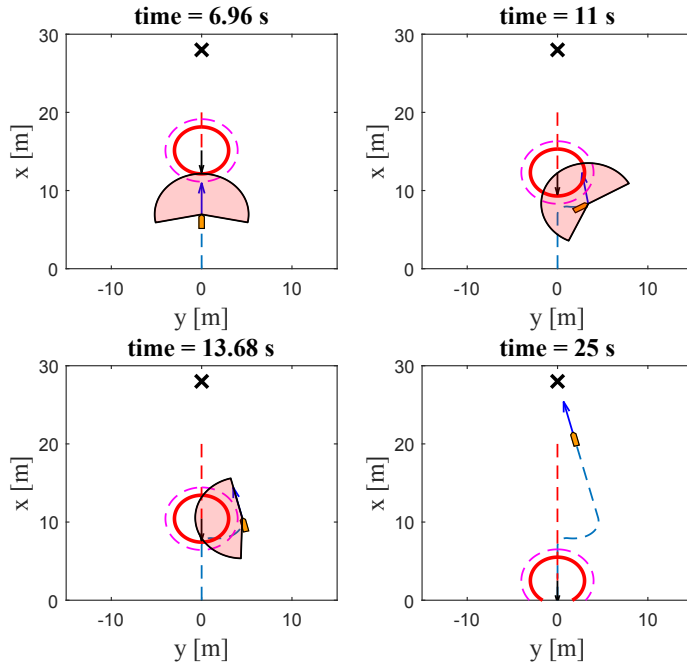


Figure 8.2: The first scenario, where the vehicle meets an obstacle head on. The vehicle is the orange polygon, with $\mathbf{p}_b^n(t)$ at the nose tip. The obstacle is the solid red circle. The vehicle and obstacle trajectories are the dashed blue and red line, respectively. The dotted magenta circle shows d_{safe} , while \mathcal{V}_c is shown as a semi-opaque red sector with radius d_{switch} . The target is marked by an 'X', while the heading from the nominal guidance law, ψ_{dg}^n , is drawn as a blue arrow.

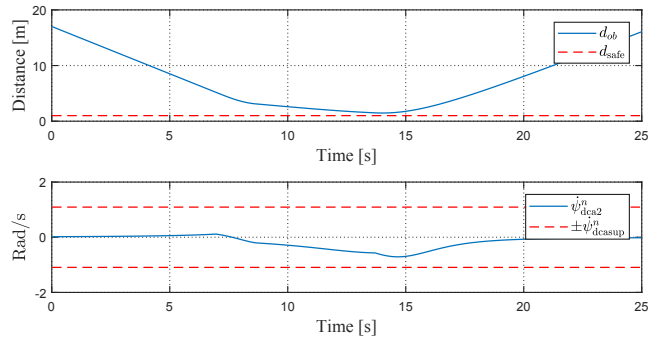


Figure 8.3: Distance between the vehicle and the obstacle in the first scenario (top), and the angular velocity of ψ_{dca2}^n (bottom), which was used during the collision avoidance maneuver.

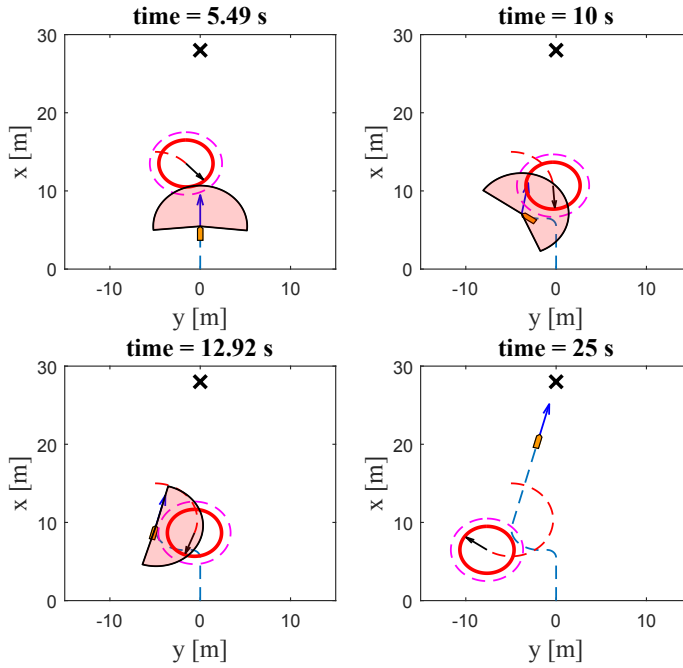


Figure 8.4: The second scenario, where the obstacle is moving in a clockwise circle starting to the left of the vehicle.

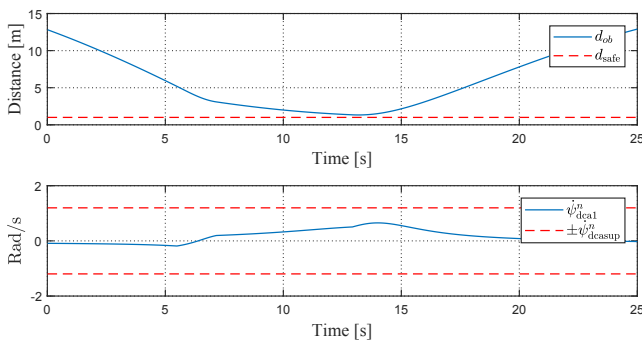


Figure 8.5: Distance between the vehicle and the obstacle in the second scenario (top), and the angular velocity of ψ_{dca1}^n (bottom), which was used during the collision avoidance maneuver.

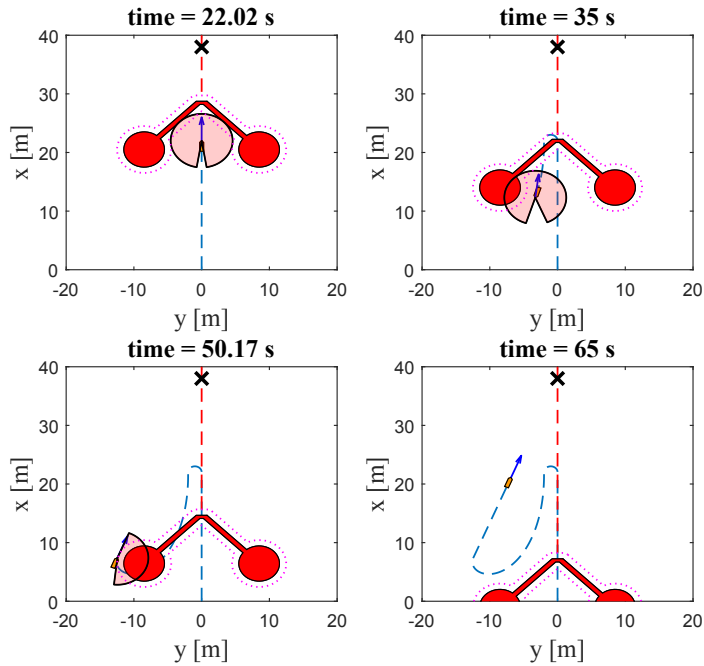


Figure 8.6: The third scenario, with a concave obstacle moving straight towards the vehicle

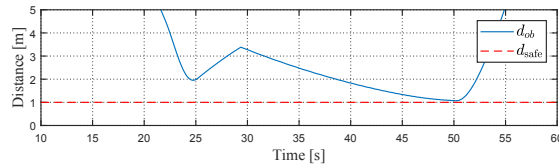


Figure 8.7: Distance between the vehicle and the obstacle when avoiding a convex obstacle.

of two connected arms with circles of radius 3 m at the extremities. The circle radius was used as input to (8.31) to obtain a minimum avoidance angle of $\alpha_o = 0.72$ rad, while (8.33) gives a minimum switching distance of $d_{\text{switch}} = 4.57$ m, both of which were used in the simulation. At time 22.02 s the obstacle comes within switching distance. The vehicle travels along the edge of the obstacle until time 50.17 s, when the direction to the target becomes safe and the vehicle continues towards it. Figure 8.7 shows that $d(t) \geq d_{\text{safe}}$ during the simulation.

8.6 Conclusions

In this chapter, we have applied the CAA algorithm presented in Chapter 7 to a kinematically modeled unicycle with limited turning rate. In order to demonstrate the applicability of the algorithm to vehicles with a limited speed envelope, and to accentuate the advantage of using the vehicle speed as an input to, rather than an output from, the algorithm, we have allowed the unicycle to maintain a constant speed.

Under these conditions, we have applied the results of the algorithm analysis in the previous chapter to derive conditions under which the vehicle is guaranteed to avoid a moving obstacle. Specifically, we have derived a lower bound on the switching distance in order to ensure that the vehicle is able to turn away from the obstacle in time. Additionally, we have derived a lower bound on the safety distance the vehicle must keep from the obstacle. If the safety distance is below this bound, the aggressive maneuvering required to circumvent the obstacle may make the required yaw rate exceed the limits of the vehicle. These theoretical results have been validated through simulations.

The lower bound on the safety distance was used to find a lower bound on the constant avoidance angle the vehicle will keep to the obstacle during the maneuver. Hence, if we know the minimum radius of the obstacles the vehicle is likely to encounter in a scenario, the CAA algorithm can be tuned appropriately. If the obstacles are not circular, it is possible to use the minimum curvature of the obstacles in the same manner to derive the avoidance angle. An analysis of maneuvers around such obstacles is, however, beyond the scope of this thesis.

The bounds on the avoidance parameters depend on the maneuverability of both the vehicle and the obstacle. In effect, the faster and more maneuverable the obstacle is with respect to the vehicle, the larger safety distance, avoidance angle and switching distance are required; a result which matches with intuition.

While the unicycle scenario presented in this chapter is valuable in and of itself, it can also be seen as a first step in applying the CAA algorithm to a vehicle modeled using the full dynamic 3 DOF maneuvering model described in Section 3.2.1. In the next chapter, we will augment the unicycle model with the underactuated dynamics of a marine vehicle, including the sideways sway movement induced by turning.

Chapter 9

Including the Underactuated Dynamics in the CAA Algorithm

Never mind maneuvers, always go at them.

— Patrick O'Brian, *Master and Commander*

While we in the previous chapter applied the CAA algorithm to a kinematically modeled unicycle, we will in this chapter extend the vehicle model to include the underactuated dynamics of marine vehicles steered by a rudder and a propeller. Specifically, the vehicle will have an underactuation in the sideways (sway) speed, which is induced when the vehicle turns. Thus, the vehicle course, which is the direction of the vehicle's velocity vector, and the vehicle heading will not be the same. We will modify the control system to steer the vehicle course, and will thus show how conditions can still be found under which the CAA algorithm is guaranteed to make the vehicle avoid a moving obstacle. In doing so, we will in particular examine the effect of the underactuation on the vehicle's total speed, which will contain a component which is now time-varying.

We will start this chapter by giving a description of the underactuated vehicle model in Section 9.1, and of the course controller and nominal guidance law in Section 9.2. The CAA collision avoidance algorithm is summarized in Section 9.3, and the performance of the system is analysed mathematically in Section 9.4. The results are validated in the simulations section, Section 9.5, before the chapter is concluded in Section 9.6.

The work presented in this chapter is based on Wiig et al. [113].

9.1 System description

9.1.1 Vehicle model

In this chapter we will consider a marine vehicle moving in 3 DOF. We model the vehicle using the maneuvering model described in Section 3.2.1. However, we assume that the directly actuated dynamics in surge u_b and yaw rate r_b are perfectly controlled and hence can be neglected. These dynamics are included in the next chapter.

Assumption 9.1. The surge speed u_b and yaw rate r_b are perfectly controlled, and can thus be considered as virtual control inputs. Furthermore, u_b is positive and constant.

The vehicle model then becomes:

$$\dot{x}_b^n = u_b \cos(\psi_b^n) - v_b \sin(\psi_b^n), \quad (9.1a)$$

$$\dot{y}_b^n = u_b \sin(\psi_b^n) + v_b \cos(\psi_b^n), \quad (9.1b)$$

$$\dot{\psi}_b^n = r_b, \quad (9.1c)$$

$$\dot{v}_b = X_v(u_b)r_b + Y_v(u_b)v_b. \quad (9.1d)$$

The terms X_v and Y_v are linear in u_b , and are defined in Section 3.2.1 and restated in Appendix 9.A for convenience. Since u_b is assumed to be constant, so are the X_v and Y_v terms. Hence, we will for brevity in this chapter employ the notation $X_v = X_v(u_b)$ and $Y_v = Y_v(u_b)$. We ensure that the vehicle is nominally stable in sway with the following assumption:

Assumption 9.2. The Y_v term satisfies $Y_v < 0$.

The direction of the vehicle's velocity vector is of main interest to us when steering the vehicle to avoid an obstacle. We call this direction the vehicle course, which we denote ψ_f^n , where the frame f is called the Flow frame, as defined in Fossen [35]. The Flow frame is obtained by rotating the b frame around the z -axis. The angle between f and b is called the sideslip angle, which can be found from v_b and u_b :

$$\beta_b \triangleq \psi_f^n - \psi_b^n = \text{atan2}(v_b, u_b). \quad (9.2)$$

In order to control the direction of the vehicle's velocity vector, we will control the vehicle course instead of its heading ψ_b^n . To this end, we express the model using the flow frame:

$$\dot{x}_b^n = U_b \cos(\psi_f^n), \quad (9.3a)$$

$$\dot{y}_b^n = U_b \sin(\psi_f^n), \quad (9.3b)$$

$$\dot{\psi}_f^n = r_f, \quad (9.3c)$$

$$\dot{v}_b = \frac{U_b^2}{X_v u_b + U_b^2} (X_v r_f + Y_v v_b), \quad (9.3d)$$

where $U_b \triangleq \sqrt{u_b^2 + v_b^2}$ and the course rate r_f is found as

$$r_f \triangleq \frac{(X_v u_b + U_b^2) r_b + Y_v u_b v_b}{U_b^2}. \quad (9.4)$$

The following assumption is required to ensure that (9.3d) is well defined [12]:

Assumption 9.3. The X_v term satisfies $X_v + u_b > 0$.

As long as Assumption 9.3 is satisfied, the denominator of (9.3d) is bounded by

$$X_v u_b + U_b^2 \geq a u_b, \quad a > 0. \quad (9.5)$$

Hence, the expression for \dot{v}_b in (9.3d) is nonsingular. Furthermore, it is then ensured that in the nominal case, when $v_b = 0$, a change in the heading ψ_b^n will always result in a change in the course ψ_f^n .

Remark 9.1. Assumption 9.3 imposes a restriction on the mechanical design on the vehicle, namely that as the vehicle turns, at least some of its momentum is kept in the forward direction. This is satisfied for most marine vehicles.

9.1.2 Obstacle model

Recall from Section 7.1 that the obstacle is modeled as a unicycle-type, circular vehicle of radius R_o :

$$\dot{x}_o^n = u_o \cos(\psi_o^n), \quad (9.6a)$$

$$\dot{y}_o^n = u_o \sin(\psi_o^n), \quad (9.6b)$$

$$\dot{\psi}_o^n = r_o, \quad (9.6c)$$

$$\dot{a}_o = a_o, \quad (9.6d)$$

where the obstacle yaw rate and acceleration are limited:

Assumption 9.4. The obstacle forward acceleration a_o and course rate r_o are bounded by

$$a_o \in [-a_{o\max}, a_{o\max}], \quad (9.7)$$

$$r_o \in [-r_{o\max}, r_{o\max}], \quad (9.8)$$

where $a_{o\max} \geq 0$ and $r_{o\max} \geq 0$ are constant parameters.

As in Chapter 7, we assume that the obstacle speed is upper bounded by the vehicle forward speed. However, the mathematical analysis in Section 9.4 will show that if the maneuvering capabilities of the vehicle are poor, the obstacle speed must be restricted further:

Assumption 9.5. The obstacle forward speed u_o satisfies $u_o \in [0, u_{o\max}]$, where

$$u_{o\max} < \begin{cases} 2\sqrt{-X_v^2 - X_v u_b} & -u_b < X_v \leq -\frac{u_b}{2} \\ u_b & -\frac{u_b}{2} < X_v. \end{cases} \quad (9.9)$$

9.1.3 Control objective

The control system and the collision avoidance algorithm should make the vehicle come within an acceptance distance $d_a > 0$ within a target position $\mathbf{p}_t^n = [x_t^n, y_t^n]^T$ while keeping a minimum safety distance, d_{safe} , to the obstacle,

$$d_{ob}(t) \geq d_{\text{safe}} > 0 \quad \forall t \geq t_0. \quad (9.10)$$

Furthermore, the sway velocity of the vehicle is required to be bounded,

$$|v_b(t)| < v_{\text{sup}} \quad \forall t \geq t_0 \quad (9.11)$$

where $v_{\text{sup}} > 0$ is a constant design parameter.

Assumption 9.6. The initial sway speed satisfies $|v_b(t_0)| < v_{\text{sup}}$.

9.2 Control system

The control system has two modes, guidance mode and collision avoidance mode, which are switched between according to a rule given in Section 9.3. The desired course during guidance mode is given by a pure pursuit guidance law described in Section 9.2.2, while in collision avoidance mode it is given by the CAA collision avoidance algorithm, which we describe in Section 9.3.

9.2.1 Course controller

To obtain exponential course convergence, the desired course reference ψ_{fd}^n is tracked using the controller

$$r_f = \dot{\psi}_{fd}^n - k_\psi \tilde{\psi}_f^n, \quad (9.12)$$

where k_ψ is a positive control gain. The course error $\tilde{\psi}_f^n \triangleq \psi_f^n - \psi_d^n$ is defined to lie in the interval $\tilde{\psi}_f^n \in (-\pi, \pi]$, to ensure that the vehicle always makes the shortest turn towards ψ_d^n . From (9.3c) it is clear that (9.12) provides exponential stability of the course error dynamics. We find the corresponding yaw rate by inserting (9.12) into (9.4):

$$r_b = \frac{U_b^2 r_f - Y_v u_b v_b}{X_v u_b + U_b^2}, \quad (9.13)$$

which is ensured to be well defined by Assumption 9.3.

9.2.2 Guidance law

When the control system is in guidance mode, the course reference is given by a pure pursuit guidance law [16, 44], which will steer the vehicle towards the target position \mathbf{p}_t^n by directing the vehicle course straight towards the target:

$$\psi_{dg}^n \triangleq \Psi(\mathbf{p}_t^{nb}) = \text{atan2}(y_t^n - y_b^n, x_t^n - x_b^n), \quad (9.14)$$

where $\psi_{dg}^n \in [0, 2\pi)$ is the course reference and the function Ψ is defined in (2.5).

9.3 The CAA algorithm

The CAA algorithm will be used to provide course references when the control system is in collision avoidance mode. While the algorithm is defined in Section 7.2, it is summarized here for convenience.

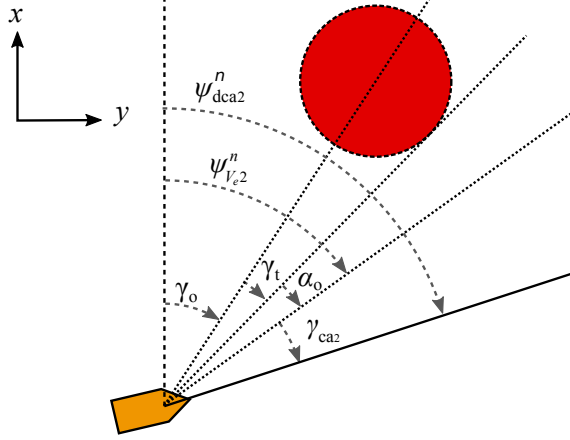


Figure 9.1: Geometry of the CAA algorithm.

The geometry of the algorithm is shown in Figure 9.1. Recall that the two heading reference candidates during collision avoidance is

$$\psi_{dcaj}^n \triangleq \psi_{V_{ej}}^n + \gamma_{caj}, \quad j = \{1, 2\}, \quad (9.15)$$

where $\psi_{V_{ej}}^n$ is the heading of edge j of the extended vision cone and γ_{caj} is the compensation angle for the obstacle velocity:

$$\gamma_{caj} = \sin^{-1} \left(\frac{u_o \sin(\gamma_{voj})}{U_b} \right), \quad j = \{1, 2\}. \quad (9.16)$$

The angle γ_{voj} is found geometrically as

$$\gamma_{voj} = \pi - (\psi_o^n - \psi_{V_{ej}}^n), \quad j = \{1, 2\}. \quad (9.17)$$

The vehicle will enter collision avoidance mode if the desired heading from the nominal guidance law is within \mathcal{V}_c when the vehicle is too close to the obstacle:

$$\psi_{dg}^n(t_1) \in \mathcal{V}_c(t_1), \quad (9.18a)$$

$$d_{ob}(t_1) \leq d_{switch}, \quad d_{switch} > d_{safe}. \quad (9.18b)$$

Nominal guidance towards the target will resume at a time t_2 when $\psi_{dg}^n(t_2)$ moves outside $\mathcal{V}_c(t_2)$, in such a way that the vehicle course will not cross \mathcal{V}_c ,

$$\begin{aligned} j = 1 : \psi_{dg}^n(t_2) - \psi_{dca1}^n(t_2) &\leq 0, \\ j = 2 : \psi_{dg}^n(t_2) - \psi_{dca2}^n(t_2) &\geq 0. \end{aligned} \quad (9.19)$$

The turning parameter j is chosen to make the vehicle seek to move behind the obstacle:

$$j = \arg \max_{j=1,2} |\psi_o^n(t_1) - \psi_{dcaj}^n(t_1)|, \quad d_{ob}(t_1) = d_{switch}. \quad (9.20)$$

If the obstacle is closer than d_{switch} when the vehicle enters collision avoidance mode, the vehicle will make the shortest turn towards a safe direction:

$$j = \arg \min_{j=1,2} |\psi_f^n(t_1) - \psi_{\text{dca}j}^n(t_1)|, \quad d_{\text{ob}}(t_1) < d_{\text{switch}}. \quad (9.21)$$

9.4 Analysis

This section presents a mathematical analysis of the vehicle (9.3) when the collision avoidance law in Section 9.3 is used in combination with the course controller and guidance law in Section 9.2. Specifically, we derive conditions on the course control gain k_ψ , the safety distance d_{safe} and the switching distance d_{switch} which ensure that a circular obstacle moving with a time-varying velocity can be safely avoided.

When the course rate $r_f \neq 0$, a sway motion v_b is induced by (9.3d). To prevent the vehicle from being driven into the obstacle by the sway motion, we need to bound v_b , which is done in the next two lemmas.

Lemma 9.1. *Consider a vehicle modeled by (9.3). Suppose that the course rate r_f is dependent on the sway motion v_b in such a way that for $v_b = v_{\text{sup}}$,*

$$|r_f(\pm v_{\text{sup}})| < \frac{|Y_v|}{|X_v|} v_{\text{sup}}. \quad (9.22)$$

Then, if $|v_b(t_0)| < v_{\text{sup}}$, the solutions of v_b are bounded by

$$|v_b(t)| < v_{\text{sup}} \quad \forall t \geq t_0. \quad (9.23)$$

Proof. Consider the Lyapunov function

$$V = \frac{1}{2} v^2. \quad (9.24)$$

The time derivative of V along the solutions of (9.3d) is

$$\dot{V} = \frac{U_b^2}{U_b^2 + X_v u_b} (X_v v_b r_f + Y_v v_b^2). \quad (9.25)$$

When Assumption 9.2 holds, (9.25) is bounded by

$$\dot{V} \leq \frac{U_b^2}{U_b^2 + X_v u_b} (|X_v| |v_b| |r_f(v_b)| - |Y_v| v_b^2). \quad (9.26)$$

Let the set Ω_V be defined as

$$\Omega_V \triangleq \{v_b \in \mathbb{R} \mid V \leq \frac{1}{2} v_{\text{sup}}^2\}, \quad (9.27)$$

which is a level set of V with $v_b = v_{\text{sup}}$ on the boundary. Equation (9.22) ensures that $\dot{V} \leq 0$ on the boundary of Ω_V . It follows that any solution of v_b starting in the set Ω_V cannot leave it. Hence, if $|v_b(t_0)| \leq v_{\text{sup}}$, then $|v_b(t)| \leq v_{\text{sup}} \forall t \geq t_0$. \square

We will use the sway bound v_{sup} as a design parameter, which we can use to set how aggressive the collision avoidance maneuver should be. A large v_{sup} implies a large turning rate and an aggressive maneuver, while a small v_{sup} implies a less aggressive maneuver. Before stating the next lemma, we define the following term for conciseness:

$$F_\psi \triangleq |Y_v| v_{\text{sup}} \left(\frac{1}{|X_v|} - 2 \frac{v_{\text{sup}} u_{\text{omax}}}{\sqrt{U_{\text{bsup}}^2 - u_{\text{omax}}^2} (X_v u_b + U_{\text{bsup}}^2)} \right) - r_{\text{omax}} \frac{u_{\text{omax}}}{u_b} - \frac{a_{\text{omax}}}{\sqrt{u_b^2 - u_{\text{omax}}^2}}, \quad (9.28)$$

where $U_{\text{bsup}} \triangleq \sqrt{u_b^2 + v_{\text{sup}}^2}$.

Remark 9.2. Since U_{bsup} increases with increasing v_{sup} , it is always possible to choose a v_{sup} large enough to ensure a positive value of F_ψ .

We also introduce the design parameter $\lambda_\psi \in (0, 1)$, which is used to prioritize between the control gain k_ψ and the safety distance d_{safe} . A high value of λ_ψ will give priority to a high k_ψ , while a low value of λ_ψ prioritizes a low d_{safe} .

Lemma 9.2. Consider a vehicle modeled by (9.3), controlled by the course controller (9.12) - (9.13), with a desired course given by the collision avoidance law (9.15). Let $\lambda_\psi \in (0, 1)$, and assume that the distance between the vehicle and the obstacle satisfies $d_{\text{ob}}(t) > d_{\text{safe}} \forall t \geq t_0$. If Assumptions 9.1-9.4 hold, the course control gain k_ψ satisfies

$$k_\psi \leq \frac{\lambda_\psi}{\pi} F_\psi, \quad (9.29)$$

the safety distance d_{safe} satisfies

$$d_{\text{safe}} \geq \frac{(U_{\text{bsup}} + u_{\text{omax}})^2}{U_{\text{bsup}}} \frac{1}{(1 - \lambda_\psi) F_\psi}, \quad (9.30)$$

and the initial sway speed satisfies $|v_b(t_0)| \leq v_{\text{sup}}$, then

$$|v_b(t)| \leq v_{\text{sup}} \quad \forall t \geq t_0 \quad (9.31)$$

Proof. We prove Lemma 9.2 by finding an upper bound on r_f for a given v_{sup} . Lemma 9.1 is then applied by inserting the upper bound into (9.22), and solving for k_ψ and d_{safe} to obtain (9.29) and (9.30).

Recall from Chapter 8 that the time derivative of ψ_{dcaj}^n is

$$\dot{\psi}_{\text{dcaj}}^n = \dot{\psi}_{V_{e_j}}^n + \dot{\gamma}_{\text{caj}} \quad (9.32)$$

where $\psi_{V_{e_j}}^n$ is the heading to edge j of the extended vision cone \mathcal{V}_e , and γ_{caj} is the compensation angle for the obstacle's velocity. The time derivative of $\psi_{V_{e_j}}^n$ is found

as in the same manner as in Chapter 8 as

$$\begin{aligned} \psi_{V_{ej}}^n &= \frac{U_b \sin(\gamma_o - \psi_f^n) - u_o \sin(\gamma_o - \psi_o^n)}{R_o + d_{ob}} \\ &\mp R_o \frac{U_b \cos(\gamma_o - \psi_f^n) - u_o \cos(\gamma_o - \psi_f^n)}{(R_o + d_{ob}) \sqrt{d_{ob}(2R_o + d_{ob})}}. \end{aligned} \quad (9.33)$$

The time derivative of γ_{caj} is found from (9.16) as

$$\dot{\gamma}_{caj} = \frac{u_o \left(\sin(\gamma_{voj}) \left(\frac{\dot{u}_o}{u_o} - \frac{\dot{U}_b}{U_b} \right) + \cos(\gamma_{voj}) \left(\dot{\psi}_{V_{ej}}^n - \dot{\psi}_o^n \right) \right)}{\sqrt{U_b^2 - u_o^2 \sin^2(\gamma_{voj})}}, \quad (9.34)$$

where

$$\dot{U}_b = U_b v_b \frac{X_v r_f + Y_v v_b}{X_v u_b + U_b^2}, \quad (9.35)$$

and γ_o is the angle between the x -axis and the vehicle-obstacle line, as shown in Figure 9.1.

Note that $\dot{\psi}_{dcaj}^n$ depends on r_f . Hence, when inserting (9.32) into the course control law (9.12), we need to solve for r_f in order to ensure that it is well defined. The resulting expression for r_f is of the form

$$r_f = \frac{G_{rn}}{G_{rd}}, \quad (9.36)$$

where

$$G_{rn} \triangleq \dot{\psi}_{V_{ej}}^n + \frac{u_o \left(\sin(\gamma_{voj}) \left(\frac{\dot{u}_o}{u_o} - \frac{Y_v v_b^2}{U_b^2 + X_v u_b} \right) + \cos(\gamma_{voj}) \left(\dot{\psi}_{V_{ej}}^n - \dot{\psi}_o^n \right) \right)}{\sqrt{U_b^2 - u_o^2 \sin^2(\gamma_{voj})}} - k_\psi \tilde{\psi}_f^n, \quad (9.37)$$

and

$$G_{rd} \triangleq 1 + \frac{u_o \sin(\gamma_{voj}) v_b X_v}{(U_b^2 + X_v u_b) \sqrt{U_b^2 - u_o^2 \sin^2(\gamma_{voj})}}. \quad (9.38)$$

Assumptions 9.3 and 9.5 ensure that (9.38) is well defined. In order for r_f to be well defined, it is required that $G_{rd} \neq 0$. Since $G_{rd}(u_o = 0) = 1$, this can be ensured by requiring that G_{rd} is lower bounded by a positive value. Minimizing with respect to γ_{voj} gives a lower bound of (9.38) as

$$G_{rd} > 1 - \frac{u_{o\max} |v_b| |X_v|}{(U_b^2 + X_v u_b) \sqrt{U_b^2 - u_{o\max}^2}} := G_{rd\text{inf}}. \quad (9.39)$$

Minimizing (9.39) with respect to v_b and solving for $u_{o\max}$ gives the following bound on $u_{o\max}$ to ensure that $G_{rd} > 0$ for all $u_o \in [0, u_{o\max}]$:

$$u_{o\max} < \begin{cases} 2\sqrt{-X_v^2 - X_v u_b} & -u_b < X_v \leq -\frac{u_b}{2} \\ u_b & -\frac{u_b}{2} < X_v. \end{cases} \quad (9.40)$$

Assumption 9.5 ensures that (9.40) is satisfied.

When $d_{ob} \geq d_{\text{safe}}$, a bound on $|G_{rn}|$ can be found by using Assumption 9.2, which states that Y_v is negative, Assumption 9.4, which bounds the heading rate and acceleration of the obstacle, and Assumption 9.5, which bounds the obstacle speed:

$$\begin{aligned} |G_{rn}| &< \frac{v_{\text{sup}}^2 |Y_v| u_{\text{omax}}}{\sqrt{U_{\text{bsup}}^2 - u_{\text{omax}}^2} (X + U_{\text{bsup}}^2)} + r_{\text{omax}} \frac{u_{\text{omax}}}{u_b} \\ &+ \frac{a_{\text{omax}}}{\sqrt{u_b^2 - u_{\text{omax}}^2}} + \frac{(U_{\text{bsup}} + u_{\text{omax}})^2}{d_{\text{safe}} U_{\text{bsup}}} + k_\psi \pi := G_{rn\text{sup}}. \end{aligned} \quad (9.41)$$

Equations (9.39) and (9.41) are even in v_{sup} , hence

$$|r_f(\pm v_{\text{sup}})| < \frac{G_{rn\text{sup}}}{G_{rd\text{inf}}}. \quad (9.42)$$

Inserting (9.42) into (9.22) bounds d_{safe} and k_ψ to:

$$\frac{(U_{\text{bsup}} + u_{\text{omax}})^2}{d_{\text{safe}} U_{\text{bsup}}} + k_\psi \pi \leq F_\psi, \quad (9.43)$$

where F_ψ is given in (9.28). The design parameter λ_ψ can be used to rewrite (9.43) as

$$\frac{(U_{\text{bsup}} + u_{\text{omax}})^2}{d_{\text{safe}} U_{\text{bsup}}} + k_\psi \pi \leq \lambda_\psi F_\psi + (1 - \lambda_\psi) F_\psi. \quad (9.44)$$

Hence, conditions (9.29) and (9.30) ensure that (9.43), and thus (9.22), is satisfied. Lemma 9.1 then applies, and it follows that if $|v_b(t_0)| < v_{\text{sup}}$, then $|v_b(t)| < v_{\text{sup}} \forall t > t_0$. \square

In the next lemma, we will derive a bound on the minimum required switching distance d_{switch} . In this lemma we will employ the sine integral function Si , which is defined as

$$\text{Si}(\tau) = \int_0^\tau \frac{\sin(\hat{\tau})}{\hat{\tau}} d\hat{\tau}. \quad (9.45)$$

Lemma 9.3. *Consider a vehicle modeled by (9.3), controlled by (9.12) - (9.13). Let the vehicle enter collision avoidance mode at time t_1 , with $d(t_1) = d_{\text{switch}}$. Let Assumptions 9.1 and 9.5 hold, the vehicle speed satisfy $U_b < U_{\text{bsup}}$, and the switching distance satisfy*

$$d_{\text{switch}} \geq u_{\text{omax}} t_\epsilon + d_{\text{safe}} + d_{\text{turn}}, \quad (9.46)$$

where

$$t_\epsilon \triangleq -\frac{\ln(\epsilon/\pi)}{k_\psi}, \quad \epsilon \in (0, \pi/2] \quad (9.47)$$

is an upper bound on the time it takes for the vehicle to converge to within ϵ rad of ψ_{dcaj}^n , and

$$d_{\text{turn}} \triangleq \frac{U_{\text{bsup}}}{k_\psi} \text{Si}\left(\frac{\pi}{2}\right). \quad (9.48)$$

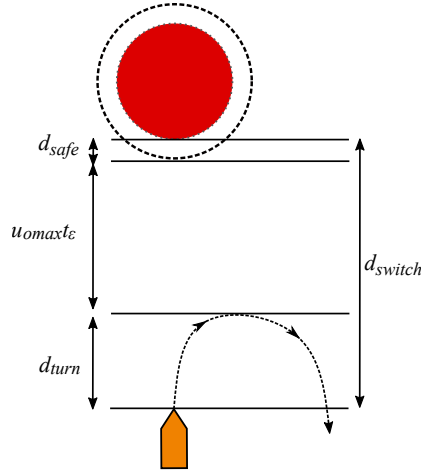


Figure 9.2: Illustration of the minimum switching distance.

is the maximum distance covered in the initial longitudinal direction of the vehicle when making a $\pi/2$ turn. Then, the vehicle is able to converge to within ϵ rad of ψ_{dcaj}^n before the obstacle can be within d_{safe} of the vehicle.

Proof. We will prove Lemma 9.3 by showing that the distance traveled by the vehicle and the obstacle towards each other while the vehicle is turning is not enough to make the vehicle come within d_{safe} of the obstacle. The idea behind the proof is illustrated in Figure 9.2.

Without loss of generality, let $x_o^n(t_1) > x_b^n(t_1)$. Consider a worst case scenario where $R_o \rightarrow \infty$, so that the obstacle tangents are $\psi_{V_o,j}^n = \pm\pi/2$, $j = \{1, 2\}$, and let the vehicle and obstacle move at maximum speed towards each other: $U_b \rightarrow U_{bsup}$, $\psi_f^n(t_1) = 0$, $u_o = u_{omax}$ and $\psi_o^n(t_1) = \pi$. The worst case behavior of the obstacle is then to continue moving at maximum speed and course $\psi_o^n(t \geq t_1) = \pi$.

As the vehicle enters collision avoidance mode, it starts to turn towards ψ_{dcaj}^n . The course error dynamics, obtained by inserting the course controller (9.12) into (9.3c), are

$$\dot{\tilde{\psi}}_f^n = -k_\psi \tilde{\psi}_f^n, \quad (9.49)$$

which has the solution

$$\tilde{\psi}_f^n(t) = \tilde{\psi}_f^n(t_0) e^{-k_\psi(t-t_0)}. \quad (9.50)$$

From the definition of $\tilde{\psi}_f^n$, the initial condition is bounded by $|\tilde{\psi}_f^n(t_0)| \leq \pi$, and hence $\tilde{\psi}_f^n(t) = \tilde{\psi}_f^n(t_0) e^{-k_\psi(t-t_0)}$. It follows that the convergence time of the course error to $|\tilde{\psi}_f^n| \leq \epsilon$, where $\epsilon \in (0, \pi/2]$, is bounded by

$$t - t_0 \leq -\frac{\ln(\epsilon/\pi)}{k_\psi} := t_\epsilon. \quad (9.51)$$

Hence, the distance covered by the obstacle towards the vehicle is upper bounded by $u_{\text{omax}}t_\epsilon$.

The distance traveled by the vehicle in the x direction before it has turned $\pm\pi/2$ rad is upper bounded by the distance traveled when making a $\pi/2$ turn. This can be found by solving (9.3a) when inserting $\tilde{\psi}_f^n(t) = -\frac{\pi}{2}e^{-k_\psi t}$:

$$\begin{aligned} & \int_0^\infty U_{\text{bsup}} \cos(\tilde{\psi}_f^n + \frac{\pi}{2}) dt \\ &= \int_0^\infty U_{\text{bsup}} \cos(\frac{\pi}{2} - \frac{\pi}{2}e^{-k_\psi t}) dt = \frac{U_{\text{bsup}}}{k_\psi} \text{Si}(\frac{\pi}{2}). \end{aligned} \quad (9.52)$$

It follows that if (9.46) holds, then the distance from the obstacle to the vehicle trajectory will not be less than d_{safe} before the vehicle course has converged to within ϵ rad of ψ_{dcaj}^n , and this also holds for the distance d_{ob} from the obstacle to the vehicle. \square

Before we state the main theorem of this chapter, we assume that the target position is outside the circle of convergence around the obstacle:

Assumption 9.7. The distance $d_{ot}(t)$ from an obstacle to the target position \mathbf{p}_t^n satisfies

$$d_{ot}(t) \geq \frac{R_o}{\cos(\alpha_o)} - R_o \quad \forall t \geq t_0. \quad (9.53)$$

In addition, the vehicle must be able to start safely:

Assumption 9.8.

$$d_{ob}(t_0) > d_{\text{switch}}. \quad (9.54)$$

Finally, we assume that if there are more than one obstacle, they are far enough apart to make it possible to consider them one by one:

Assumption 9.9. The distance between any two obstacles are always at least $2d_{\text{switch}}$.

We are now ready to state the main theorem:

Theorem 9.4. *Let Assumptions 9.1-9.9 hold, the avoidance angle satisfy*

$$\alpha_0 \in \left[\cos^{-1} \left(\frac{R_o}{R_o + d_{\text{safe}}} \right) + \epsilon, \frac{\pi}{2} \right) \quad (9.55)$$

and the switching distance satisfy

$$d_{\text{switch}} \geq u_{\text{omax}}t_\epsilon + d_{\text{safe}} + d_{\text{turn}}. \quad (9.56)$$

Furthermore, let the course control gain k_ψ and safety distance d_{safe} satisfy the conditions of Lemma 9.2:

$$k_\psi \leq \frac{\lambda_\psi}{\pi} F_\psi, \quad (9.57)$$

$$d_{\text{safe}} \geq \frac{(U_{\text{bsup}} + u_{\text{omax}})^2}{U_{\text{bsup}}} \frac{1}{(1 - \lambda_\psi) F_\psi}, \quad (9.58)$$

for $\lambda_\psi \in (0, 1)$, and let the target reaching acceptance distance satisfy

$$d_a > \frac{U_{\text{bsup}} |X_v|}{|Y_v| v_{\text{sup}} - |X_v| k_\psi \pi}. \quad (9.59)$$

Then, a vehicle described by (9.1), controlled by the yaw rate and course controller (9.12) - (9.13), the guidance law (9.14) and the collision avoidance law (9.15) will maneuver among obstacles described by (9.6) while ensuring that.

$$d_{\text{ob}}(t) \geq d_{\text{safe}} > 0 \quad \forall t \geq t_0. \quad (9.60)$$

Furthermore, if there is just one obstacle, then there is a time $t_f > t_0$ at which the vehicle will arrive at the target position \mathbf{p}_t^n .

Proof. An upper bound on the required turning rate of the pure pursuit guidance law (9.14) can be found geometrically as:

$$|\dot{\psi}_{dg}^n| < \frac{U_{\text{bsup}}}{d_a} \quad (9.61)$$

Inserting (9.61) into the course controller (9.12) gives the following maximum course rate when the system is in nominal guidance mode:

$$|r_f| < \frac{U_{\text{bsup}}}{d_a} + k_\psi \pi. \quad (9.62)$$

From Lemma 9.1 it then follows that if

$$d_a > \frac{U_{\text{bsup}} |X_v|}{|Y_v| v_{\text{sup}} - |X_v| k_\psi \pi}, \quad (9.63)$$

and $|v_b(t_0)| < v_{\text{sup}}$, then $|v_b(t)| < v_{\text{sup}}$ until a time t_1 when the vehicle enters collision avoidance mode. It then follows from Lemma 9.2 that v_b is bounded by

$$|v_b(t)| < v_{\text{sup}} \quad \forall t \in [t_0, t_f]. \quad (9.64)$$

Hence, the vehicle speed is bounded by $U_b < U_{\text{bsup}}$. Let the distance to the obstacle be reduced to d_{switch} at a time t_1 , making the vehicle enter collision avoidance mode as described in Section 7.2.2. Lemma 9.3 then ensures that there is a time $t_2 > t_1$ when $d(t_2) \geq d_{\text{safe}}$ and $\psi_f^n(t_2) - \psi_{\text{dca}}^n(t_2) \leq \epsilon$. Since $\tilde{\psi}_f^n = 0$ is an exponentially stable equilibrium, it is then assured that

$$\psi_f^n(t) - \psi_{\text{dca}}^n(t) \leq \epsilon, \quad \forall t \in [t_2, t_3], \quad (9.65)$$

where t_3 is the time when the vehicle will exit collision avoidance mode. Condition (9.55) can then be used along with Lemma 7.2 to ensure that

$$d_{\text{ob}}(t) \geq d_{\text{safe}} \quad \forall t \in [t_2, t_3]. \quad (9.66)$$

Since the vehicle circles around the obstacle, there will be a time $t_3 > t_2$ when the line of sight to the target \mathbf{p}_t^n will be outside of \mathcal{V}_c , and hence have a larger avoidance angle than α_o to \mathcal{V}_o . The vehicle will then exit collision avoidance mode and proceed towards the target.

A nearby obstacle may turn so that ψ_{dg}^n comes within \mathcal{V}_c at a time when $d_{ob} < d_{\text{switch}}$, making the vehicle enter collision avoidance mode when (9.56) is not satisfied. However, since \mathbf{v}_{dca1}^n and \mathbf{v}_{dca2}^n are first order differentiable, and ψ_{dca}^n is then chosen to be the closest of \mathbf{v}_{dca1}^n and \mathbf{v}_{dca2}^n by (9.20), the vehicle is immediately able to follow ψ_{dca}^n to avoid the obstacle again.

Finally, since $u_b > u_{\text{omax}}$, the vehicle will eventually escape the obstacle, and thus reach the target. The control objectives in Section 9.1.3 are thus met, which concludes the proof. \square

9.5 Simulations

In this section we present numerical simulations of an underactuated marine vehicle using the CAA collision avoidance algorithm. The simulated vehicle is a Hugin autonomous underwater vehicle [43] operating in a horizontal plane. The vehicle surge speed is set to $u_b = 2$ m/s, and the maximum allowable sway speed is set to $v_{\text{sup}} = 4$ m/s. It can be verified that Assumption 9.2 is satisfied with $Y_v = -1.10$, and that Assumption 9.3 is satisfied with $X_v = -1.59$.

The first scenario contains a circular obstacle with radius $R_o = 10$ m. The maximum obstacle speed is $u_{\text{omax}} = 1.35$ m/s, which satisfies Assumption 9.1. The obstacle keeps the maximum speed, and hence does not accelerate. The maximum turning rate is set to $r_{\text{omax}} = 0.25$ rad/s. The course control gain k_ψ is set to 0.37, and the safety distance is set to $d_{\text{safe}} = 10$ m, which satisfies the conditions of Lemma 9.2 with $\lambda_\psi = 0.6$. The convergence parameter ϵ is set to $\epsilon = 0.1$ rad. A lower bound on the avoidance angle is then given by (9.55) as $\alpha_o = 1.15$ rad, while a minimum switching distance is given by (9.56) as $d_{\text{switch}} = 39.1$ m, both of which are used in the simulation.

The vehicle and obstacle behavior in the first scenario is illustrated in Figure 9.3. The obstacle starts in front of the vehicle on a head on collision course, and is set to turn with the maximum turning rate towards the vehicle in order to pursue it. At time 7.73 s the vehicle reaches the switching distance d_{switch} from the obstacle, and enters collision avoidance mode in accordance with the switching rule in Section 9.3. Since the obstacle and vehicle is on a head on collision course, the choice of turning direction given in (9.20) becomes random. In this case, the vehicle makes a starboard turn.

Figure 9.4 shows that $d_{ob} > d_{\text{safe}}$, even though the obstacle is in pursuit of the vehicle. Furthermore, the vehicle sway v_b is well within the designated v_{sup} , suggesting that the requirements on d_{safe} and k_ψ are conservative. Hence, the simulation supports the theoretical results given by Theorem 9.4. At time 70.03 s, the direction from the vehicle to the target comes outside the compensated vision cone \mathcal{V}_c , and following (9.19) the vehicle exits collision avoidance mode and enters guidance mode. It then proceeds towards the target using the pure pursuit guidance law (9.14).

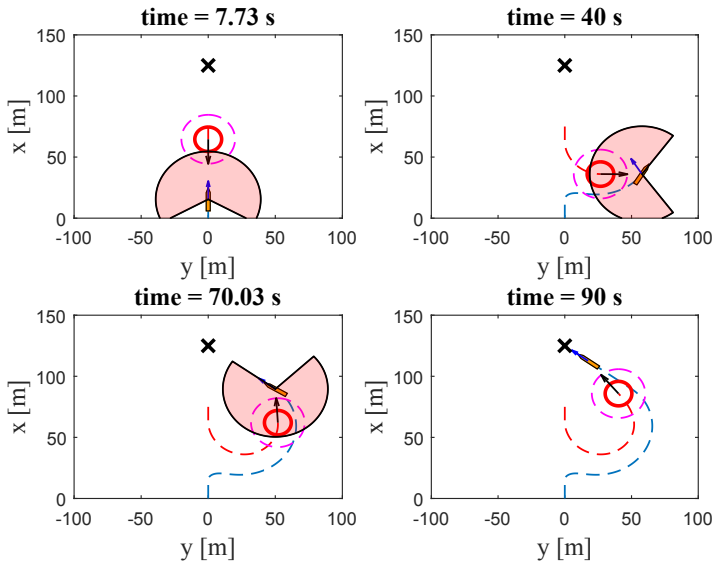


Figure 9.3: The first scenario, with a circular obstacle in pursuit of the vehicle. The vehicle is shown in orange, while the obstacle is a solid red circle. The vehicle and obstacle trajectories are a dashed blue and a dashed red line, respectively. A dashed magenta circle shows d_{safe} , while \mathcal{V}_c is shown as a semi-opaque red sector with radius d_{switch} . The target position is marked by an 'X', while the desired heading from guidance is marked as a blue arrow. For clarity, the size of the vehicle has been exaggerated in the figure.

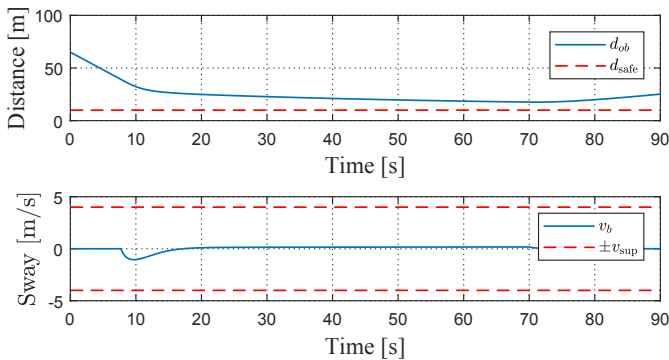


Figure 9.4: Obstacle distance and vehicle sway in the second scenario.

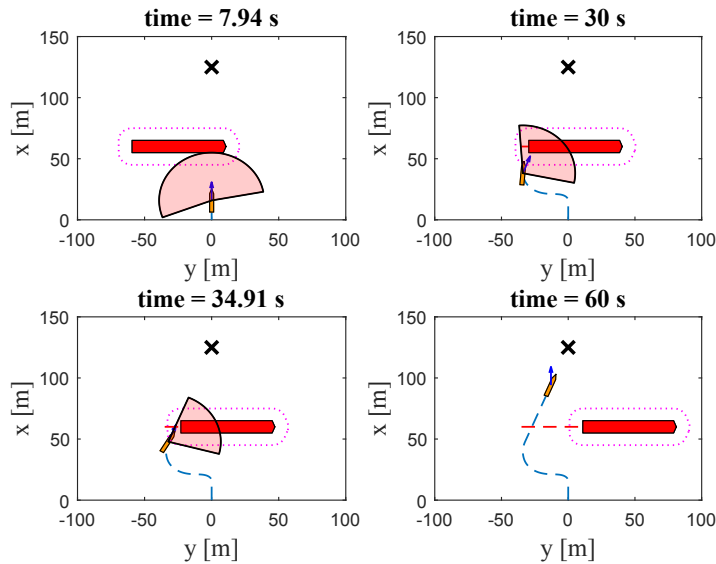


Figure 9.5: The third scenario, where the obstacle has the shape of a ship.

The mathematical analysis in Section 9.4 only applies to circular obstacles. However, the proposed collision avoidance algorithm may also be applied to obstacles of a more general shape. This is demonstrated in the second scenario, where the obstacle has the shape of a ship that is 70 m long and 10 m wide. The simulation parameters are the same as in the first simulation. Figure 9.5 shows the behavior of system during the simulation, where the obstacle moves along a straight line from left to right, crossing in front of the vehicle.

Figure 9.6 shows that $d_{ob} > d_{safe}$ and $v_b < v_{sup}$ during the maneuver. Note, however, that the analysis in Section 9.4 only applies for circular obstacles, or for obstacles modeled as a circular domain covering it. In this case, the covering domain would be quite large compared to the obstacle. Hence, the simulation demonstrates that a circular obstacle shape is a conservative requirement.

9.6 Conclusions

In this chapter, we have applied the CAA collision avoidance algorithm presented in Chapter 7 on a vehicle with underactuated dynamics. Specifically, we have examined a vehicle which is underactuated in sway, an underactuation seen for example in marine vehicles steered by a rudder and a propeller.

When such a vehicle turns, a sway speed is induced. Typically, the sway motion induced when the vehicle turns away from an obstacle will make the vehicle glide towards the obstacle. In effect, the vehicle course will thus bring the vehicle closer to the obstacle than the vehicle heading would imply. We have addressed this issue

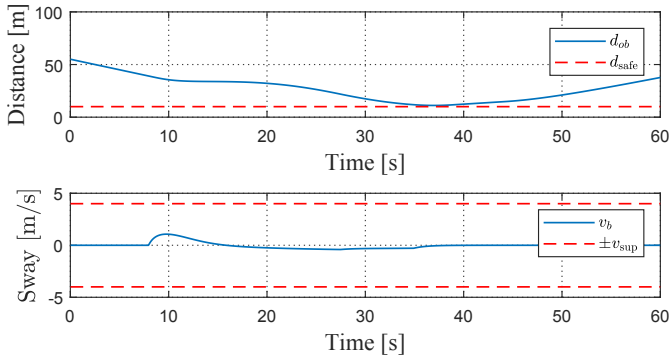


Figure 9.6: Obstacle distance and vehicle sway in the third scenario.

by implementing a course controller, and by letting the CAA algorithm steer the vehicle course rather than the vehicle heading.

A marine vehicle often has limited forward acceleration and a limited surge speed envelope in which it retains controllability of the vehicle heading. To show that the algorithm is applicable to such marine vehicles, we have restricted the surge speed to always remain constant. The underactuated sway component of the vehicle velocity adds a time-varying component to the total speed of the vehicle. Since the CAA algorithm uses the vehicle speed as an input, this component is inherently accounted for by the algorithm. However, in order to derive a minimum safe switching distance, we have derived conditions under which the sway movement remains bounded during the maneuver. Under these conditions, it is furthermore ensured that the output from the course controller is well defined.

To derive these conditions we have used the upper bound on the sway movement as a design parameter. This bound has then been used to find a course control gain and a minimum safety distance. A small safety distance will make the vehicle maneuver aggressively as it circumvents the obstacle, while a large course control gain will make the vehicle turn away from the obstacle when entering collision avoidance too sharp. We have shown how these parameters can be balanced against each other, and have thus provided sufficient conditions in order to guarantee collision avoidance.

The theoretical results have been validated by simulations showing successful avoidance of both a circular obstacle in pursuit of the vehicle, and a ship-shaped obstacle crossing in front of the vehicle. The simulations imply that the theoretical conditions for collision avoidance are quite conservative; the sway movement remained well below the designed limit throughout the maneuver.

In the next chapter, we will apply the CAA algorithm to a vehicle modeled using a full 3 DOF maneuvering model, including dynamics in the directly actuated surge and yaw variables.

9.A Functional expressions

The functions X_v and Y_v are defined in Chapter 3, and reiterated here for convenience:

$$X_v(u_b) \triangleq \frac{m_{23}^2 - m_{11}m_{33}}{m_{22}m_{33} - m_{23}^2}u_b + \frac{d_{33}m_{23} - d_{23}m_{33}}{m_{22}m_{33} - m_{23}^2}, \quad (9.67)$$

$$Y_v(u_b) \triangleq \frac{(m_{22} - m_{11})m_{23}}{m_{22}m_{33} - m_{23}^2}u_b - \frac{d_{22}m_{33} - d_{32}m_{23}}{m_{22}m_{33} - m_{23}^2}, \quad (9.68)$$

Chapter 10

The CAA algorithm for underactuated surface vehicles

Helge Ingstad, drei! (Helge Ingstad, turn!)

— Resigned crewman of the tanker T/S Sola, moments before collision with the frigate KNM Helge Ingstad, November 8, 2018

In this chapter, we will implement the CAA algorithm on a marine vehicle modeled using a complete 3 DOF kinematic and dynamic model. We will build on the results of the previous chapter, and will extend the control system to include controllers in the directly actuated surge and yaw variables.

When the vehicle enters collision avoidance mode, there is a discontinuity in the desired yaw rate. We will remove this discontinuity using a simple, linear bump function, and we will show how this function can be incorporated in the analysis. Furthermore, we will augment the course controller to include a saturation, which gives better control of the turning rate of the vehicle. Thus, the conditions under which collision avoidance is guaranteed will be less conservative than in Chapter 9. We will, however, show how simulations and experiments still imply some conservativeness of the conditions.

While we in Chapters 8 and 9 focused on target reaching as the nominal control objective, we will in this chapter also examine the behavior of the algorithm in combination with the line of sight path following guidance law. By proving that the vehicle is able to safely reach its control objectives in both a target reaching and a path following scenario, we will demonstrate the modular nature of the algorithm. The results are validated through both numerical simulations and through full-scale experiments on the R/V Gunnerus, where we also include scenarios with multiple obstacles.

The remainder of this chapter is organized as follows: The vehicle, obstacle and control objectives are described in Section 10.1. The CAA collision avoidance algorithm is summarized in Section 10.2, while the target reaching and path following guidance laws are given in Section 10.3. The controller used to follow the course references from these algorithms is presented in Section 10.4, which includes the smoothing function ensuring that the resulting yaw rate reference trajectory is feasible. The surge and yaw rate controllers are presented in Section 10.5. A mathematical analysis of the system is provided in Section 10.6, which gives conditions of provable safe maneuvering. The results are validated through simulations

in Section 10.7 and experiments in Section 10.8, before some concluding remarks are given in Section 10.9.

The work presented in this chapter is based on Wiig et al. [119].

10.1 System description

The vehicle is modeled using a full 3 DOF model as described in Section 3.2.1. Recall that the vehicle kinematics and dynamics, expressed in component form, are

$$\dot{x}_b^n = u_b \cos(\psi_b^n) - v_b \sin(\psi_b^n), \quad (10.1a)$$

$$\dot{y}_b^n = u_b \sin(\psi_b^n) + v_b \cos(\psi_b^n), \quad (10.1b)$$

$$\dot{\psi}_b^n = r_b, \quad (10.1c)$$

$$\dot{u}_b = F_u(u_b, v_b, r_b) + \tau_u, \quad (10.1d)$$

$$\dot{v}_b = X_v(u_b)r_b + Y_v(u_b)v_b, \quad (10.1e)$$

$$\dot{r}_b = F_r(u_b, v_b, r_b) + \tau_r. \quad (10.1f)$$

The functions $F_u(v_b, r_b)$, $X_v(u_b)$, $Y_v(u_b)$ and $F_r(u_b, v_b, r_b)$ contain mass and damping parameters. The functions are defined in Section 3.2.1, and restated in Appendix 10.A for convenience.

Since the vehicle dynamics in (10.1) are described using a maneuvering model, we assume that the vehicle operates at maneuvering speed:

Assumption 10.1. The vehicle surge speed u_b satisfies $u_b \geq u_{b\min}$, where $u_{b\min} > 0$ is a constant parameter.

To ensure that the vehicle is nominally stable in sway (10.1e), we make the following assumption on $Y_v(u_b)$:

Assumption 10.2. The function $Y_v(u_b)$ satisfies

$$Y_v(u_b) < 0, \forall u_b > u_{b\min}. \quad (10.2)$$

If Assumption 10.2 does not hold, then a small disturbance in sway would lead to a steadily increasing sway motion, which is not the case for commercial vessels by design.

10.1.1 The Flow frame

The vehicle velocity in the Body frame b , $\mathbf{v}_{b/n}^b \triangleq [u_b, v_b]^T$, contains a forward and a sideways velocity component. For collision avoidance purposes, we are interested in the magnitude and direction of $\mathbf{v}_{b/n}^b$, rather than the forward speed and heading of the vehicle. Like in the previous chapter, we can express this through the Flow frame f , which is a body-fixed frame rotated so that its x -axis is aligned with the flow of water around the vehicle as defined in Fossen [35]. The rotation from b to f is a rotation of the sideslip angle β_b around the z -axis, where $\beta_b \triangleq \text{atan2}(v_b, u_b)$. Hence, the vehicle kinematics can be expressed as

$$\dot{x}_b^n = U_b \cos(\psi_f^n), \quad (10.3a)$$

$$\dot{y}_b^n = U_b \sin(\psi_f^n), \quad (10.3b)$$

$$\dot{\psi}_f^n = r_f, \quad (10.3c)$$

where $\psi_f^n \triangleq \psi_b^n + \beta$ is termed the vehicle course and $U_b \triangleq \sqrt{u_b^2 + v_b^2}$. The course rate r_f is found by taking the time derivative of β_b and inserting for \dot{v}_b (10.1e):

$$r_f \triangleq \dot{\psi}_f^n = \frac{(X_v(u_b)u_b + U_b^2)r_b + Y_v(u_b)u_bv_b - \dot{u}_bv_b}{U_b^2}. \quad (10.4)$$

The expression for \dot{v}_b as a function of r_f is found as

$$\dot{v}_b = \frac{U_b^2(X_v(u_b)r_f + Y_v(u_b)v_b)}{X_v(u_b)u_b + U_b^2} + \frac{X_v(u_b)v_b\dot{u}_b}{X_v(u_b) + U_b^2}. \quad (10.5)$$

In order for (10.5) to be well defined, the following assumption needs to be met [12]:

Assumption 10.3. The function $X_v(u_b)$ satisfies

$$X_v(u_b) + u_b > 0 \quad \forall u_b > u_{b\min}. \quad (10.6)$$

Remark 10.1. This assumption ensures that a change in the vehicle heading ψ_b^n will always result in a change in the vehicle course in the nominal case when $\dot{u}_b = 0$ and $v_b = 0$. This is the case for most marine vehicles by design.

10.1.2 Control objective

The nominal control objective in this chapter is either target reaching or path following. When the system is in target reaching mode, then the control system should make the vehicle come within an acceptance distance $d_a > 0$ within a target position $\mathbf{p}_t^n = [x_t^n, y_t^n]^T$.

When the system is in path following mode, the control system should make the vehicle converge to and follow a straight-line path. To simplify the analysis, without any loss of generality, the desired path \mathcal{P} lies along the x -axis of the n frame:

$$\mathcal{P} \triangleq \{(x, y) \in \mathbb{R}^2 : y = 0\}. \quad (10.7)$$

Both of these objectives should be met while keeping a minimum safety distance, d_{safe} , to the obstacle,

$$d_{ob}(t) \geq d_{\text{safe}} > 0 \quad \forall t \geq t_0. \quad (10.8)$$

Furthermore, these control objectives should be met while maintaining a desired surge speed $u_{bd} \geq u_{b\min}$, which we set to be constant.

10.1.3 Obstacle model

As in the previous chapters, we model the obstacle as a unicycle-type, circular vehicle of radius R_o :

$$\dot{x}_o^n = u_o \cos(\psi_o^n), \quad (10.9a)$$

$$\dot{y}_o^n = u_o \sin(\psi_o^n), \quad (10.9b)$$

$$\dot{\psi}_o^n = r_o, \quad (10.9c)$$

$$\dot{u}_o = a_o, \quad (10.9d)$$

where the obstacle yaw rate and acceleration are limited:

Assumption 10.4. The obstacle forward acceleration a_o and yaw rate r_o are bounded by

$$a_o \in [-a_{o\max}, a_{o\max}], \quad (10.10)$$

$$r_o \in [-r_{o\max}, r_{o\max}], \quad (10.11)$$

where $a_{o\max} \geq 0$ and $r_{o\max} \geq 0$ are constant parameters.

In this chapter we also need to assume that the obstacle yaw rate and acceleration are continuous:

Assumption 10.5. The obstacle forward acceleration $a_o(t)$ and yaw rate $r_o(t)$ are continuous signals.

The obstacle speed is assumed to be upper bounded by the desired vehicle surge speed. As in Chapter 9, the obstacle speed will be further restricted if the maneuvering capabilities of the vehicle are poor:

Assumption 10.6. The obstacle forward speed u_o satisfies $u_o \in [0, u_{o\max}]$, where

$$u_{o\max} < \begin{cases} 2\sqrt{-X_{vd}^2 - X_{vd}u_{bd}} & -u_b < X_{vd} \leq -\frac{u_{bd}}{2} \\ u_{bd} & -\frac{u_{bd}}{2} < X_{vd}, \end{cases} \quad (10.12)$$

where $X_{vd} \triangleq X_v(u_{bd})$.

10.2 The CAA algorithm

The CAA algorithm defined in Section 7.2 will be used to provide course references when the control system is in collision avoidance mode. As in the previous chapters, we will summarize the algorithm here for convenience.

The geometry of the algorithm is shown in Figure 10.1. Recall that the two heading reference candidates during collision avoidance is

$$\psi_{dcaj}^n \triangleq \psi_{V_{e,j}}^n + \gamma_{caj}, \quad j = \{1, 2\}, \quad (10.13)$$

where $\psi_{V_{e,j}}^n$ is the heading of edge j of the extended vision cone and γ_{caj} is the compensation angle for the obstacle velocity:

$$\gamma_{caj} = \sin^{-1} \left(\frac{u_o \sin(\gamma_{voj})}{U_b} \right), \quad j = \{1, 2\}. \quad (10.14)$$

The angle γ_{voj} is found geometrically in Figure 10.1 as

$$\gamma_{voj} = \pi - (\psi_o^n - \psi_{V_{e,j}}^n), \quad j = \{1, 2\}. \quad (10.15)$$

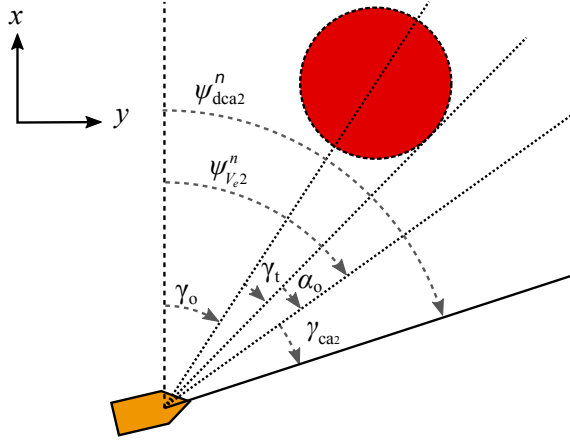


Figure 10.1: Geometry of the CAA algorithm.

The vehicle will enter collision avoidance mode if the desired heading from the nominal guidance law is within \mathcal{V}_c when the vehicle is too close to the obstacle:

$$\psi_{dg}^n(t_1) \in \mathcal{V}_c(t_1), \quad (10.16a)$$

$$d_{ob}(t_1) \leq d_{switch}, \quad d_{switch} > d_{safe}. \quad (10.16b)$$

Nominal guidance towards the target will resume at a time t_2 when $\psi_{dg}^n(t_2)$ moves outside $\mathcal{V}_c(t_2)$, in such a way that the vehicle course will not cross \mathcal{V}_c ,

$$\begin{aligned} j = 1 : \psi_{dg}^n(t_2) - \psi_{dca1}^n(t_2) &\leq 0, \\ j = 2 : \psi_{dg}^n(t_2) - \psi_{dca2}^n(t_2) &\geq 0. \end{aligned} \quad (10.17)$$

The turning parameter j is chosen to make the vehicle seek to move behind the obstacle:

$$j = \arg \max_{j=1,2} |\psi_o^n(t_1) - \psi_{dcaj}^n(t_1)|, \quad d_{ob}(t_1) = d_{switch}. \quad (10.18)$$

If the obstacle is closer than d_{switch} when the vehicle enters collision avoidance mode, the vehicle will make the shortest turn towards a safe direction:

$$j = \arg \min_{j=1,2} |\psi_f^n(t_1) - \psi_{dcaj}^n(t_1)|, \quad d_{ob}(t_1) < d_{switch}. \quad (10.19)$$

10.3 Nominal guidance laws

When the control system is not in collision avoidance mode, it is in nominal guidance mode. In this mode, the vehicle course is steered by a guidance law in order to fulfill the goals of the current scenario. The modular nature of the control system makes it possible to implement a wide array of guidance laws, and in this chapter we will present two examples. The first guidance law is for target reaching, which

we will achieve using the pure pursuit guidance law also used in Chapters 8 and 9. The second guidance law is a line of sight (LOS) guidance law for path following of straight-line paths.

10.3.1 Pure pursuit guidance

The pure pursuit guidance law [16, 44] is a target reaching guidance law which we will employ when we wish to make the vehicle reach a static target position $\mathbf{p}_t^n \triangleq [x_t^n, y_t^n]$. To reach the target as soon as possible, we set the desired course to point towards the target position:

$$\psi_{pp}^n \triangleq \Psi(\mathbf{p}_t^{nb}) = \text{atan2}(y_t^n - y_b^n, x_t^n - x_b^n), \quad (10.20)$$

where ψ_{pp}^n is the desired course during pure pursuit guidance and the function Ψ is defined in (2.5).

Remark 10.2. If the target was not static, a velocity compensation term like the one computed in (10.14) could be used to compensate for the target velocity. The resulting course reference would then make the vehicle reach a (slower moving) target.

10.3.2 Line of sight guidance

In Chapters 4 and 5 we examined the integral line of sight (ILOS) path following law for underactuated surface vehicles in the presence of ocean currents. In this chapter, as the guidance law will provide course rather than heading references, we will assume that the effect of the ocean current is negligible, and remove the integral effect. LOS guidance without integral effect has been analyzed in Fossen and Pettersen [36], where it was proved that it provided uniform semiglobal exponential path convergence when applied to an underactuated marine vehicle as the one modeled in (10.1).

The guidance law is illustrated in Figure 10.2. The idea is to mimic the way an experienced helmsman steers a vehicle by aiming the vehicle course towards a point ahead of it on the path. Specifically, the target point lies a lookahead distance Δ meters ahead of the vehicle along the path, where Δ is a positive control parameter.

The LOS guidance law steers the vehicle almost straight towards the path when far away, and more parallel to the path as the vehicle gets closer. Thus, the vehicle makes a smooth turn onto the path.

In order to follow the path \mathcal{P} (10.7), the LOS guidance law is defined as:

$$\psi_{los}^n \triangleq \text{atan2}(-y_b^n, \Delta), \quad (10.21)$$

where ψ_{los}^n is the desired course during LOS guidance.

10.4 Course controller

In this section we will present the course controller used to follow the references from either the CAA guidance law or from a nominal guidance law. The course

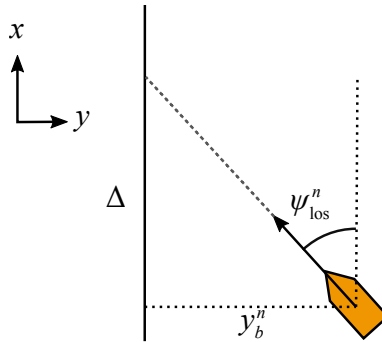


Figure 10.2: Illustration of the LOS guidance law steering the orange vehicle onto the path \mathcal{P} , which is drawn as a solid black line.

controller gives references to the yaw rate controller presented in Section 10.5, and is implemented as a proportional controller. To limit the turning rate, and hence the induced sway motion, the proportional effect is saturated. The controller is defined as:

$$r_{fd} \triangleq \dot{\psi}_{fd}^n - \text{sat}(k_\psi \tilde{\psi}_f^n, \sigma_\psi), \quad (10.22)$$

where r_{fd} is the desired course rate signal, the course error is denoted $\tilde{\psi}_f^n \triangleq \psi_{fd}^n - \psi_f^n \in (-\pi, \pi]$, the control gain k_ψ is a positive design parameter, and ψ_{fd}^n is the course reference from either one of the nominal guidance laws presented in Section 10.3, or from the CAA collision avoidance law in Section 10.2. The saturation function sat is defined as

$$\text{sat}(a, b) \triangleq \begin{cases} b, & a > b, \\ a, & a \in [-b, b], \\ -b, & a < -b. \end{cases} \quad (10.23)$$

The saturation parameter $\sigma_\psi > 0$ is a constant design parameter. In order to ensure that the saturation is in effect on an error in the interval $\tilde{\psi}_f^n \in (-\pi, \pi]$, we make the following assumption on σ_ψ :

Assumption 10.7.

$$\sigma_\psi \leq k_\psi \pi. \quad (10.24)$$

Remark 10.3. If Assumption 10.7 is not met, the saturation will not have any effect and can be removed.

A yaw rate reference signal \bar{r}_{bd} is then created by solving (10.4) for r_b :

$$\bar{r}_{bd} \triangleq \frac{U_b^2 r_{fd} - Y_v(u_b) u_b v_b + \dot{u}_b v_b}{X_v(u_b) u_b + U_b^2}. \quad (10.25)$$

This signal is ensured to be well defined by Assumption 10.3. Note that, when the control system switches mode, there is a discontinuity in \bar{r}_{bd} . To avoid this, we will in the next section introduce a bump function to ensure that the yaw rate signal is always continuous.

10.4.1 Yaw rate bump function

To avoid discontinuities in the desired yaw rate, and thus ensuring that the yaw rate controller in Section 10.5 is always able to follow the yaw rate reference, we introduce a linear bump function $\text{bump}(t_b)$:

$$\text{bump}(t_b) = \begin{cases} 1, & t_b \geq T_b, \\ \frac{t_b}{T_b}, & 0 < t_b < T_b, \\ 0, & t_b \leq 0, \end{cases} \quad (10.26)$$

where the bump time T_b is a positive constant.

As long as the yaw rate signal \bar{r}_{bd} from (10.25) is smooth, $r_{bd} = \bar{r}_{bd}$. However, if there is a jump in \bar{r}_{bd} at time t_1 , we apply the bump function:

$$r_{bd}(t) = r_{bd}(t_1) [1 - \text{bump}(t - t_1)] + \bar{r}_{bd}(t) \text{bump}(t - t_1). \quad (10.27)$$

This ensures that when $t \geq t_1 + T_b$, $r_{bd}(t) = \bar{r}_{bd}(t)$. If, at a time $t_2 \in (t_1, t_1 + T_b)$, $r_{bd}(t_2) = \bar{r}_{bd}(t_2)$, use of the smoothing function is stopped until the next discontinuity in \bar{r}_{bd} .

Remark 10.4. The value of T_b is a tuning parameter, which can be chosen to make the desired course rate comply with actuator constraints.

10.5 Surge and yaw rate controllers

The surge (10.1d) and yaw rate (10.1f) are controlled using the feedback linearizing controllers introduced in Section 4.2.2:

$$\tau_u = -F_u(u_b, v_b, r_b) + \dot{u}_{bd} - k_u(\tilde{u}_b), \quad (10.28a)$$

$$\tau_r = -F_r(u_b, v_b, r_b) + \dot{r}_{bd} - k_r(\tilde{r}_b), \quad (10.28b)$$

where $k_u > 0$ and $k_r > 0$ are constant control gains, and $\tilde{u}_b \triangleq u_b - u_{bd}$ and $\tilde{r}_b \triangleq r_b - r_{bd}$.

Inserting these controllers into (10.1d) and (10.1f) gives the following error dynamics:

$$\dot{\tilde{u}}_b = -k_u \tilde{u}_b, \quad (10.29a)$$

$$\dot{\tilde{r}}_b = -k_r \tilde{r}_b. \quad (10.29b)$$

The error dynamics are linear, and globally exponentially stable at the origin. Hence, as long as r_{bd} and u_{bd} are continuous signals, a vehicle described by (10.1) will be able to follow them as long as the following assumption is met:

Assumption 10.8. At time t_0 , the system has operated long enough for the surge and yaw rate to converge, i.e. $\tilde{u}_b(t_0) = 0$ and $\tilde{r}_b(t_0) = 0$.

Remark 10.5. To fulfill this assumption, the vehicle needs to be properly initialized before control is handed over to the automatic collision avoidance system, which is reasonable.

Remark 10.6. We have assumed that the vehicle is able to follow the surge speed reference during the maneuver. However, if there is a perturbation in the vehicle surge, the CAA algorithm will compensate the desired course according to the actual surge speed, as seen in (10.14). Thus, the output from the algorithm remains safe.

10.6 Analysis

This section contains a mathematical analysis of the system when in collision avoidance mode. For this section, we make the following assumption:

Assumption 10.9. The distance between any two obstacles are always at least $2d_{\text{switch}}$.

This assumption ensures that the vehicle will only have to avoid one obstacle at a time. We will throughout this section use the notation $X_{vd} = X_v(u_{bd})$ and $Y_{vd} = Y_v(u_{bd})$.

10.6.1 Upper bound on the vehicle sway

During the collision avoidance maneuver, the switching distance and the required course rate of the vehicle will depend on the vehicle's total speed $U_b = \sqrt{u_b^2 + v_b^2}$. To find an upper bound on the U_b , we need to find an upper bound on the sway movement v_b . This is done in the following lemma.

Lemma 10.1. *Let the vehicle be modeled by (3.26), and let Assumptions 10.2-10.8 hold. Suppose that r_{fd} depends on the vehicle sway speed v_b , and that for $v_{\text{sup}} > 0$,*

$$|r_{fd}(v_{\text{sup}})| < \frac{|Y_{vd}|}{|X_{vd}|} v_{\text{sup}}. \quad (10.30)$$

Finally, let $v_b(t_0) < v_{\text{sup}}$. Then,

$$v_b(t) < v_{\text{sup}} \quad \forall t \geq t_0. \quad (10.31)$$

Proof. When Assumption 10.8 holds, Lemma 10.1 is equivalent to Lemma 9.1 in the previous chapter. \square

We will treat v_{sup} as a design parameter. This parameter is in the next section used to find bounds on the minimum safety distance d_{safe} and on the course control proportional saturation σ_ψ , and can be used to adjust the aggressiveness of the collision avoidance maneuver to satisfy both scenario preferences and actuator constraints.

10.6.2 Bounds on safety distance and course control saturation

Before stating the next lemma, we recall the following term from Chapter 9:

$$F_\psi \triangleq |Y_{vd}|v_{\text{sup}} \left(\frac{1}{|X_{vd}|} - 2 \frac{v_{\text{sup}}u_{\text{omax}}}{\sqrt{U_{\text{bsup}}^2 - u_{\text{omax}}^2} (X_{vd}u_{bd} + U_{\text{bsup}}^2)} \right) - r_{\text{omax}} \frac{u_{\text{omax}}}{u_b} - \frac{a_{\text{omax}}}{\sqrt{u_b^2 - u_{\text{omax}}^2}}, \quad (10.32)$$

where $U_{\text{bsup}} \triangleq \sqrt{u_{bd}^2 + v_{\text{sup}}^2}$.

We also introduce the design parameter $\lambda_\psi \in (0, 1)$, which is used to prioritize between the course control proportional saturation σ_ψ and the safety distance d_{safe} . A high value of λ_ψ will give priority to a high σ_ψ , which will enable the vehicle to turn faster, while a low value of λ_ψ prioritizes a low d_{safe} , which will require a higher turning rate as the vehicle will maneuver closer to the obstacle.

Lemma 10.2. *Consider a vehicle modeled by (10.1). Let the vehicle be governed by the surge and yaw rate controllers (10.28) and the course controller (10.22). Let the control system enter collision avoidance mode at time t_1 , and let the course then be guided by the CAA algorithm (10.13). Furthermore, assume that the vehicle course satisfies $\psi_f^n(t_2) = \psi_{\text{dca}}^n(t_2)$ at some time $t_2 \geq t_1 + t_b$. Finally, let $\lambda_\psi \in (0, 1)$, and assume that the distance between the vehicle and the obstacle satisfies $d_{\text{ob}}(t) > d_{\text{safe}} \forall t \geq t_1$. If Assumptions 10.1-10.9 hold, the course control proportional saturation σ_ψ satisfies*

$$\sigma_\psi \leq \lambda_\psi F_\psi, \quad (10.33)$$

the safety distance d_{safe} satisfies

$$d_{\text{safe}} \geq \frac{(U_{\text{bsup}} + u_{\text{omax}})^2}{U_{\text{bsup}}} \frac{1}{(1 - \lambda_\psi)F_\psi}, \quad (10.34)$$

and the sway speed satisfies $|v_b(t_0)| < v_{\text{sup}}$, then

$$|v_b(t)| < v_{\text{sup}} \quad \forall t \geq t_0. \quad (10.35)$$

Proof. When Assumption 10.8 holds, we can use the proof of Lemma 9.2 to show that

$$\frac{(U_{\text{bsup}} + u_{\text{omax}})^2}{d_{\text{safe}}U_{\text{bsup}}} + \sigma_\psi \leq F_\psi, \quad (10.36)$$

where F_ψ is given in (10.32). The design parameter λ_ψ can be used to rewrite (10.36) as

$$\frac{(U_{\text{bsup}} + u_{\text{omax}})^2}{d_{\text{safe}}U_{\text{bsup}}} + \sigma_\psi \leq \lambda_\psi F_\psi + (1 - \lambda_\psi)F_\psi. \quad (10.37)$$

Hence, conditions (10.33) and (10.34) ensure that (10.36) is satisfied. It follows that Condition (10.30) of Lemma 10.1 then also applies, and hence if $|v_b(t_0)| < v_{\text{sup}}$, then $|v_b(t)| < v_{\text{sup}} \forall t \geq t_0$. \square

Remark 10.7. Lemma 10.2 and Lemma 9.2 are mostly equivalent. However, in Lemma 10.2 we use the saturation in the course controller to arrive at less conservative bounds than in Lemma 9.2.

10.6.3 Minimum switching distance

We will now provide a lower bound on the switching distance in order to ensure that the vehicle course angle is within ϵ radians of the desired course from the CAA algorithm before the obstacle can get too close to the vehicle.

Lemma 10.3. *Let a vehicle be modeled by (10.1), and let it be controlled by the feedback linearizing controllers (10.28) and the course controller (10.22). At a time $t_1 \geq t_0$, let the control system enter collision avoidance mode according to the switching rule (10.16), and let the vehicle course then be set by the collision avoidance law (10.13). Furthermore, let Assumptions 10.1-10.6 be satisfied, the vehicle speed satisfy $U_b < U_{b\text{sup}}$, and the switching distance satisfy*

$$d_{\text{switch}} \geq u_o t_\epsilon + d_{\text{safe}} + d_{\text{turn}} + d_{T_b}, \quad (10.38)$$

where

$$t_\epsilon \triangleq T_b + \left(\frac{\pi}{\sigma_\psi} - \frac{1}{k_\psi} \right) - \frac{\ln(k_\psi \epsilon / \sigma_\psi)}{k_\psi}, \quad \epsilon \in (0, \frac{\pi}{2}] \quad (10.39)$$

is the maximum amount of time the course controller (10.22) will use to make the vehicle converge to within ϵ rad of ψ_{dca}^n , and

$$d_{\text{turn}} \triangleq \frac{U_{b\text{sup}}}{\min(\sigma_\psi, k_\psi \frac{\pi}{2})} \quad (10.40)$$

upper bounds the distance traveled by the vehicle in the $\psi_f^n(t_1)$ direction when making a complete π rad turn. The distance d_{T_b} is

$$d_{T_b} \triangleq U_{b\text{sup}} T_b. \quad (10.41)$$

Then, the vehicle is able to converge to within ϵ rad of ψ_{dca}^n before the obstacle can come within the distance d_{safe} .

Proof. The main idea behind the proof is to show that the distance traveled by the obstacle during the convergence time t_ϵ is not enough to reduce the distance between the obstacle and the vehicle trajectory as it turns away from the obstacle to less than d_{safe} . This is illustrated in Figure 10.3.

We consider a worst case scenario with an obstacle of infinite size, $R_o \rightarrow \infty$. The obstacle tangent angle is then $\gamma_t = \pi/2$. Furthermore, the vehicle and the obstacle move at maximum speed, i.e. $U_b(t_1) = U_{b\text{sup}}$ and $u_o(t_1) = u_{o\text{max}}$. We assume, without loss of generality, that the obstacle is ahead of the vehicle on the x -axis of the NED frame, $x_o^n(t_1) - x_b^n(t_1) = d_{\text{switch}}$, while $y_o^n(t_1) = x_o^n(t_1) = 0$, and that they move straight towards each other, $\psi_f^n(t_1) = 0$ and $\psi_o^n(t_1) = \pi$. The worst case behavior of the obstacle is then to continue moving straight towards the vehicle at maximum speed, $u_o(t > t_1) = u_{o\text{max}}$ and $\psi_o^n(t > t_1) = \pi$.

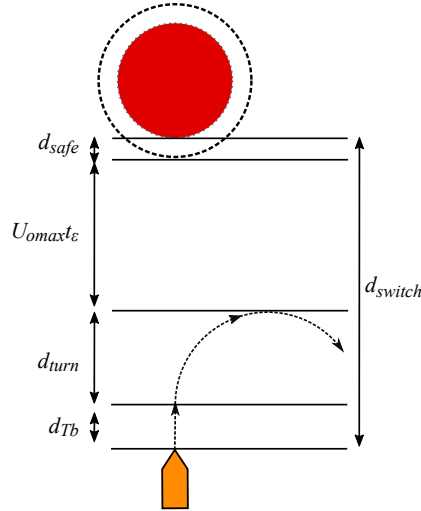


Figure 10.3: Illustration of the minimum required switching distance.

At time t_1 , when the control system enters collision avoidance mode, the vehicle starts to make a turn towards ψ_{dca}^n . There will then be a jump in the desired yaw rate from the course controller, and the yaw rate smoothing (10.27) will commence. The smoothing is complete at time $t_1 + T_b$. Since $\tilde{\psi}_f^n \in (-\pi, \pi]$, the maximum course error at time $t = t_1 + T_b$ is π radians. The convergence time from $|\tilde{\psi}_f^n| = \pi$ to $|\tilde{\psi}_f^n| = \sigma_{\psi}/k_{\psi}$ is found from (10.22) to be $\pi/\sigma_{\psi} - 1/k_{\psi}$, which is ensured to be positive from Assumption 10.7. From this point, the course converges exponentially, and hence the convergence time from $|\tilde{\psi}_f^n| = \sigma_{\psi}/k_{\psi}$ to $|\tilde{\psi}_f^n| < \epsilon$ is $\frac{\ln(k_{\psi}\epsilon/\sigma_{\psi})}{k_{\psi}}$.

It follows that the total time from t_1 until $|\tilde{\psi}_f^n| \leq \epsilon$ is t_{ϵ} as defined in (10.39). During this time, the obstacle will, at worst, have traversed $u_{\text{omax}} t_{\epsilon}$ towards the vehicle.

During the smoothing interval $t \in (t_1, t_1 + T_b]$, the distance covered by the vehicle towards the obstacle is upper bounded by d_{T_b} . During the first $\pi/2$ radians of the following turn, the vehicle will move towards the obstacle. We see from geometry that the compensated vision cone \mathcal{V}_c will then expand. Hence, ψ_{dca}^n will move away from ψ_f^n during this part of the turn, and the turning rate of the vehicle can be lower bounded by setting $\dot{\psi}_{fd}^n = 0$ in the course controller. In a worst case scenario, the vehicle has to turn completely around. Assumption 10.7 then ensures that the vehicle will move at most d_{turn} towards the obstacle when turning.

Hence, if condition (10.38) holds, then the distance between the obstacle and the vehicle trajectory will not be reduced to less than d_{safe} before the vehicle course has converged to within ϵ rad of ψ_{dca}^n . It follows that the distance to the obstacle is more than d_{safe} , which concludes the proof. \square

We are now ready to state the main theorems of the chapter, namely safe maneuvering both in a target reaching and in a path following scenario. Before we

state these theorems, we need to assume that the vehicle starts safely:

Assumption 10.10.

$$d_{ob}(t_0) > d_{\text{switch}}. \quad (10.42)$$

Remark 10.8. Like Assumption 10.8, this assumption corresponds to assuming that the vehicle is safely initialized before control is handed over to the automatic collision avoidance system.

Due to the smoothing time T_b of the yaw rate reference signal, we also need at least one of the following assumptions to hold:

Assumption 10.11. The obstacle will not actively turn towards the vehicle when $d_{ob} \leq d_{\text{switch}}$.

or

Assumption 10.12. The smoothing time T_b is small enough to be neglected, i.e.

$$(u_{\text{omax}} + U_{\text{bsup}})T_b \ll d_{\text{safe}}. \quad (10.43)$$

Remark 10.9. These assumptions require the obstacle to at least not be actively seeking a collision with the vehicle if the vehicle dynamics make T_b large. Such behavior is for example in accordance with the COLREGs, which both states that a vehicle should behave predictably in a collision avoidance scenario, and that if one vehicle has significantly better maneuverability than the other, then the most maneuverable one should yield. At one extreme, we could consider an oil tanker which use a very long time to initiate a turn, and thus would rely on Assumption 10.11, while on the other extreme we could consider a small speed boat, where Assumption 10.12 can safely be made.

10.6.4 Safe target reaching

In this section, we will provide conditions to ensure that the CAA collision avoidance algorithm (10.13) in combination with the pure pursuit guidance law (10.20) enables the vehicle to safely maneuver to the target. In order to do this, we must assume that the distance from the target to the obstacle is greater than the minimum obstacle distance:

Assumption 10.13. The distance $d_{ot}(t)$ from the target to the obstacle satisfies

$$d_{ot}(t) > \frac{R_o}{\cos(\alpha_o)} - R_o \quad \forall t \geq t_0. \quad (10.44)$$

Theorem 10.4. *Let Assumptions 10.1-10.10 and 10.13 hold, and let either Assumption 10.11 or Assumption 10.12 hold as well. Let the avoidance angle satisfy*

$$\alpha_o \in \left[\cos^{-1} \left(\frac{R_o}{R_o + d_{\text{safe}}} \right) + \epsilon, \frac{\pi}{2} \right) \quad (10.45)$$

and the switching distance satisfy

$$d_{\text{switch}} \geq u_{\text{omax}}t_\epsilon + d_{\text{safe}} + d_{\text{turn}} + d_{T_b}, \quad (10.46)$$

where t_ϵ , d_{turn} and d_{T_b} are defined in Lemma 10.3. Furthermore, let the course control proportional saturation level σ_ψ and the safety distance d_{safe} satisfy the conditions of Lemma 10.2:

$$\sigma_\psi \leq \lambda_\psi F_\psi, \quad (10.47)$$

$$d_{\text{safe}} \geq \frac{(U_{\text{bsup}} + u_{\text{omax}})^2}{U_{\text{bsup}}} \frac{1}{(1 - \lambda_\psi)F_\psi}. \quad (10.48)$$

Finally, let the initial vehicle sway speed satisfy $|v_b(t_0)| < v_{\text{sup}}$ and the target reaching acceptance distance satisfy

$$d_a > \frac{U_{\text{bsup}}|X_{vd}|}{|Y_{vd}|v_{\text{sup}} - |X_{vd}|\sigma_\psi}. \quad (10.49)$$

Then, a vehicle described by (10.1), controlled by the surge and yaw rate controllers (10.28), the course controller (10.22), the pure pursuit guidance law (10.20) and the CAA collision avoidance law (10.13) will maneuver among obstacles described by (10.9) while ensuring that

$$d_{\text{ob}}(t) \geq d_{\text{safe}} > 0 \quad \forall t \geq t_0. \quad (10.50)$$

Furthermore, if there is just one obstacle, then there is a time $t_f > t_0$ at which

$$|\mathbf{p}_t^{n_b}| = |\mathbf{p}_t^n - \mathbf{p}_b^n| \leq d_a. \quad (10.51)$$

Proof. An upper bound on the required turning rate of the pure pursuit guidance law (10.20) can be found geometrically as:

$$|\dot{\psi}_{\text{pp}}^n| < \frac{U_{\text{bsup}}}{d_a} \quad (10.52)$$

When we insert (10.52) into the course controller (10.22) we get a maximum course rate of

$$|r_{f\text{pp}}| < \frac{U_{\text{bsup}}}{d_a} + \sigma_\psi. \quad (10.53)$$

From Lemma 10.1 it then follows that if

$$d_a > \frac{U_{\text{bsup}}|X_v|}{|Y_v|v_{\text{sup}} - |X_v|\sigma_\psi}, \quad (10.54)$$

and $|v_b(t_0)| < v_{\text{sup}}$, then $|v_b(t)| < v_{\text{sup}}$ until a time t_1 when the vehicle enters collision avoidance mode. It then follows from Lemma 10.2 that v_b is bounded by

$$|v_b(t)| < v_{\text{sup}} \quad \forall t \in [t_0, t_f]. \quad (10.55)$$

Hence, the vehicle speed is bounded by $U_b < U_{b\text{sup}}$. Denote the time when (10.16) is fulfilled by $t_1 \geq t_0$. At this time, the control system enters collision avoidance mode. Lemma 10.3 then ensures that there is a time $t_2 > t_1$ when $d(t_1) \geq d_{\text{safe}}$ and $\psi_f^n(t_2) - \psi_{dca}^n(t_2) \leq \epsilon$. Since the yaw rate reference signal r_{bd} is smooth by (10.27), the vehicle course has a locally exponentially stable equilibrium at $\tilde{\psi}_f^n = 0$ when the course controller (10.22) is employed. Hence, it is ensured that

$$\psi_f^n(t) - \psi_{dca}^n(t) \leq \epsilon, \quad \forall t \in [t_2, t_3], \quad (10.56)$$

where t_3 is the time when the control system will exit collision avoidance mode. Hence, Lemma 7.2 ensures that

$$d_{ob}(t) \geq d_{\text{safe}} \quad \forall t \in [t_2, t_3], \quad (10.57)$$

which satisfies condition (10.50).

Since the vehicle circles the obstacle, there will be a time t_3 when the direction to the target will be outside of \mathcal{V}_c . The vehicle will then exit collision avoidance mode and proceed towards the target. \square

10.6.5 Safe path following

In this section, we will provide conditions to ensure that the CAA collision avoidance algorithm (10.13) in combination with the line of sight guidance law (10.21) enables the vehicle to safely maneuver around an obstacle and reach the path. In this Section we will assume that there is just one obstacle.

Theorem 10.5. *Let Assumptions 10.1-10.8, 10.10 and 10.13 hold, and let either Assumption 10.11 or Assumption 10.12 hold as well. Let the avoidance angle satisfy*

$$\alpha_o \in \left[\cos^{-1} \left(\frac{R_o}{R_o + d_{\text{safe}}} \right) + \epsilon, \frac{\pi}{2} \right) \quad (10.58)$$

and the switching distance satisfy

$$d_{\text{switch}} \geq u_{\text{omax}} t_\epsilon + d_{\text{safe}} + d_{\text{turn}} + d_{T_b}, \quad (10.59)$$

where t_ϵ , d_{turn} and d_{T_b} are defined in Lemma 10.3. Furthermore, let the course control proportional saturation level σ_ψ and the safety distance d_{safe} satisfy the conditions of Lemma 10.2:

$$\sigma_\psi \leq \lambda_\psi F_\psi, \quad (10.60)$$

$$d_{\text{safe}} \geq \frac{(U_{b\text{sup}} + u_{\text{omax}})^2}{U_{b\text{sup}}} \frac{1}{(1 - \lambda_\psi) F_\psi}. \quad (10.61)$$

Finally, let the initial vehicle sway speed satisfy $|v_b(t_0)| < v_{\text{sup}}$ and the lookahead distance Δ satisfy

$$\Delta \geq \frac{U_{b\text{sup}} |X_{vd}|}{(|Y_{vd}| v_{\text{sup}} - |X_{vd}| \sigma_\psi)}. \quad (10.62)$$

Then, a vehicle described by (10.1), controlled by the surge and yaw rate controllers (10.28), the course controller (10.22), the line of sight guidance law (10.21) and the CAA collision avoidance law (10.13) will converge to and follow a path \mathcal{P} given by (10.7) until it encounters an obstacle modeled by (10.9). The obstacle will be safely avoided, and the vehicle will converge to the path again after the collision avoidance maneuver. Furthermore, it is ensured that

$$d_{ob}(t) \geq d_{\text{safe}} > 0 \quad \forall t \geq t_0. \quad (10.63)$$

Proof. The required turning rate of the LOS guidance law is found as

$$\dot{\psi}_{\text{los}}^n = -\frac{\Delta \dot{y}_b^n}{\Delta^2 + y_b^{n2}}, \quad (10.64)$$

which is bounded as

$$|\dot{\psi}_{\text{los}}^n| \leq \frac{U_{b\text{sup}}}{\Delta}. \quad (10.65)$$

Inserting (10.65) into the course controller (10.22) gives a maximum desired course rate of

$$|r_{f\text{los}}| \leq \frac{U_{b\text{sup}}}{\Delta} + \sigma_\psi. \quad (10.66)$$

Applying Lemma 10.1 on (10.66) gives that if

$$\Delta \geq \frac{U_{b\text{sup}} |X_{vd}|}{(|X_{vd}| v_{\text{sup}} - |X_{vd}| \sigma_\psi)}, \quad (10.67)$$

and $|v_b(t_0)| < v_{\text{sup}}$, then $|v_b(t)| < v_{\text{sup}}$ until a time t_2 when the vehicle enters collision avoidance mode. Along with Lemma 10.2, we then obtain that

$$|v_b(t)| < v_{\text{sup}} \quad \forall t \in [t_0, t_f]. \quad (10.68)$$

The rest of the proof is equivalent to the proof of Theorem 10.4. \square

10.7 Simulation results

In this section we present numerical simulations of an underactuated marine vehicle using the proposed collision avoidance algorithm. The simulated vehicle is a Hugin AUV [43] operating in a horizontal plane. The desired vehicle surge speed is set to $u_{bd} = 2$ m/s, and the maximum allowable sway speed is set to $v_{\text{sup}} = 2$ m/s. It can be verified that Assumption 10.2 is satisfied with $Y_{vd} = -1.10$, and that Assumption 10.3 is satisfied with $X_{vd} = -1.59$. The initial sway velocity was zero in all simulations, while $u_b(t_0) = 2$ m/s and $\psi_b^n(t_0) = 0$ rad.

In the three first scenarios the vehicle encounters an obstacle head on, from the starboard side and from the port side, respectively. These scenarios all contain a circular obstacle with radius $R_o = 15$ m. The obstacle speed is $u_o = 1$ m/s, which satisfies Assumption 10.6, and the obstacle does not turn or accelerate. The course control proportional saturation level σ_ψ is set to 0.17 rad/s, and the safety distance is set to $d_{\text{safe}} = 10$ m, which satisfies the conditions of Lemma 10.2 with $\lambda_\psi = 0.25$.

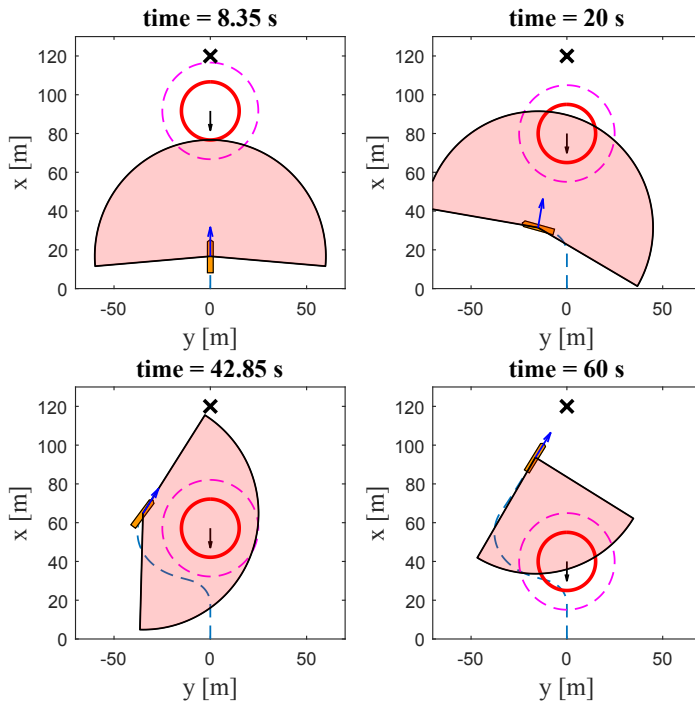


Figure 10.4: The vehicle meets an obstacle head on in the first scenario. The vehicle is shown in orange, while the obstacle is a solid red circle. A dashed magenta circle shows d_{safe} , while \mathcal{V}_c is shown as a semi-opaque red sector of radius d_{switch} . The target position is marked by an 'X', and the blue arrow denotes ψ_{pp}^n . The size of the vehicle has been exaggerated for clarity.

The course control gain k_ψ is set to 0.4 s^{-1} , satisfying (10.24), while the convergence parameter ϵ is set to $\epsilon = 0.05 \text{ rad}$. The switching distance d_{switch} is set to 60 m, while α_o is set to 0.97 rad, satisfying (10.34) and (10.45).

The first scenario is illustrated in Figure 10.4. The vehicle steers towards a target position using the pure pursuit guidance law (10.20). The obstacle starts in front of the vehicle on a head on collision course. At time 8.35 s the vehicle reaches the switching distance d_{switch} from the obstacle, and enters collision avoidance mode in accordance with the switching rule (10.16). Since the vehicle and the obstacle are on a head on collision course, the choice of turning direction (10.18) becomes random. In this case, the vehicle makes a port turn. The vehicle maneuvers safely around the vehicle until time 42.85 s, when the direction towards the target comes outside of the unsafe cone. The vehicle then proceeds towards the target in accordance with Theorem 10.4.

In the second scenario, which is shown in Figure 10.5, the obstacle crosses from starboard. The pure pursuit guidance law is again employed to take the vehicle

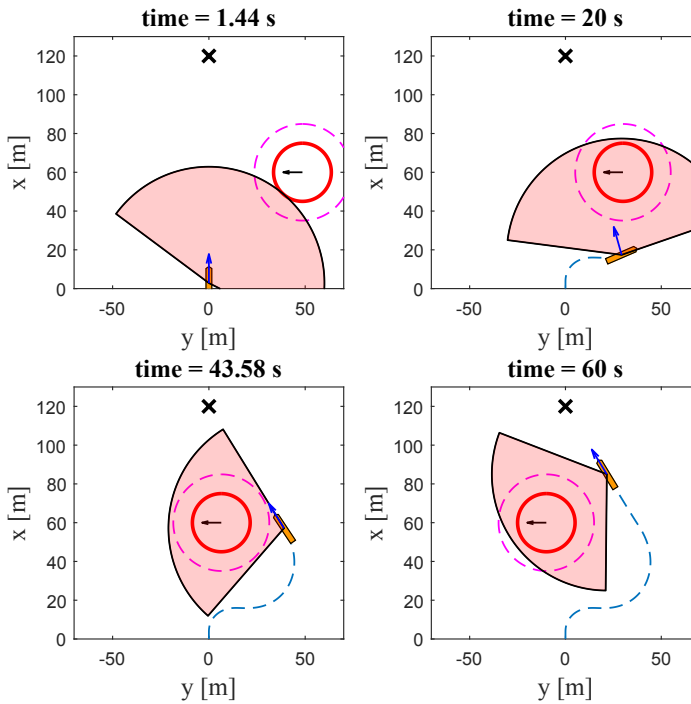


Figure 10.5: The second scenario, where the obstacle crosses from starboard.

towards the target position. When the control system enters collision avoidance mode at time 1.44s, the vehicle turns starboard to maneuver behind the obstacle. At time 43.58s, the direction to the target is safe and the vehicle proceeds towards it.

The collision avoidance algorithm in combination with the LOS guidance law (10.21) is demonstrated in the third scenario, which is shown in Figure 10.6. The obstacle now crosses in front of the vehicle from the port side, while the vehicle follows a straight-line path along the x^n -axis. At time 6.47s the desired course from the LOS guidance law, ψ_{los}^n , comes within \mathcal{V}_c , and the control system enters collision avoidance mode. The vehicle maneuvers safely behind the obstacle, until ψ_{los}^n becomes safe again. At this point, the vehicle converges to the path as stated in Theorem 10.5.

The obstacle distance during the three scenarios is shown in Figure 10.7, where it can be seen that the distance is always above the safety distance d_{safe} . In Figure 10.8, the sway velocity of the vehicle during the three scenarios are shown. The magnitude of the vehicle sway increases as the vehicle turns, but remains well below the limit of 2 m/s. Hence, the simulations validate the results of Theorems 10.4 and 10.5.

While the analysis in Section 10.6 assumes that the obstacle is circular, the

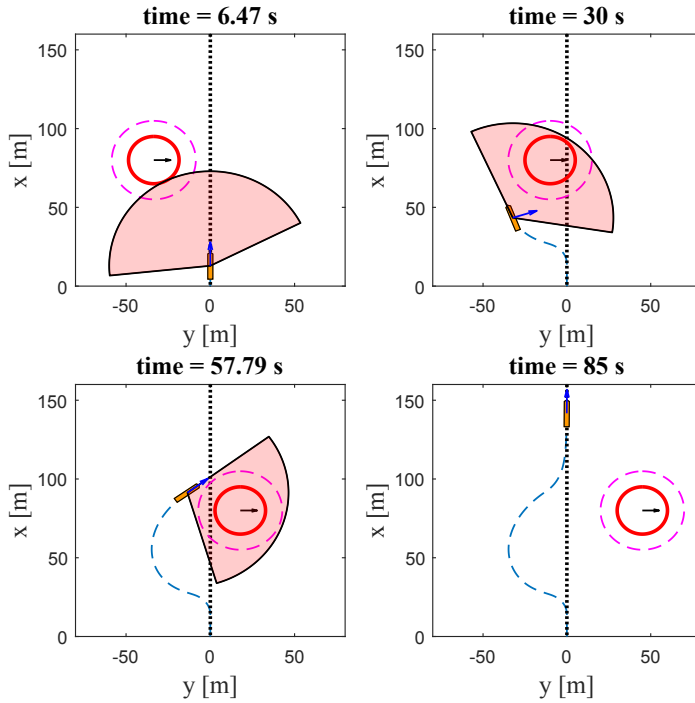


Figure 10.6: The third scenario, where the obstacle crosses from port and the vehicle follows a straight-line path marked by the dotted black line. The blue arrow here denotes ψ_{los}^n .

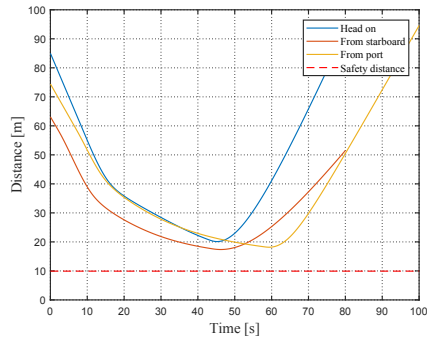


Figure 10.7: The distance from the vehicle to the obstacle during the three scenarios.

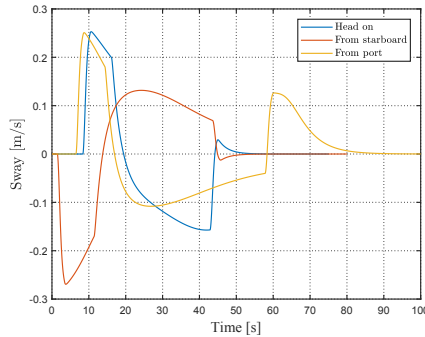


Figure 10.8: The vehicle sway during the three scenarios.

CAA collision avoidance algorithm can be applied to obstacles of any shape. This is demonstrated in the fourth scenario, shown in Figure 10.9, where the obstacle has the shape of a ship that is 70 m long and 10 m wide. The ship approaches the vehicle from the north east, and again the vehicle moves safely behind the obstacle in order to avoid it.

10.8 Experimental results

The CAA algorithm has been implemented into the control system of the research vessel R/V Gunnerus as part of an experimental setup. The R/V Gunnerus, a research vessel owned and operated by the Norwegian University of Science and Technology (NTNU), is a 31.25 m long vehicle steered by two azimuth thrusters. The control system is a Kongsberg Maritime K-Pos DP-11 system. Further details on the R/V Gunnerus can be found in Skjetne et al. [98]. The CAA collision avoidance algorithm (Section 10.2) and the LOS path following guidance law (Section 10.3.2) were implemented at the guidance level of the K-Pos DP-11 system. Our algorithm thus provided heading references to an underlying heading controller, which included smoothing and control allocation. The details of the heading controller was not available to us, but the modular nature of both the CAA and LOS algorithm still made it possible to implement and tune the algorithms. We received measurements of all vehicle states, and added a simple low-pass filter to the surge and sway measurements in order to filter out the effect of waves. The heading controller allowed us to set a maximum turning rate, which was set to $90^\circ/\text{s}$. The speed controller was not available in this experimental mode, and the thrust level was set to a constant, providing a forward speed of about 4 m/s.

The experiments were conducted in the Trondheim fjord. The vehicle was set to follow straight-line path segments. Along the path, the vehicle encountered virtual obstacles in several different scenarios. One scenario is shown in Figure 10.10, where the vehicle encountered two obstacles with a radius of 100 m. The obstacles moved with a speed of 2 m/s; one straight towards the vehicle slightly on its port side, and one approaching from starboard. The avoidance angle was set to 1.1 rad,

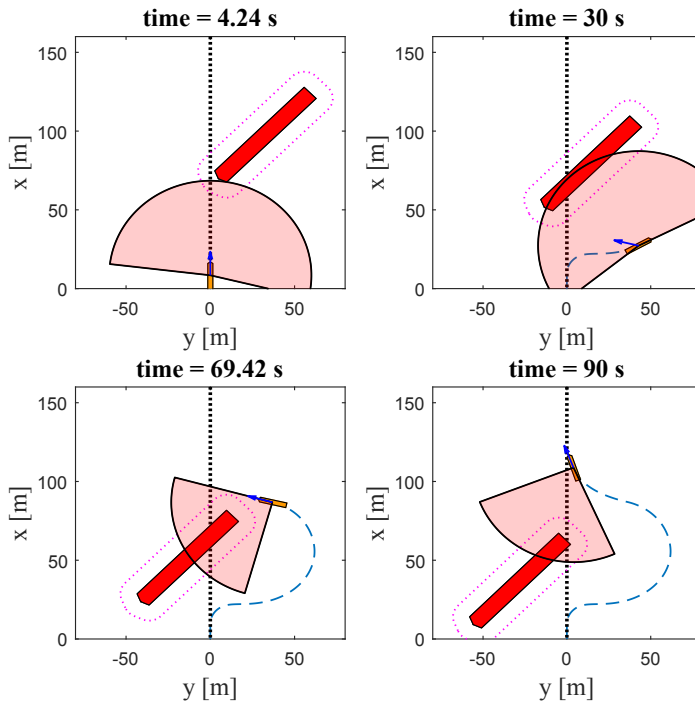


Figure 10.9: The fourth scenario, where the obstacle is ship shaped.

and the safety distance to 120.4m. At 15:07:30, the first obstacle came within a switching distance, and the vehicle turned starboard to avoid it according to the switching rule presented in Section 10.2. At 15:10:30, the second obstacle came within switching distance, and the vision cone to this obstacle was merged with the vision cone to the first. The vehicle adjusted its course to also avoid this obstacle. At 15:17:00, both obstacles had been successfully avoided and the vehicle returned to path following.

In another scenario, shown in Figure 10.11, the vehicle encountered a convoy of five obstacles moving straight towards it at a speed of 2 m/s. Again, the obstacle radius was set to 100m, while the avoidance angle was set to 0.9 rad, the safety distance to 60.9m and the switching distance to 800m. The first obstacle was encountered at 11:20:00, and the vehicle entered collision avoidance mode and turned starboard. As the vehicle moved along the convoy, it encountered the obstacles one by one and adjusted its course to avoid them. As described in Section 7.2.4, the turning direction was kept constant (in this case $j = 1$), thus avoiding that the vehicle tried to cross the convoy during the maneuver. The vehicle successfully avoided all five obstacles, and returned to path following.

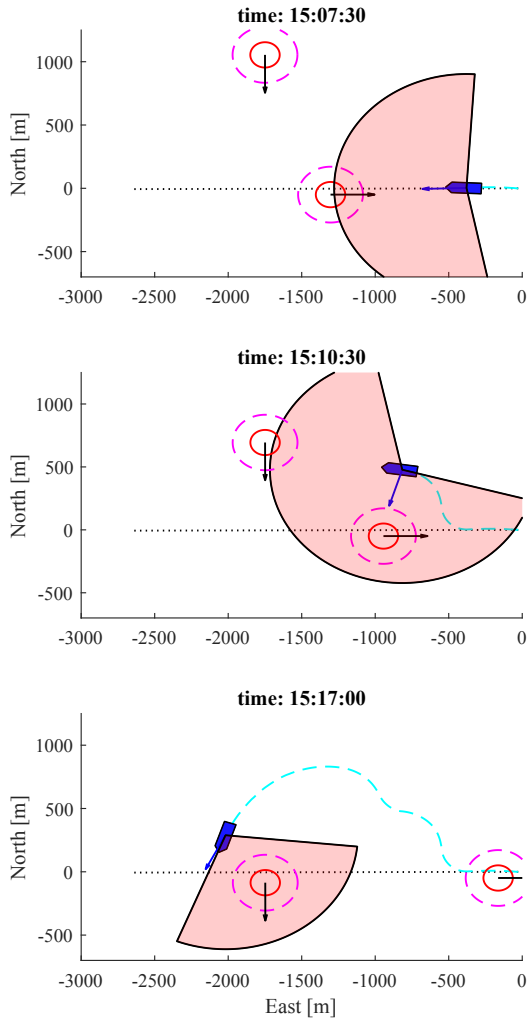


Figure 10.10: Experimental run with two obstacles. The size of the vehicle is exaggerated in the picture for clarity.

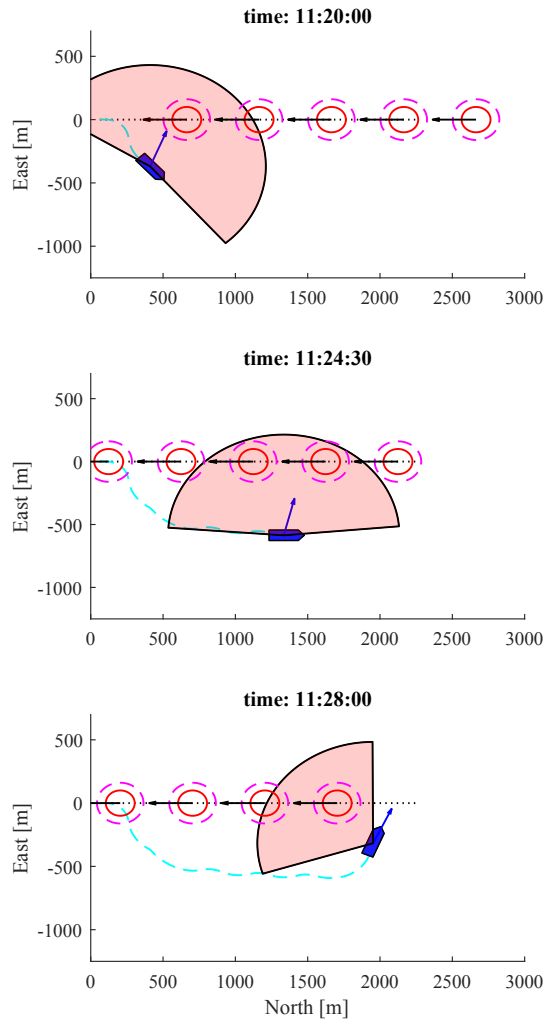


Figure 10.11: Experimental run with five obstacles.

10.9 Conclusions

We have in this chapter applied the CAA algorithm to a vehicle modeled using a 3 DOF maneuvering model of a marine craft. Specifically, we have added controllers to the directly actuated surge and yaw dynamics, and have shown how a smoothing of the yaw rate reference signal enables the system to handle the discontinuities that arise when entering and leaving collision avoidance mode. By augmenting the analysis to consider also the time required for the yaw rate controller to converge, we have thus extended the results of the previous chapter to include a complete dynamic vehicle model.

The CAA algorithm is designed to be modular, in order to facilitate implementation both on vehicles with different nominal guidance controllers, and vehicles with different and possibly unknown low-level controllers. We have demonstrated the former by analyzing the algorithm both in combination with the pure pursuit target reaching algorithm employed in Chapters 8 and 9, and with a line of sight path following law related to the one examined in Part II. In both cases, conditions have been found under which the vehicle is guaranteed to be safe, and under which the control objectives will be reached while keeping a limited sway movement.

Modularity with respect to the underlying controllers has been verified using full-scale experiments aboard the R/V Gunnerus. We have thus shown that the algorithm can be used on marine vessels with widely different characteristics and maneuvering capabilities. Furthermore, the experimental results indicate that the algorithm is robust to noise such as wave disturbances, as well as to operating on a vessel where the details of the low-level controllers and vehicle model are not available. Both the simulations and the experiments show that the vehicle keeps well away from the obstacle, which suggest that the conditions derived in Theorems 10.4 and 10.5 are conservative.

Finally, while the analyses in Part III of this thesis have assumed sparse scenarios with circular obstacles that can be avoided one at a time, we have shown in the simulations and the experiments both that the algorithm can be applied to obstacles of different shapes, and how to extend the algorithm to a multi-obstacle scenario. However, a thorough analysis of such scenarios, which would include extending the algorithm to several, cooperative agents, remains a topic of future work.

This chapter is the final chapter in which we examine the CAA algorithm in 2D. It is thus a conclusion of Part III of the thesis. In Part IV, we will extend the algorithm to 3D, which provides more flexibility when choosing a safe velocity direction, but at the cost of a higher complexity in the design and the analysis of the control system.

10.A Functional expressions

The functions F_u , F_r , X_v and Y_v are defined in Section 3.2.1, and reiterated here for convenience:

$$F_u(u_b, v_b, r_b) \triangleq \frac{1}{m_{11}}(m_{22}v_b + m_{23}r_b)r_b - \frac{d_{11}}{m_{11}}u_b, \quad (10.69)$$

$$\begin{aligned}
 F_r(u_b, v_b, r_b) &\triangleq \frac{m_{23}d_{22} + m_{22}(d_{32} + (m_{22} - m_{11})u_b)}{m_{22}m_{33} - m_{23}^2}v_b \\
 &+ \frac{m_{23}(d_{23} - m_{11}u_b) - m_{22}(d_{33} + m_{23}u_b)}{m_{22}m_{33} - m_{23}^2}r_b,
 \end{aligned} \tag{10.70}$$

$$X_v(u_b) \triangleq \frac{m_{23}^2 - m_{11}m_{33}}{m_{22}m_{33} - m_{23}^2}u_b + \frac{d_{33}m_{23} - d_{23}m_{33}}{m_{22}m_{33} - m_{23}^2}, \tag{10.71}$$

$$Y_v(u_b) \triangleq \frac{(m_{22} - m_{11})m_{23}}{m_{22}m_{33} - m_{23}^2}u_b - \frac{d_{22}m_{33} - d_{32}m_{23}}{m_{22}m_{33} - m_{23}^2}. \tag{10.72}$$

Part IV

Collision Avoidance in 3D

Chapter 11

The CAA algorithm in 3D

That's no moon, it's a space station!

— Obi-Wan Kenobi, *Star Wars episode IV - A New Hope*

In Part IV of this thesis we will extend the CAA algorithm presented in Part III to 3 dimensions. In this chapter we give a detailed description of the algorithm. The main idea behind the algorithm is to create a 3D extended vision cone around the obstacle. Each ray of the vision cone keeps a constant avoidance angle to the obstacle, and it is thus ensured that a vehicle following one of these rays will maintain at least a minimum safety distance to the obstacle during a collision avoidance maneuver.

If the obstacle is moving, the extended vision cone is transformed to compensate for the obstacle motion, creating a compensated vision cone. Any direction along this cone is proven to be safe, and the algorithm thus offers the opportunity to exploit the flexibility of operating in 3D space when choosing among the rays. We will show this flexibility can be utilized by making the vehicle move behind a moving obstacle, while also minimizing the desired pitch and yaw rate. The pitch of the desired velocity direction can furthermore be bounded in order to make the vehicle comply to constraints on the allowable pitch angle. For safety reasons, such constraints are often present vehicles operating in 3D.

In Section 11.1 of this chapter we will provide the obstacle model used in Part IV of this thesis. In Section 11.2, we will provide a description of the algorithm, including a method to choose which among the rays of the compensated vision cone the vehicle should follow. A preliminary analysis of the algorithm is given in Section 11.3, and some concluding remarks and an overview of the remainder of Part IV is provided in Section 11.4.

The work presented in this chapter is based on Wiig et al. [115], Wiig et al. [116] and Wiig et al. [118].

11.1 Obstacle model

This section contains a mathematical description of the obstacle, as well as a description of the sensor measurements required to implement the 3D CAA algorithm described in Section 11.2.

The obstacle is modeled in 5 DOF as a sphere with radius R_o , with the obstacle frame o at the center. The position and orientation of o with respect to the NED

frame is represented by $\boldsymbol{\eta}_o^n \triangleq [\mathbf{p}_o^n, \theta_o^n, \psi_o^n]^T$, where $\mathbf{p}_o^n \triangleq [x_o^n, y_o^n, z_o^n]^T$. The obstacle speed is u_o , and the obstacle's angular velocity is $\boldsymbol{\omega}_{o/n}^o \triangleq [q_o, r_o]^T$, where q_o and r_o are the pitch and yaw rate of the obstacle, respectively. Thus, the obstacle model is

$$\dot{\boldsymbol{\eta}}_o^n = \mathbf{J}(\boldsymbol{\eta}_o^n) \boldsymbol{\nu}_{o/n}^o, \quad (11.1a)$$

$$\dot{u}_o = a_o, \quad (11.1b)$$

where $\boldsymbol{\nu}_{o/n}^o \triangleq [u_o, 0, 0, q_o, r_o]^T$, a_o is the obstacle's acceleration and the transformation matrix $\mathbf{J}(\boldsymbol{\eta}_o^n)$ is

$$\mathbf{J}(\boldsymbol{\eta}_o^n) \triangleq \begin{bmatrix} \mathbf{R}_{zy}(\theta_o^n, \psi_o^n) & 0 \\ 0 & \mathbf{T}_o^n(\theta_o^n) \end{bmatrix}, \quad (11.2)$$

where $\mathbf{T}_o^n(\theta_o^n) = \text{diag}\{1, 1/\cos(\theta_o^n)\}$. We furthermore denote the obstacle's linear velocity in n as $\mathbf{v}_{o/n}^n \triangleq \dot{\mathbf{p}}_o^n$. Since the dynamic parameters of the obstacle can be difficult to estimate, we do not include them in the model. However, we assume that the obstacle's acceleration and angular velocity are bounded:

Assumption 11.1. The obstacle acceleration a_o and angular velocity are bounded by

$$a_o \in [-a_{o\max}, a_{o\max}], \quad (11.3a)$$

$$\|\boldsymbol{\omega}_{o/n}^o\| \in [-\omega_{o\max}, \omega_{o\max}], \quad (11.3b)$$

where $a_{o\max} \geq 0$ and $\omega_{o\max} \geq 0$ are constant parameters.

Remark 11.1. The algorithm can also be applied to non-spherical obstacles. However, an analysis containing such obstacles is beyond the scope of this thesis.

To ensure that the vehicle is able to circumvent the obstacle, we need to assume that the obstacle speed is less than the desired vehicle surge speed:

Assumption 11.2. The obstacle forward speed u_o satisfies $u_o \in [0, u_{o\max}]$, where $u_{o\max} < u_{bd}$.

11.1.1 Required obstacle measurements

We require that the vehicle is able to measure the distance $d_{ob} \triangleq \|\mathbf{p}_b^n - \mathbf{p}_o^n\|$ to the obstacle, as well as the angles to the edge of the obstacle. These angles define a three-dimensional vision cone \mathcal{V}_o , which is illustrated in Figure 11.1. For underwater vehicles, sensors such as sonars can give both d_{ob} and \mathcal{V}_o .

In addition, we require that the vehicle is able to sense the obstacle velocity, $\mathbf{v}_{o/n}^n$, which can either be measured directly using a sensor with Doppler effects, or indirectly using a tracking algorithm.

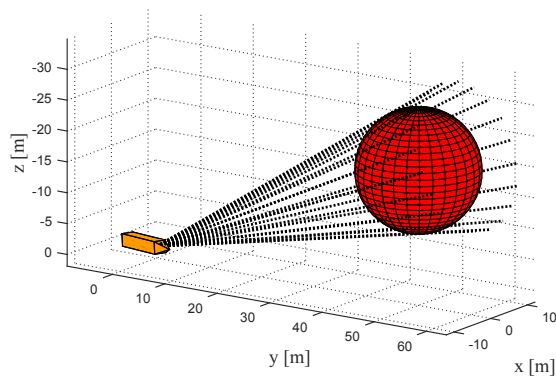


Figure 11.1: A sample of rays (dotted black) creating the vision cone from the vehicle (yellow) to the obstacle (red).

11.2 Algorithm definition

In this section we will present the CAA algorithm in 3D. The algorithm consists of three components; the creation of a motion compensated vision cone \mathcal{V}_c (Section 11.2.1), choosing a direction among the rays of \mathcal{V}_c , and a rule for entering and leaving collision avoidance mode (Section 11.2.3). In addition, we provide a brief description in Section 11.2.4 of how to extend the algorithm to handle multiple obstacles.

11.2.1 The motion compensated vision cone

To get a cone from the vehicle to the obstacle where each ray has an avoidance angle $\alpha_o \in [0, \pi/2)$ to the obstacle, the vision cone \mathcal{V}_o is extended to a cone \mathcal{V}_e as illustrated in Figure 11.2. In the case of a spherical obstacle, an analytical expression for the apex angle of \mathcal{V}_o is $2\gamma_a$, where

$$\gamma_a \triangleq \sin^{-1} \left(\frac{R_o}{R_o + d_{ob}} \right), \quad (11.4)$$

while the apex angle of \mathcal{V}_e can be found as $\gamma_e \triangleq 2(\gamma_a + \alpha_o)$.

Remark 11.2. If the obstacle is not spherical, each ray of the vision cone \mathcal{V}_o is rotated α_o radians in the direction normal to the obstacle surface to obtain \mathcal{V}_e .

In the case of a static obstacle, any directions along \mathcal{V}_e will maintain the avoidance angle α_o to the obstacle, and thus avoid it. If the obstacle is moving, we will perform a transformation of \mathcal{V}_e in order to compensate for the obstacle movement. This transformation ensures that when the resulting cone is observed through a non-rotating coordinate frame moving with the obstacle, each ray will still keep the constant avoidance angle to the obstacle edge.

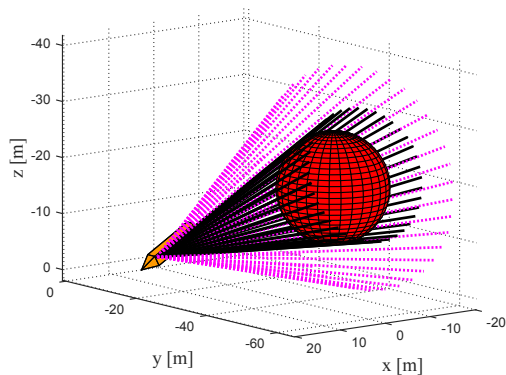


Figure 11.2: The vision cone \mathcal{V}_o (black) and the extended vision cone \mathcal{V}_e (dotted magenta).

To compensate a ray ρ for the obstacle velocity, we will find a frame F_ρ which is such that the x^{F_ρ} -axis points along ρ , while the obstacle velocity lies in the x^{F_ρ} - y^{F_ρ} -plane. We start by defining an intermediate frame A where the x^A -axis is coincident with the x^{F_ρ} -axis. We will then find a rotation from the A frame to the F_ρ frame.

The A frame is obtained in two steps. First we do a rotation from the n_b frame to the b_{bo} frame, which is a Body-fixed frame with the x -axis pointing from the vehicle to the obstacle: $\mathbf{R}_{n_b}^{b_{bo}} \triangleq \mathbf{R}_{zy}(\Theta(\mathbf{p}_o^{n_b}), \Psi(\mathbf{p}_o^{n_b}))^T$. The functions Θ and Ψ are used to find the pitch and heading of a vector, and are defined in Chapter 2. We then do a rotation from the b_{bo} frame to the A frame using a rotation of ϕ radians around the $x^{b_{bo}}$ -axis, followed by a rotation of γ_e radians around the resulting z -axis, $\mathbf{R}_{b_{bo}}^A \triangleq \mathbf{R}_z(\gamma_e)^T \mathbf{R}_x(\phi)^T$. The angle ϕ thus becomes a parameter which can uniquely identify each ray of the vision cone.

The obstacle velocity in the A frame is $\mathbf{v}_o^A = \mathbf{R}_{n_b}^A \mathbf{v}_{o/n}^n$. To obtain the frame F_ρ , we will rotate the A frame around the x^A -axis until $\mathbf{v}_o^{F_\rho}$ lies in the x^{F_ρ} - y^{F_ρ} -plane. The required rotation angle can be geometrically found as $\hat{\phi} \triangleq \text{atan2}(\mathbf{v}_{oz}^A, \mathbf{v}_{oy}^A)$. Hence, $\mathbf{R}_A^{F_\rho} = \mathbf{R}_x(\hat{\phi})$, and

$$\mathbf{v}_o^{F_\rho} = \mathbf{R}_{n_b}^{F_\rho} \mathbf{v}_{o/n}^n = \mathbf{R}_A^{F_\rho} \mathbf{R}_{b_{bo}}^A \mathbf{R}_{n_b}^{b_{bo}} \mathbf{v}_{o/n}^n. \quad (11.5)$$

We are now ready to perform the motion compensation. We define a velocity vector $\mathbf{v}_\rho^{F_\rho}$ along ρ . We seek a vector

$$\mathbf{v}_{ca\rho}^{F_\rho} \triangleq \mathbf{v}_\rho^{F_\rho} + \mathbf{v}_o^{F_\rho}, \quad (11.6)$$

i.e. we compensate the vector $\mathbf{v}_\rho^{F_\rho}$ for the obstacle velocity, as illustrated in Figure 11.3. The vector $\mathbf{v}_{ca\rho}^{F_\rho}$ is a possible desired velocity from the collision avoidance algorithm. Hence, we would like to specify its magnitude, in particular we require that $\|\mathbf{v}_{ca\rho}^{F_\rho}\| = U_b$, where U_b is the vehicle's speed. We do this by finding the angle

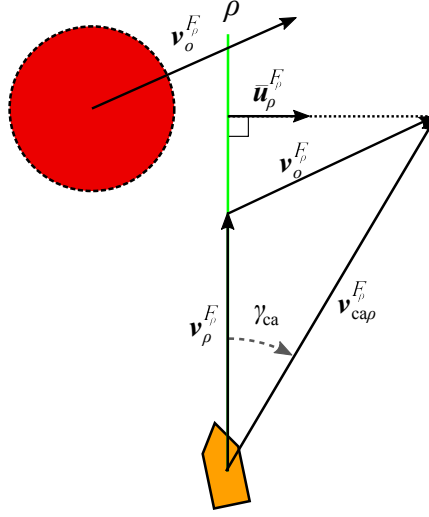


Figure 11.3: A plane containing both the ray ρ , the obstacle velocity vector $\mathbf{v}_o^{n/n}$ and the resulting candidate for desired velocity in collision avoidance mode, $\mathbf{v}_{ca\rho}^n$.

γ_{ca} between $\mathbf{v}_\rho^{F_\rho}$ and $\mathbf{v}_{ca\rho}^{F_\rho}$, which is given by

$$\gamma_{ca}(\phi) \triangleq \sin^{-1} \left(\frac{(\mathbf{v}_o^{F_\rho})^T \bar{\mathbf{u}}_\rho^{F_\rho}}{U_b} \right), \quad (11.7)$$

where $\bar{\mathbf{u}}_\rho^{F_\rho}$ is a unit vector orthogonal to $\mathbf{v}_\rho^{F_\rho}$ as shown in Figure 11.3. The expression for γ_{ca} is ensured to be well defined by Assumption 11.2. The vector $\mathbf{v}_{ca\rho}^{F_\rho}$ is thus given by

$$\mathbf{v}_{ca\rho}^{F_\rho} \triangleq U_b [\cos(\gamma_{ca}), \sin(\gamma_{ca}), 0]^T, \quad (11.8)$$

while

$$\mathbf{v}_{ca\rho}^n = (\mathbf{R}_{nb}^{F_\rho})^T \mathbf{v}_{ca\rho}^{F_\rho}. \quad (11.9)$$

The velocity direction required to follow a motion compensation ray is given by the heading and pitch of the ray:

$$\psi_\rho^n(\phi) \triangleq \Psi(\mathbf{v}_{ca\rho}^n(\phi)), \quad (11.10a)$$

$$\theta_\rho^n(\phi) \triangleq \Theta(\mathbf{v}_{ca\rho}^n(\phi)), \quad (11.10b)$$

where the functions $\Psi(\cdot)$ and $\Theta(\cdot)$ are defined in (2.5) and (2.6), respectively. The collection of motion compensated rays composes the motion compensated vision cone \mathcal{V}_c , which is shown in Figure 11.4. The desired heading and pitch angle in collision avoidance are chosen by minimizing a cost function $C(\phi)$. Thus, if

$$\phi_{ca} \triangleq \arg \min_{\phi} C(\phi), \quad (11.11)$$

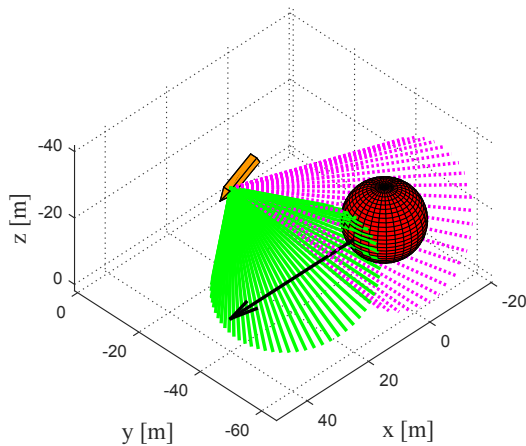


Figure 11.4: The extended vision cone \mathcal{V}_e (dotted magenta) is compensated for the velocity of the obstacle (black arrow) to create the compensated vision cone \mathcal{V}_c (solid green).

we obtain the desired heading and pitch angle in collision avoidance as

$$\langle \theta_{dca}^n, \psi_{dca}^n \rangle \triangleq \langle \theta_{\rho}^n(\phi_{ca}), \psi_{\rho}^n(\phi_{ca}) \rangle. \quad (11.12)$$

Equation (11.12) forms the core of the collision avoidance law presented in part IV of this thesis. Even though there are several steps leading up to this expression, they are straightforward to implement and based on measurements that are readily available on most platforms. We will now provide an example for the cost function $C(\phi)$.

11.2.2 Choosing a safe direction

When the vehicle enters collision avoidance mode, any direction along \mathcal{V}_c is a safe candidate for collision avoidance. This provides flexibility, and a ray can for example be chosen to minimize the angular distance to a safe direction, or to satisfy some external rules of the road. We will here make the vehicle move behind the obstacle, which we do by maximizing the angular distance from the obstacle's velocity vector to the chosen ray. This is done if the vehicle enters collision avoidance when $d_{ob} = d_{switch}$. If the vehicle enters collision avoidance when the obstacle is closer than d_{switch} , it will move to the closest safe direction. Upon entering collision avoidance mode, we thus seek to minimize the cost function C_{enter} , defined as

$$C_{enter} \triangleq \begin{cases} -\sqrt{(\theta_o^n - \theta_{\rho}^n)^2 + (\psi_o^n - \psi_{\rho}^n)^2}, & d_{ob} = d_{switch} \\ \sqrt{(\theta_b^n - \theta_{\rho}^n)^2 + (\psi_b^n - \psi_{\rho}^n)^2}, & d_{ob} < d_{switch}. \end{cases} \quad (11.13)$$

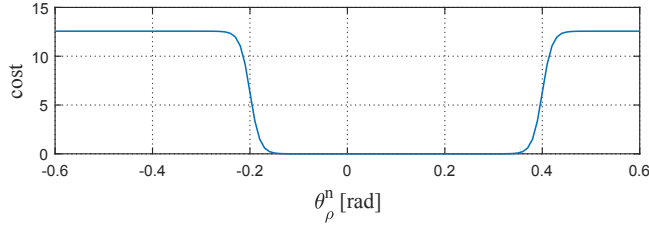


Figure 11.5: The cost function C_θ when $\theta_{\min} = -0.2$, $\theta_{\max} = 0.4$ and $\lambda = 50$.

In Chapters 12 and 13, we will require that the desired pitch is in the interval $\theta_d^n \in [\theta_{\min}, \theta_{\max}]$. In order to achieve this, we add the following cost function:

$$C_\theta \triangleq 2\pi (1 + \tanh(\lambda[\theta_{\min} - \theta_\rho^n])) + 2\pi (1 + \tanh(\lambda[\theta_\rho^n - \theta_{\max}])), \quad (11.14)$$

where $\lambda > 0$ is a design parameter used to set the slope of C_θ . The smoothness of C_θ ensures the smoothness of $\hat{\theta}_{dca}^n$ during the collision avoidance maneuver. An example C_θ is shown in Figure 11.5, where $\theta_{\min} = -0.2$, $\theta_{\max} = 0.4$ and $\lambda = 50$.

When the control system is already in collision avoidance mode, we will avoid discontinuities in θ_{dca}^n and ψ_{dca}^n by minimizing the change in desired heading and pitch when choosing a ray:

$$C_{in} \triangleq \sqrt{(\theta_{dca}^n - \theta_{dca1}^n)^2 + (\psi_{dca}^n - \psi_{dca1}^n)^2}, \quad (11.15)$$

where θ_{dca1}^n and ψ_{dca1}^n is the desired pitch and heading during the previous optimization. Thus, if the system enters collision avoidance mode at a time t_1 , the cost function C becomes

$$C \triangleq \begin{cases} C_{enter} + C_\theta, & t = t_1, \\ C_{in} + C_\theta, & t > t_1. \end{cases} \quad (11.16)$$

11.2.3 Switching rule

We define that the vehicle enters collision avoidance mode at a time t_1 if the distance $d_{ob}(t_1)$ to the obstacle is less than or equal to a chosen distance d_{switch} , and the desired velocity vector $\mathbf{v}_{dg}^n(t_1)$ from nominal guidance is within the extended vision cone $\mathcal{V}_e(t_1)$:

$$\mathbf{v}_{dg}^n(t_1) \in \mathcal{V}_e(t_1), \quad (11.17a)$$

$$d_{ob}(t_1) \leq d_{switch} > d_{safe}. \quad (11.17b)$$

Nominal guidance towards the target will resume at a time t_2 when $\mathbf{v}_{dg}^n(t_2)$ moves outside $\mathcal{V}_e(t_2)$:

$$\mathbf{v}_{dg}^n(t_2) \notin \mathcal{V}_e(t_2). \quad (11.18)$$

11.2.4 Multiple obstacles

The CAA algorithm can be extended to multi-obstacle scenarios. In such scenarios, there will be multiple vision cones, which may be overlapping. The overlapping cones will be merged, so that only the outermost rays of the cones are considered. Then, a safe ray can be chosen in the same manner as for a single obstacle scenario.

If the vehicle encounters a new obstacle while already in collision avoidance mode, we need to ensure that the safe direction chosen by the algorithm when the new obstacle is included does not make the vehicle maneuver across the vision cone of any of the previous obstacles. We achieve this by making the vehicle maintain a constant horizontal turning direction, like in the 2D case in Chapter 7. Thus, if the vehicle starts an avoidance maneuver by going around the obstacles in a clockwise fashion, it will continue to do so until the avoidance maneuver is completed.

While the detailed analysis of a multi-obstacle scenario is beyond the scope of this thesis, we have included simulations with multiple obstacles in Chapter 13 to demonstrate the applicability to such scenarios.

11.3 Algorithm analysis

In this section we will prove that a vehicle which is always moving along the surface of \mathcal{V}_c will remain at a safe distance from the obstacle. We start by proving this for a static obstacle, before extending the result to moving obstacles.

Lemma 11.1. *If the obstacle is static, the vehicle's velocity vector maintains an avoidance angle α_o to the obstacle for $t \geq t_1$, the initial obstacle distance satisfies $d_{ob}(t_1) \geq d_{\text{safe}}$ and α_o satisfies*

$$\alpha_o \in \left[\cos^{-1} \left(\frac{R_o}{R_o + d_{\text{safe}}} \right), \pi/2 \right), \quad d_{\text{safe}} > 0, \quad (11.19)$$

then $d_{ob}(t) \geq d_{\text{safe}}$ for all $t \in [t_1, t_2]$, where $t_2 > t_1$ is the time when the vehicle exits collision avoidance in accordance with the switching rule in (11.18).

Proof. When the angle between vision cone from the vehicle to the obstacle and the vehicles's velocity vector is α_o , the distance d_{ob} between the vehicle and the obstacle evolves as:

$$\dot{d}_{ob} = -U_b \cos(\gamma_a(t) + \alpha_o). \quad (11.20)$$

Equation (11.20) has an equilibrium point at $\gamma_a(t) = \pi/2 - \alpha_o$. Recall from (11.4) that

$$\gamma_a \triangleq \sin^{-1} \left(\frac{R_o}{R_o + d_{ob}} \right). \quad (11.21)$$

Hence, we obtain that $\gamma_a(t) = \pi/2 - \alpha_o$ when

$$d_{ob}(t) = d_{\min} \triangleq \frac{R_o}{\cos(\alpha_o)} - R_o. \quad (11.22)$$

Furthermore, when $d_{ob}(t) < d_{\min}$, $\dot{d}_{ob}(t) > 0$, while when $d_{ob}(t) > d_{\min}$, $\dot{d}_{ob}(t) < 0$. It follows that if $d_{\text{safe}} = d_{\min}$, $d_{ob}(t_1) \geq d_{\text{safe}}$, and the avoidance angle satisfies

(11.19), then a vehicle maintaining the avoidance angle α_o will not get closer than d_{safe} to the obstacle. \square

Thus, if knowledge of the obstacle curvature is available, it is possible to design the avoidance angle in order to assure that the vehicle will keep at least a minimum safety distance d_{safe} from the obstacle during the maneuver. The next lemma shows that this also applies for a moving obstacle.

Lemma 11.2. *Consider an obstacle moving with a time-varying velocity satisfying Assumption 11.2. Let the avoidance angle satisfy (11.19), and let a vehicle maintain a velocity $\mathbf{v}_{\text{cap}}^n$ (11.9) along the motion compensated vision cone \mathcal{V}_c . Then, if $d_{ob}(t_1) \geq d_{\text{safe}}$,*

$$d_{ob}(t) \geq d_{\text{safe}} \quad \forall t \in [t_1, t_2], \quad (11.23)$$

where $t_2 > t_1$ is the time when the vehicle exits collision avoidance in accordance with the switching rule in (11.18).

Proof. Consider a coordinate frame n_o which is attached to the obstacle and aligned with the n frame. Thus, the frame n_o has the velocity $\mathbf{v}_{n_o/n}^n = \mathbf{v}_{o/n}^n$. In this frame, the obstacle is static and the vehicle velocity is \mathbf{v}_ρ^n , i.e. the vehicle moves along the extended vision cone \mathcal{V}_e shown in Figure 11.2, keeping the avoidance angle α_o to the obstacle. The speed of the vehicle in n_o lies in the interval

$$\|\mathbf{v}_{b/n_o}^{n_o}\| = \|\mathbf{v}_{b/n}^n - \mathbf{v}_{o/n}^n\| \in [U_b - u_o, U_b + u_o]. \quad (11.24)$$

By Assumption 11.2, the velocity $\|\mathbf{v}_{b/n_o}^{n_o}\| > 0$. Hence, we can apply Lemma 11.1 to ensure that the vehicle will remain at least a minimum safety distance away from the obstacle during the avoidance maneuver. \square

11.4 Overview of Part IV

In this chapter, we have presented the CAA algorithm in 3D. The algorithm extends the algorithm presented in Part III by creating an extended vision cone around the obstacle, where each ray of the cone keeps an avoidance angle α_o to the obstacle. A preliminary analysis in Lemma 11.1 has shown that a vehicle maintaining a velocity along the extended vision cone is guaranteed to remain at least a minimum safety distance away from the obstacle. The extended vision cone is transformed to compensate for obstacle motion, and we proved in Lemma 11.2 that if the vehicle maintains a velocity along this compensated vision cone, it is able to maintain a safe distance to a moving obstacle.

In the remainder of Part IV we will apply the 3D CAA algorithm to a kinematically modeled vehicle with nonholonomic constraints (Chapter 12), and to an underactuated marine vehicle modeled in 5 DOF (Chapter 13). In each of these chapters, we will provide conditions on the switching distance, the avoidance angle and on the underlying controllers under which it is ensured that the vehicle will initiate the avoidance maneuver early enough, that it is able to follow the yaw and pitch references from the CAA algorithm, and that all the signals in the control system remain well defined.

Chapter 12

The CAA Algorithm for 3D Kinematic Vehicles

Mellow greetings. What seems to be your boggle?

— Boggle guard, *Demolition Man*

In this chapter, we will apply the 3D CAA algorithm presented in Chapter 11 to a kinematically modeled vehicle with nonholonomic constraints in sway and heave. The vehicle is restricted to keep a constant forward speed, and has limited pitch and yaw rates. Furthermore, we will impose restrictions on the vehicle pitch, which is a common safety restriction on both underwater vehicles and fixed-wing aircraft. Thus, the vehicle model we employ in this chapter can be used to describe a wide array of vehicles moving in 3D.

The vehicle will be tasked with reaching a target position, for which we will employ a 3D pure pursuit target reaching law [17] as the nominal guidance law. If an obstacle is encountered on the way, the vehicle will enter collision avoidance mode and employ the CAA algorithm in order to avoid the obstacle. From the previous chapter, we know that if the vehicle is able to follow the heading and pitch reference of the algorithm, it is ensured to maintain at least a minimum safety distance to the obstacle.

In this chapter, we will derive a minimum switching distance which ensures that the vehicle will reach the desired velocity direction from the CAA algorithm before the obstacle can get too close. This distance is dependent on both the vehicle's and the obstacle's maneuvering capabilities. Furthermore, we will derive bounds on the required pitch and yaw rate during the maneuver. These bounds are dependent on the minimum safety distance, and thus on the constant avoidance angle, and hence the algorithm can be tuned in order to ensure that the vehicle is able to follow the control references from the collision avoidance algorithm. These theoretical results are validated through numerous simulations involving both static and moving obstacles.

The remainder of this chapter is organized as follows. In Section 12.1 we describe the model of the vehicle and obstacle, while the 3D CAA algorithm is summarized in Section 12.2. The nominal guidance law and the underlying controllers are described in Section 12.3, and the collision avoidance algorithm is formally analyzed in Section 12.4. The simulations are presented in Section 12.5, before some concluding remarks are given in Section 12.6.

The work presented in this chapter is based on Wiig et al. [115], Wiig et al. [116] and Wiig et al. [118].

12.1 System description

12.1.1 Vehicle model

The vehicle is modeled on the kinematic level as in Section 3.1.2, using the Euler angles pitch (θ_b^n) and yaw (ψ_b^n) to describe the rotation from the body frame b to the NED frame n . The vehicle model is then given by the following equations:

$$\dot{\mathbf{p}}_b^n = \mathbf{R}_b^n(\theta_b^n, \psi_b^n) \mathbf{v}_{b/n}^b = \begin{bmatrix} c(\psi_b^n)c(\theta_b^n) & -s(\psi_b^n) & c(\psi_b^n)s(\theta_b^n) \\ s(\psi_b^n)c(\theta_b^n) & c(\psi_b^n) & s(\psi_b^n)s(\theta_b^n) \\ -s(\theta_b^n) & 0 & c(\theta_b^n) \end{bmatrix} \mathbf{v}_{b/n}^b, \quad (12.1a)$$

$$\dot{\theta}_b^n = q_b, \quad (12.1b)$$

$$\dot{\psi}_b^n = \frac{r_b}{\cos(\theta_b^n)}, \quad (12.1c)$$

where \mathbf{p}_b^n is the vehicle position in the NED frame, $\mathbf{v}_{b/n}^b = [u_b, 0, 0]^T$ is the vehicle velocity in the body frame. Note that the last two elements of $\mathbf{v}_{b/n}^b$, i.e. the sway and heave speeds, are zero due to the nonholonomic constraints on the vehicle.

As the vehicle is modeled only on the kinematic level in the chapter, we assume that the pitch and yaw rate are directly actuated. Furthermore, we assume that they are bounded:

Assumption 12.1. The angular velocities in yaw, r_b , and pitch, q_b , are assumed to be directly controlled. The angular velocities are furthermore bounded by

$$r_b \in [-r_{\max}, r_{\max}], \quad (12.2a)$$

$$q_b \in [-q_{\max}, q_{\max}], \quad (12.2b)$$

where $r_{\max} > 0$ and $q_{\max} > 0$ are constant vehicle parameters.

We also assume that the directly controlled forward speed is kept constant throughout the maneuver:

Assumption 12.2. The vehicle surge speed u_b is directly controlled and constant.

To avoid a singularity in the heading rate in (12.1c), we impose a bound on the initial pitch:

Assumption 12.3. The initial pitch satisfies

$$\theta_b^n(t_0) \in [\theta_{\min}, \theta_{\max}], \quad (12.3)$$

where $\theta_{\min} \in (-\pi/2, 0)$ and $\theta_{\max} \in (0, \pi/2)$ are constant design parameters.

Remark 12.1. It is common to impose limits on the maximum and minimum pitch angle of vehicles such as AUVs and many fixed-wing aircraft. For AUVs, such limits can increase the vehicle safety by ensuring that it does not move too fast towards the sea floor or the surface. Similarly, aircraft with such limits avoid going too fast towards the ground, and can also avoid stalling scenarios.

Remark 12.2. Note that the pitch limits do not include zero, in order to ensure that the vehicle is able to move both up and down.

The collision avoidance algorithm presented in the previous chapter is designed to ensure that the pitch limits are not violated, and we will also design the control system in Section 12.3 to ensure that the pitch will not exceed these limits.

12.1.2 Obstacle model

Recall from Section 11.1 that the obstacle is modeled as a moving sphere with radius R_o :

$$\dot{\boldsymbol{\eta}}_o^n = \mathbf{J}(\boldsymbol{\eta}_o^n) \boldsymbol{\nu}_{o/n}^o, \quad (12.4a)$$

$$\dot{u}_o = a_o, \quad (12.4b)$$

where $\boldsymbol{\eta}_o^n \triangleq [\mathbf{p}_o^n, \theta_o^n, \psi_o^n]^T$ and $\boldsymbol{\nu}_{o/n}^o \triangleq [u_o, 0, 0, q_o, r_o]^T$. The obstacle's angular velocity and acceleration is assumed to be bounded:

Assumption 12.4. The obstacle acceleration a_o and angular velocity $\boldsymbol{\omega}_{o/n}^o$ are bounded by

$$a_o \in [-a_{o\max}, a_{o\max}], \quad (12.5a)$$

$$\|\boldsymbol{\omega}_{o/n}^o\| \in [-\omega_{o\max}, \omega_{o\max}], \quad (12.5b)$$

where $a_{o\max} \geq 0$ and $\omega_{o\max} \geq 0$ are constant parameters.

Furthermore, in order to enable the vehicle to circumvent the obstacle, and to ensure that the motion compensation in the CAA algorithm is well defined, we assume that the vehicle is able to move faster than the obstacle:

Assumption 12.5. The obstacle speed u_o lies in the interval $u_o \in [0, u_{o\max}]$, where $u_{o\max} < u_b$.

12.1.3 Control objectives

Let \mathbf{p}_t^n be a target position in the NED frame. The objective of the control system and the collision avoidance algorithm is to make the vehicle come within an acceptance distance $d_a \geq u_b/r_{\max}$ of the target position \mathbf{p}_t^n at some unspecified time $t_f \in [t_0, \infty)$, i.e.

$$\|\mathbf{p}_t^{n_b}(t_f)\| \leq d_a, \quad (12.6)$$

where $\mathbf{p}_t^{n_b} = \mathbf{p}_t^n - \mathbf{p}_b^n$ is the target position in the body-fixed NED frame n_b . This goal should be achieved while keeping at least a minimum safety distance d_{safe}

to the obstacle, i.e. the distance d_{ob} between the vehicle and the obstacle should satisfy:

$$d_{ob}(t) \geq d_{\text{safe}} > 0 \quad \forall t \in [t_0, t_f]. \quad (12.7)$$

To accommodate the pitch limitations often encountered in practice as discussed in Remark 12.1, the control system should bound the vehicle pitch:

$$\theta_b^n(t) \in [\theta_{\min}, \theta_{\max}] \quad \forall t \in [t_0, t_f]. \quad (12.8)$$

12.2 The CAA algorithm in 3D

The 3D CAA algorithm is defined in Section 11.2 and summarized here for convenience.

The algorithm creates an extended vision cone \mathcal{V}_e from the vehicle to the obstacle, where the apex angle of the vision cone is $\gamma_e \triangleq 2(\gamma_a + \alpha_o)$, and

$$\gamma_a \triangleq \sin^{-1} \left(\frac{R_o}{R_o + d_{ob}} \right). \quad (12.9)$$

The vision cone is transformed to compensate for the obstacle speed u_o . For each ray ρ of \mathcal{V}_e , we find a frame F_ρ which is such that the x^{F_ρ} -axis points along ρ , while the obstacle velocity lies in the x^{F_ρ} - y^{F_ρ} -plane. We first find an intermediate frame A where the x^A -axis is coincident with the x^{F_ρ} -axis:

$$\mathbf{R}_{n_b}^A \triangleq \mathbf{R}_z(\gamma_e)^T \mathbf{R}_x(\phi)^T \mathbf{R}_{zy}(\Theta(\mathbf{p}_o^{n_b}), \Psi(\mathbf{p}_o^{n_b}))^T, \quad (12.10)$$

where the $\mathbf{p}_o^{n_b} = \mathbf{p}_o^n - \mathbf{p}_b^n$ and the angle $\phi \in [0, 2\pi)$ is a parameter uniquely identifying each ray of the vision cone.

To obtain the frame F_ρ , we will rotate the A frame around the x^A -axis until $\mathbf{v}_o^{F_\rho}$ lies in the x^{F_ρ} - y^{F_ρ} -plane. The required rotation angle can be geometrically found as $\hat{\phi} \triangleq \text{atan2}(\mathbf{v}_{oz}^A, \mathbf{v}_{oy}^A)$. Hence, $\mathbf{R}_A^{F_\rho} = \mathbf{R}_x(\hat{\phi})$, and

$$\mathbf{v}_o^{F_\rho} = \mathbf{R}_{n_b}^{F_\rho} \mathbf{v}_{o/n}^n = \mathbf{R}_A^{F_\rho} \mathbf{R}_{n_b}^A \mathbf{v}_{o/n}^n. \quad (12.11)$$

We define a velocity vector $\mathbf{v}_\rho^{F_\rho}$ along ρ , and seek a vector

$$\mathbf{v}_{ca\rho}^{F_\rho} \triangleq \mathbf{v}_\rho^{F_\rho} + \mathbf{v}_o^{F_\rho}, \quad (12.12)$$

illustrated in Figure 12.1. To ensure that $\|\mathbf{v}_{ca\rho}^{F_\rho}\| = u_b$, we find the compensation angle γ_{ca} between $\mathbf{v}_\rho^{F_\rho}$ and $\mathbf{v}_{ca\rho}^{F_\rho}$ as

$$\gamma_{ca}(\phi) \triangleq \sin^{-1} \left(\frac{(\mathbf{v}_o^{F_\rho})^T \bar{\mathbf{u}}_\rho^{F_\rho}}{u_b} \right), \quad (12.13)$$

where $\bar{\mathbf{u}}_\rho^{F_\rho}$ is a unit vector orthogonal to $\mathbf{v}_\rho^{F_\rho}$ as shown in Figure 12.1. The vector $\mathbf{v}_{ca\rho}^{F_\rho}$ is thus

$$\mathbf{v}_{ca\rho}^{F_\rho} \triangleq u_b [\cos(\gamma_{ca}), \sin(\gamma_{ca}), 0]^T, \quad (12.14)$$

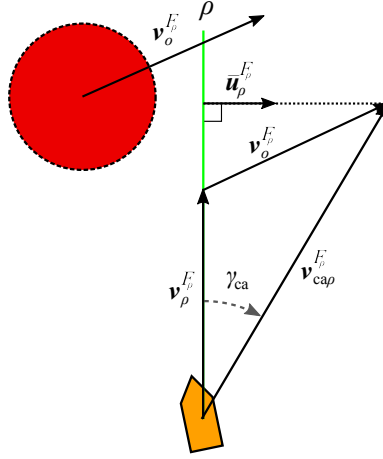


Figure 12.1: A plane containing both the ray ρ , the obstacle velocity vector $\mathbf{v}_{o/n}^n$ and the resulting candidate for desired velocity in collision avoidance mode, $\mathbf{v}_{ca\rho}^n$.

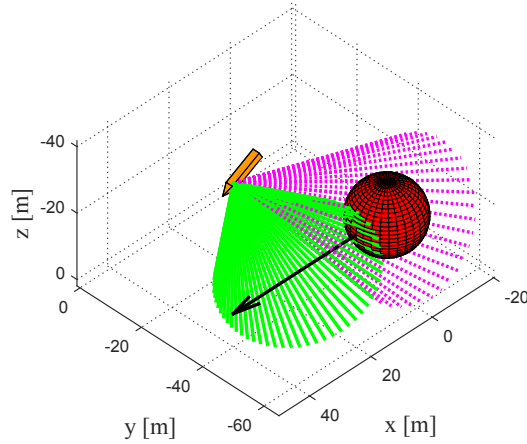


Figure 12.2: The extended vision cone \mathcal{V}_e (magenta) and the compensated vision cone \mathcal{V}_c (green).

while

$$\mathbf{v}_{ca\rho}^n = (\mathbf{R}_{n_b}^{F_\rho})^T \mathbf{v}_{ca\rho}^{F_\rho}. \quad (12.15)$$

The collection of motion compensated rays compose a compensated vision cone \mathcal{V}_c , shown in Figure 12.2. The velocity direction required to follow a motion compensated ray is

$$\psi_\rho^n(\phi) \triangleq \Psi(\mathbf{v}_{ca\rho}^n(\phi)), \quad (12.16a)$$

$$\theta_\rho^n(\phi) \triangleq \Theta(\mathbf{v}_{ca\rho}^n(\phi)). \quad (12.16b)$$

To obtain the desired heading and pitch angle in collision avoidance we define the parameter ϕ_{ca} as

$$\phi_{ca} \triangleq \arg \min_{\phi} C(\phi). \quad (12.17)$$

The cost function C is defined as

$$C \triangleq \begin{cases} C_{\text{enter}} + C_\theta & t = t_1 \\ C_{\text{in}} + C_\theta & t > t_1, \end{cases} \quad (12.18)$$

where t_1 is the time when the vehicle enters collision avoidance mode. The function C_{enter} will make the vehicle move behind the obstacle as it enters collision avoidance mode, the function C_θ ensures that the desired pitch from the algorithm remains within the bounds in (12.3), and the function C_{in} minimizes the required pitch and yaw rate during the collision avoidance maneuver. These components of the cost function C are defined as

$$C_{\text{enter}} \triangleq \begin{cases} -\sqrt{(\theta_o^n - \theta_\rho^n)^2 + (\psi_o^n - \psi_\rho^n)^2}, & d_{ob} = d_{\text{switch}} \\ \sqrt{(\theta_b^n - \theta_\rho^n)^2 + (\psi_b^n - \psi_\rho^n)^2}, & d_{ob} < d_{\text{switch}}, \end{cases} \quad (12.19)$$

$$C_\theta \triangleq 2\pi (1 + \tanh(\lambda[\theta_{\min} - \theta_\rho^n])) + 2\pi (1 + \tanh(\lambda[\theta_\rho^n - \theta_{\max}])), \quad (12.20)$$

$$C_{\text{in}} \triangleq \sqrt{(\theta_{dca}^n - \theta_{dca1}^n)^2 + (\psi_{dca}^n - \psi_{dca1}^n)^2}, \quad (12.21)$$

where θ_{dca1}^n and ψ_{dca1}^n is the desired pitch and heading during the previous optimization, and $\lambda > 0$ is a design parameter used to set the slope of C_θ .

Thus, we obtain the desired pitch and heading in collision avoidance mode as

$$\langle \theta_{dca}^n, \psi_{dca}^n \rangle \triangleq \langle \theta_\rho^n(\phi_{ca}), \psi_\rho^n(\phi_{ca}) \rangle. \quad (12.22)$$

The vehicle will enter collision avoidance mode at a time t_1 when

$$\mathbf{v}_{dg}^n(t_1) \in \mathcal{V}_e(t_1), \quad (12.23a)$$

$$d_{ob}(t_1) \leq d_{\text{switch}} > d_{\text{safe}}, \quad (12.23b)$$

where \mathbf{v}_{dg}^n is the desired velocity vector from the guidance law, which is described in Section 12.3.2, and d_{switch} is a chosen switching distance. The vehicle will leave collision avoidance mode and enter nominal guidance mode at a time t_2 when

$$\mathbf{v}_{dg}^n(t_2) \notin \mathcal{V}_e(t_2). \quad (12.24)$$

12.3 Control system

The control system can be either in guidance mode, where it drives the vehicle towards the target using the guidance law given in Section 12.3.2, or in collision avoidance mode where it actively avoids an obstacle as described in the previous section. In this section we describe the low-level control laws and the nominal guidance law.

12.3.1 Heading and pitch control

We want the vehicle to reach the desired heading ψ_d^n and pitch θ_d^n as fast as possible. Hence, we make it turn at the maximum rate towards the desired direction:

$$r_b(\psi_d^n) \triangleq \begin{cases} 0 & \tilde{\psi}_b^n = 0, \\ r_{\max} & \tilde{\psi}_b^n \in (-\pi, 0), \\ -r_{\max} & \tilde{\psi}_b^n \in (0, \pi]. \end{cases} \quad (12.25a)$$

$$q_b(\theta_d^n) \triangleq \begin{cases} 0 & \tilde{\theta}_b^n = 0, \\ q_{\max} & \tilde{\theta}_b^n \in (-\pi, 0), \\ -q_{\max} & \tilde{\theta}_b^n \in (0, \pi]. \end{cases} \quad (12.25b)$$

The heading error variable $\tilde{\psi}_b^n \triangleq \psi_b^n - \psi_d^n$ and the pitch error variable $\tilde{\theta}_b^n \triangleq \theta_b^n - \theta_d^n$ are chosen to belong to the interval $\tilde{\psi}_b^n, \tilde{\theta}_b^n \in (-\pi, \pi]$. This ensures that the vehicle always makes the shortest possible turn towards ψ_d^n and θ_d^n . The desired heading ψ_d^n and pitch θ_d^n are given in Section 12.3.2 when the control system is in guidance mode, and in Section 12.2 when the control system is in collision avoidance mode.

12.3.2 Guidance law

When the control system is in guidance mode, we choose to use a 3D pure pursuit guidance law [16] for the desired heading and pitch. The desired heading is thus chosen as:

$$\psi_{dg}^n \triangleq \Psi(\mathbf{p}_t^{nb}), \quad (12.26)$$

where $\psi_{dg}^n \in [0, 2\pi)$ is the desired heading in guidance mode.

The desired pitch is saturated to ensure that control objective (12.8) is met:

$$\theta_{dg}^n = \begin{cases} \theta_{\max} & \Theta(\mathbf{p}_t^{nb}) > \theta_{\max}, \\ \Theta(\mathbf{p}_t^{nb}) & \Theta(\mathbf{p}_t^{nb}) \in [\theta_{\min}, \theta_{\max}], \\ \theta_{\min} & \Theta(\mathbf{p}_t^{nb}) < \theta_{\min}, \end{cases} \quad (12.27)$$

where $\theta_{dg}^n \in [\theta_{\min}, \theta_{\max}]$ is the desired pitch. If $\Theta(\mathbf{p}_t^{nb}) \notin [\theta_{\min}, \theta_{\max}]$, the guidance law will drive the vehicle towards the target at maximum or minimum pitch, and then make the vehicle circle up or down until $\|\mathbf{p}_t^{nb}(t_f)\| \leq d_a$, and control objective (12.6) is met.

The desired velocity vector in guidance mode, \mathbf{v}_{dg}^n , is then found from (12.26) and (12.27) as:

$$\mathbf{v}_{dg}^n \triangleq \mathbf{R}_{zy}(\theta_{dg}^n, \psi_{dg}^n) \mathbf{v}_{b/n}^n, \quad (12.28)$$

where $\mathbf{v}_{b/n}^n = [u_b, 0, 0]^T$ as in Section 12.1.1.

12.4 Analysis

In this section we give an analysis of the collision avoidance algorithm described in Section 12.2, applied to the vehicle described by the model (12.1). The vehicle model is in closed-loop configuration with the heading and pitch controllers (12.25).

The vehicle is nominally moving towards a target position \mathbf{p}_t^n using the guidance law for heading (12.26) and pitch (12.27). When the vehicle encounters an obstacle, it switches into collision avoidance mode using the switching criterion in (12.23), and follows the heading and pitch reference given by (12.22) to avoid the obstacle.

12.4.1 Required pitch and yaw rate

Recall from Lemma 11.2 in the previous chapter that if the avoidance angle α_o is chosen such that

$$\alpha_o \in \left[\cos^{-1} \left(\frac{R_o}{R_o + d_{\text{safe}}} \right), \pi/2 \right), \quad d_{\text{safe}} > 0, \quad (12.29)$$

the initial distance to the obstacle satisfies $d_{ob}(t_0) \geq d_{\text{safe}}$, and the vehicle follows the control references (12.22) from the CAA algorithm, then the obstacle distance will always be at least d_{safe} . To ensure that the vehicle is able to follow θ_{dca}^n and ψ_{dca}^n , we require that

$$|\dot{\theta}_{dca}^n| \leq q_{\text{max}}, \quad (12.30a)$$

$$|\dot{\psi}_{dca}^n| \leq r_{\text{max}}. \quad (12.30b)$$

Since the use of the cost function (12.18) minimizes $\dot{\theta}_{dca}^n$ and $\dot{\psi}_{dca}^n$ when the system is in collision avoidance mode, the required control effort in each DOF will maximize for either a purely vertical or a purely horizontal maneuver. Thus, we will examine such maneuvers in the next two lemmas, in order to find bounds on $|\dot{\theta}_{dca}^n|$ and $|\dot{\psi}_{dca}^n|$ as a function of d_{safe} . We start by looking at a pure vertical maneuver, where we temporarily omit the pitch limitations of the vehicle in order to enable it to go around the obstacle. We do this by setting the partial cost function C_θ to zero in the next lemma.

Lemma 12.1. *Consider a vehicle and an obstacle moving in the same vertical plane, and let the obstacle be modeled by (12.4). If Assumptions 12.2, 12.4 and 12.5 hold, the vehicle follows the pitch reference from (12.22) for $t \geq t_1$, the distance to the obstacle satisfies*

$$d_{ob}(t_1) \geq d_{\text{safe}}, \quad (12.31)$$

and the partial cost function $C_\theta = 0$, then $\dot{\theta}_{dca}^n$ is bounded by

$$|\dot{\theta}_{dca}^n| < \dot{\theta}_{dca}^{n \text{ sup}} \triangleq \frac{a_{\text{omax}}}{\sqrt{u_b^2 - u_{\text{omax}}^2}} + \frac{u_{\text{omax}}}{u_b} \omega_{\text{omax}} + \frac{(u_b + u_{\text{omax}})^2}{u_b \sqrt{(R_o + d_{\text{safe}})^2 - R_o^2}}. \quad (12.32)$$

Proof. With out loss of generality, let the vehicle maneuver above the obstacle, and we allow the pitch angles of the vehicle and the obstacle to lie in the interval $(-\pi, \pi]$. Thus, the vehicle and the obstacle can move towards each other while keeping the same heading. The vehicle-obstacle geometry is illustrated in Figure 12.3, where it can be seen that

$$\dot{\theta}_{dca}^n = \dot{\theta}_{\alpha_o}^n + \dot{\gamma}_{ca}, \quad (12.33)$$

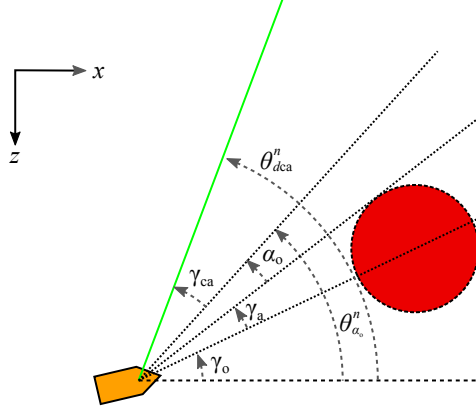


Figure 12.3: Geometry of a collision avoidance maneuver in the vertical plane.

and that $\theta_{\alpha_o}^n$ can be further decomposed as

$$\theta_{\alpha_o}^n = \gamma_o + \gamma_a + \alpha_o. \quad (12.34)$$

Hence, since α_o is constant by definition,

$$\dot{\theta}_{\alpha_o}^n = \dot{\gamma}_o + \dot{\gamma}_a. \quad (12.35)$$

The angular velocity of γ_o can be found geometrically as

$$\dot{\gamma}_o = \frac{(u_o \sin(\theta_o^n - \gamma_o) - u_b \sin(\theta_b^n - \gamma_o))}{R_o + d_{ob}}. \quad (12.36)$$

Recall that angle γ_a is found in (12.9) as

$$\gamma_a = \sin^{-1} \left(\frac{R_o}{R_o + d_{ob}} \right), \quad (12.37)$$

which gives

$$\dot{\gamma}_a = -\dot{d}_{ob} \frac{R_o}{(R_o + d_{ob}) \sqrt{(R_o + d_{ob})^2 - R_o^2}}. \quad (12.38)$$

where

$$\dot{d}_{ob} = u_o \cos(\theta_o^n - \gamma_o) - u_b \cos(\theta_b^n - \gamma_o). \quad (12.39)$$

Combining (12.36) - (12.39) gives

$$\dot{\theta}_{\alpha_o}^n = \frac{u_b \sin(\gamma_o - \theta_b^n) - u_o \sin(\gamma_o - \theta_o^n)}{R_o + d_{ob}} - R_o \frac{u_b \cos(\gamma_o - \theta_b^n) - u_o \cos(\gamma_o - \theta_o^n)}{(R_o + d_{ob}) \sqrt{(R_o + d_{safe})^2 - R_o^2}}. \quad (12.40)$$

By applying Assumptions 12.5 to bound the obstacle speed and Assumption 12.2 to bound the vehicle speed, and then maximizing with respect to ψ_b^n and ψ_o^n , we obtain the following bound:

$$|\dot{\theta}_{\alpha_o}^n| \leq \frac{u_b + u_{o\max}}{\sqrt{(R_o + d_{safe})^2 - R_o^2}}. \quad (12.41)$$

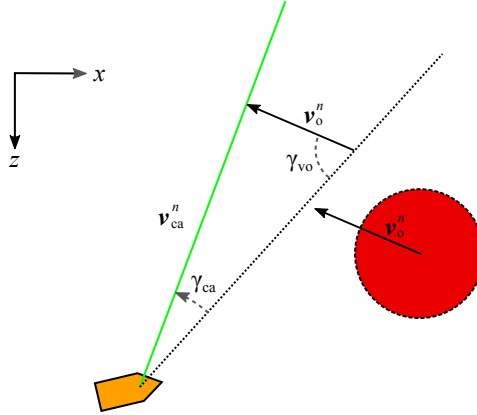


Figure 12.4: An alternative expression for γ_{ca} can be found using the sine rule on this triangle.

When both the vehicle and the obstacle moves in the same vertical plane, the dot product $(\mathbf{v}_o^{F\rho})^T \bar{\mathbf{u}}_{\rho}^{F\rho}$ can be rewritten as $u_o \sin(\gamma_{vo})$, where

$$\gamma_{vo} \triangleq \pi - (\theta_o^n - \theta_{\alpha_o}^n), \quad (12.42)$$

The expression (12.13) for γ_{ca} can then be rewritten as

$$\gamma_{ca} = \sin^{-1} \left(\frac{u_o \sin(\gamma_{vo})}{u_b} \right), \quad (12.43)$$

where we in effect have used the sine rule on the triangle shown in Figure 12.4. Assumption 12.5 ensures that (12.43) is well defined. We use (12.43) to find

$$\dot{\gamma}_{ca} = \frac{u_o \cos(\gamma_{vo}) (\dot{\theta}_{\alpha_o}^n - q_o) + \sin(\gamma_{vo}) a_o}{\sqrt{u_b^2 - u_o^2 \sin^2(\gamma_{vo})}}. \quad (12.44)$$

We now use Assumptions 12.5 and 12.4 to bound the obstacle speed, acceleration and pitch rate in the expression for $\dot{\gamma}_{ca}$, which gives

$$|\dot{\gamma}_{ca}| < \frac{a_{o\max}}{\sqrt{u_b^2 - u_{o\max}^2}} + \frac{u_{o\max}}{u_b} \omega_{o\max} + \frac{u_{o\max}}{u_b} |\dot{\theta}_{\alpha_o}^n|. \quad (12.45)$$

Combining (12.41) and (12.45) gives

$$|\dot{\theta}_{dca}^n| < \dot{\theta}_{dca\sup}^n \triangleq \frac{a_{o\max}}{\sqrt{u_b^2 - u_{o\max}^2}} + \frac{u_{o\max}}{u_b} \omega_{o\max} + \frac{(u_b + u_{o\max})^2}{u_b \sqrt{(R_o + d_{\text{safe}})^2 - R_o^2}}. \quad (12.46)$$

which concludes the proof. \square

In the next lemma, we find an equivalent bound for the required yaw rate during a horizontal maneuver.

Lemma 12.2. *Consider a vehicle and an obstacle moving in the same horizontal plane, and let the obstacle be modeled by (12.4). If Assumptions 12.2, 12.4 and 12.5 hold, the vehicle follows the heading reference from (12.22) for $t \geq t_1$, the distance to the obstacle satisfies*

$$d_{ob}(t_1) \geq d_{\text{safe}}, \quad (12.47)$$

then $\dot{\psi}_{\text{dca}}^n$ is bounded by

$$|\dot{\psi}_{\text{dca}}^n| < \dot{\psi}_{\text{dca}}^n \triangleq \frac{a_{\text{omax}}}{\sqrt{u_b^2 - u_{\text{omax}}^2}} + \frac{u_{\text{omax}}}{u_b} \omega_{\text{omax}} + \frac{(u_b + u_{\text{omax}})^2}{u_b d_{\text{safe}}}. \quad (12.48)$$

Proof. The proof of Lemma 12.2 is equivalent to the proof of Lemma 12.1, however we also maximize the expression with respect to R_o , in effect setting $R_o = 0$ in the bound. This follows from the vehicle pitch limitations; if we consider a limiting scenario where the vehicle is not allowed to pitch and encounters an obstacle which is slightly below it, the radius of the vehicle's horizontal turn will be less than $R_o + d_{\text{safe}}$, and the required turning rate is hence maximized when $R_o = 0$. \square

12.4.2 Switching distance

In this section we will derive a minimum safety distance guaranteeing that the vehicle is able to turn around before the obstacle distance is reduced to less than d_{safe} .

Lemma 12.3. *Consider a vehicle modeled by (12.1) and an obstacle modeled by (12.4), and let the vehicle be controlled by the heading and pitch controllers (12.25). At a time $t_1 \geq t_2$ let the control system enter collision avoidance mode according to the switching rule in (12.23), and let the vehicle then be guided by the collision avoidance law (12.22). Furthermore, let Assumptions 12.1-12.5 be satisfied. Finally, let the switching distance satisfy*

$$d_{\text{switch}} \geq u_{\text{omax}} t_{\text{turn}} + d_{\text{turn}} + d_{\text{safe}}, \quad (12.49)$$

where

$$t_{\text{turn}} \triangleq \max \left\{ \frac{\theta_{\text{max}} - \theta_{\text{min}}}{q_{\text{max}}}, \frac{\pi}{r_{\text{max}}} \right\}. \quad (12.50)$$

is the maximum amount of time the vehicle will spend turning before reaching \mathcal{V}_c , and

$$d_{\text{turn}} \triangleq \max \left\{ \frac{u_b}{r_{\text{max}}}, \frac{u_b}{q_{\text{max}}} \right\}. \quad (12.51)$$

upper bounds the distance traveled by the vehicle towards the obstacle when making a complete 180° turn. Then, the vehicle is able to reach \mathcal{V}_c before the obstacle can come within the distance d_{safe} .

Proof. We consider a worst case scenario with an obstacle of infinite size, $R_o \rightarrow \infty$, moving at maximum speed, $u_o(t_1) = u_{o\max}$. The half apex angle of the vision cone angle is then $\gamma_a = \pi/2$. We assume, without loss of generality, that the obstacle is ahead of the vehicle along the x -axis of the NED frame, such that $x_o^n(t_1) - x_b^n(t_1) = d_{\text{switch}}$, while $y_o^n(t_1) = y_b^n(t_1)$ and $z_o^n(t_1) = z_b^n(t_1)$. Furthermore, we assume that the vehicle and obstacle move straight towards each other at time t_1 . The worst case behavior of the obstacle is then to continue moving straight ahead at maximum speed.

The time taken for a vehicle to make a complete horizontal turn is

$$t_{\text{hturn}} \triangleq \frac{\pi}{r_{\max}}, \quad (12.52)$$

while the time taken for the vehicle to pitch from θ_{\min} to θ_{\max} or vice versa is

$$t_{\text{vturn}} \triangleq \frac{\theta_{\max} - \theta_{\min}}{q_{\max}}. \quad (12.53)$$

Hence, the distance covered by the obstacle towards the vehicle when the vehicle is turning towards $\langle \theta_{dca}^n, \psi_{dca}^n \rangle$ is upper bounded by $u_{o\max} t_{\text{turn}}$, where

$$t_{\text{turn}} \triangleq \max \{ t_{\text{hturn}}, t_{\text{vturn}} \}. \quad (12.54)$$

The distance covered by the vehicle towards the obstacle when turning is upper bounded by

$$d_{\text{turn}} \triangleq \max \left\{ \frac{u_b}{r_{\max}}, \frac{u_b}{q_{\max}} \right\}. \quad (12.55)$$

It follows that if the switching distance satisfies

$$d_{\text{switch}} \geq u_{o\max} t_{\text{turn}} + d_{\text{turn}} + d_{\text{safe}}, \quad (12.56)$$

then there exists a time $t_2 \geq t_1$ when $\theta_b^n = \theta_{dca}^n$, $\psi_b^n = \psi_{dca}^n$ and it holds that

$$d_{ob}(t) \geq d_{\text{safe}} \quad \forall t \in [t_1, t_2]. \quad (12.57)$$

The proof is illustrated in Figure 12.5 □

12.4.3 Safe target reaching

Before stating the main theorem, assume that the vehicle is able to start safely, and that the obstacle does not cover the target:

Assumption 12.6. The initial distance between the vehicle and the obstacle satisfies

$$d_{ob}(t_0) > d_{\text{switch}}. \quad (12.58)$$

Assumption 12.7. The distance d_{ot} from the obstacle to the target position \mathbf{p}_t^n satisfies

$$d_{ot}(t) > \frac{R_o}{\cos(\alpha_o)} - R_o \quad \forall t \geq t_0. \quad (12.59)$$

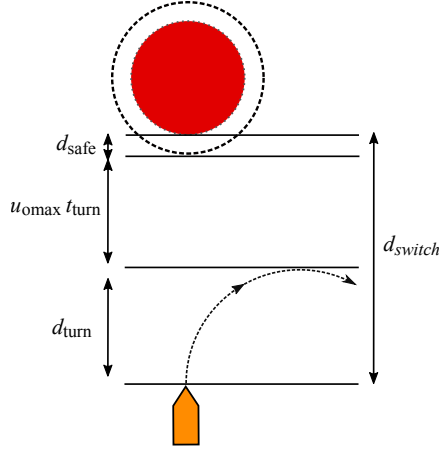


Figure 12.5: Illustration of the minimum required switching distance.

Finally, we assume that distance between any two obstacles is large enough to allow the vehicle to consider one obstacle at a time:

Assumption 12.8. The distance between any two obstacles are always at least $2d_{\text{switch}}$.

Theorem 12.4. Consider a vehicle modeled by (12.1), controlled by the controllers (12.25), guidance laws (12.26) and (12.27), and collision avoidance law (12.22). Furthermore, let the vehicle operate in the presence of obstacles described by (12.4). If Assumptions 12.2-12.8 hold, the avoidance angle satisfies

$$\alpha_o \in \left[\cos^{-1} \left(\frac{R_o}{R_o + d_{\text{safe}}} \right), \frac{\pi}{2} \right), \quad (12.60)$$

the maximum vehicle pitch and yaw rate satisfy

$$q_{\text{max}} \geq \dot{\theta}_{\text{dcasup}}^n, \quad (12.61a)$$

$$r_{\text{max}} \geq \dot{\psi}_{\text{dcasup}}^n, \quad (12.61b)$$

and the switching distance satisfies

$$d_{\text{switch}} \geq u_{\text{omax}} t_{\text{turn}} + d_{\text{turn}} + d_{\text{safe}}, \quad (12.62)$$

then vehicle will maneuver among the obstacles while ensuring that

$$d_{\text{ob}}(t) \geq d_{\text{safe}} > 0 \quad \forall t \geq t_0, \quad (12.63)$$

and

$$\theta_b^n \in [\theta_{\text{min}}, \theta_{\text{max}}]. \quad (12.64)$$

Furthermore, if there is just a single obstacle in the scenario, then there exists a time $t_f \geq t_0$ at which the distance to the target position \mathbf{p}_t^n satisfies

$$\|\mathbf{p}_b^n - \mathbf{p}_t^n\| \leq d_a. \quad (12.65)$$

Proof. Let the distance between the vehicle and the obstacle be reduced to d_{switch} at time $t = t_1$, and let $\mathbf{v}_{dg}^n(t_1) \in \mathcal{V}_c$. The switching distance d_{switch} given in (12.62) then ensures that the vehicle is able to reach \mathcal{V}_c before the obstacle can be within the safety distance d_{safe} of the vehicle's turning circle. There is then a time $t_2 \geq t_1$ when $d_{ob}(t_2) \geq d_{\text{safe}}$, $\psi_b^n(t_2) = \psi_{dca}^n(t_2)$ and $\theta_b^n(t_2) = \theta_{dca}^n(t_2)$. It follows from Lemmas 12.1 and 12.2 that $q_{\text{max}} \geq |\dot{\theta}_{dca}^n(t)| \forall t > t_1$ and $r_{\text{max}} \geq |\dot{\psi}_{dca}^n(t)| \forall t > t_1$. Hence, the vehicle's velocity vector will point along the surface of \mathcal{V}_c for $t \in [t_2, t_3]$, where t_3 is the time when the vehicle will exit collision avoidance mode.

The conditions of Lemma 11.2 are then satisfied, and it is ensured that

$$d_{ob}(t) \geq d_{\text{safe}} \quad \forall t \in [t_1, t_3]. \quad (12.66)$$

Thus, the control objective (12.7) is satisfied. Since the vehicle moves around the obstacle, Assumption 12.7 ensures that a time t_2 when the line of sight to the target \mathbf{p}_t^n is outside of \mathcal{V}_c exists. In accordance with the switching rule (12.24), the vehicle will then exit collision avoidance mode and proceed towards the target.

The obstacle may turn so that the line of sight to \mathbf{p}_t^n comes within \mathcal{V}_c before $d_{ob} > d_{\text{switch}}$, making the vehicle enter collision avoidance mode again. However, since \mathbf{v}_{dca1}^n and \mathbf{v}_{dca2}^n are first order differentiable and $\langle \theta_{dca}^n, \psi_{dca}^n \rangle$ is then chosen to be the closest of \mathbf{v}_{dca1}^n and \mathbf{v}_{dca2}^n by (12.19), the vehicle is immediately able to follow a velocity along \mathcal{V}_c to avoid the obstacle again.

Since $u_b > u_{\text{omax}}$, the vehicle will eventually be able to escape the obstacle and reach the target, satisfying control objective (12.6). Finally, since neither the pitch guidance law (12.27) nor the collision avoidance law will give pitch references outside of $[\theta_{\text{min}}, \theta_{\text{max}}]$, Assumption 12.3 ensures that the vehicle pitch does not violate its limits, satisfying control objective (12.8). \square

12.5 Simulations

In this section we will present numerical simulations to validate the analysis in Section 12.4. We will first show the performance of the algorithm when avoiding a static obstacle, and then extend the simulations to moving obstacles.

12.5.1 Static obstacles

The parameters used in the simulations with a static obstacle are summarized in Table 12.1.

Table 12.1: Simulation parameters

r_{max}	0.5 rad/s	θ_{min}	-0.5 rad
q_{max}	0.5 rad/s	θ_{max}	0.5 rad
u_b	2 m/s	$\mathbf{p}_b^n(t_0)$	$[0, 0, 0]^T$ (m)
R_o	10 m	$\mathbf{p}_o^n(t_0)$	$[125, 0, 0]^T$ (m)
d_{safe}	6 m	d_a	10 m

The avoidance angle α_o was set using (12.60) to 0.9 rad, while the switching distance was set using (12.62) to $d_{\text{switch}} = 10$ m. The upper bounds on the required pitch and heading rate during collision avoidance was calculated using (12.32) and (12.48) to $\dot{\theta}_{d\text{casup}}^n = 0.16$ rad/s and $\dot{\psi}_{d\text{casup}}^n = 0.33$ rad/s.

The obstacle position was set to $\mathbf{p}_o^n = [70, y_{\text{osim}}^n, z_{\text{osim}}^n]^T$ (m), where y_{osim}^n and z_{osim}^n were set to increase incrementally from -15 m to 15 m in steps of 1 m for each simulation, creating a set of 961 simulations. The results of the simulations are summarized in Table 12.2, where d_{obmin} denotes the minimum obstacle distance during a simulation, θ_{bmin}^n denotes the minimum pitch during a simulation, while θ_{bmax}^n denotes the maximum pitch value.

Table 12.2: Simulation results

Min d_{obmin}	6.1 m	Min $t_f - t_0$	60.0 s
Max d_{obmin}	11.2 m	Max $t_f - t_0$	65.1 s
Min θ_{bmin}^n	-0.43 rad	Min θ_{bmax}^n	0 rad
Max θ_{bmin}^n	0 rad	Max θ_{bmax}^n	0.43 rad
Max $ \dot{\theta}_{\text{dca}}^n $	0.10 rad	Max $ \dot{\psi}_{\text{dca}}^n $	0.21 rad

The results in Table 12.2 verify the results of Theorem 12.4: The vehicle always reaches the target, the safety distance is never violated, the bounds on θ_b^n are upheld and the required pitch and yaw rate does not exceed $\dot{\theta}_{d\text{casup}}^n$ and $\dot{\psi}_{d\text{casup}}^n$.

An example scenario is shown in Figure 12.6, where $y_{\text{osim}}^n = 4$ m and $z_{\text{osim}}^n = 5$ m. The direction along \mathcal{V}_e minimizing the cost function C is then to the upper port side of the vehicle. The pitch is limited by θ_{max} , and the maneuver is dominated by horizontal movement. When the line of sight to the target comes outside \mathcal{V}_e , the vehicle leaved collision avoidance mode and continued under nominal guidance.

The distance to the obstacle during the simulation is shown in Figure 12.7, where it can be seen that the vehicle approached, but did not cross, the safety distance d_{safe} during the collision avoidance maneuver. Furthermore, the vehicle heading θ_b^n remains within $[\theta_{\text{min}}, \theta_{\text{max}}]$ as shown in the lower parts of the figure, where it can be seen that the vehicle started the maneuver by pitching up, going above the obstacle, before pitching down again.

The required pitch and yaw rate during the collision avoidance maneuver, $\dot{\theta}_{d\text{casup}}^n$ and $\dot{\psi}_{d\text{casup}}^n$, are displayed in Figure 12.8. After an initial increase in magnitude as the vehicle approached the obstacle and turned towards \mathcal{V}_c , the rates remained relatively constant and well within the theoretical limits of Lemmas 12.1 and 12.2.

12.5.2 Moving obstacle

In the next two scenarios the obstacle is moving with a speed of $u_o = u_{\text{omax}} = 1$ m/s. The maximum acceleration and angular velocity are set to $a_{\text{omax}} = 0$ m/s and $\omega_{\text{omax}} = 0.4$ rad/s, respectively. The safety distance was increased to $d_{\text{safe}} = 15$ m, which gives an avoidance angle according to (12.60) of $\alpha_o = 1.16$ rad and a switching

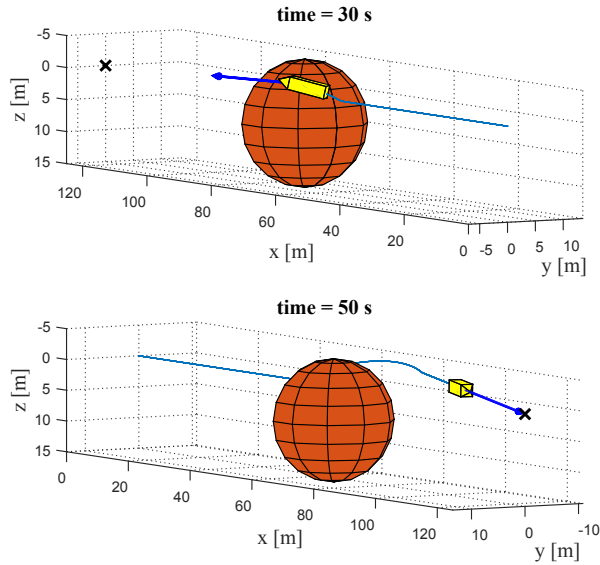


Figure 12.6: A scenario where $y_{osim}^n = 4\text{ m}$ and $z_{osim}^n = 5\text{ m}$. The vehicle is the yellow polyhedron, and the obstacle is the red sphere. The blue line is the vehicle trajectory, the target is marked by an 'X', and the desired direction from guidance is shown by a blue arrow.

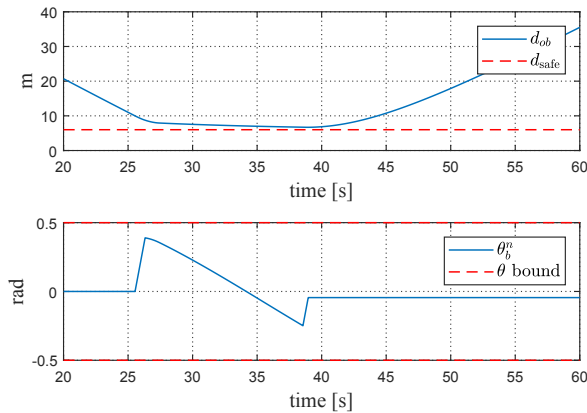


Figure 12.7: The distance d_{ob} to the obstacle and the vehicle pitch θ_b^n during the simulation with the static obstacle.

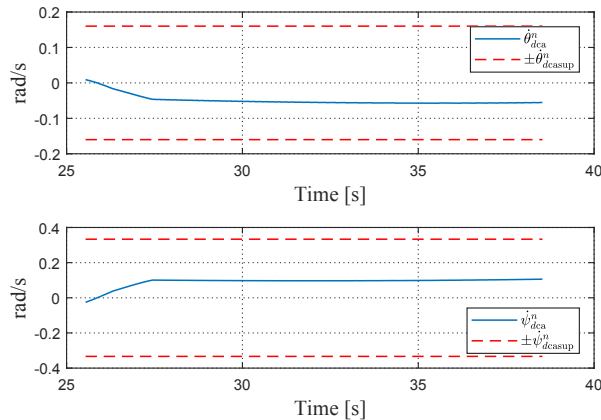


Figure 12.8: The required pitch and yaw rate during the collision avoidance maneuver around a static obstacle.

distance according to (12.62) of $d_{\text{switch}} = 25.3$ m. The resulting bounds on the required angular rates are $\dot{\theta}_{dcasup}^n = 0.40$ rad and $\dot{\psi}_{dcasup}^n = 0.50$ rad. Thus, the conditions of Theorem 12.4 are satisfied.

In the first scenario, shown in Figure 12.9, the obstacle crosses in front of the vehicle, passing from the port side. The vehicle chooses to move down and behind the obstacle, minimizing the cost function C in (12.18), and safely maneuvers around the obstacle.

As can be seen from Figure 12.10, the obstacle distance is greater than the minimum safety distance throughout the maneuver, and the vehicle pitch stays within its limits. Furthermore, the required angular rates on the vehicle during the avoidance maneuver is well within the theoretical limits, as shown in Figure 12.11. Thus, the theoretical results of Theorem 12.4 and of Lemmas 12.1 and 12.2 are verified by this simulation.

In the final simulation scenario, shown in Figure 12.12 the vehicle encounters an obstacle head on. The vehicle moves up and to starboard in order to avoid collision. The obstacle, however, is set to be in pursuit of the vehicle, with a desired velocity direction always pointing towards the vehicle. Hence, the obstacle follows the vehicle throughout the maneuver. In spite of the collision-seeking obstacle behavior, the CAA algorithm makes the vehicle successfully exploit its superior maneuvering capabilities. Thus, as seen in Figure 12.13, the distance to the obstacle is always kept above d_{safe} , and the vehicle pitch remains within $[\theta_{\min}, \theta_{\max}]$. Furthermore, the required pitch and yaw rate again stays well within the theoretical constraints of Lemmas 12.1 and 12.2, as seen in Figure 12.14.

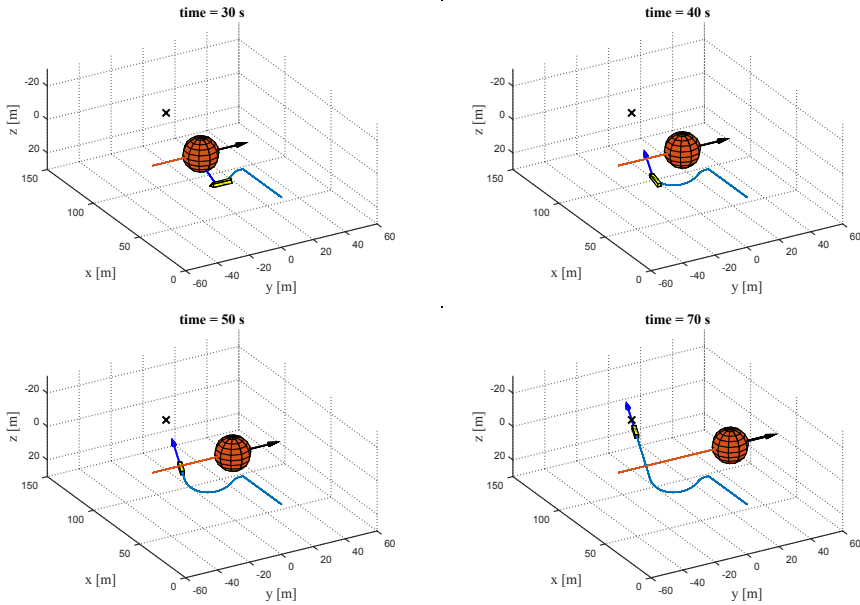


Figure 12.9: A scenario where the obstacle crosses in front of the vehicle. The direction of obstacle velocity is shown by a black arrow.

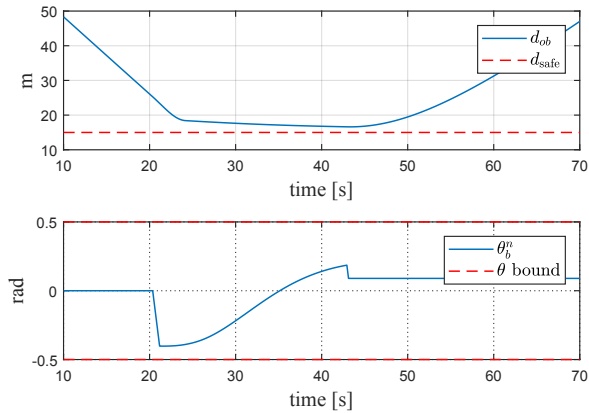


Figure 12.10: The distance d_{ob} to the obstacle and the vehicle pitch θ_b^n when the vehicle avoids a crossing obstacle.

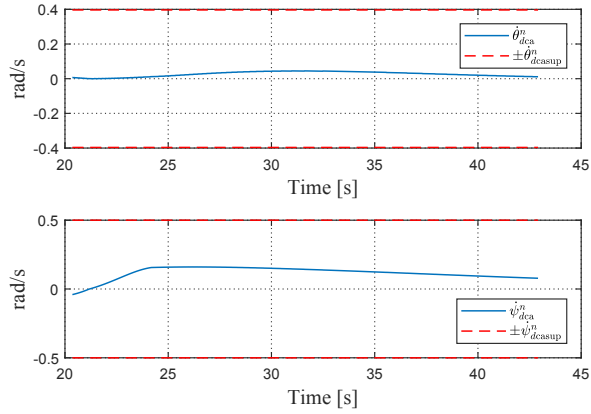


Figure 12.11: The required pitch and yaw rate during the collision avoidance maneuver around a crossing obstacle.

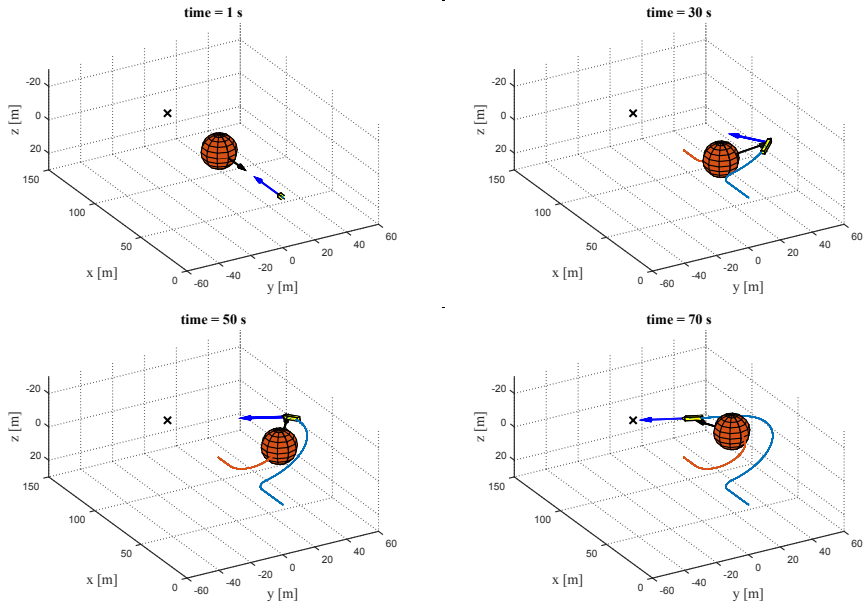


Figure 12.12: A scenario where the obstacle is in pursuit of the vehicle in front of the vehicle.

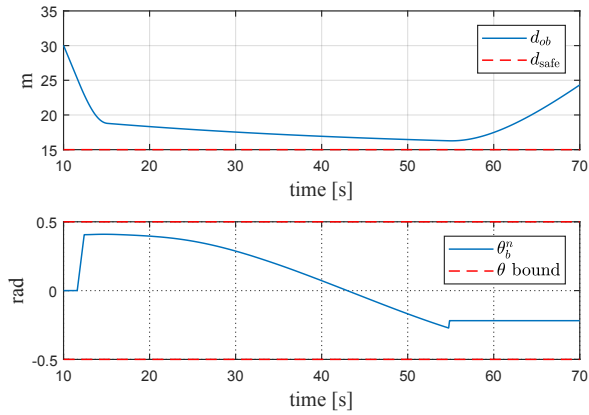


Figure 12.13: The distance d_{ob} to the obstacle and the vehicle pitch θ_b^n when the vehicle avoids a pursuing obstacle.

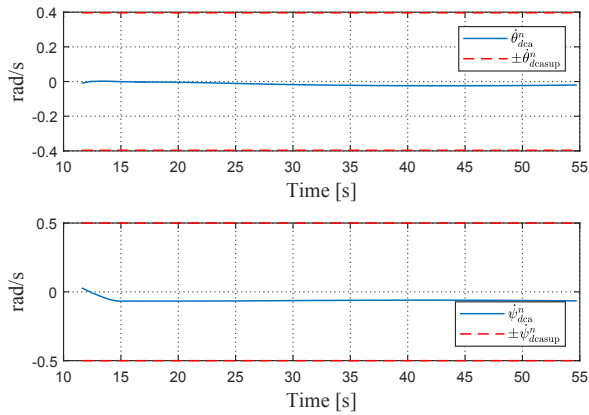


Figure 12.14: The required pitch and yaw rate during the collision avoidance maneuver around a pursuing obstacle.

12.6 Conclusions

In this chapter, we have applied the 3D CAA algorithm presented in Chapter 11 to a kinematically modeled vehicle with nonholonomic constraints in sway and heave, and with limited pitch and yaw rates. The vehicle has been restricted to keep a constant forward speed, and to have a safety limitation on the vehicle pitch. Such pitch bounds are commonly seen in real life scenarios involving, for example, fixed-wing aircraft or AUVs. We have shown how the optimality criterion used to choose among the directions along the safe, compensated vision cone ensures that these pitch limitations are upheld.

The main theorem in this chapter states the minimum switching distance required in order to ensure that the vehicle is able to turn around and reach the safe, compensated vision cone before the obstacle can get too close. We have also derived upper bounds on the required pitch and yaw rate when following a direction along this cone. Specifically, since the optimality criterion chooses the direction which minimizes the desired pitch and yaw rate, we can consider the horizontal and vertical plane separately. Thus, we have been able to build on the results from the analysis of the 2D CAA algorithm in Part III. In particular, we have used the results from the unicycle analysis in Chapter 8 in order to prove safe avoidance also in 3D for a kinematic vehicle with nonholonomic constraints.

In the next chapter, we will extend the vehicle model to a full 5 DOF dynamic model of a maneuvering underwater vehicle. Such a vehicle has underactuation both in sway and heave, and we will use the bounds on the required pitch and yaw rate derived in this chapter in order to limit the induced sway and heave motion during the maneuver.

Chapter 13

The CAA algorithm for underactuated underwater vehicles

Don't panic.

— Douglas Adams, *The Hitchhiker's Guide to the Galaxy*

While we in the previous chapter applied the 3D CAA algorithm to a kinematically modeled vehicle with nonholonomic constraints and a constant forward speed, we will in this chapter extend the vehicle model to include the full 5 DOF dynamics of an underactuated marine vehicle, such as an AUV steered by rudders, sternplanes and a propeller. We saw in Chapter 10 that for an underactuated surface vehicle, a sway movement is induced while the vehicle is turning. In the 5 DOF case, there is an additional underactuation in heave, and a heave motion towards the obstacle is induced when the vehicle is pitching away.

We will include the underactuated speeds in sway and heave by steering the direction of the vehicle's velocity vector rather than the vehicle's orientation. Specifically, we derive a method for converting a desired angular velocity of the vehicle's linear velocity vector into control inputs to the rudders and sternplanes, using a novel Flow frame controller. We will show that the sway and heave dynamics remain bounded during the maneuver, and that the pitch of the velocity vector can be limited in order to adhere to safety constraints.

In the previous chapter, we derived upper bounds on the required pitch and yaw rate during the maneuver. In this chapter, we will include a time-varying vehicle speed in these expressions, in order to show that the required angular rates of the vehicle's velocity vector remain well defined. Specifically, we will include the underactuated sway and heave components of the vehicle speed. These will make the vehicle speed tend to increase as the vehicle pitches and turns with a constant forward speed. We show how these underactuated speed components are inherently accounted for by the algorithm, and provide conditions under which the avoidance maneuver is still provably safe.

During the switch from nominal operation to collision avoidance, there is a discontinuity in the desired angular rates of the vehicle. To ensure that the directly actuated pitch and yaw rates are always able to follow their references, we include a linear bump function to remove this discontinuity.

We are, in this work, mainly concerned with the avoidance of sparsely spaced obstacles, and an analysis of multi-obstacle scenarios is beyond the scope. How-

ever, it is possible to extend the algorithm to include multiple moving hindrances. We will provide a qualitative description of this process, and will demonstrate its applicability in numerical simulations.

The algorithm has been implemented into the control system of a Hugin AUV [43], which is a commercially widespread AUV jointly developed by the Norwegian Defence Research Establishment and Kongsberg Maritime. Even though access to the low-level control system was not available, the modular nature of the algorithm made it straightforward to implement it on top of the existing control system. To demonstrate the algorithm's capabilities in a controlled manner, the vehicle was made to avoid moving virtual obstacles in a sequence of several experiments with time-varying parameters. The vehicle was able to avoid all the obstacles, even in the presence of sensor noise and unmodeled environmental disturbances, which implies robustness of the algorithm from a control perspective.

The remainder of this chapter is organized as follows. In Section 13.1 we summarize the vehicle and obstacle model, and state the current control objectives. A reiteration of the 3D CAA algorithm is provided in Section 13.2, while the underlying control system, including the Flow frame controller and a target reaching guidance law, is presented in Section 13.3. An analysis of the system is given in Section 13.4, and the analysis is validated by both simulations in Section 13.5, and through experiments in Section 13.6. Finally, the chapter is concluded in Section 13.7.

The work presented in this chapter is based on Wiig et al. [115], Wiig et al. [116] and Wiig et al. [118].

13.1 System description

13.1.1 Vehicle model

In this chapter we will model the vehicle using the 5 DOF maneuvering model described in Chapter 3. The 5 DOF kinematics of the vehicle are described by

$$\dot{\boldsymbol{\eta}}_b^n = \mathbf{J}(\boldsymbol{\eta}_b^n) \boldsymbol{\nu}_{b/n}^b, \quad (13.1)$$

where $\boldsymbol{\eta}_b^n \triangleq [\mathbf{p}_b^n, \theta_b^n, \psi_b^n]^T$ contains the position and orientation of the vehicle's Body frame b with respect to the inertial frame n and $\boldsymbol{\nu}_{b/n}^b \triangleq [\mathbf{v}_{b/n}^b, q_b, r_b]^T$ contains the body fixed linear velocities $\mathbf{v}_{b/n}^b \triangleq [u_b, v_b, w_b]^T$, pitch rate q_b and yaw rate r_b . The transformation matrix $\mathbf{J}(\boldsymbol{\eta}_b^n)$ is defined as

$$\mathbf{J}(\boldsymbol{\eta}_b^n) \triangleq \begin{bmatrix} \mathbf{R}_{zy}(\theta_b^n, \psi_b^n) & 0 \\ 0 & \mathbf{T}_b^n(\theta_b^n) \end{bmatrix}, \quad (13.2)$$

where $\mathbf{T}_b^n(\theta_b^n) \triangleq \text{diag}\{1, 1/\cos(\theta_b^n)\}$, $|\theta_b^n| \neq \frac{\pi}{2}$.

The dynamics of the vehicle are obtained in component form as

$$\dot{u}_b = F_u(u_b, v_b, w_b, r_b, q_b) + \tau_u, \quad (13.3a)$$

$$\dot{v}_b = X_v(u_b)r_b + Y_v(u_b)v_b, \quad (13.3b)$$

$$\dot{w}_b = X_w(u_b)q_b + Y_w(u_b)w_b + Z_w \sin(\theta_b^n), \quad (13.3c)$$

$$\dot{q}_b = F_q(\theta_b^n, u_b, w_b, q_b) + \tau_q. \quad (13.3d)$$

$$\dot{r}_b = F_r(u_b, v_b, r_b) + \tau_r. \quad (13.3e)$$

The functions $F_u, X_v, Y_v, X_w, Y_w, Z_w, F_q$ and F_r contain hydrodynamic parameters. These functions are defined in Section 3.2.2, and restated in Appendix 13.A for convenience.

Since the vehicle dynamics in (13.3) are described using a maneuvering model, we assume that the vehicle operates at maneuvering speed:

Assumption 13.1. The vehicle surge speed u_b satisfies $u_b \geq u_{b\min}$, where $u_{b\min} > 0$ is a constant parameter.

Even though sway and heave can not be directly controlled, we can still ensure that these dynamics are nominally stable by making the following assumption:

Assumption 13.2. The functions $Y_v(u_b)$ and $Y_w(u_b)$ are negative for all $u_b \geq u_{b\min}$.

This assumption holds for most AUVs by design.

13.1.2 The Flow frame

The direction of the vehicle's velocity vector is of main interest to us when steering the vehicle to avoid an obstacle. Thus, we would like to represent the vehicle kinematics in such a way that we obtain

$$\dot{\mathbf{p}}_b^n = \mathbf{R}_f^n(\theta_f^n, \psi_f^n) \mathbf{v}_{f/n}^f, \quad (13.4)$$

where $\mathbf{v}_{f/n}^f \triangleq [U_b, 0, 0]^T$ and $U_b \triangleq \|\mathbf{v}_{b/n}^b\|$. The frame f is defined in Fossen [35] as the Flow frame, and the rotation from b to f is found using the angle of attack $\alpha_b \triangleq \text{atan2}(w_b, u_b)$ and sideslip angle $\beta_b \triangleq \text{atan2}(v_b, U_w)$, where $U_w \triangleq \sqrt{u_b^2 + w_b^2}$:

$$\mathbf{R}_b^f \triangleq \mathbf{R}_{zy}(\alpha_b, -\beta_b). \quad (13.5)$$

The vehicle kinematics can then be written as

$$\dot{\mathbf{p}}_b^n = \mathbf{R}_{zy}(\theta_b^n, \psi_b^n) \mathbf{R}_{zy}(\alpha_b, -\beta_b)^T \mathbf{v}_{f/n}^f, \quad (13.6)$$

$$= \mathbf{R}_{zyx}(\varphi_f^n, \theta_f^n, \psi_f^n) \mathbf{v}_{f/n}^f. \quad (13.7)$$

To steer the Flow frame, we require expressions for the Euler angles φ_f^n , θ_f^n and ψ_f^n , as well as the Flow frame angular velocity vector $\boldsymbol{\omega}_{n/f}^f \triangleq [p_f, q_f, r_f]^T$ containing the roll, pitch and yaw rate, respectively. Using the procedure from Fossen [35], the Euler angles are found as

$$\varphi_f^n = \tan^{-1} [s(\beta_b)t(\gamma_b)], \quad (13.8)$$

$$\theta_f^n = \sin^{-1} [c(\beta_b)s(\gamma_b)], \quad (13.9)$$

$$\psi_f^n = \tan^{-1} \left(\frac{c(\gamma_b)s(\psi_b^n)c(\beta_b) + c(\psi_b^n)s(\beta_b)}{c(\gamma_b)s(\psi_b^n)c(\beta_b) + c(\psi_b^n)s(\beta_b)} \right), \quad (13.10)$$

where $\gamma_b \triangleq \theta_b^n - \alpha_b$. The Euler angle derivatives are

$$\begin{bmatrix} \dot{\varphi}_f^n \\ \dot{\theta}_f^n \\ \dot{\psi}_f^n \end{bmatrix} = \begin{bmatrix} 1 & s(\varphi_f^n)t(\theta_f^n) & c(\varphi_f^n)t(\theta_f^n) \\ 0 & c(\varphi_f^n) & -s(\varphi_f^n) \\ 0 & s(\varphi_f^n)/c(\theta_f^n) & c(\varphi_f^n)/c(\theta_f^n) \end{bmatrix} \boldsymbol{\omega}_{n/f}^f. \quad (13.11)$$

The angular velocity vector $\boldsymbol{\omega}_{n/f}^f$ is found as in Børhaug and Pettersen [12]:

$$\boldsymbol{\omega}_{n/f}^f = \boldsymbol{\omega}_{n/b}^f + \boldsymbol{\omega}_{b/f}^f = \mathbf{R}_{zy}(\alpha_b, -\beta_b)\boldsymbol{\omega}_{n/b}^f + \boldsymbol{\omega}_{b/f}^f, \quad (13.12)$$

where $\boldsymbol{\omega}_{n/b}^f = [0, q_b, r_b]^T$ and $\boldsymbol{\omega}_{b/f}^f$ is derived as $\boldsymbol{\omega}_{b/f}^f = [-\dot{\beta}_b \sin(\alpha_b), -\dot{\alpha}_b, \dot{\beta}_b \cos(\alpha_b)]^T$.

To obtain an expression for q_f and r_f as a function of the pitch and yaw rate in b , we insert for $\dot{\alpha}_b$ and $\dot{\beta}_b$ in (13.12) to obtain

$$\begin{bmatrix} q_f \\ r_f \end{bmatrix} = \mathbf{A}_f \begin{bmatrix} q_b \\ r_b \end{bmatrix} + \mathbf{B}_f, \quad (13.13)$$

where

$$\mathbf{A}_f \triangleq \begin{bmatrix} c(\beta_b) - \frac{X_w u_b}{U_w^2} & -s(\beta_b)s(\alpha_b) \\ c(\alpha_b) \frac{X_w w_b v_b}{U_w U_b^2} & c(\alpha_b) \frac{U_w X_v + U_b^2}{U_w U_b^2} \end{bmatrix}, \quad (13.14)$$

and

$$\mathbf{B}_f \triangleq \begin{bmatrix} -u_b \frac{Z_w s(\theta_b^n) + Y_w w_b}{U_w^2} & v_b c(\alpha_b) \frac{Z_w s(\theta_b^n) w_b + Y_v U_w^2 + Y_w w_b^2}{U_w U_b^2} \end{bmatrix}^T. \quad (13.15)$$

It can be shown that \mathbf{A}_f is nonsingular when the following assumption is met:

Assumption 13.3. The functions $X_v(u_b)$ and $X_w(u_b)$ satisfy $X_v(u_b) + u_b > 0$ and $-X_w(u_b) + u_b > 0$ for all $u_b \geq u_{b\min}$.

This assumption ensures that a change in θ_b^n or ψ_b^n will result in a change in θ_f^n or ψ_f^n , respectively, and holds for most AUVs operating at maneuvering speed by design. The expression in (13.13) enables us to control q_f and r_f , and hence the direction of the vehicle's velocity vector, by controlling the angular rates q_b and r_b of the Body frame.

13.1.3 Analysis model

We would like to remove the $q_b - r_f$ and $r_b - q_f$ couplings in (13.13) to simplify the analysis in Section 13.4. This can be done by assuming that the angle of attack α_b and sideslip angle β_b are small, and then make the small angle approximations $c(\alpha_b) \approx 1$, $c(\beta_b) \approx 1$ and $s(\alpha_b)s(\beta_b) \approx 0$. The sideslip angle can then be further simplified as $\beta_b \approx \text{atan2}(v_b, u_b)$. Equation (13.13) can then be reduced to

$$q_f \approx q_b - \dot{\alpha}_b \quad (13.16)$$

$$r_f \approx r_b + \dot{\beta}_b. \quad (13.17)$$

The sway and heave dynamics in (13.3b) and (13.3c) can then be rewritten in terms of q_f and r_f as

$$\dot{v}_b \approx \frac{u_b^2 + v_b^2}{X_v u_b + u_b^2 + v_b^2} (X_v r_f + Y_v v_b), \quad (13.18)$$

$$\dot{w}_b \approx \frac{U_w^2}{U_w^2 - X_w u_b} (X_w q_f + Y_w w_b + Z_w \sin(\theta_b^n)). \quad (13.19)$$

The small angle assumption for α_b and β_b holds for vehicles where the hydrodynamic damping and rudder saturation ensures that turning rate is not too large, which is the case of most AUVs at maneuvering speed.

13.1.4 Obstacle model

Recall from Section 11.1 that the obstacle is modeled as a moving sphere with radius R_o :

$$\dot{\boldsymbol{\eta}}_o^n = \mathbf{J}(\boldsymbol{\eta}_o^n) \boldsymbol{\nu}_{o/n}^o, \quad (13.20a)$$

$$\dot{a}_o = a_o, \quad (13.20b)$$

where $\boldsymbol{\eta}_o^n \triangleq [\mathbf{p}_o^n, \theta_o^n, \psi_o^n]^T$ and $\boldsymbol{\nu}_{o/n}^o \triangleq [u_o, 0, 0, q_o, r_o]^T$. The obstacle's angular velocity and acceleration is assumed to be bounded, and in this chapter we also assume that they are smooth:

Assumption 13.4. The obstacle acceleration a_o and angular velocity $\boldsymbol{\omega}_{o/n}^o$ are smooth and bounded by

$$a_o \in [-a_{o\max}, a_{o\max}], \quad (13.21a)$$

$$\|\boldsymbol{\omega}_{o/n}^o\| \in [-\omega_{o\max}, \omega_{o\max}], \quad (13.21b)$$

where $a_{o\max} \geq 0$ and $\omega_{o\max} \geq 0$ are constant parameters.

To ensure that the vehicle is able to circumvent the obstacle, we need to assume that the obstacle speed is less than the desired vehicle surge speed, u_{bd} . The obstacle speed is further restricted if a large vehicle sway or heave speed is induced towards the obstacle when the vehicle turns away from it, i.e. if the maneuvering capabilities of the vehicle are poor. This restriction comes from the mathematical analysis in Section 13.4.

Assumption 13.5. The obstacle velocity lies in the interval $u_o \in [0, u_{o\max}]$. The upper bound should satisfy $u_{o\max} < \min\{u_{omv}, u_{omw}\}$, where

$$u_{omv} < \begin{cases} 2\sqrt{-X_v^2 - X_v u_{bd}}, & -u_{bd} < X_v \leq -\frac{u_{bd}}{2} \\ u_{bd}, & -\frac{u_{bd}}{2} < X_v, \end{cases} \quad (13.22)$$

and

$$u_{omw} < \begin{cases} 2\sqrt{-X_w^2 + X_w u_{bd}}, & \frac{u_{bd}}{2} < X_w \leq u_{bd} \\ u_{bd}, & X_w < \frac{u_{bd}}{2}. \end{cases} \quad (13.23)$$

13.1.5 Control objectives

In this chapter, the nominal control objective is target reaching. Thus, the goal of the control system is to make the vehicle safely reach a target position \mathbf{p}_t^n at some unspecified time $t_f \geq t_0$. We formalize this as

$$\exists t_f \in [t_0, \infty) \quad \text{s.t.} \quad \|\mathbf{p}_t^{nb}(t_f)\| \leq d_a, \quad (13.24)$$

$$d_{ob}(t) \geq d_{\text{safe}} > 0 \quad \forall t \in [t_0, t_f], \quad (13.25)$$

where $\mathbf{p}_t^{nb} = \mathbf{p}_t^n - \mathbf{p}_b^n$ is the target position in n_b , $d_a > 0$ is a user-specified acceptance distance, d_{ob} is the distance to the obstacle and $d_{\text{safe}} > 0$ is a design parameter.

Many AUVs have pitch limitations to ensure that they do not move too fast towards the sea floor or the surface, and to keep them within the roll stable regime. For this reason, we require that the control system bounds the pitch of the vehicle in the Flow frame as:

$$\theta_f^n(t) \in [\theta_{\min}, \theta_{\max}] \quad \forall t \in [t_0, t_f], \quad (13.26)$$

where $\theta_{\min} \in (-\pi/2, 0)$ and $\theta_{\max} \in (0, \pi/2)$ are constant design parameters.

The surge speed u_b will be controlled by using the feedback linearizing controller described in Section 13.3.4 to reach a desired surge speed u_{bd} . We set the desired surge speed to a positive constant:

Assumption 13.6. The desired surge speed is constant and satisfies $u_{bd} \geq u_{b\min}$.

For brevity, we introduce the notation $X_{vd} \triangleq X_v(u_{bd})$, $Y_{vd} \triangleq Y_v(u_{bd})$, $X_{wd} \triangleq X_w(u_{bd})$ and $Y_{wd} \triangleq Y_w(u_{bd})$.

13.2 The CAA algorithm in 3D

The 3D CAA algorithm is defined in Section 11.2 and summarized here for convenience.

The algorithm creates an extended vision cone \mathcal{V}_e from the vehicle to the obstacle, where the apex angle of the vision cone is $\gamma_e \triangleq 2(\gamma_a + \alpha_o)$, and

$$\gamma_a \triangleq \sin^{-1} \left(\frac{R_o}{R_o + d_{ob}} \right). \quad (13.27)$$

The vision cone is transformed to compensate for the obstacle speed u_o . For each ray ρ of \mathcal{V}_e , we find a frame F_ρ which is such that the x^{F_ρ} -axis points along ρ , while the obstacle velocity lies in the x^{F_ρ} - y^{F_ρ} -plane. We first find an intermediate frame A where the x^A -axis is coincident with the x^{F_ρ} -axis:

$$\mathbf{R}_{n_b}^A \triangleq \mathbf{R}_z(\gamma_e)^T \mathbf{R}_x(\phi)^T \mathbf{R}_{zy}(\Theta(\mathbf{p}_o^{nb}), \Psi(\mathbf{p}_o^{nb}))^T, \quad (13.28)$$

where the $\mathbf{p}_o^{nb} = \mathbf{p}_o^n - \mathbf{p}_b^n$ and the angle $\phi \in [0, 2\pi)$ is a parameter uniquely identifying each ray of the vision cone.

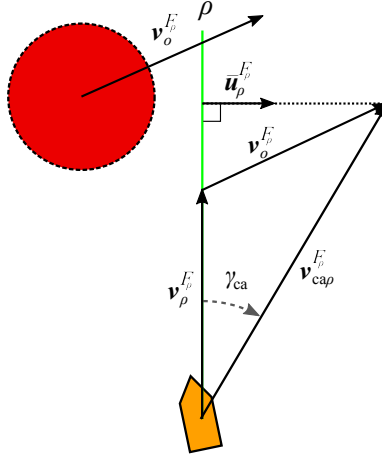


Figure 13.1: A plane containing both the ray ρ , the obstacle velocity vector $\mathbf{v}_{o/n}^n$ and the resulting candidate for desired velocity in collision avoidance mode, $\mathbf{v}_{ca\rho}^n$.

To obtain the frame F_ρ , we will rotate the A frame around the x^A -axis until $\mathbf{v}_o^{F_\rho}$ lies in the x^{F_ρ} - y^{F_ρ} -plane. The required rotation angle can be geometrically found as $\hat{\phi} \triangleq \text{atan2}(\mathbf{v}_{oz}^A, \mathbf{v}_{oy}^A)$. Hence, $\mathbf{R}_A^{F_\rho} = \mathbf{R}_x(\hat{\phi})$, and

$$\mathbf{v}_o^{F_\rho} = \mathbf{R}_{n_b}^{F_\rho} \mathbf{v}_{o/n}^n = \mathbf{R}_A^{F_\rho} \mathbf{R}_{n_b}^A \mathbf{v}_{o/n}^n. \quad (13.29)$$

We define a velocity vector $\mathbf{v}_\rho^{F_\rho}$ along ρ , and seek a vector

$$\mathbf{v}_{ca\rho}^{F_\rho} \triangleq \mathbf{v}_\rho^{F_\rho} + \mathbf{v}_o^{F_\rho}, \quad (13.30)$$

illustrated in Figure 13.1. The total speed of the vehicle is U_b , and we design the algorithm to compensate for the obstacle speed using U_b as input. Hence, we ensure that $\|\mathbf{v}_{ca\rho}^{F_\rho}\| = U_b$, which we do by finding the compensation angle γ_{ca} between $\mathbf{v}_\rho^{F_\rho}$ and $\mathbf{v}_{ca\rho}^{F_\rho}$ as

$$\gamma_{ca}(\phi) \triangleq \sin^{-1} \left(\frac{(\mathbf{v}_o^{F_\rho})^T \bar{\mathbf{u}}_\rho^{F_\rho}}{U_b} \right), \quad (13.31)$$

where $\bar{\mathbf{u}}_\rho^{F_\rho}$ is a unit vector orthogonal to $\mathbf{v}_\rho^{F_\rho}$ as shown in Figure 13.1. The vector $\mathbf{v}_{ca\rho}^{F_\rho}$ is thus

$$\mathbf{v}_{ca\rho}^{F_\rho} \triangleq U_b [\cos(\gamma_{ca}), \sin(\gamma_{ca}), 0]^T, \quad (13.32)$$

while

$$\mathbf{v}_{ca\rho}^n = (\mathbf{R}_{n_b}^{F_\rho})^T \mathbf{v}_{ca\rho}^{F_\rho}. \quad (13.33)$$

The collection of motion compensated rays compose a compensated vision cone \mathcal{V}_c , shown in Figure 13.2. The velocity direction required to follow a motion compensated ray is

$$\psi_\rho^n(\phi) \triangleq \Psi(\mathbf{v}_{ca\rho}^n(\phi)), \quad (13.34a)$$

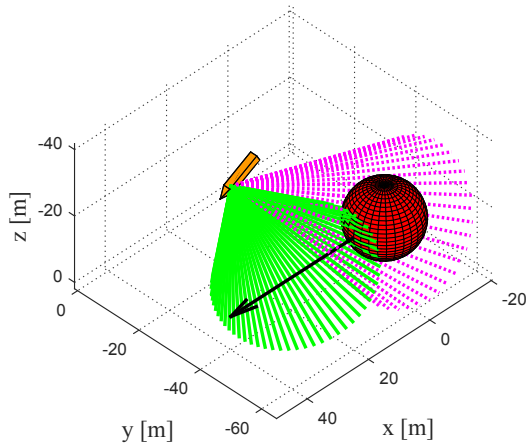


Figure 13.2: The compensated vision cone \mathcal{V}_c (green).

$$\theta_\rho^n(\phi) \triangleq \Theta(\mathbf{v}_{ca\rho}^n(\phi)). \quad (13.34b)$$

To obtain the desired heading and pitch angle in collision avoidance we obtain the parameter ϕ_{ca} as

$$\phi_{ca} \triangleq \arg \min_{\phi} C(\phi). \quad (13.35)$$

The cost function C is defined as

$$C \triangleq \begin{cases} C_{\text{enter}} + C_\theta & t = t_1 \\ C_{\text{in}} + C_\theta & t > t_1, \end{cases} \quad (13.36)$$

where t_1 is the time when the vehicle enters collision avoidance mode. The function C_{enter} will make the vehicle move behind the obstacle as it enters collision avoidance mode, the function C_θ ensures that the desired pitch from the algorithm remains within the bounds in (13.26), and the function C_{in} minimizes the required Flow frame pitch and yaw rate during the collision avoidance maneuver. These components of the cost function C are defined as

$$C_{\text{enter}} \triangleq \begin{cases} -\sqrt{(\theta_o^n - \theta_\rho^n)^2 + (\psi_o^n - \psi_\rho^n)^2}, & d_{ob} = d_{\text{switch}} \\ \sqrt{(\theta_f^n - \theta_\rho^n)^2 + (\psi_f^n - \psi_\rho^n)^2}, & d_{ob} < d_{\text{switch}}, \end{cases} \quad (13.37)$$

$$C_\theta \triangleq 2\pi (1 + \tanh(\lambda[\theta_{\min} - \theta_\rho^n])) + 2\pi (1 + \tanh(\lambda[\theta_\rho^n - \theta_{\max}])), \quad (13.38)$$

$$C_{\text{in}} \triangleq \sqrt{(\theta_{dca}^n - \theta_{dca1}^n)^2 + (\psi_{dca}^n - \psi_{dca1}^n)^2}, \quad (13.39)$$

where θ_{dca1}^n and ψ_{dca1}^n is the desired pitch and heading during the previous optimization, and $\lambda > 0$ is a design parameter used to set the slope of C_θ .

Thus, we obtain the desired Flow frame pitch and heading angle in collision avoidance mode as

$$\langle \theta_{dca}^n, \psi_{dca}^n \rangle \triangleq \langle \theta_\rho^n(\phi_{ca}), \psi_\rho^n(\phi_{ca}) \rangle. \quad (13.40)$$

The vehicle will enter collision avoidance mode at a time t_1 when

$$\mathbf{v}_{dg}^n(t_1) \in \mathcal{V}_e(t_1), \quad (13.41a)$$

$$d_{ob}(t_1) \leq d_{switch} > d_{safe}, \quad (13.41b)$$

where \mathbf{v}_{dg}^n is the desired velocity vector from the guidance law described in Section 13.3.1, and d_{switch} is a chosen switching distance. The vehicle will leave collision avoidance mode and enter nominal guidance mode at a time t_2 when

$$\mathbf{v}_{dg}^n(t_2) \notin \mathcal{V}_e(t_2). \quad (13.42)$$

13.3 Control system

When no obstacles are at risk of collision with the vehicle, the vehicle will be in guidance mode and under the control of a target reaching guidance law described in this section. If there is a risk of collision, the control system will enter into collision avoidance mode according to a rule in (13.41). The vehicle will then be under the control of the 3D CAA algorithm, described in Section 13.2.

In this section we also describe the controllers used to steer the Flow frame of the vehicle, as well as the low-level yaw rate, pitch rate and surge controllers.

13.3.1 Target reaching guidance law

We will employ a pure pursuit guidance law [16] to make the vehicle reach the target position \mathbf{p}_t^n . The desired heading ψ_{dg}^n is thus set to point towards the target:

$$\psi_{dg}^n \triangleq \Psi(\mathbf{p}_t^{nb}), \quad (13.43)$$

where Ψ is defined in (2.5).

The desired pitch θ_{dg}^n in guidance mode is saturated to ensure that control objective (13.26) is met:

$$\theta_{dg}^n = \begin{cases} \theta_{\max} & \Theta(\mathbf{p}_t^{nb}) > \theta_{\max}, \\ \Theta(\mathbf{p}_t^{nb}) & \Theta(\mathbf{p}_t^{nb}) \in [\theta_{\min}, \theta_{\max}], \\ \theta_{\min} & \Theta(\mathbf{p}_t^{nb}) < \theta_{\min}, \end{cases} \quad (13.44)$$

where Θ is defined in (2.6).

The desired velocity vector in guidance mode, \mathbf{v}_{dg}^n , is then found from the guidance laws (13.43) and (13.44) as:

$$\mathbf{v}_{dg}^n \triangleq \mathbf{R}_{zy}(\theta_{dg}^n, \psi_{dg}^n) [U_b \quad 0 \quad 0]^T. \quad (13.45)$$

13.3.2 Flow frame control

To account for the underactuated dynamics, we will steer the direction of the vehicle's velocity vector, i.e. we will control $\dot{\theta}_f^n$ and $\dot{\psi}_f^n$. To this end, we use (13.13) to obtain

$$\begin{bmatrix} \bar{q}_{bd} \\ \bar{r}_{bd} \end{bmatrix} = \mathbf{A}_f^{-1} \left(\begin{bmatrix} q_{fd} \\ r_{fd} \end{bmatrix} - \mathbf{B}_f \right). \quad (13.46)$$

The desired Flow frame angular rates q_{fd} and r_{fd} are obtained as

$$q_{fd} = c(\varphi_f^n) \dot{\theta}_{fc}^n + c(\theta_f^n) s(\varphi_f^n) \dot{\psi}_{fc}^n, \quad (13.47)$$

$$r_{fd} = -s(\varphi_f^n) \dot{\theta}_{fc}^n + c(\theta_f^n) c(\varphi_f^n) \dot{\psi}_{fc}^n. \quad (13.48)$$

The signals $\dot{\theta}_{fc}^n$ and $\dot{\psi}_{fc}^n$ are set using a proportional controller in order to obtain exponential convergence of the Flow frame heading and pitch. To limit the yaw and pitch rate, and hence the induced sway and heave motions, the proportional effect is saturated:

$$\dot{\psi}_{fc}^n \triangleq \dot{\psi}_{fd}^n - \text{sat}(k_\psi \tilde{\psi}_f^n, \sigma_\psi), \quad (13.49a)$$

$$\dot{\theta}_{fc}^n \triangleq \dot{\theta}_{fd}^n - \text{sat}(k_\theta \tilde{\theta}_f^n, \sigma_\theta), \quad (13.49b)$$

where $\tilde{\theta}_f^n \triangleq \theta_f^n - \theta_{fd}^n$ and $\tilde{\psi}_f^n \triangleq \psi_f^n - \psi_{fd}^n$. We define these error variables to lie in the interval $(-\pi, \pi]$ to ensure that the vehicle makes the shortest turn towards ψ_{fd}^n and θ_{fd}^n . The desired heading and pitch are given in Section 13.3.1 when the control system is in nominal guidance mode, and in Section 13.2 when the control system is in collision avoidance mode. The control gains $k_\psi > 0$ and $k_\theta > 0$ are positive design variables, while the variables $\sigma_\psi > 0$ and $\sigma_\theta > 0$ are saturation parameters used in the saturation function

$$\text{sat}(a, b) \triangleq \begin{cases} b, & a > b, \\ a, & a \in [-b, b], \\ -b, & a < -b. \end{cases} \quad (13.50)$$

In order to ensure that the Flow frame heading saturation acts on an error in the interval $\tilde{\psi}_f^n \in (-\pi, \pi]$, we make the following assumption on σ_ψ :

Assumption 13.7.

$$\sigma_\psi < k_\psi \pi. \quad (13.51)$$

Similarly, in order to ensure that the Flow frame pitch rate saturation acts on an error in the interval $\tilde{\theta}_f^n \in (-\pi/2, \pi/2)$ we assume that:

Assumption 13.8.

$$\sigma_\theta < k_\theta \frac{\pi}{2}. \quad (13.52)$$

Remark 13.1. If Assumptions 13.7 and 13.8 are not met, the saturation will not have any effect and can be removed.

13.3.3 Yaw and pitch rate bump function

When the control system switches mode, there is a discontinuity in ψ_{fd}^n and θ_{fd}^n , and hence in \bar{r}_{bd} and \bar{q}_{bd} obtained in (13.46). To avoid the discontinuity in the desired yaw and heading rate, we use the linear bump function $\text{bump}(t_b)$ introduced in Chapter 10:

$$\text{bump}(t_b) = \begin{cases} 1, & t_b \geq T_b, \\ \frac{t_b}{T_b}, & 0 < t_b < T_b \\ 0, & t_b \leq 0, \end{cases} \quad (13.53)$$

where the bump time T_b is a positive constant.

As long as the yaw rate signal \bar{r}_{bd} from (13.46) is smooth, $r_{bd} = \bar{r}_{bd}$. However, if there is a jump in \bar{r}_{bd} at time t_1 , we apply the bump function:

$$r_{bd}(t) = r_{bd}(t_1) [1 - \text{bump}(t - t_1)] + \bar{r}_{bd}(t) \text{bump}(t - t_1). \quad (13.54)$$

This ensures that when $t \geq t_1 + T_b$, $r_{bd}(t) = \bar{r}_{bd}(t)$. If, at a time $t_2 \in (t_1, t_1 + T_b)$, $r_{bd}(t_2) = \bar{r}_{bd}(t_2)$, use of the smoothing function is stopped until the next discontinuity in \bar{r}_{bd} . The pitch rate signal \bar{q}_{bd} is smoothed in the same way.

13.3.4 Low-level controllers

The surge (13.3a), pitch rate (13.3d) and yaw rate (13.3e) are controlled using feedback linearizing controllers:

$$\tau_u = -F_u(\theta_b^n, u_b, v_b, w_b, r_b, q_b) + \dot{u}_{bd} - k_u \tilde{u}_b, \quad (13.55a)$$

$$\tau_q = -F_q(\theta_b^n, u_b, w_b, q_b) + \dot{q}_{bd} - k_q \tilde{q}_b, \quad (13.55b)$$

$$\tau_r = -F_r(u_b, v_b, r_b) + \dot{r}_{bd} - k_r \tilde{r}_b, \quad (13.55c)$$

where $k_u > 0$, $k_q > 0$ and $k_r > 0$ are constant control gains, and $\tilde{u}_b \triangleq u_b - u_{bd}$, $\tilde{q}_b \triangleq q_b - q_{bd}$ and $\tilde{r}_b \triangleq r_b - r_{bd}$.

Inserting these controllers into (13.3a), (13.3d) and (13.3e) gives the following error dynamics:

$$\dot{\tilde{u}}_b = -k_u \tilde{u}_b, \quad (13.56a)$$

$$\dot{\tilde{q}}_b = -k_q \tilde{q}_b, \quad (13.56b)$$

$$\dot{\tilde{r}}_b = -k_r \tilde{r}_b. \quad (13.56c)$$

The error dynamics are linear, and the origin is globally exponentially stable. Hence, as long as q_{bd} , r_{bd} and u_{bd} are continuous signals, a vehicle described by (13.3) will be able to follow them as long as the following assumption is met:

Assumption 13.9. At time t_0 , the system has operated long enough for the surge speed, yaw rate and pitch rate to converge, i.e. $\tilde{u}_b(t_0) = 0$, $\tilde{q}_b(t_0) = 0$ and $\tilde{r}_b(t_0) = 0$.

Remark 13.2. To fulfill this assumption, the vehicle needs to be properly initialized before control is handed over to the automatic collision avoidance system, which is reasonable.

13.4 Analysis

In this section, we provide an analysis of the CAA algorithm described in Section 13.2, which we apply to an underactuated marine vehicle modeled as in Section 13.1.1. The algorithm will provide heading and pitch references to the Flow frame controller in Section 13.3.2, which again will provide references to the yaw and pitch rate controller in Section 13.3.4. When the vehicle is not in collision avoidance mode, it is in nominal guidance mode, employing the pure pursuit guidance law described in Section 13.3.1 to steer it towards a target position.

From Lemma 11.2 we know that if the avoidance angle α_o is chosen such that

$$\alpha_o \in \left[\cos^{-1} \left(\frac{R_o}{R_o + d_{\text{safe}}} \right), \pi/2 \right), \quad d_{\text{safe}} > 0, \quad (13.57)$$

and the vehicle is able to maintain a direction lying on the surface of the compensated vision cone \mathcal{V}_c , then the obstacle distance is lower bounded by d_{safe} during the collision avoidance maneuver.

We will here show how we can bound the sway and heave speed during the maneuver, and demonstrate how we can use these bounds as design parameters in order to ensure a maneuver that is feasible, well defined and safe. These bounds are used to find a minimum switching distance, ensuring that the vehicle is able to safely enter collision avoidance mode. Finally, we use these results to derive conditions under which the vehicle is mathematically guaranteed to reach the target without collisions.

We assume that the obstacles are sparsely spaced, ensuring that the vehicle will only have to avoid one obstacle at a time:

Assumption 13.10. The distance between any two obstacles are always at least $2d_{\text{switch}}$.

We will also employ the notation $X_{vd} \triangleq X_v(u_{bd})$, $Y_{vd} \triangleq Y_v(u_{bd})$, $X_{wd} \triangleq X_w(u_{bd})$ and $Y_{wd} \triangleq Y_w(u_{bd})$ as defined in Section 13.1.5.

13.4.1 Limiting sway and heave

In this section we will provide a lower bound on the safety distance d_{safe} and upper bounds on the Flow frame control saturation parameters σ_ψ and σ_θ in order to ensure that the sway and heave motions are bounded by v_{sup} and w_{sup} , respectively. The required control effort in heading and pitch is maximized if the entire avoidance maneuver is made in either the horizontal or vertical plane, and if the obstacle moves in the same plane. Thus, even though the use of the cost function (13.36) combines a yaw and pitch movement to minimize the control effort required in each degree of freedom, we will examine a pure pitch and a pure yaw maneuver in order to determine the bounds on the control parameters.

The desired Flow frame angular rates during collision avoidance is dependent on v_b and w_b . In the next lemma, we will utilize the analysis model (13.16)-(13.19) in order to derive a requirement on this dependency which ensures that v_b and w_b remain bounded:

Lemma 13.1. *Let the sway and heave velocities be modeled by (13.18) and (13.19). Suppose that the Flow frame pitch rate q_f and yaw rate r_f are functions of the sway and heave motions, respectively, in such a way that:*

$$|q_f(w_{\text{sup}})| < \frac{|Y_{wd}|}{|X_{wd}|} w_{\text{sup}} - \frac{|Z_w|}{|X_{wd}|}, \quad (13.58)$$

$$|r_f(v_{\text{sup}})| < \frac{|Y_{vd}|}{|X_{vd}|} v_{\text{sup}}, \quad (13.59)$$

where $v_{\text{sup}} > 0$ and

$$w_{\text{sup}} > \frac{|Z_w|}{|Y_{wd}|}. \quad (13.60)$$

Then, if Assumption 13.9 holds, $v_b(t_0) < v_{\text{sup}}$ and $w_b(t_0) < w_{\text{sup}}$,

$$v_b(t) < v_{\text{sup}} \quad \forall t \geq t_0, \quad (13.61)$$

$$w_b(t) < w_{\text{sup}} \quad \forall t \geq t_0. \quad (13.62)$$

Proof. Consider the Lyapunov function candidate $V(w_b) = 0.5w_b^2$ of (13.19) with time derivative

$$\dot{V} = \frac{U_w^2}{U_w^2 - X_{wd}u_b} (X_{wd}w_b q_f(w_b) + Y_{wd}w_b^2 + Z_w \sin(\theta_b^n) w_b), \quad (13.63)$$

where we recall that $U_w = \sqrt{u_b^2 + w_b^2}$. Using Assumption 13.2 we can upper bound \dot{V} as

$$\dot{V} \leq \frac{U_w^2}{U_w^2 - X_{wd}u_b} (|X_{wd}||w_b||q_f(w_b)| - |Y_{wd}|w_b^2 + |Z_w||w_b|). \quad (13.64)$$

Inserting for (13.58), we obtain that $\dot{V} \leq 0$ on a set

$$\Omega_V \triangleq \{w_b \in \mathbb{R} \mid V \leq \frac{1}{2}w_{\text{sup}}^2\}, \quad (13.65)$$

which is a level set of V with $w_b = w_{\text{sup}}$ on the boundary. Hence, the set Ω_V is positively invariant, and any solution of w_b starting in Ω_V cannot leave it, which proves the that bound (13.62) holds. The proof for the bound (13.61) on v_b is equivalent. \square

Remark 13.3. The lower bound on w_{sup} in (13.60) stems from the effect of gravity. Specifically, when $\theta_b^n \neq 0$, a pitch moment is induced around CB. The distance between CB and b makes part of this moment into an acceleration in heave, which is reflected in (13.60).

We are now ready to derive bounds on the Flow frame controllers (13.49) and on the minimum safety distance d_{safe} which ensures that (13.58) and (13.59) are satisfied. We do this in the next two lemmas, which consider a pure vertical and a

pure horizontal maneuver. These results will then be combined in Theorem 13.5. In the next Lemma, we will use the following term:

$$F_\theta \triangleq \frac{w_{\text{sup}}|Y_{wd}| - |Z_w|}{|X_{wd}|} - \frac{2w_{\text{sup}}^2|Y_{wd}|u_{\text{omax}}}{(U_{w\text{sup}}^2 - X_{wd}u_b)\sqrt{U_{w\text{sup}}^2 - u_{\text{omax}}^2}} - \omega_{\text{omax}}\frac{u_{\text{omax}}}{u_b} - \frac{a_{\text{omax}}}{\sqrt{u_b^2 - u_{\text{omax}}^2}}, \quad (13.66)$$

where $U_{w\text{sup}} \triangleq \sqrt{u_b^2 + w_{\text{sup}}^2}$.

Lemma 13.2. *Consider a vehicle and an obstacle moving in the same vertical plane. Let the vehicle kinematics be modeled by (13.1), the actuated surge, pitch and yaw dynamics be modeled by (13.3a), (13.3d) and (13.3e), and the underactuated sway and heave dynamics be modeled by (13.18)-(13.19). Let the vehicle be governed by the surge controller (13.55a), pitch rate controller (13.55b), and the Flow frame pitch controller (13.49b). Let the control system enter collision avoidance mode at time t_1 , and let the vehicle Flow frame then be steered by the CAA algorithm in Section 13.2. Define a parameter $\lambda_\theta \in (0, 1)$, and assume that the distance between the vehicle and the obstacle satisfies $d_{\text{ob}}(t) \geq d_{\text{safe}} \forall t \geq t_0$. If Assumptions 13.2-13.6 and 13.9-13.10 hold, the Flow frame proportional saturation σ_θ satisfies*

$$\sigma_\theta \leq \lambda_\theta F_\theta, \quad (13.67)$$

the safety distance d_{safe} satisfies

$$d_{\text{safe}} \geq \frac{(U_{w\text{sup}} + u_{\text{omax}})^2}{U_{w\text{sup}}} \frac{1}{(1 - \lambda_\theta)F_\theta}, \quad (13.68)$$

and the heave motion satisfies $|w_b(t_0)| < w_{\text{sup}}$, where

$$w_{\text{sup}} \geq \frac{|Z_w|}{|Y_{wd}|}, \quad (13.69)$$

then

$$|w_b(t)| < w_{\text{sup}} \quad \forall t \geq t_0. \quad (13.70)$$

Proof. The proof of Lemma 13.2 includes the gravity restoration term Z_w , but otherwise follows along the lines of the proof of 10.2. The lemma is proved by finding an upper bound on q_{fd} for a given w_{sup} . The upper bound is inserted into (13.58), which allows us to apply Lemma 13.1. We then obtain (13.67) and (13.68) by solving for σ_θ and d_{safe} .

Without loss of generality, we assume that the maneuver is made by moving above the obstacle. Furthermore, since there is no horizontal movement or turning, we allow the pitch angles of the vehicle and the obstacle to lie in the interval $(-\pi, \pi]$. Thus, the vehicle and the obstacle can move towards each other while

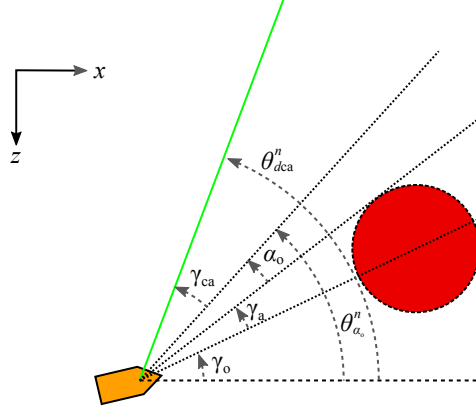


Figure 13.3: Geometry of a collision avoidance maneuver in the vertical plane.

keeping the same heading. The collision avoidance geometry in the x - z -plane is shown in Figure 13.3. The time derivative of θ_{dca}^n is

$$\dot{\theta}_{dca}^n = \dot{\theta}_{\alpha_o}^n + \dot{\gamma}_{ca}. \quad (13.71)$$

As shown in Figure 13.3, the angle $\theta_{\alpha_o}^n$ can be decomposed into

$$\theta_{\alpha_o}^n = \gamma_o + \gamma_a + \alpha_o. \quad (13.72)$$

Hence,

$$\dot{\theta}_{\alpha_o}^n = \dot{\gamma}_o + \dot{\gamma}_a. \quad (13.73)$$

The angular rate $\dot{\gamma}_o$ can be found geometrically as

$$\dot{\gamma}_o = \frac{u_o \sin(\theta_o^n - \gamma_o) - U_b \sin(\theta_f^n - \gamma_o)}{R_o + d_{ob}}, \quad (13.74)$$

while $\dot{\gamma}_a$ is found as

$$\dot{\gamma}_a = -\dot{d}_{ob} \frac{R_o}{(R_o + d_{ob}) \sqrt{(R_o + d_{ob})^2 - R_o^2}}, \quad (13.75)$$

where

$$\dot{d}_{ob} = u_o \cos(\theta_o^n - \gamma_o) - U_b \cos(\theta_f^n - \gamma_o). \quad (13.76)$$

Combining (13.74) - (13.76) gives

$$\dot{\theta}_{\alpha_o}^n = \frac{U_b \sin(\gamma_o - \theta_f^n) - u_o \sin(\gamma_o - \theta_o^n)}{R_o + d_{ob}} - R_o \frac{U_b \cos(\gamma_o - \theta_f^n) - u_o \cos(\gamma_o - \theta_o^n)}{(R_o + d_{ob}) \sqrt{d_{ob} (2R_o + d_{ob})}}. \quad (13.77)$$

When both the vehicle and the obstacle move in the same vertical plane, the dot product $(\mathbf{v}_o^{F_\rho})^T \bar{\mathbf{u}}_\rho^{F_\rho}$ can be rewritten as $u_o \sin(\gamma_{vo})$, where

$$\gamma_{vo} \triangleq \pi - (\theta_o^n - \theta_{\alpha_o}^n), \quad (13.78)$$

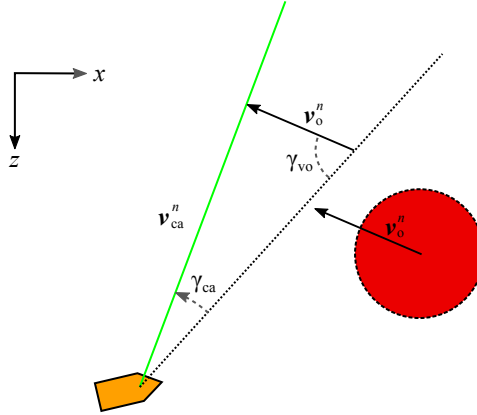


Figure 13.4: An alternative expression for γ_{ca} can be found using the sine rule on this triangle.

The expression (13.31) for γ_{ca} can then be rewritten as

$$\gamma_{ca} = \sin^{-1} \left(\frac{u_o \sin(\gamma_{vo})}{U_b} \right), \quad (13.79)$$

where we in effect have used the sine rule on the triangle shown in Figure 13.4. We use (13.79) to find

$$\dot{\gamma}_{ca} = \frac{u_o \left(\cos(\gamma_{vo}) \left(\dot{\theta}_{\alpha_o}^n - q_o \right) + \sin(\gamma_{vo}) \left(\frac{a_o}{u_o} - \frac{\dot{U}_b}{U_b} \right) \right)}{\sqrt{U_b^2 - u_o^2 \sin^2(\gamma_{vo})}}. \quad (13.80)$$

The total vehicle acceleration \dot{U}_b is found as

$$\dot{U}_b = U_b w_b \frac{X_{wd} q_f + Y_{wd} w_b + Z_w \sin(\theta_b^n)}{U_b^2 - X_{wd} u_b}, \quad (13.81)$$

where we have used the fact that $\dot{u}_b = \dot{u}_{bd}$ by Assumption 13.9, and that $\dot{u}_{bd} = 0$ by Assumption 13.6.

Note that $\dot{\theta}_{dca}^n$ depends on q_{fd} , which again depends on $\dot{\theta}_{dca}^n$ when the control system is in collision avoidance mode. A closed expression for q_{fd} is found by inserting (13.71) into the Flow frame pitch control law (13.49b), which gives

$$q_{fd}(w_b) = \frac{G_{rn}(w_b)}{G_{rd}(w_b)}, \quad (13.82)$$

where

$$G_{rn} \triangleq \dot{\theta}_{\alpha_o}^n - \text{sat}(k_\theta \tilde{\theta}_f^n) + \frac{u_o \cos(\gamma_{vo}) \left(\dot{\theta}_{\alpha_o}^n - q_o \right) + \sin(\gamma_{vo}) \left(a_o - \frac{u_o w_b (Y_{wd} w_b + Z_w \sin(\theta_b^n))}{U_b^2 + X_{wd} u_b} \right)}{\sqrt{U_b^2 - u_o^2 \sin^2(\gamma_{vo})}}, \quad (13.83)$$

and

$$G_{rd} \triangleq 1 + \frac{u_o \sin(\gamma_{vo}) w_b X_{wd}}{\sqrt{U_b^2 - u_o^2 \sin^2(\gamma_{vo})} (U_b^2 - X_{wd} u_b)}. \quad (13.84)$$

The expression for (13.84) is ensured to be well defined by Assumptions 13.3 and 13.5. However, in order to ensure that q_{fd} in (13.82) is well defined, we require that $G_{rd} > 0$. We obtain a lower bound on (13.84) by minimizing with respect to γ_{vo} and w_b :

$$G_{rd} > 1 - \frac{u_{o\max} |w_b| |X_{wd}|}{(U_b^2 - X_{wd} u_b) \sqrt{U_b^2 - u_{o\max}^2}} := G_{rd\text{inf}}(w_b). \quad (13.85)$$

Minimizing (13.85) with respect to w_b and solving for $u_{o\max}$ gives the following bound on $u_{o\max}$ to ensure that $G_{rd} > 0$ for all $u_o \in [0, u_{o\max}]$:

$$u_{o\max} < \begin{cases} 2\sqrt{-X_{wd}^2 + X_{wd} u_b} & \frac{u_b}{2} < X_{wd} \leq u_b, \\ u_b & X_{wd} < \frac{u_b}{2}. \end{cases} \quad (13.86)$$

Assumption 13.5 ensures that (13.86) is satisfied.

When $d_{ob} \geq d_{\text{safe}}$, a bound $|G_{rn}| < G_{rn\text{sup}}$ can be found by using Assumptions 13.2, 13.5, 13.6 and 13.9:

$$\begin{aligned} G_{rn\text{sup}}(w_{\text{sup}}) &\triangleq \frac{u_{o\max} w_{\text{sup}} (|Y_{wd}| w_{\text{sup}} + |Z_w|)}{(X_{wd} + U_{w\text{sup}}^2) \sqrt{U_{w\text{sup}}^2 - u_{o\max}^2}} + \frac{(U_{w\text{sup}} + u_{o\max})^2}{d_{\text{safe}} U_{w\text{sup}}} \\ &+ \omega_{o\max} \frac{u_{o\max}}{u_b} + \frac{a_{o\max}}{\sqrt{u_b^2 - u_{o\max}^2}} + \sigma_\theta. \end{aligned} \quad (13.87)$$

Equations (13.85) and (13.87) are even in w_b and w_{sup} , respectively. Hence,

$$|q_{fd}(\pm w_{\text{sup}})| < \frac{G_{rn\text{sup}}(w_{\text{sup}})}{G_{rd\text{inf}}(w_{\text{sup}})}. \quad (13.88)$$

Inserting (13.88) into (13.58) bounds d_{safe} and σ_θ to:

$$\frac{(U_{w\text{sup}} + u_{o\max})^2}{d_{\text{safe}} U_{w\text{sup}}} + \sigma_\theta \leq F_\theta, \quad (13.89)$$

where F_θ is given in (13.66). The design parameter λ_θ can be used to rewrite (13.89) as

$$\frac{(U_{w\text{sup}} + u_{o\max})^2}{d_{\text{safe}} U_{w\text{sup}}} + \sigma_\theta \leq \lambda_\theta F_\theta + (1 - \lambda_\theta) F_\theta. \quad (13.90)$$

Hence, conditions (13.67) and (13.68) ensure that (13.89) is satisfied. It follows that Condition (13.58) of Lemma 13.1 then also applies, and hence if $|w_b(t_0)| < w_{\text{sup}}$, then $|w_b(t)| < w_{\text{sup}} \forall t \geq t_0$. \square

The sway velocity can be ensured to be bounded in a similar fashion by considering a pure yaw maneuver. We will do this in the next lemma, where we will

use the parameter

$$F_\psi \triangleq \frac{v_{\text{sup}}|Y_{vd}|}{|X_{vd}|} - \frac{2v_{\text{sup}}^2|Y_{vd}|u_{\text{omax}}}{(U_{v\text{sup}}^2 + X_{vd}u_b)\sqrt{U_{v\text{sup}}^2 - u_{\text{omax}}^2}} - \omega_{\text{omax}}\frac{u_{\text{omax}}}{u_b} - \frac{a_{\text{omax}}}{\sqrt{u_b^2 - u_{\text{omax}}^2}}, \quad (13.91)$$

where $U_{v\text{sup}} \triangleq \sqrt{u_b^2 + v_{\text{sup}}^2}$.

Lemma 13.3. *Consider a vehicle and an obstacle moving in the same horizontal plane. Let the vehicle kinematics be modeled by (13.1), the actuated surge, pitch and yaw dynamics be modeled by (13.3a), (13.3d) and (13.3e), and the underactuated sway and heave dynamics be modeled by (13.18)-(13.19). Let the vehicle be governed by the surge controller (13.55a), yaw rate controller (13.55c), and the Flow frame yaw controller (13.49a). Let the control system enter collision avoidance mode at time t_1 , and let the vehicle Flow frame then be steered by the CAA algorithm in Section 13.2. Define the parameter $\lambda_\psi \in (0, 1)$, and assume that the distance between the vehicle and the obstacle satisfies $d_{ob}(t) \geq d_{\text{safe}} \forall t \geq t_0$. If Assumptions 13.2-13.6 and 13.9-13.10 hold, the Flow frame proportional saturation σ_ψ satisfies*

$$\sigma_\psi \leq \lambda_\psi F_\psi, \quad (13.92)$$

the safety distance d_{safe} satisfies

$$d_{\text{safe}} \geq \frac{(U_{v\text{sup}} + u_{\text{omax}})^2}{U_{v\text{sup}}} \frac{1}{(1 - \lambda_\psi)F_\psi}, \quad (13.93)$$

and the sway motion satisfies $|v_b(t_0)| < v_{\text{sup}}$, then

$$|v_b(t)| < v_{\text{sup}} \quad \forall t \geq t_0. \quad (13.94)$$

The proof of Lemma 13.3 is equivalent to the proof of Lemma 13.2.

13.4.2 Minimum switching distance

In this section we will use the bound on sway and heave speeds from the previous section in order to derive a minimum safety distance guaranteeing that the vehicle is able to safely reach the desired heading and pitch from the collision avoidance algorithm.

Lemma 13.4. *Let the vehicle kinematics be modeled by (13.1), the actuated surge, pitch and yaw dynamics be modeled by (13.3a), (13.3d) and (13.3e), and the underactuated sway and heave dynamics be modeled by (13.18)-(13.19). Let the vehicle be controlled by the feedback linearizing controllers (13.55) and the Flow frame controller (13.46). At a time $t_1 \geq t_0$, let the control system enter collision avoidance mode according to the switching rule in (13.41), and let the Flow frame heading and pitch then be set by the collision avoidance law (13.40). Furthermore, let Assumptions 13.2-13.10 be satisfied, the vehicle speed satisfy $U_b < U_{b\text{sup}} = \sqrt{u_{bd}^2 + v_{\text{sup}}^2 + w_{\text{sup}}^2}$, and the switching distance satisfy*

$$d_{\text{switch}} \geq u_{\text{omax}}t_\epsilon + d_{\text{safe}} + d_{\text{turn}} + d_{T_b}, \quad (13.95)$$

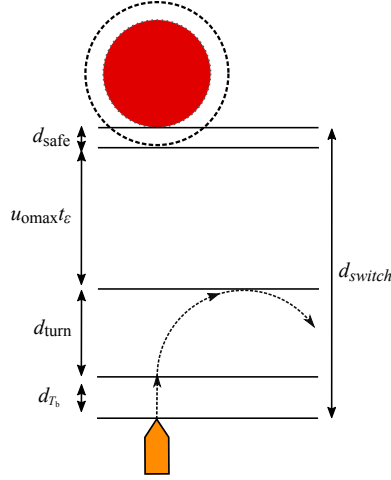


Figure 13.5: Illustration of the minimum required switching distance.

where

$$t_\epsilon \triangleq \max_j \left(T_b + \left(\frac{\pi}{\sigma_j} - \frac{1}{k_j} \right) - \frac{\ln(k_j \epsilon / \sigma_j)}{k_j} \right), \quad j = \{\psi, \theta\}, \quad \epsilon \in (0, \frac{\pi}{2}] \quad (13.96)$$

is the maximum amount of time the Flow frame yaw controller (13.49a) will use to make the vehicle converge to within ϵ rad of \mathcal{V}_c , and

$$d_{\text{turn}} \triangleq \max_j \left(\frac{U_{\text{bsup}}}{\min(\sigma_j, k_j \frac{\pi}{2})} \right), \quad j = \{\psi, \theta\} \quad (13.97)$$

upper bounds the distance traveled by the vehicle towards the obstacle when making a complete 180° turn. The distance d_{T_b} is

$$d_{T_b} \triangleq U_{\text{bsup}} T_b. \quad (13.98)$$

Then, the vehicle is able to converge to within ϵ rad of \mathcal{V}_c before the obstacle can come within the distance d_{safe} .

Proof. The main idea behind the proof is to show that the distance traveled by the obstacle during the convergence time t_ϵ is not sufficient to reduce the distance between the obstacle and the vehicle trajectory to less than d_{safe} . This is illustrated in Figure 13.5.

We consider a worst case scenario with an obstacle of infinite size, $R_o \rightarrow \infty$. The half apex angle of the vision cone angle is then $\gamma_a = \pi/2$. Furthermore, the vehicle and obstacle move at maximum speed, i.e. $U_b(t_1) = U_{\text{bsup}}$ and $u_o(t_1) = u_{\text{omax}}$. We assume, without loss of generality, that the obstacle is ahead of the vehicle along the x_n -axis of the NED frame, such that $x_o^n(t_1) - x_b^n(t_1) = d_{\text{switch}}$, while $y_o^n(t_1) = y_b^n(t_1)$ and $z_o^n(t_1) = z_b^n(t_1)$. Furthermore, we assume that the vehicle and

obstacle move straight towards each other at time t_1 . The worst case behavior of the obstacle is then to continue moving straight ahead at maximum speed.

At time t_1 , when the control system enters collision avoidance mode, the vehicle starts to make a turn towards ψ_{dca}^n and θ_{dca}^n . There will then be a jump in the desired yaw and pitch rate from the Flow frame controller, and the rate smoothing will commence. The smoothing is complete at the latest at time $t_1 + T_b$. Since $\tilde{\psi}_f^n$ and $\tilde{\theta}_f^n$ both lie in the interval $(-\pi, \pi]$, the maximum error at time $t = t_1 + T_b$ is π radians in each direction. The convergence time from $|\tilde{\psi}_f^n| = \pi$ to $|\tilde{\psi}_f^n| = \sigma_\psi/k_\psi$ is found from (13.49a) to be $\pi/\sigma_\psi - 1/k_\psi$, which is ensured to be positive by Assumption 13.7. From this point, the flow frame heading error converges exponentially to zero, and hence the convergence time from $|\tilde{\psi}_f^n| = \sigma_\psi/k_\psi$ to $|\tilde{\psi}_f^n| < \epsilon$ is $\frac{\ln(k_\psi \epsilon / \sigma_\psi)}{k_\psi}$. Similar convergence times can be found for $|\tilde{\theta}_f^n|$.

It follows that the total time from t_1 until the vehicle's velocity vector is less than $\sqrt{2}\epsilon$ away from \mathcal{V}_c is upper bounded by t_ϵ as defined in (13.96). During this time, the obstacle will, at worst, have traversed $u_{\max} t_\epsilon$ towards the vehicle.

During the smoothing interval $t \in (t_1, t_1 + T_b]$, the distance covered by the vehicle towards the obstacle is upper bounded by d_{T_b} . In a worst case scenario, the vehicle then has to turn completely around. Assumption 13.7 ensures that the vehicle will move at most d_{turn} towards the obstacle when turning.

Hence, if condition (13.95) holds, then the distance between the obstacle and the vehicle trajectory will not be reduced to less than d_{safe} before the vehicle velocity direction has converged to within ϵ rad of \mathcal{V}_c . It follows that the obstacle is thus more than d_{safe} meters from the vehicle, which concludes the proof. \square

13.4.3 Safe target reaching

We have now proved that a vehicle following the collision avoidance law (13.40) is sure to keep a minimum distance away from the obstacle (Lemma 11.2), that the vehicle sway and heave will remain bounded during a maneuver around a moving obstacle (Lemmas 13.1-13.3), and we have found a minimum distance at which the vehicle must enter collision avoidance mode in order to ensure that it is able to turn away in time (Lemma 13.4). In this section, we will use these Lemmas to prove that the vehicle will safely traverse an environment containing an obstacle and reach the target position. This is the main theorem of the chapter. Before we state the theorem, we make the assumptions that the vehicle is able to start safely, and that the obstacle does not cover the target.

Assumption 13.11.

$$\theta_f^n(t_0) \in [\theta_{\min}, \theta_{\max}]. \quad (13.99)$$

Assumption 13.12.

$$d_{ob}(t_0) > d_{\text{switch}}. \quad (13.100)$$

Assumption 13.13. The distance d_{ot} from the obstacle to the target position \mathbf{p}_t^n satisfies

$$d_{ot} > \frac{R_o}{\cos(\alpha_o)} - R_o \quad \forall t \geq t_0. \quad (13.101)$$

Remark 13.4. Vehicle safety is guaranteed even if this assumption is not met, but it is then not ensured that the target will be reached.

Due to the smoothing time T_b of the yaw rate reference signal, we also need at least one of the following assumptions to hold:

Assumption 13.14. The obstacle will not actively turn towards the vehicle when $d_{ob} \leq d_{\text{switch}}$.

or

Assumption 13.15. The smoothing time T_b is small enough to be neglected, i.e.

$$(u_{\text{omax}} + U_{\text{bsup}}) T_b \ll d_{\text{safe}}. \quad (13.102)$$

Remark 13.5. These assumptions require the obstacle to at least not be actively seeking a collision with the vehicle if the vehicle dynamics make T_b large. Specifically, if the vehicle lacks maneuverability, the safety distance d_{safe} must either be chosen large enough to account for the limited turning capabilities, or the vehicle must rely on at least some level of cooperation from the obstacle. Recall the 2D example in Chapter 10: An oil tanker which use a very long time to initiate a turn would rely on Assumption 13.14, while a small speed boat can safely employ Assumption 13.15.

Theorem 13.5. *Let Assumptions 13.2-13.13 and either 13.14 or 13.15 hold, the avoidance angle α_o satisfy*

$$\alpha_o \in \left[\cos^{-1} \left(\frac{R_o}{R_o + d_{\text{safe}}} \right) + \sqrt{2}\epsilon, \frac{\pi}{2} \right), \quad (13.103)$$

where

$$\epsilon \in \left(0, \frac{\pi}{2\sqrt{2}} - \frac{R_o}{\sqrt{2}(R_o + d_{\text{safe}})} \right), \quad (13.104)$$

and the switching distance satisfy

$$d_{\text{switch}} \geq u_{\text{omax}} t_\epsilon + d_{\text{safe}} + d_{\text{turn}} + d_{T_b}. \quad (13.105)$$

Moreover, let the safety distance satisfy $d_{\text{safe}} \geq \max\{d_{\text{safe}\psi}, d_{\text{safe}\theta}\}$, where

$$d_{\text{safe}\psi} \geq \frac{(U_{\text{vsup}} + u_{\text{omax}})^2}{U_{\text{vsup}}} \frac{1}{(1 - \lambda_\psi) F_\psi}, \quad (13.106)$$

and

$$d_{\text{safe}\theta} \geq \frac{(U_{\text{wsup}} + u_{\text{omax}})^2}{U_{\text{wsup}}} \frac{1}{(1 - \lambda_\theta) F_\theta}. \quad (13.107)$$

Assume that the saturations in the Flow frame yaw and pitch controllers satisfy

$$\sigma_\psi \leq \lambda_\psi F_\psi, \quad (13.108)$$

$$\sigma_\theta \leq \lambda_\theta F_\theta, \quad (13.109)$$

and that the initial sway and heave speeds satisfy

$$v_b(t_0) < v_{\text{sup}}, \quad (13.110)$$

$$w_b(t_0) < w_{\text{sup}}, \quad (13.111)$$

where $v_{\text{sup}} > 0$ and $w_{\text{sup}} > |Z_w|/|Y_{wd}|$.

Furthermore, let the vehicle kinematics be modeled by (13.1), the actuated surge, pitch and yaw dynamics be modeled by (13.3a), (13.3d) and (13.3e), and the underactuated sway and heave dynamics be modeled by (13.18)-(13.19). Finally, let the vehicle be governed by the surge, yaw and pitch rate controllers (13.55), the Flow frame controllers (13.49), the guidance laws (13.43) and (13.44), and the collision avoidance law (13.40). Then, the vehicle will maneuver among obstacles described by (13.20) while ensuring that

$$d_{ob}(t) \geq d_{\text{safe}} \quad \forall t \geq t_0, \quad (13.112)$$

and

$$\theta_f^n(t) \in [\theta_{\min}, \theta_{\max}] \quad \forall t \geq t_0, \quad (13.113)$$

meeting the control objectives (13.25) and (13.26). Furthermore, if it is a single-obstacle scenario, then there exists a time $t_f \geq t_0$ such that

$$\|\mathbf{p}_t^{nb}(t_f)\| \leq d_a. \quad (13.114)$$

Hence, the control objective (13.24) is met.

Proof. Conditions (13.106)-(13.111), Lemma 13.2 and Lemma 13.3 ensure that $U_b < U_{b\text{sup}} \quad \forall t \in [t_0, t_f]$. Consider a time $t_1 \geq t_0$, at which the vehicle enters collision avoidance mode in accordance with (13.41). The vehicle then chooses a direction which minimizes the cost function C , and starts turning towards this direction.

Lemma 13.4 ensures that there is a time $t_2 \geq t_1 + T_b$ when the angular distance between the vehicle's velocity direction and the closest point on the compensated vision cone will be less than ϵ radians, while $d_{ob}(t) > d_{\text{safe}}$ for $t \in [t_1, t_2]$. Since the yaw rate reference signal r_{bd} and the pitch rate reference signal q_{fd} are smooth, the error dynamics of the Flow frame controllers (13.46) have a locally exponentially stable equilibrium at the origin. Hence, it is ensured that the angular distance between $\dot{\mathbf{p}}_b^n$ and \mathcal{V}_c remains less than ϵ radians until a time $t_3 \geq t_2$, at which time the vehicle exits collision avoidance mode.

In a coordinate frame moving with the obstacle's velocity vector $\mathbf{v}_{o/n}^n$, the direction of the vehicle's velocity vector is less than $\sqrt{2}\epsilon$ radians from the extended vision cone \mathcal{V}_e . Hence, condition (13.103) and Lemma 11.2 then ensure that $d_{ob}(t) \geq d_{\text{safe}} \quad \forall t \in [t_2, t_3]$.

The guidance laws in (13.43) and (13.44) steer the vehicle towards the target. Hence, it is ensured that there exists a finite time t_f when $\|\mathbf{p}_t^{nb}(t_f)\| \leq d_a$, fulfilling condition (13.114).

While the definition of C ensures that $\theta_{dca}^n \in [\theta_{\min}, \theta_{\max}]$, the definition of the pitch guidance law (13.44) ensures that $\theta_{dg}^n \in [\theta_{\min}, \theta_{\max}]$. Assumption 13.11 and the pitch control law (13.49b) then ensure that condition (13.113) is fulfilled. \square

Table 13.1: Simulation parameters

u_b	2.0 m/s	θ_{\min}	-0.5 rad
v_{sup}	2.0 m/s	θ_{\max}	0.5 rad
w_{sup}	2.0 m/s	$\mathbf{p}_b^n(t_0)$	$[0, 0, 0]^T$ (m)
R_o	20 m	u_o	1.0 m/s
$\omega_{o\max}$	0 rad/s	$a_{o\max}$	0 m/s ²
d_{safe}	11 m	σ_θ	0.15 rad/s
α_o	0.94 rad	σ_ψ	0.15 rad/s
d_{switch}	61 m	$\mathbf{p}_t^n(t_0)$	$[150, 0, 0]^T$ (m)
ϵ	0.05 rad	T_b	1.0 s
λ	50		

13.5 Simulations

This section contains simulations of different collision avoidance scenarios in order to illustrate the behavior of the algorithm, and to verify the theoretical results in Theorem 13.5. The simulation parameters are summarized in Table 13.1.

The simulated vehicle is a Hugin AUV [43] of approximately the same kind as the one used for the experiments in Section 13.6. The hydrodynamic parameters of the AUV make $F_\theta = 0.64$ and $F_\psi = 0.70$. Hence, the values chosen for σ_ψ , σ_θ and d_{safe} satisfy the conditions of Theorem 13.5 with $\lambda_\theta = \lambda_\psi = 0.25$. Furthermore, it can be verified the obstacle speed satisfies (13.23). The avoidance angle α_o and the switching distance d_{switch} are set using equations (13.103) and (13.105), respectively.

The first scenario contains a head on situation and is shown in Figure 13.6. The initial position of the obstacle is $\mathbf{p}_o^n(t_0) = [100, 5, 5]^T$ m, and it moves along a straight line with $\psi_o^n = \pi$ rad and $\theta_o^n = 0$ rad. When the vehicle enters collision avoidance mode, the obstacle is slightly below and to the starboard side of it. The vehicle thus makes a port turn and pitches upwards, choosing a safe direction which minimizes the cost function C (13.36). The vehicle continues the maneuver until the line of sight to the target becomes safe, at which point it exits collision avoidance mode according to the switching criterion in (13.41), and proceeds towards the target.

The sway and heave speeds of the vehicle are shown in Figure 13.7. They are both well within the limit of 2 m/s, which verifies Lemmas 13.2 and 13.3. The magnitude of the difference between the Flow frame rates q_f and r_f obtained from using the analysis model (13.16)-(13.17) and the more precise model in (13.13) is shown in the lower part of the figure. The error remains small throughout the maneuver, which justifies the use of the analysis model when deriving the bounds on the Flow frame controller saturation parameters σ_θ and σ_ψ , and the safety distance d_{safe} .

The distance between the vehicle and the obstacle remains above the safety distance d_{safe} throughout the maneuver, which can be seen in Figure 13.8. Furthermore, the Flow frame pitch angle θ_f^n remains within $[\theta_{\min}, \theta_{\max}]$. Thus, the

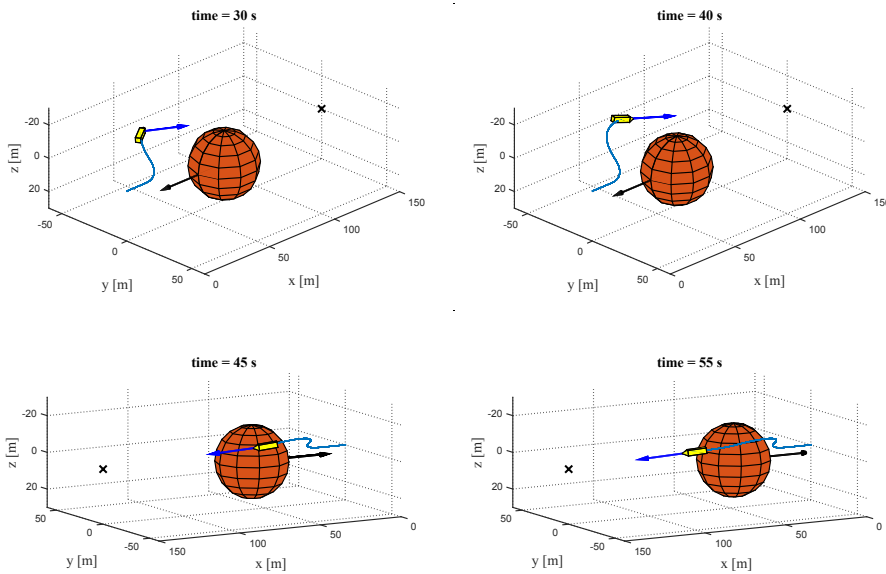


Figure 13.6: A scenario where the vehicle and obstacle meet head on head. The vehicle is the yellow polyhedron, and the obstacle is the red sphere. The blue line is the vehicle trajectory, the target is marked by an 'X', and the direction of the vehicle and obstacle velocity are shown by a blue and black arrow, respectively. The vehicle size is exaggerated for clarity, and the view has been rotated in the lower two snapshots of the simulation.

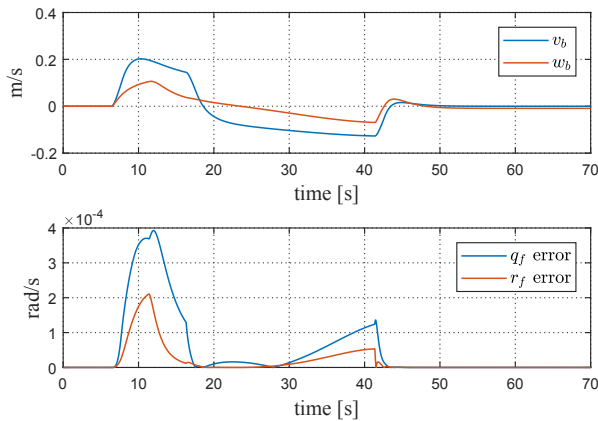


Figure 13.7: The sway v_b and heave w_b speeds of the vehicle during the first scenario (top), and the error resulting from using the analysis model to find q_f and r_f (bottom).

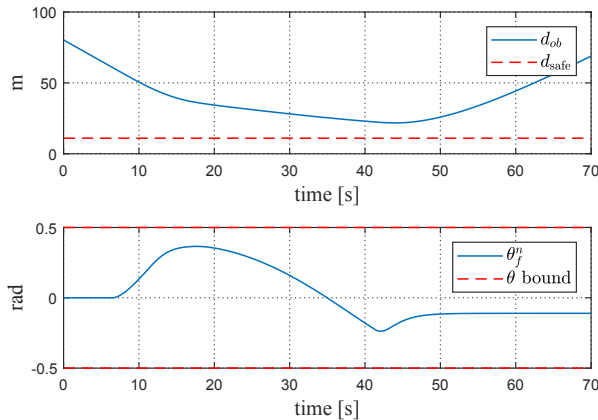


Figure 13.8: The distance d_{ob} between the vehicle and the obstacle during the first scenario (top), and the Flow frame pitch angle θ_f^n (bottom).

simulation shows that the vehicle is able to start the collision avoidance maneuver early enough to safely reach the desired velocity direction during collision avoidance, and that it maneuvers around the obstacle without exceeding the bounds on v_b , w_b and θ_f^n . Hence, the simulation verifies the results of Theorem 13.5.

In the next scenario, displayed in Figure 13.9, the obstacle crosses in front of the vehicle, moving horizontally. Upon entering collision avoidance, the vehicle thus chooses a ray of \mathcal{V}_c which takes it behind the obstacle, in accordance with (13.36). Since the vehicle and obstacle both move horizontally when collision avoidance is initialized, the choice of going above or below the obstacle becomes random. In this case, the vehicle maneuvers below the obstacle.

As shown in Figures 13.10 and 13.11, the limits on sway, heave and Flow frame pitch are upheld throughout the maneuver, and the distance to the obstacle is never less than d_{safe} . Thus, this scenario also verifies the results of Theorem 13.5.

Figure 13.12 shows the final scenario, where the obstacle crosses in front of the vehicle from below, moving vertically. The vehicle maneuvers below the obstacle while keeping it on the port side, until the direction towards the target becomes safe. The vehicle then exits collision avoidance mode and proceeds with nominal guidance. As in the previous scenarios, the bounds on the vehicle sway and heave, and on the Flow frame pitch are upheld, and the vehicle remains at a safe distance to the obstacle throughout the maneuver.

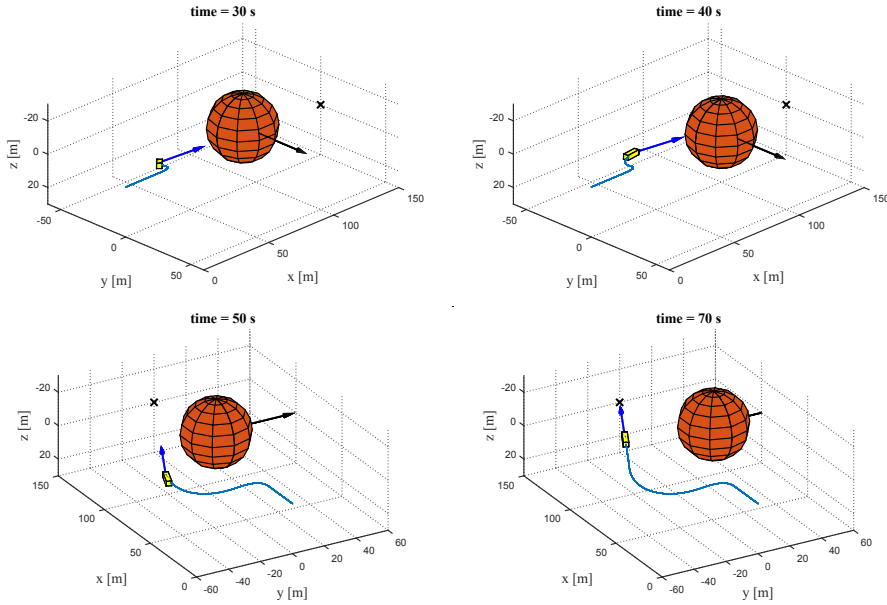


Figure 13.9: A scenario where the obstacle crosses horizontally in front of the vehicle.

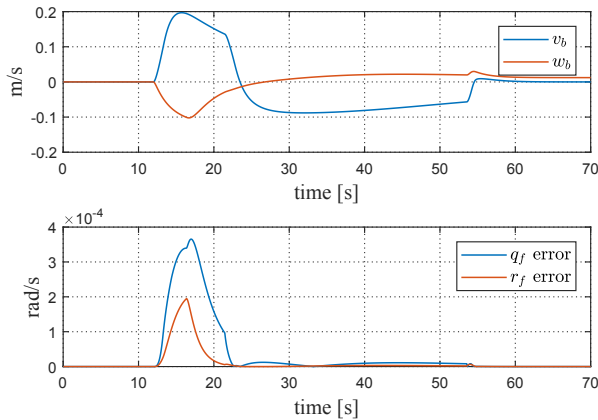


Figure 13.10: The sway v_b and heave w_b speeds of the vehicle during the second scenario (top), and the error resulting from using the analysis model to find q_f and r_f (bottom).

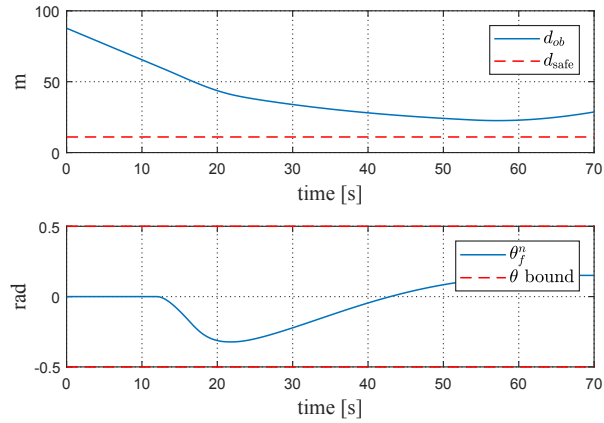


Figure 13.11: The distance d_{ob} between the vehicle and the obstacle during the second scenario (top), and the Flow frame pitch angle θ_f^n (bottom).

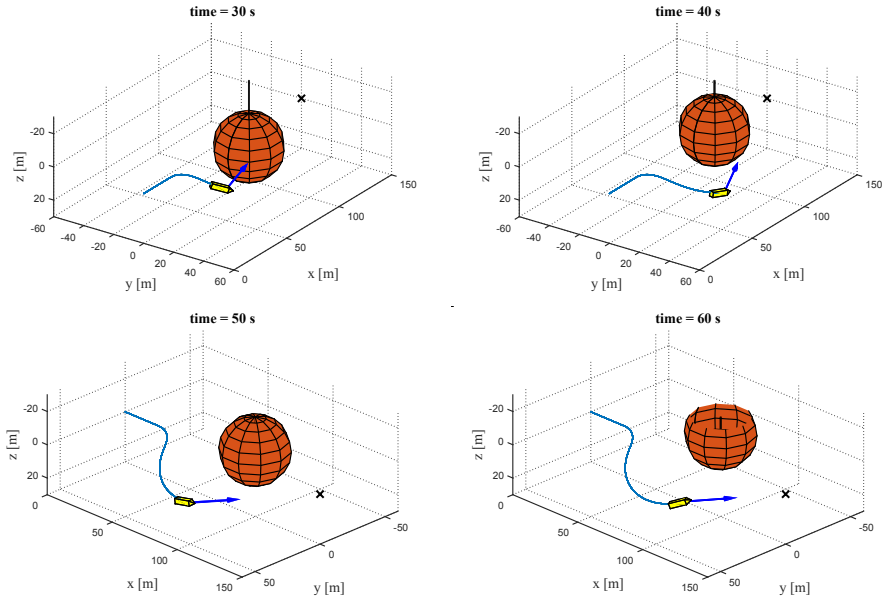


Figure 13.12: A scenario where the obstacle crosses vertically in front of the vehicle.

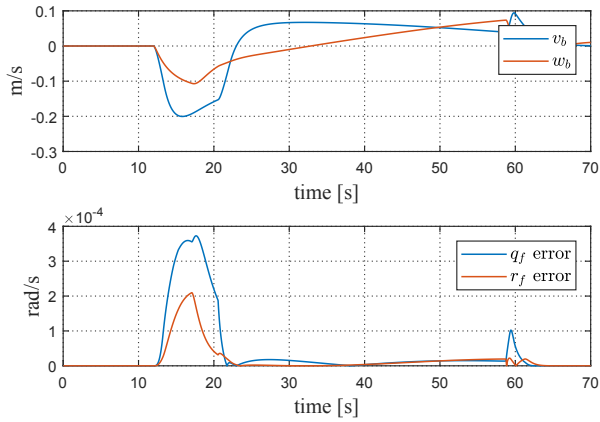


Figure 13.13: The sway v_b and heave w_b speeds of the vehicle during the third scenario (top), and the error resulting from using the analysis model to find q_f and r_f (bottom).

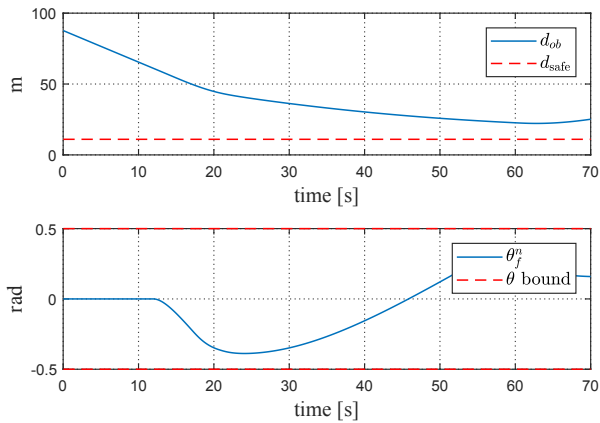


Figure 13.14: The distance d_{ob} between the vehicle and the obstacle during the third scenario (top), and the Flow frame pitch angle θ_f^z (bottom).

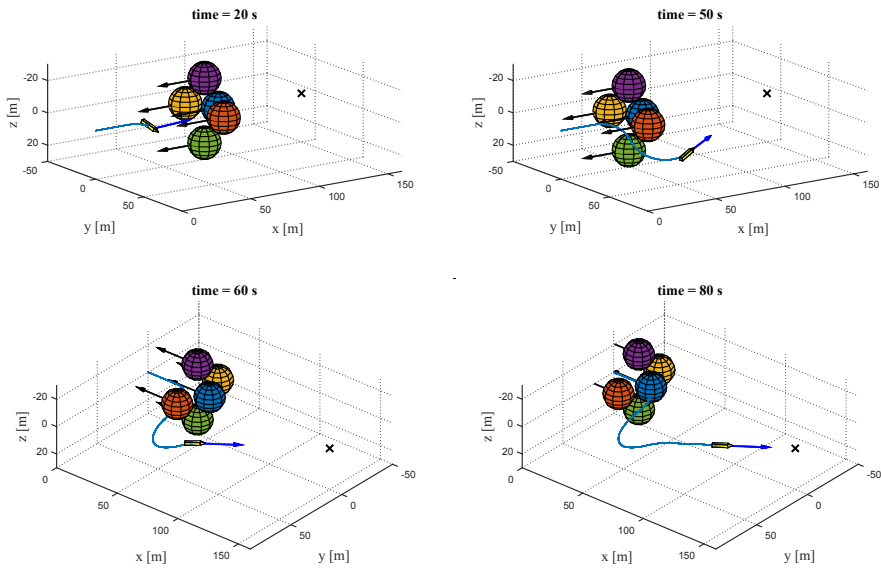


Figure 13.15: Snapshots from a simulation where the vehicle meets a cluster of five obstacles.

13.5.1 Multiple obstacles

In this section, we present simulations demonstrating the applicability of the CAA algorithm to multi-obstacle scenarios. For these simulations, the radius of the obstacle is reduced to 10 m, while the avoidance angle α_o is increased to 1.15 rad. Otherwise, the simulation parameters are the same as for the single-obstacle simulations in the previous section.

The first scenario contains a cluster of five obstacles approaching the vehicle head on. Snapshots from the simulation are shown in Figure 13.15, where it can be seen that the vehicle heads up and to starboard around the the obstacles. The vehicle successfully maneuvers around the cluster as if it was a single, non-convex obstacle. When the line of sight to the target comes outside of the vision cones of all the obstacles, the vehicle exits collision avoidance mode and proceeds towards it. At no point in the maneuver is the vehicle closer than d_{safe} to any of the obstacles, as seen in Figure 13.16.

In the second scenario, illustrated in Figure 13.17, the vehicle first encounters two obstacles crossing in front of it. While the vehicle maneuvers to avoid these obstacles, it encounters a third obstacle, and adjusts its course and pitch in order to avoid this obstacle as well. After the last obstacle has been safely avoided, the vehicle proceeds towards the target. Again, as seen in Figure 13.18, the distance to each of the obstacles were always above the safety distance.

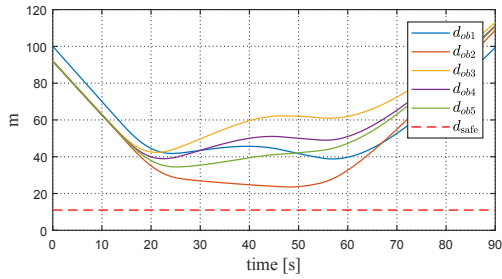


Figure 13.16: The distances to each of the obstacles in the first multi-obstacle scenario.

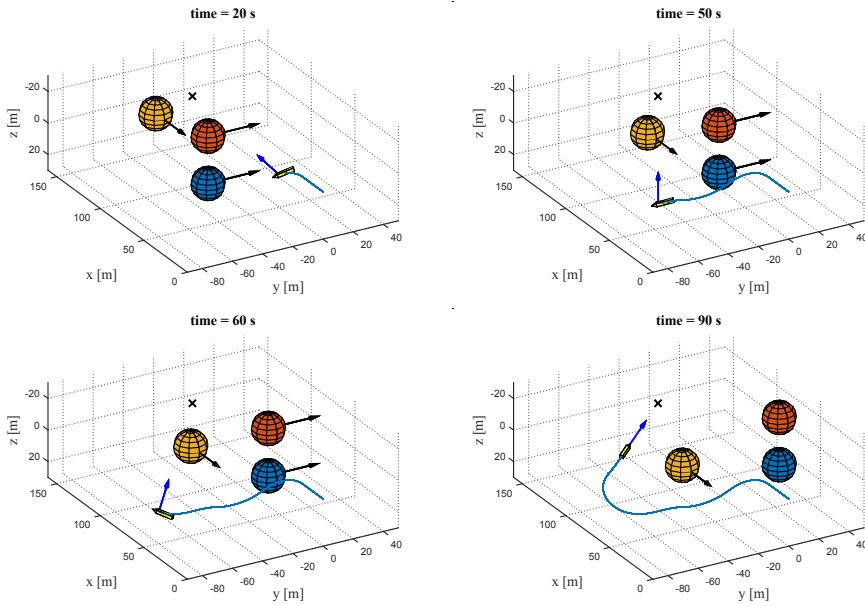


Figure 13.17: Snapshots from a simulation where the vehicle meets three obstacles, two crossing in front of it and one moving towards it.

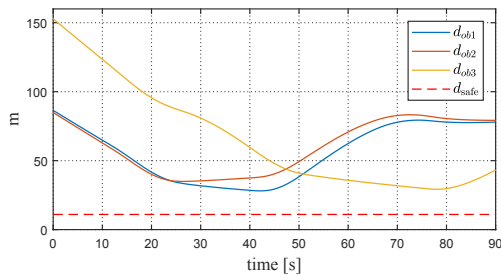


Figure 13.18: The distances to each of the obstacles in the second multi-obstacle scenario.



Figure 13.19: The Hugin HUS vehicle.

13.6 Experiments

The CAA algorithm described in Section 13.2, as well as the pure pursuit guidance law in Section 13.3.1, have been implemented in an experimental setup on the Hugin HUS AUV, shown in Figure 13.19. This vehicle is owned and operated by the Norwegian Defence Research Establishment (FFI) and can be operated from any appropriate vessel of opportunity. For this experiment, the AUV was operated from the FFI research vessel H.U. Sverdrup II. The algorithms were implemented using a back seat driver interface enabling third party and prototype software modules to take control of the vehicle.

The exact hydrodynamic model of the vehicle is not available, but it is similar to the vehicle simulated in the previous section. Furthermore, the implementation details of the low-level controllers are not available; however, the modular nature of the collision avoidance algorithm and guidance law made it possible to send desired pitch and heading to the controllers. The vehicle's forward thrust is set to a constant value, giving a surge velocity of about 2 m/s.

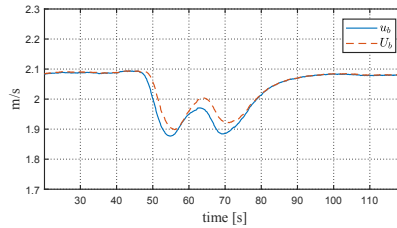
For the experiments, the cost function used to choose a safe ray was modified to choose the ray minimizing the maximum heading or pitch error:

$$C_{\text{exp}} \triangleq \begin{cases} |\mathbf{e}_\rho|_\infty, & \theta_\rho^n \in [\theta_{\min}, \theta_{\max}], \\ |\mathbf{e}_\rho|_\infty + 2\pi, & \theta_\rho^n \notin [\theta_{\min}, \theta_{\max}], \end{cases} \quad (13.115)$$

where $\mathbf{e}_\rho \triangleq [\psi_f^n - \psi_\rho^n(\phi), \theta_f^n - \theta_\rho^n(\phi)]^T$. This cost function will tend to make the vehicle employ both the sternplanes and the rudders in order to avoid the obstacle.

Table 13.2: Experiment parameters

α_o	0.8 rad	u_b	~ 2 m/s
d_{safe}	4.4 m	u_o (Run 1-8)	1.0 m/s
d_{switch}	50 m	u_o (Run 9-16)	1.5 m/s
θ_{min}	-0.35 rad	R_o	10 m
θ_{max}	0.44 rad		

Figure 13.20: The surge speed u_b and the total vehicle speed U_b during run 4.

A total of 16 runs were executed. In each of the runs, the vehicle moved towards a target position and encountered a moving obstacle along the way. In order to focus on the performance of the algorithm under ideal sensing conditions, and in order to be able to perform more controlled underwater experiments, the vehicle encountered only virtual obstacles during the experiments. When the obstacle got too close to the vehicle, the control system entered collision avoidance mode and safely executed an avoidance maneuver before proceeding towards the target. When the target was reached, the run ended and the next run automatically began. The parameters of the experiments are shown in Table 13.2.

Rather than following a constant surge speed, the vehicle was set to maintain a constant thrust in the experiments. Thus, the surge speed varied during the maneuver, as it encountered damping while turning. The surge speed u_b and the total vehicle speed U_b during run 4 are shown in Figure 13.20. Since the CAA algorithm uses the vehicle speed as an input, the desired Flow frame heading and pitch during the maneuver readily compensated for the damping in U_b .

A summary of each run is shown in Table 13.3. The column marked 'T' contains the scenario type of the run, where 'H' denotes a head on scenario and 'C' denotes a crossing scenario. The vehicle never got closer than d_{safe} from the obstacle during any of the maneuvers. However, due to an unmodeled disturbance on the vehicle and a time delay in the backseat driver system, the Flow frame pitch slightly exceeded the minimum limit on run 1, 5, 9, 12 and 15.

Figure 13.21 shows the maneuver of run 6, which was a head on scenario. When the vehicle got closer than 50 m to the obstacle, it entered into collision avoidance mode and began the avoidance maneuver. The obstacle was on the lower, port side of the vehicle, and hence it maneuvered up and starboard in accordance with (13.115). When the obstacle was safely avoided, the vehicle proceeded towards the

Table 13.3: Experiments summary

Run	T	$\min(d_{ob})$	$\min(\theta_f^n)$	$\max(\theta_f^n)$	$\max(v_b)$	$\max(w_b)$	z_o^n
1	H	24.5 m	-0.37 rad	0.13 rad	0.49 m/s	0.36 m/s	0 m
2	H	20.0 m	-0.33 rad	0.35 rad	0.48 m/s	0.32 m/s	10 m
3	C	30.4 m	-0.24 rad	0.08 rad	0.48 m/s	0.30 m/s	0 m
4	C	23.7 m	-0.19 rad	0.33 rad	0.46 m/s	0.32 m/s	0 m
5	H	26.1 m	-0.36 rad	0.13 rad	0.50 m/s	0.35 m/s	-10 m
6	H	16.6 m	-0.32 rad	0.38 rad	0.52 m/s	0.32 m/s	7 m
7	C	27.2 m	-0.35 rad	0.12 rad	0.51 m/s	0.34 m/s	0 m
8	C	18.4 m	-0.32 rad	0.35 rad	0.34 m/s	0.31 m/s	5 m
9	H	21.9 m	-0.36 rad	0.09 rad	0.50 m/s	0.33 m/s	0 m
10	H	15.2 m	-0.20 rad	0.35 rad	0.48 m/s	0.31 m/s	10 m
11	C	35.0 m	-0.24 rad	0.08 rad	0.48 m/s	0.21 m/s	0 m
12	C	7.9 m	-0.37 rad	0.35 rad	0.45 m/s	0.30 m/s	0 m
13	H	24.9 m	-0.33 rad	0.09 rad	0.53 m/s	0.32 m/s	-10 m
14	H	13.0 m	-0.18 rad	0.38 rad	0.49 m/s	0.32 m/s	7 m
15	C	27.6 m	-0.38 rad	0.10 rad	0.50 m/s	0.34 m/s	0 m
16	C	14.4 m	-0.31 rad	0.32 rad	0.28 m/s	0.30 m/s	5 m

target position. As shown in Figure 13.22, the distance to the obstacle remained well above the safety distance, and the Flow frame pitch remained within its limits. The sideslip β_b and angle of attack α_b remained small during the maneuver, as seen in Figure 13.23, justifying the small angle assumption used in the analysis.

Another example is shown in Figure 13.24, which displays the crossing scenario in run 4. Again, when the obstacle got closer than 50 m, the vehicle entered into collision avoidance mode. The relative positions of the vehicle and the obstacle made the algorithm choose to move up and to port in accordance with (13.115). This made the vehicle maneuver behind the obstacle, which is the same behavior that would result from using the optimization criterion (13.36). The obstacle distance remained well above the safety distance, as shown in Figure 13.25, and the Flow frame pitch angle stayed within its limits. Moreover, the sideslip and angle of attack, displayed in Figure 13.26, remained small.

13.7 Conclusions

The 3D CAA algorithm proposed in this thesis has in this chapter been implemented on an underactuated underwater vehicle, modeled using both kinematics and dynamics in 5 DOF. When such a vehicle turns or pitches, a movement in sway and heave is induced. This movement must be accounted for both during nominal operation and during collision avoidance. To this end, we have proposed a novel Flow frame controller, which steers the direction of the vehicle's velocity direction rather than the vehicle orientation. The performance of the CAA algorithm when combined with the Flow frame controller has been analyzed, and we have derived

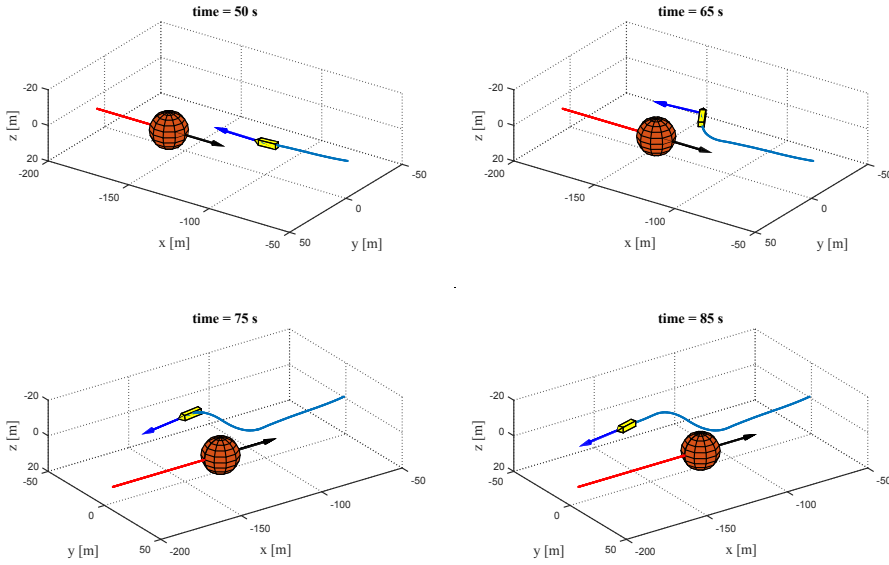


Figure 13.21: Snapshots from the maneuver during run 6. The vehicle is the yellow polyhedron, and the obstacle is the red sphere. The blue line is the vehicle trajectory, while the dashed red line marks the obstacle trajectory. The black arrow denotes the velocity direction of the obstacle, while the blue arrow denotes the velocity direction of the vehicle. The vehicle size is exaggerated for clarity.

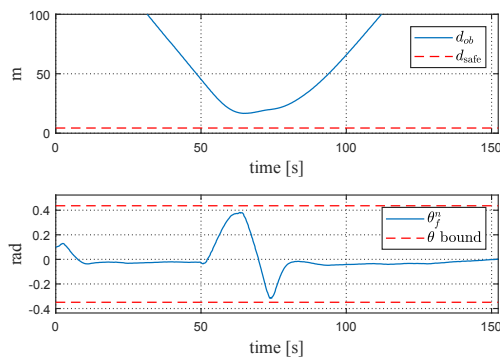


Figure 13.22: The distance d_{ob} between the vehicle and the obstacle during run 6 (top), and Flow frame pitch angle θ_f^n (bottom).

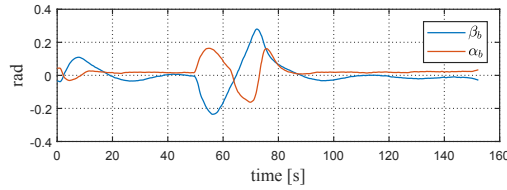


Figure 13.23: The sideslip β_b and angle of attack α_b during run 6.

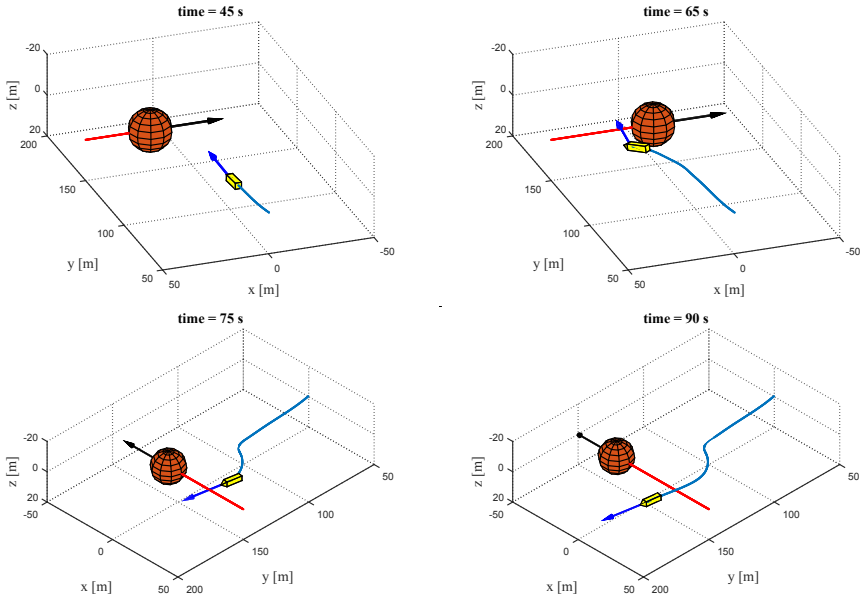


Figure 13.24: Snapshots from run 4, where the obstacle crosses horizontally in front of the vehicle.

bounds on the controller parameters and on the minimum safety distance ensuring that the sway and heave speeds are bounded during the maneuver, and that the control signals remain well defined. Informally, the Flow frame controller must not be too aggressive, and the safety distance not too small. We have used these results to obtain a minimum obstacle distance at which the vehicle must start the collision avoidance maneuver in order to be sure that it turns away in time. Finally, we were then able to prove that the entire collision avoidance maneuver is safe and successful.

Underwater vehicles are often subject to limited surge speed envelopes, with an upper bound due to limited motor power and a lower bound to retain controllability of the vehicle. The proposed collision avoidance algorithm provides a safe velocity direction using the current vehicle speed as an input. Thus, it can be used to accommodate a variety of desired surge speed trajectories, including ones satisfying limited speed envelopes. We have demonstrated this by implementing the algorithm

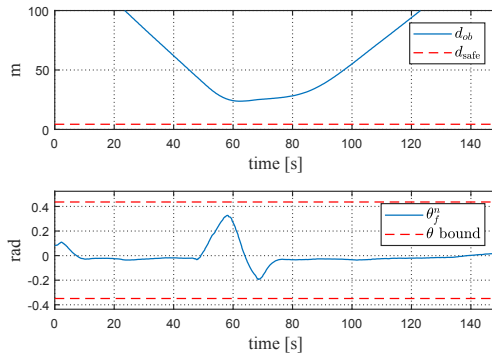


Figure 13.25: The distance d_{ob} between the vehicle and the obstacle during run 4 (top), and Flow frame pitch angle θ_f^n (bottom).

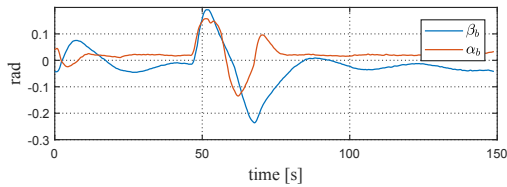


Figure 13.26: The sideslip β_b and angle of attack α_b during run 4.

on a vehicle where we have put the strict requirement of maintaining a constant desired surge speed throughout the maneuver.

The theoretical results have been validated through simulations and through experiments on a survey class autonomous underwater vehicle, the Hugin HUS AUV. While the simulations illustrate the performance of the system under ideal conditions, the experiments further strengthen the results by showing the successful performance on a vehicle where the precise model is not known, the underlying controllers are unavailable and there is a presence of sensor noise and disturbances. Furthermore, the vehicle was set to keep a constant forward thrust rather than maintaining a controlled speed trajectory, showing the applicability of the CAA algorithm also to vehicles where the surge speed is not explicitly controlled.

The design and analysis of the CAA algorithm, both in 2D and 3D, have mainly been concerned with sparse obstacle scenarios where the vehicle can avoid a single obstacle at a time. While this can be argued to be the most common scenario in an underwater domain, we have also described an extension of the algorithm to multiple, clustered obstacles. A detailed analysis of such a scene is beyond the scope of this thesis, but simulations of the proposed approach show promising results.

13.A Functional expressions

The functions $F_u, X_v, Y_v, X_w, Y_w, Z_w, F_q$ and F_r are defined in Section 3.2.2, and reiterated here for convenience:

$$F_u \triangleq \frac{1}{m_{11}} [(m_{22}v_b + m_{25}r_b)r_b - (m_{33}w_b + m_{34}q_b)q_b - d_{11}u_b] \quad (13.116)$$

$$X_v \triangleq \frac{m_{25}^2 - m_{11}m_{55}}{m_{22}m_{55} - m_{25}^2}u_b + \frac{d_{55}m_{25} - d_{25}m_{55}}{m_{22}m_{55} - m_{25}^2}, \quad (13.117)$$

$$Y_v \triangleq \frac{(m_{22} - m_{11})m_{25}}{m_{22}m_{55} - m_{25}^2}u_b - \frac{d_{22}m_{55} - d_{52}m_{25}}{m_{22}m_{55} - m_{25}^2}, \quad (13.118)$$

$$X_w \triangleq \frac{-m_{34}^2 - m_{11}m_{44}}{m_{33}m_{44} - m_{34}^2}u_b + \frac{d_{44}m_{34} - d_{34}m_{44}}{m_{33}m_{44} - m_{34}^2}, \quad (13.119)$$

$$Y_w \triangleq \frac{(m_{11} - m_{33})m_{34}}{m_{33}m_{44} - m_{34}^2}u_b - \frac{d_{33}m_{44} - d_{43}m_{34}}{m_{33}m_{44} - m_{34}^2}, \quad (13.120)$$

$$Z_w \triangleq \frac{BG_z W m_{34}}{m_{33}m_{44} - m_{34}^2}, \quad (13.121)$$

$$\begin{aligned} F_q \triangleq & -\frac{BG_z W m_{33}}{m_{33}m_{44} - m_{34}^2} \sin(\theta_b^n) + \frac{m_{34}d_{33} - m_{33}(d_{43} - (m_{33} - m_{11})u_b)}{m_{33}m_{44} - m_{34}^2}w_b \\ & + \frac{m_{34}(d_{34} - m_{11}u_b) - m_{33}(d_{44} - m_{34}u_b)}{m_{33}m_{44} - m_{34}^2}q_b, \end{aligned} \quad (13.122)$$

$$\begin{aligned} F_r \triangleq & \frac{m_{25}d_{22} - m_{22}(d_{52} + (m_{22} - m_{11})u_b)}{m_{22}m_{55} - m_{25}^2}v_b \\ & + \frac{m_{25}(d_{25} + m_{11}u_b) - m_{22}(d_{55} + m_{25}u_b)}{m_{22}m_{55} - m_{25}^2}r_b. \end{aligned} \quad (13.123)$$

Chapter 14

Conclusions and Future Work

Begin at the beginning, the King said gravely, and go on till you come to the end: then stop.

— Lewis Carroll, *Alice in Wonderland*

This thesis has mainly been concerned with the development and analysis of a collision avoidance algorithm, the constant avoidance angle (CAA) algorithm, in 2D and 3D. We have also investigated a path following algorithm, the integral line of sight (ILOS) algorithm, and provided some new stability results and modifications. Both of these algorithms have been applied to underactuated marine vehicles. This is a wide class of vehicles which can be modeled as if they are steered by a propeller, rudder and, in the 3D case, sternplanes. Thus, there is actuation in surge, yaw and pitch, but not in sway and heave. Rather, the sway and heave speeds are induced when the vehicle is turning and pitching.

During path following, the vehicle has in this thesis been tasked with following straight-line paths. As the vehicle converges to the path, it will cease turning and pitching, and the analysis have showed that the sway speed will converge to zero and the heave speed will converge to a constant equilibrium value. During a collision avoidance maneuver, however, the vehicle will continue to turn and pitch during the entire maneuver. To compensate for this, we have included the underactuated dynamics in the control design by using a course controller in 2D, and a Flow frame controller in 3D, both of which steers the direction of the vehicle's velocity vector rather than the vehicle's orientation.

The ILOS guidance law for straight-line path following aims the vehicle towards a point a certain distance, called the lookahead distance, ahead of it on the path. Thus, when the vehicle is far away from the path, the algorithm will steer the vehicle along a trajectory which is almost perpendicular to the path. However, as the vehicle gets closer, the desired heading becomes more and more parallel to the path, providing a smooth turn onto it. The algorithm is designed to reject disturbances, specifically the disturbance resulting from a constant and irrotational ocean current. In effect, as the integrator builds up, the vehicle is made to aim towards a path which is parallel to the nominal path, but offset a distance proportional to the magnitude of the ocean current. Thus, the vehicle is allowed to move along the path while pointing away from it, counteracting the current.

Previous works on the ILOS guidance law have been able to prove uniform UGAS and ULES convergence properties to the path. We have in this thesis ex-

tended this to the stronger stability result of USGES, which is the strongest stability result possible for a guidance law for vehicles with bounded speed. To do this, we have both employed the well-known comparison lemma, as well as recently developed Lyapunov-sufficient conditions, where the latter serve as an example of a more convenient way to prove USGES. These results hold when the desired forward speed of the vehicle is constant, while in the case when the desired forward speed is time-varying, the integrator is not able to perfectly compensate for the current. However, we show that the cross-track error will remain ultimately bounded, and that the vehicle will converge to the bounded set with UGAS convergence. These results have been shown when the lookahead distance increases with speed. It is, however, straightforward to extend them to a constant lookahead distance. An interesting future line of research is to investigate if the controller can be modified in order to ensure that the system still achieves USGES. Possible venues include the use of ocean current observers, or the use of course control. Both of these approaches has been used in the literature to achieve convergence to curved paths, where the cross track effect of the current varies along the path, again making the integrator unable to perfectly compensate for the current.

For the 2D ILOS law, we have investigated the case when the lookahead distance increases linearly with the vehicle speed. This has in part been motivated by intuition; both an experienced driver of a car and helmsman of a ship will look further ahead when the speed is high. It has also been motivated by practical considerations which arose during implementation of the ILOS guidance law; in vehicles with constrained actuators and limited convergence rate of the underlying controllers, oscillations and overshoot may occur when the lookahead distance is low at high speeds. The guidance law has been shown to provide USGES convergence also with a speed-dependent lookahead distance, and the results have been verified both in simulations and full-scale experiments on an unmanned surface vehicle. An interesting further development would be to investigate the use of more complex functions to determine the lookahead distance, both as functions of speed and distance. By appropriate design of such functions, it may also be possible to investigate using the lookahead distance as an optimization variable in a motion planning algorithm, which would reduce the search space significantly.

In the case of 3D path following, we examined the ILOS guidance law applied to a vehicle which was not neutrally buoyant. While neutral buoyancy is a common assumption, it is difficult to achieve in practice. Indeed, the buoyancy of a vehicle will often change during an operation, as it is dependent on the salinity, temperature and pressure of the water. We provided conditions under which the ILOS guidance law still achieved USGES, and showed how these conditions were stricter due to the positive or negative buoyancy of the vehicle. A topic for future work in 3D path following is to exploit the flexibility offered by operating in 3D space to a higher degree, for example by prioritizing between the convergence speed in the horizontal and the vertical plane.

The third part of the thesis presented the constant avoidance angle algorithm in 2D. This algorithm makes a vehicle avoid a moving obstacle by steering it to either the port or starboard side of an obstacle, while maintaining a constant avoidance angle between the vehicle's velocity vector and the vision cone from the vehicle to the obstacle. Various rules of the road can be implemented by proper design of the

rule used to choose between a clockwise and counter-clockwise maneuver; we have in this thesis implemented a conservative approach where the vehicle moves behind the obstacle. The desired velocity direction is compensated for the obstacle motion, in such a way that it provides a safe heading or course reference at a given vehicle speed. Thus, the speed trajectory of the vehicle can be designed independently of the CAA algorithm, which makes the algorithm suitable for vehicles with a limited speed envelope. We demonstrated this by both implementing the algorithm on a unicycle with an imposed, constant speed, and on an underactuated marine vehicle. The latter keeps a constant forward speed, but has an underactuated component in the total speed of the vehicle, which is thus time-varying. We have shown how the algorithm inherently compensates for such a time-varying speed by adjusting the desired vehicle course accordingly.

In the algorithm analysis, we showed that the vehicle is guaranteed to keep at least a minimum distance from the obstacle, where the minimum distance is a function of the avoidance angle and the obstacle curvature; the larger avoidance angle, the larger minimum distance. Thus, the implementation of the algorithm is not dependent on estimating the obstacle shape, something which reduces the computational complexity associated with the CAA algorithm. We furthermore derived an upper bound on the required yaw rate during the maneuver in the case when the vehicle keeps a constant speed. Thus, we were able to find conditions on the vehicle's controller, on the avoidance angle, and on the switching distance, which guarantee that a constant speed unicycle maintains at least a minimum safety distance to the obstacle. We have furthermore proved that a target-reaching unicycle will safely maneuver through an environment with an obstacle and reach the target position.

The analysis is more complicated when the CAA algorithm is applied to an underactuated marine vehicle, due to the underactuated component in the vehicle's velocity. In addition to making the vehicle speed time-varying and not directly controlled, the underactuated sway dynamics makes the vehicle glide towards the obstacle even as it is turning away from it. To compensate for this, we have applied an underlying course controller, which allows the CAA algorithm to provide references to the vehicle course rather than the vehicle heading. We have furthermore provided conditions under which it is guaranteed that these references are well defined, and under which the sway velocity is bounded by a desired value. This result has finally been used to prove that an underactuated marine vehicle is able to safely achieve both target reaching and path following when in the presence of moving obstacles. We have verified these results both in simulations, where we have employed a model of the Hugin AUV operating in the horizontal plane, and in full-scale experiments with the research vessel R/V Gunnerus.

The CAA algorithm is extended to 3D in the final part of this thesis. In 3D, the algorithm employs the concept of an extended vision cone. This cone is created by measuring the directions to the outline of the obstacle as seen from the vehicle, i.e. the vision cone from the vehicle to the obstacle, and then rotating each ray of this cone a constant avoidance angle away from the obstacle. Thus, a continuum of possible safe directions is provided, each keeping the constant avoidance angle to the obstacle. The extended vision cone is transformed in order to compensate for the obstacle motion, where the idea behind the motion compensation is the

same as in the 2D case. Thus, again, the vehicle speed is used as an input to the algorithm, rather than an output, making the algorithm suitable for vehicles with requirements on the speed, or where speed control is not directly available.

The continuum of safe directions offers flexibility, which we have exploited by implementing an optimization function when choosing among them. Specifically, we have chosen to make the vehicle maximize the difference between the chosen direction and the obstacle's heading and pitch, making the vehicle move behind the obstacle when starting the collision avoidance maneuver. During the maneuver, the safe direction is continuously chosen in order to minimize the required control effort. Finally, we ensure that the chosen direction does not violate the vehicle's pitch limits, a type of safety limit often imposed on vehicles operating in 3D.

The minimization of the required control effort enabled us to build the analysis of the 3D CAA algorithm on the analysis of the 2D algorithm. Specifically, we were able to analyze a horizontal and a vertical maneuver separately. In the case of a 3D kinematic vehicle with nonholonomic constraints in sway and heave and a constant forward speed, we obtained an upper bound on both the required pitch rate and the required yaw rate. Thus, we were able to provide conditions under which the vehicle was guaranteed to safely traverse an environment with obstacles, while keeping the pitch within the required envelope, in order to reach a target. Specifically, we provided conditions on the vehicle's maximum yaw and pitch rate, on the avoidance angle and on the switching distance.

When the 3D CAA algorithm was applied to an underactuated underwater vehicle, we designed a controller to steer the vehicle's velocity direction rather than the vehicle's orientation. We derived conditions on the vehicle's maneuverability under which the Flow frame controller is always feasible, and furthermore derived conditions on the controller parameters and on the avoidance angle in order to ensure that the control signals in the systems were always well defined, and that the induced sway and heave speeds remained within a required bound. Finally, these results were utilized to prove that the vehicle was able to safely maneuver to a target in the presence of a 3D obstacle, and while upholding bounds on the pitch of the vehicle's velocity direction. The results were verified both through simulations, and through full-scale experiments on the Hugin autonomous underwater vehicle. In the simulations, it was furthermore shown how the algorithm can be extended to handle multiple, clustered obstacles.

There are several interesting lines of future research and development of the CAA algorithm which can provide further insight and enhanced results. Extension of the analysis to multi-obstacle scenarios is a natural next step, as is the investigation of multi-agent scenarios. In the latter case, the flexibility offered in 2D by choosing the turning direction, and in 3D when choosing among the safe directions, can be utilized to implement rules of the roads, ensuring safety of the vehicles. However, the use of a constant avoidance angle might be overly conservative when an obstacle or other agent is far away, as the unsafe cone can then become unnecessarily large. A possible solution to this is to let the avoidance angle be time-varying. For example, by increasing the avoidance angle with the inverse of the distance to the obstacle, a higher priority will be given to closer obstacles than to more distant obstacles. Such a distance-dependent avoidance angle can also enhance the capabilities of the algorithm to avoid obstacles with a very high

curvature in the obstacle boundary.

We have focused on keeping the desired vehicle speed independent of the collision avoidance angle throughout this thesis. However, it can also be interesting to investigate different speed trajectories. Custom speed trajectories can be used to implement rules of the roads, or satisfy mission preferences. During path following, for example, it might be better for the vehicle to slow down and let the obstacle pass rather than steer away from the path. It is also possible to control the forward speed so that the total speed of the vehicle remains constant, which might give less conservative theoretical conditions for vehicle safety.

A major limitation of the algorithm is the assumption that the obstacle moves slower than the vehicle. In scenarios where we can assume that the obstacle is at least not actively seeking a collision, it is likely that this assumption can be lifted, or at least weakened.

A strength of the algorithm is that knowledge of the obstacle shape is not required for algorithm implementation. This is in contrast to many other algorithms, where it is required that the obstacle is virtually enlarged in order to guarantee a minimum distance of separation. However, if the vehicle is equipped with the sensors and computational power required to estimate the obstacle shape, it will be interesting to apply the analysis tools developed in this thesis to an algorithm with no avoidance angle, and where the vehicle points towards the tangent to the enlarged obstacle. This would, in effect, be an implementation of the well known velocity obstacle approach, although with more rigorous analysis tools at hand both for unicycles and for underactuated vehicles. Furthermore, the velocity compensation angle developed in this thesis would serve as an analytical method for choosing a desired forward speed.

References

- [1] B. Abdurahman, A. Savvaris, and A. Tsourdos. A Switching LOS Guidance with Relative Kinematics for Path-Following of Underactuated Underwater Vehicles. In *Proc. 20th IFAC World Congress*, pages 2326–2331, Toulouse, France, 2017.
- [2] M. Aicardi, G. Cannata, G. Casalino, and G. Indiveri. On The Stabilization Of The Unicycle Model Projecting A Holonomic Solution. In *Proc. 8th International Symposium on Robotics with Applications*, Maui, HI, USA, 2000.
- [3] A. D. Ames, X. Xu, J. W. Grizzle, and P. Tabuada. Control barrier function based quadratic programs with application to automotive safety systems. In *Proc. 53th IEEE Conference on Decision and Control*, pages 6271–6278, Los Angeles, CA, USA, 2014.
- [4] H. Ashrafiuon, K. R. Muske, and L. C. McNinch. Review of nonlinear tracking and setpoint control approaches for autonomous underactuated marine vehicles. In *Proc. American Control Conference*, pages 5203–5211, Baltimore, MD, USA, 2010.
- [5] D. Bareiss and J. van den Berg. Generalized reciprocal collision avoidance. *The International Journal of Robotics Research*, 34(12):1501–1514, 2015.
- [6] D. Belleter, M. A. Maghenem, C. Paliotta, and K. Y. Pettersen. Observer based path following for underactuated marine vessels in the presence of ocean currents: A global approach. *Automatica*, 100:123–134, 2019.
- [7] D. J. W. Belleter and K. Y. Pettersen. Path following for formations of underactuated marine vessels under influence of constant ocean currents. In *Proc. 53th IEEE Conference on Decision and Control*, pages 4521–4528, Los Angeles, CA, USA, 2014.
- [8] D. J. W. Belleter and K. Y. Pettersen. Path following with disturbance rejection for inhomogeneous formations with underactuated agents. In *Proc. IEEE European Control Conference*, pages 1023–1030, Linz, Austria, 2015.
- [9] V. Bertram. Unmanned Surface Vehicles – A Survey. *Skibsteknisk Selskab, Copenhagen, Denmark*, 2008.

- [10] J. Borenstein and Y. Koren. The Vector Field Histogram–Fast Obstacle Avoidance for Mobile Robots. *IEEE Transactions on Robotics and Automation*, 7(3):278–288, 1991.
- [11] E. Børhaug and K. Y. Pettersen. Cross-track control for underactuated autonomous vehicles. In *Proc. 44th IEEE Conference on Decision and Control*, volume 2005, pages 602–608, Seville, Spain, Dec. 2005.
- [12] E. Børhaug and K. Y. Pettersen. LOS path following for underactuated underwater vehicle. In *Proc. 7th IFAC Conference on Manoeuvring and Control of Marine Craft*, Lisbon, Portugal, 2006.
- [13] E. Børhaug, A. Pavlov, and K. Y. Pettersen. Integral LOS control for path following of underactuated marine surface vessels in the presence of constant ocean currents. In *Proc. 47th IEEE Conf. Decision and Control*, pages 4984–4991, Cancun, Mexico, 2008.
- [14] E. Børhaug, A. Pavlov, E. Panteley, and K. Y. Pettersen. Straight line path following for formations of underactuated surface vessels. *IEEE Transactions on Control Systems Technology*, 19(3):493–506, 2011.
- [15] M. Breivik and T. Fossen. Path following for marine surface vessels. In *Proc. Oceans '04 MTS/IEEE Techno-Ocean '04*, pages 2282–2289, Nov. 2004.
- [16] M. Breivik and T. I. Fossen. Guidance laws for planar motion control. In *Proc. IEEE Conference on Decision and Control*, pages 570–577, Cancun, Mexico, 2008.
- [17] M. Breivik and T. I. Fossen. Guidance laws for autonomous underwater vehicles. In A. V. Inzartsev, editor, *Intelligent Underwater Vehicles*, chapter 4, pages 51–76. I-Tech Education and Publishing, Vienna, Austria, 2009.
- [18] W. Caharija, K. Y. Pettersen, M. Bibuli, P. Calado, E. Zereik, J. Braga, J. T. Gravdahl, A. J. Sørensen, M. Milovanović, and G. Bruzzone. Integral line-of-sight guidance and control of underactuated marine vehicles: Theory, simulations and experiments. *IEEE Transactions on Control Systems Technology*, 24(5), 2016.
- [19] J. Canny and J. Reif. New lower bound techniques for robot motion planning problems. In *Proc. 28th Annual Symposium on Foundations of Computer Science*, pages 49–60, Los Angeles, CA, USA, 1987.
- [20] C. Carbone, U. Ciniglio, F. Corraro, and S. Luongo. A Novel 3D Geometric Algorithm for Aircraft Autonomous Collision Avoidance. In *Proc. 45th IEEE Conference on Decision and Control*, pages 1580–1585, San Diego, CA, USA, 2006.
- [21] A. Chakravarthy and D. Ghose. Obstacle avoidance in a dynamic environment: A collision cone approach. *IEEE Transactions on Systems, Man, and Cybernetics Part A: Systems and Humans*, 28(5):562–574, 1998.

-
- [22] D. E. Chang, S. C. Shadden, J. E. Marsden, and R. Olfati-Saber. Collision Avoidance for Multiple Agent Systems. In *Proc. 42nd IEEE Conference on Decision and Control*, pages 539–543, 2003. ISBN 0780379241.
- [23] Y. Chen, H. Peng, and J. Grizzle. Obstacle avoidance for low-speed autonomous vehicles with barrier function. *IEEE Transactions on Control Systems Technology*, 26(1):194–206, 2018.
- [24] D. V. Dimarogonas and K. J. Kyriakopoulos. Distributed cooperative control and collision avoidance for multiple kinematic agents. In *Proc. 45th IEEE Conference on Decision and Control*, pages 721–725, San Diego, CA, USA, 2006.
- [25] K. D. Do, Z. P. Jiang, and J. Pan. Underactuated ship global tracking under relaxed conditions. *IEEE Transactions on Automatic Control*, 47(9):1529–1536, 2002.
- [26] L. E. Dubins. On curves of minimal length with a constraint on average curvature, and with prescribed initial and terminal positions and tangents. *American Journal of Mathematics*, 79(3):497–516, 1957.
- [27] P. Encarnação and A. Pascoal. Combined trajectory tracking and path following: An application to the coordinated control of autonomous marine craft. In *Proc. 40th IEEE Conference on Decision and Control*, pages 964–969, Orlando, FL, USA, 2001.
- [28] B. O. H. Eriksen, M. Breivik, K. Y. Pettersen, and M. S. Wiig. A modified dynamic window algorithm for horizontal collision avoidance for AUVs. In *Proc. 2016 IEEE Conference on Control Applications (CCA)*, pages 499–506, Buenos Aires, Brazil, 2016.
- [29] B. O. H. Eriksen, E. F. Wilthil, A. L. Flåten, E. F. Brekke, and M. Breivik. Radar-based maritime collision avoidance using dynamic window. In *IEEE Aerospace Conference Proceedings*, Big Sky, MT, USA, 2018.
- [30] G. Fasano, D. Accardo, A. Moccia, C. Carbone, U. Ciniglio, F. Corraro, and S. Luongo. Multi-Sensor-Based Fully Autonomous Non-Cooperative Collision Avoidance System for Unmanned Air Vehicles. *Journal of Aerospace Computing, Information, and Communication*, 5(10):338–360, 2008.
- [31] A. Filotheou, A. Nikou, and D. V. Dimarogonas. Decentralized Control of Uncertain Multi-Agent Systems with Connectivity Maintenance and Collision Avoidance. In *Proc. European Control Conference*, Limassol, Cyprus, 2018.
- [32] P. Fiorini and Z. Shiller. Motion planning in dynamic environments using velocity obstacles. *The International Journal of Robotics Research*, 17(7):760–772, 1998.
- [33] A. L. Flåten and E. F. Brekke. Stability of Line-Of-Sight Based Trajectory-Tracking in Two Dimensions. In *Proc. 1st IEEE Conference on Control Technology and Applications*, pages 760–765, Kohala Coast, HI, USA, 2017.

- [34] T. Fossen, M. Breivik, and R. Skjetne. Line-of-sight path following of under-actuated marine craft. In *Proc. 6th IFAC Conference on Manoeuvring and Control of Marine Craft*, pages 244–249, Girona, Spain, 2003.
- [35] T. I. Fossen. *Handbook of marine craft hydrodynamics and motion control*. John Wiley & Sons, 2011. ISBN 978-1-119-99149-6.
- [36] T. I. Fossen and K. Y. Pettersen. On uniform semiglobal exponential stability (USGES) of proportional line-of-sight guidance laws. *Automatica*, 50(11):2912–2917, 2014.
- [37] T. I. Fossen, K. Y. Pettersen, and R. Galeazzi. Line-of-sight path following for Dubins paths with adaptive sideslip compensation of drift forces. *IEEE Transactions on Control Systems Technology*, 23(2):820–827, 2014.
- [38] D. Fox, W. Burgard, and S. Thrun. The dynamic window approach to collision avoidance. *IEEE Robotics and Automation Magazine*, 4(1):23–33, 1997.
- [39] E. Fredriksen and K. Pettersen. Global κ -exponential way-point maneuvering of ships: Theory and experiments. *Automatica*, 42(4):677–687, Apr. 2006.
- [40] T. Gawron and M. M. Michałek. VFO path following control strategy for constrained motion of car-like robots with invariant funnels computed using the SOS optimization. In *Proc. 2nd IEEE Conference on Control Technology and Applications*, Copenhagen, Denmark, 2018.
- [41] P. Glotfelter, J. Cortes, and M. Egerstedt. Nonsmooth Barrier Functions With Applications to Multi-Robot Systems. *IEEE Control Systems Letters*, 1(2):310–315, 2017.
- [42] I. B. Hagen, D. K. M. Kufoalor, E. F. Brekke, and T. A. Johansen. MPC-based collision avoidance Strategy for existing marine vessel guidance systems. In *Proc. IEEE International Conference on Robotics and Automation*, Brisbane, Australia, 2018.
- [43] P. E. Hagen, N. Storkersen, K. Vestgard, and P. Kartvedt. The HUGIN 1000 autonomous underwater vehicle for military applications. In *Proc. Oceans 2003*, pages 1141–1145, San Diego, CA, USA, 2003.
- [44] A. Healey and D. Lienard. Multivariable sliding mode control for autonomous diving and steering of unmanned underwater vehicles. *Oceanic Engineering, IEEE Journal of*, 18(3):327–339, 1993.
- [45] R. Hegde and D. Panagou. Multi-Agent Motion Planning and Coordination in Polygonal Environments using Vector Fields and Model Predictive Control. In *Proc. IEEE European Control Conference*, pages 1856–1861, Aalborg, Denmark, 2016.
- [46] G. M. Hoffmann and C. J. Tomlin. Decentralized cooperative collision avoidance for acceleration constrained vehicles. In *Proc. 47 IEEE Conference on Decision and Control*, pages 4357–4363, Cancun, Mexico, 2008.

-
- [47] M. Hoy, A. S. Matveev, and A. V. Savkin. Algorithms for collision-free navigation of mobile robots in complex cluttered environments: a survey. *Robotica*, 33(03):463–497, 2014.
- [48] G. Indiveri, M. Aicardi, and G. Casalino. Robust global stabilization of an underactuated marine vehicle on a linear course by smooth time-invariant feedback. In *Proc. 39th IEEE Conference on Decision And Control*, pages 2156–2161, Sydney, Australia, 2000.
- [49] G. Indiveri, M. Pino, M. Aicardi, and G. Casalino. Nonlinear Time-Invariant Feedback Control Of An Underactuated Marine Vehicle Along A Straight Course. In *Proc. 5th IFAC Conference on Manoeuvring and Control of Marine Craft*, pages 221–226, Aalborg, Denmark, 2000.
- [50] Y. I. Jenie, E.-J. Van Kampen, C. C. de Visser, J. Ellerbroek, and J. M. Hoekstra. Three-Dimensional Velocity Obstacle Method for UAV Deconflicting Maneuvers. In *Proc. AIAA Guidance, Navigation, and Control Conference*, Kissimmee, FL, USA, 2015.
- [51] Y. I. Jenie, E.-J. van Kampen, C. C. de Visser, J. Ellerbroek, and J. M. Hoekstra. Three-Dimensional Velocity Obstacle Method for Uncoordinated Avoidance Maneuvers of Unmanned Aerial Vehicles. *Journal of Guidance, Control, and Dynamics*, 39(10):2312–2323, 2016.
- [52] T. A. Johansen and T. I. Fossen. Control allocation - a survey. *Automatica*, 49(5):1087–1103, 2016.
- [53] T. A. Johansen, T. Perez, and A. Cristofaro. Ship collision avoidance and COLREGs compliance using simulation-based control behavior selection with predictive hazard assessment. *IEEE Transactions on Intelligent Transportation Systems*, 17(12):3407–3422, 2016.
- [54] N. Khaled and N. G. Chalhoub. A self-tuning guidance and control system for marine surface vessels. *Nonlinear Dynamics*, 73(1-2):897–906, 2013.
- [55] H. K. Khalil. *Nonlinear Systems*. Pearson Education International inc., 3rd edition, 2000.
- [56] O. Khatib. Real-time obstacle avoidance for manipulators and mobile robots. *The International Journal of Robotics Research*, 5(1):90–98, 1986.
- [57] M. Kim and J. H. Oh. Study on optimal velocity selection using velocity obstacle (OVVO) in dynamic and crowded environment. *Autonomous Robots*, 40(8):1459–1470, 2016.
- [58] Y. Koren and J. Borenstein. Potential field methods and their inherent limitations for mobile robot navigation. In *Proc. IEEE International Conference on Robotics and Automation*, pages 1398–1404, Sacramento, CA, USA, 1991.
- [59] J. K. Kuchar and L. C. Yang. A review of conflict detection and resolution modeling methods. *IEEE Transactions on Intelligent Transportation Systems*, 1(4):179–189, 2000.

- [60] Y. Kuwata, M. T. Wolf, D. Zarzhitsky, and T. L. Huntsberger. Safe maritime autonomous navigation with COLREGs, using velocity obstacles. *IEEE Journal of Oceanic Engineering*, 39(1):110–119, 2014.
- [61] E. Lalish and K. A. Morgansen. Decentralized Reactive Collision Avoidance for Multivehicle Systems. In *Proc. 47th IEEE Conference on Decision and Control Decision Control*, Cancun, Mexico, 2008.
- [62] E. Lalish and K. A. Morgansen. Distributed reactive collision avoidance. *Autonomous Robots*, 32(3):207–226, 2012.
- [63] L. Lapierre, R. Zapata, and P. Lepinay. Combined path-following and obstacle avoidance control of a wheeled robot. *The International Journal of Robotics Research*, 26(4):361–375, 2007.
- [64] D. N. Lee. Guiding Movement by Coupling Taus. *Ecological Psychology*, 10(3-4):221–250, 1998.
- [65] G. Leitmann and J. Skowronski. Avoidance control. *Journal of Optimization Theory and Applications*, 23(4):581–591, 1977.
- [66] A. M. Lekkas and T. I. Fossen. A time-varying lookahead distance guidance law for path following. In *Proc. 9th IFAC Conference on Manoeuvring and Control of Marine Craft*, pages 398–403, Arenzano, Italy, 2012.
- [67] A. M. Lekkas and T. I. Fossen. Integral LOS path following for curved paths based on a monotone cubic hermite spline parametrization. *IEEE Transactions on Control Systems Technology*, 22(6):2287–2301, 2014.
- [68] A. M. Lekkas and T. I. Fossen. Minimization of cross-track and along-track errors for path tracking of marine underactuated vehicles. In *Proc. IEEE European Control Conference*, pages 3004–3010, Strasbourg, France, 2014.
- [69] Z. Liu, Y. Zhang, X. Yu, and C. Yuan. Unmanned surface vehicles: An overview of developments and challenges. *Annual Reviews in Control*, 41: 71–93, 2016.
- [70] A. Loria and E. Panteley. Cascaded nonlinear time-varying systems: analysis and design. In F. Lamnabhi-Lagarrigue, A. Loria, and E. Panteley, editors, *Advanced Topics in Control Systems Theory*, chapter 2, pages 23–64. Springer Verlag, London, 2004.
- [71] M. Maghenem, D. J. W. Belleter, C. Paliotta, and K. Y. Pettersen. Observer Based Path Following for Underactuated Marine Vessels in the Presence of Ocean Currents: A Local Approach. In *Proc. 20th IFAC World Congress*, Toulouse, France, 2017.
- [72] S. Mastellone, D. M. Stipanović, C. R. Graunke, K. A. Intlekofer, and M. W. Spong. Formation control and collision avoidance for multi-agent non-holonomic systems: Theory and experiments. *International Journal of Robotics Research*, 27(1):107–126, 2008.

-
- [73] A. S. Matveev, C. Wang, and A. V. Savkin. Real-time navigation of mobile robots in problems of border patrolling and avoiding collisions with moving and deforming obstacles. *Robotics and Autonomous Systems*, 60(6):769–788, 2012.
- [74] S. Moe and K. Y. Pettersen. Set-Based Line-of-Sight (LOS) Path Following with Collision Avoidance for Underactuated Unmanned Surface Vessels under the Influence of Ocean Currents. In *Proc. 1st IEEE Conference on Control Technology and Applications*, Kohala Coast, HI, USA, 2017.
- [75] S. Moe, W. Caharija, K. Y. Pettersen, and I. Schjølberg. Path following of underactuated marine surface vessels in the presence of unknown ocean currents. In *Proc. American Control Conference*, Portland, OR, USA, 2014.
- [76] L. Moreira, T. I. Fossen, and C. Guedes Soares. Path following control system for a tanker ship model. *Ocean Engineering*, 34(14-15):2074–2085, 2007.
- [77] J. Nocedal and S. J. Wright. *Numerical optimization*. Springer Science, 1999. ISBN 0-387-98793-2.
- [78] E. Owen and L. Montano. Motion planning in dynamic environments using the velocity space. In *Proc. IEEE/RSJ International Conference on Intelligent Robots and Systems*, Edmonton, Canada, 2005.
- [79] L. Pallottino, V. G. Scordio, E. Frazzoli, A. Bicchi, and E. Frazzoli. Decentralized cooperative policy for conflict resolution in multi-vehicle systems. *IEEE Transactions on Robotics*, 23(6):1170–1183, 2007.
- [80] D. Panagou. Motion Planning and Collision Avoidance using Navigation Vector Fields. In *Proc. IEEE International Conference on Robotics and Automation*, pages 2513–2518, Hong Kong, China, 2014.
- [81] D. Panagou. A Distributed Feedback Motion Planning Protocol for Multiple Unicycle Agents of Different Classes. *IEEE Transactions on Automatic Control*, 62(3):1178–1193, 2017.
- [82] D. Panagou, D. M. Stipanovic, and P. G. Voulgaris. Distributed Coordination Control for Multi-Robot Networks Using Lyapunov-Like Barrier Functions. *IEEE Transactions on Automatic Control*, 61(3):617–632, 2016.
- [83] T. Paul, T. R. Krogstad, and J. Tommy. Modelling of UAV formation flight using 3D potential field. *Simulation Modelling Practice and Theory*, 16(9):1453–1462, 2008.
- [84] K. Y. Pettersen. Lyapunov sufficient conditions for uniform semiglobal exponential stability. *Automatica*, 78, 2017.
- [85] K. Y. Pettersen and O. Egeland. Exponential stabilization of an underactuated surface vessel. In *Proc. 35th IEEE Conference on Decision and Control*, pages 1391–1396, Kobe, Japan, 1996.

- [86] K. Y. Pettersen and E. Lefeber. Way-point tracking control of ships. In *Proc. 40th IEEE Conference on Decision and Control*, pages 940–945, Orlando, FL, 2001.
- [87] K. Y. Pettersen and H. Nijmeijer. Tracking control of an underactuated surface vessel. In *Proc. 37th IEEE Conference on Decision and Control*, Tampa, FL, USA, 1998.
- [88] A. Rahmani, K. Kosuge, T. Tsukamaki, and M. Mesbahi. Multiple UAV deconfliction via navigation functions. In *Proc. AIAA Guidance, Navigation and Control Conference and Exhibit*, pages 1–8, Honolulu, HI, USA, 2008. ISBN 9781563479458.
- [89] E. Rimon and D. E. Koditschek. Exact robot navigation using artificial potential functions. *Robotics and Automation, IEEE Transactions on*, 8(5): 501–518, 1992.
- [90] E. J. Rodríguez-Seda. Decentralized trajectory tracking with collision avoidance control for teams of unmanned vehicles with constant speed. In *Proc. American Control Conference*, pages 1216–1223, Portland, OR, USA, 2014.
- [91] E. J. Rodríguez-Seda, C. Tang, M. W. Spong, and D. M. Stipanovi. Trajectory tracking with collision avoidance for nonholonomic vehicles with acceleration constraints and limited sensing. *The International Journal of Robotics Research*, 33(12):1569–1592, Aug. 2014.
- [92] E. J. Rodríguez-Seda, D. M. Stipanović, and M. W. Spong. Guaranteed Collision Avoidance for Autonomous Systems with Acceleration Constraints and Sensing Uncertainties. *Journal of Optimization Theory and Applications*, 168(3):1014–1038, 2016.
- [93] G. Roussos, D. V. Dimarogonas, and K. J. Kyriakopoulos. 3D navigation and collision avoidance for nonholonomic aircraft-like vehicles. *International Journal of Adaptive Control and Signal Processing*, 24:900–920, 2010.
- [94] S. Russell and P. Norvig. *Artificial Intelligence: A Modern Approach*. Pearson Education, 2nd edition, 2003. ISBN 0-13-080302-2.
- [95] A. V. Savkin and C. Wang. A simple biologically inspired algorithm for collision-free navigation of a unicycle-like robot in dynamic environments with moving obstacles. *Robotica*, 31(6):993–1001, 2013.
- [96] A. V. Savkin and C. Wang. Seeking a path through the crowd: Robot navigation in unknown dynamic environments with moving obstacles based on an integrated environment representation. *Robotics and Autonomous Systems*, 62(10):1568–1580, 2014.
- [97] S. Shimoda, Y. Kuroda, and K. Iagnemma. Potential Field Navigation of High Speed Unmanned Ground Vehicles on Uneven Terrain. In *Proc. IEEE International Conference on Robotics and Automation*, pages 2828–2833, Barcelona, Spain, 2005.

-
- [98] R. Skjetne, M. E. N. Sørensen, M. Breivik, S. A. T. Værnø, A. H. Brodtkorb, A. J. Sørensen, Ø. K. Kjerstad, V. Calabrò, and B. O. Vinje. AMOS DP research cruise 2016: academic full-scale testing of experimental dynamic positioning control algorithms onboard R/V Gunnerus. In *Proc. ASME 36th Int. Conf. Ocean, Offshore Arctic Eng*, Trondheim, Norway, 2017.
- [99] A. L. Smith, D. M. Coulter, and C. S. Jones. UAS Collision Encounter Modeling and Avoidance Algorithm Development for Simulating Collision Avoidance. In *Proc. AIAA Modeling and Simulations Technologies Conference and Exhibit*, Honolulu, HI, USA, 2018.
- [100] J. Snape, J. V. D. Berg, S. J. Guy, and D. Manocha. The hybrid reciprocal velocity obstacle. *IEEE Transactions on Robotics*, 27(4):696–706, 2011.
- [101] O. J. Sjørdalen and O. Egeland. Exponential stabilization of nonholonomic chained systems. *IEEE Transactions on Automatic Control*, 40(1):35–49, 1995.
- [102] A. J. Sørensen. Structural issues in the design and operation of marine control systems. *Annual Reviews in Control*, 29(1):125–149, 2005.
- [103] T. Statheros, G. Howells, and K. M. Maier. Autonomous Ship Collision Avoidance Navigation Concepts, Technologies and Techniques. *Journal of Navigation*, 61(01):129–142, 2008.
- [104] C. Tam, R. Bucknall, and A. Greig. Review of Collision Avoidance and Path Planning Methods for Ships in Close Range Encounters. *The Journal of Navigation*, 62(2009):455–476, 2009.
- [105] H. Teimoori and A. V. Savkin. A biologically inspired method for robot navigation in a cluttered environment. *Robotica*, 28(5):637–648, 2010.
- [106] J. Van Den Berg, M. Lin, and D. Manocha. Reciprocal velocity obstacles for real-time multi-agent navigation. In *Proc. IEEE International Conference on Robotics and Automation*, pages 1928–1935, Pasadena, CA, USA, 2008.
- [107] J. van den Berg, S. J. Guy, M. Lin, and D. Manocha. Reciprocal n-Body Collision Avoidance. In G. Pradalier, Cédric and Siegwart, Roland and Hirzinger, editor, *Robotics Research*, volume 70 of *Springer Tracts in Advanced Robotics*, pages 3–19. Springer Berlin Heidelberg, 2011.
- [108] J. van den Berg, J. Snape, S. J. Guy, and D. Manocha. Reciprocal collision avoidance with acceleration-velocity obstacles. In *Proc. IEEE International Conference on Robotics and Automation*, pages 3475–3482, Shanghai, China, 2011.
- [109] C. Wang, A. V. Savkin, and M. Garrett. A Strategy for Safe 3D Navigation of Non-Holonomic Under-Actuated Robots among Moving Obstacles. *Robotica*, 36(2):275–927, 2018.

- [110] L. Wang, A. D. Ames, and M. Egerstedt. Safety barrier certificates for collisions-free multirobot systems. *IEEE Transactions on Robotics*, 33(3): 661–674, 2017.
- [111] M. S. Wiig, K. Y. Pettersen, and T. R. Krogstad. Uniform semiglobal exponential stability of integral line-of-sight guidance laws. In *Proc. 10th IFAC Conference on Manoeuvring and Control of Marine Craft*, pages 61–68, Copenhagen, Denmark, 2015.
- [112] M. S. Wiig, W. Caharija, T. R. Krogstad, and K. Y. Pettersen. Integral Line-of-Sight Guidance of Underwater Vehicles Without Neutral Buoyancy. In *Proc. 10th IFAC Conference on Control Applications in Marine Systems*, pages 590–597, Trondheim, Norway, 2016.
- [113] M. S. Wiig, K. Y. Pettersen, and T. R. Krogstad. A reactive collision avoidance algorithm for vehicles with underactuated dynamics. In *Proc. 56th IEEE Conference on Decision and Control*, pages 1452–1459, Melbourne, Australia, 2017.
- [114] M. S. Wiig, K. Y. Pettersen, and A. V. Savkin. A reactive collision avoidance algorithm for nonholonomic vehicles. In *Proc. 1st IEEE Conference on Control Technology and Applications*, Kohala Coast, HI, USA, 2017.
- [115] M. S. Wiig, K. Y. Pettersen, and T. R. Krogstad. A 3D Reactive Collision Avoidance Algorithm for Nonholonomic Vehicles. In *Proc. 2nd IEEE Conference on Control Technology and Applications*, Copenhagen, Denmark, 2018.
- [116] M. S. Wiig, K. Y. Pettersen, and T. R. Krogstad. A 3D Reactive Collision Avoidance Algorithm for Underactuated Vehicles. In *Proc. 57th IEEE Conference on Decision and Control*, Miami Beach, FL, USA, 2018.
- [117] M. S. Wiig, K. Y. Pettersen, E.-L. M. Ruud, and T. R. Krogstad. An Integral Line-of-Sight Guidance Law with a Speed-dependent Lookahead Distance. In *Proc. IEEE European Control Conference*, pages 1269–1276, Limassol, Cyprus, 2018.
- [118] M. S. Wiig, K. Y. Pettersen, and T. R. Krogstad. A 3D Reactive Collision Avoidance Algorithm for Underactuated Underwater Vehicles. *Journal of Field Robotics*, 2019. Submitted.
- [119] M. S. Wiig, K. Y. Pettersen, and T. R. Krogstad. Collision Avoidance for Underactuated Marine Vehicles Using the Constant Avoidance Angle Algorithm. *IEEE Transactions on Control Systems Technology*, 2019. Accepted, in press.
- [120] D. Wilkie, J. Van Den Berg, and D. Manocha. Generalized velocity obstacles. In *Proc. IEEE/RSJ International Conference on Intelligent Robots and Systems*, pages 5573–5578, St. Louis, MA, USA, 2009.

- [121] X. Yang, L. M. Alvarez, and T. Bruggemann. A 3D collision avoidance strategy for UAVs in a non-cooperative environment. *Journal of Intelligent and Robotic Systems: Theory and Applications*, 70(1–4):315–327, 2013.